

# UC Riverside

## UC Riverside Electronic Theses and Dissertations

### Title

Plasmonic Interrogation of Biomimetic Systems for Enhanced Toxicity Assays

### Permalink

<https://escholarship.org/uc/item/95m209cf>

### Author

Hinman, Samuel S.

### Publication Date

2017

### Copyright Information

This work is made available under the terms of a Creative Commons Attribution License, available at <https://creativecommons.org/licenses/by/4.0/>

Peer reviewed|Thesis/dissertation

UNIVERSITY OF CALIFORNIA  
RIVERSIDE

Plasmonic Interrogation of Biomimetic Systems for Enhanced Toxicity Assays

A Dissertation submitted in partial satisfaction  
of the requirements for the degree of

Doctor of Philosophy

in

Environmental Toxicology

by

Samuel Stuart Hinman

June 2017

Dissertation Committee:

Dr. Quan Cheng, Chairperson

Dr. Yinsheng Wang

Dr. Wenwan Zhong

Copyright by  
Samuel Stuart Hinman  
2017

The Dissertation of Samuel Stuart Hinman is approved:

---

---

---

Committee Chairperson

University of California, Riverside

# ACKNOWLEDGEMENTS

## ■ PERSONAL ACKNOWLEDGEMENTS

I owe the majority of my successes in graduate school to my advisor, Prof. Jason Cheng. Dr. Cheng has been supportive of me since I first visited UCR in the spring of 2012. During our initial conversation, he got me extremely excited about the opportunity of designing electrochemical sensors in his research group. To date, this still has not happened. However, he has given me the freedom to perform the research that I find interesting, and always provided trust to accomplish objectives on my own schedule. I have had many opportunities as a part of his group for both personal and professional development, many provided by Dr. Cheng, and I will always be grateful for those. As I think about my own career, I will absolutely strive to be the kind of advisor that Dr. Cheng is, getting to know his mentees on a personal level and giving them room to grow; this comfort and freedom has been essential for my own research creativity and happiness within the group.

My dissertation committee members, Prof. Yinsheng Wang and Prof. Wenwan Zhong, deserve recognition, as they also have provided me with academic and professional support over the past five years. I have requested numerous letters of recommendation and received sound advice on many occasions from each of them, for which I will always be grateful. The student affairs officer of my program, Dawn Loyola, is thanked in the same regard, as she has always been willing to assist and answer questions in a kind and helpful manner.

I have been lucky to work with many talented scientists in Cheng Lab. Dr. Chih-Yuan (Derek) Chen was my assigned mentor when I joined the lab and got me started on my first project, eventually leading to our first co-authored paper which was a major milestone in my scientific career. He was patient and happy to teach, and I will forever be grateful that he got me off to such a strong start in research. Charles Ruiz joined the group during my third year, and was not only a brilliant scientist, making substantial contributions to multiple projects in this dissertation, but also a great friend. I have had the pleasure of working with multiple talented undergraduates, most notably, Romie Nguyen and Meghann Ma. Romie was a tireless worker who put a significant amount of time into a mass spectrometry project that was not featured in this dissertation, and many newer students arrived assuming that she was another graduate student based on her knowledge base and work ethic. Meghann also worked very hard in the group, preparing batch after batch of lipid vesicles at a time when we were going through them extremely quickly. I would like to thank our current postdoctoral researcher, Dr. Kristy McKeating, for all of our shared conversations and advice she has given me over the past year. She is truly an amazing friend, and my research and learning experiences have been substantially improved by her presence.

When experiments or other parts of my academic life weren't going well, I felt like I was always able to turn to my family and friends I had met at UCR, who made this area truly feel like home for perhaps the first time in my life. Both Lauren Walker and Corey Griffith stand out as two people I will always be able to turn to, and I am especially thankful to have met them both. I will cherish the times I have had with them,

in addition to those I have had with Jon Ashby, Nicole and Preston Williams, Melissa Morgan, and Yuxiang Cui. My family, notably my parents, Tim and Barb, and my youngest brother, Harry, have been instrumental to my happiness in graduate school, and I have appreciated the opportunity to go home nearly every weekend to spend time with them. I have always looked forward to those weekends (and occasional weekdays), in addition to vacations where we're also able to bond with my other brother, Albert, and his fiancé, Shelby.

Finally, I would like to thank my cats, Bonnie and Korra, for keeping me sane throughout graduate school, and who won't know or care that I wrote this.

## ■ PROFESSIONAL ACKNOWLEDGEMENTS

This dissertation was supported by a T32 training grant in Environmental Toxicology (T32 ES018827), funded by the National Institute of Environmental Health Sciences (NIEHS), as well as a Graduate Research Mentorship Program (GRMP) fellowship and a Dissertation Year Program (DYP) fellowship, both awarded by the Graduate Division at UC Riverside, and a Tejal Reddy Endowed Graduate Award, provided by the College of Natural and Agricultural Sciences (CNAS) at UC Riverside. Funding for conference travel was provided by the Graduate Student Association (GSA) at UC Riverside, an Earle C. Anthony Graduate Student Travel Award from the Graduate Division at UC Riverside, and T. Roy Fukuto endowment funds for Environmental Toxicology student travel.

I would like to thank the numerous collaborators our group has been lucky enough to work with. I met Dr. Thomas Wilkop during one of his visits to UCR during the spring of 2014 when he was performing maintenance on our SPR imager. Not only is he a brilliant engineer, but he also has wonderful ideas that led to the publication of my second paper. He was helpful throughout the experimental design and manuscript review processes, with a critical eye for discrepancies and a strong desire to make sure we were sending the message we wanted to the scientific community. My luck in working with strong collaborators continued with Prof. Ling Peng at Aix-Marseilles Université. She is constant and consistent in her communication, and pays exceptionally strong attention to detail throughout experiments and manuscript review. I was perpetually impressed with how hands-on someone could be with my research from nearly 6,000 miles away. I hold her leadership skills in very high regard, as she was able to bring additional groups and researchers on to the project, which substantially increased its impact.

## ■ COPYRIGHT ACKNOWLEDGEMENTS

The text in the “Lipid Membrane Models” section of Chapter 1 of this dissertation, in part or in full, is a reprint of the material as it appears in: Hinman, S. S. and Cheng, Q. Bioinspired Assemblies and Plasmonic Interfaces for Electrochemical Biosensing. *J. Electroanal. Chem.* **2016**, 781, 136-146. The co-author listed in that publication, Prof. Quan Cheng, provided guidance and editing for the work.

The text and figures in Chapter 2 and Appendix A of this dissertation, in part or in full, are a reprint of the material as it appears in: Hinman, S. S., et al. Mix and Match:

Coassembly of Amphiphilic Dendrimers and Phospholipids Creates Robust, Modular and Controllable Interfaces. *ACS Appl. Mater. Interfaces* **2017**, 9, 1029-1035. The co-author listed in that publication, Charles J. Ruiz, optimized and performed the SPR surfactant rinse assays. The co-author listed in that publication, Meghann C. Ma, prepared the majority of the hybrid vesicles used for analytical studies. The co-authors listed in that publication, Yu Cao and Jingjie Tang, synthesized the amphiphilic dendrimers. The co-author listed in that publication, Suzanne Giorgio, performed all electron microscopy analyses. The co-authors listed in that publication, Erik Laurini, Paulo Posocco, and Sabrina Pricl, designed and performed all computational simulations. The co-authors listed in that publication, Prof. Ling Peng and Prof. Quan Cheng, directed and supervised the research which forms the basis for Chapter 2 and Appendix A.

The text and figures in Chapter 3 and Appendix B of this dissertation, in part or in full, are a reprint of the material as it appears in: Hinman, S. S., et al. On-Demand Formation of Supported Lipid Membrane Arrays by Trehalose-Assisted Vesicle Delivery for SPR Imaging. *ACS Appl. Mater. Interfaces* **2014**, 7, 17122-17130. The co-author listed in that publication, Charles J. Ruiz, optimized the rehydration flow rate for supported lipid bilayer formation. The co-authors listed in that publication, Dr. Thomas E. Wilkop and Prof. Quan Cheng, directed and supervised the research which forms the basis for Chapter 3 and Appendix B.

The text and figures in Chapter 4 and Appendix C of this dissertation, in part or in full, are a reprint of the material as it appears in: Hinman, S. S., et al. DNA Linkers and Diluents for Ultrastable Gold Nanoparticle Bioconjugates in Multiplexed Assay

Development. *Anal. Chem.* **2017**, 89, 4272-4279. The co-author listed in that publication, Dr. Kristy S. McKeating, assisted in nanoparticle conjugation and experimental design. The co-author listed in that publication, Prof. Quan Cheng, directed and supervised the research which forms the basis for Chapter 4 and Appendix C.

The text and figures in Chapter 5 and Appendix D of this dissertation, in part or in full, are a reprint of the material as it appears in: Hinman, S. S., et al. Nanoglassified, Optically-Active Monolayer Films of Gold Nanoparticles for *in Situ* Orthogonal Detection by Localized Surface Plasmon Resonance and Surface-Assisted Laser Desorption/Ionization-MS. *Anal. Chem.* **2014**, 86, 11942-11945. The co-author listed in that publication, Dr. Chih-Yuan Chen, developed the initial fabrication protocol and assisted in experimental design. The co-author listed in that publication, Dr. Jicheng Duan, provided assistance in the mass spectrometry data collection and interpretation. The co-author listed in that publication, Prof. Quan Cheng, directed and supervised the research which forms the basis for Chapter 5 and Appendix D.

The text and figures in Chapter 6 and Appendix E of this dissertation, in part or in full, are a reprint of the material as it appears in: Hinman, S. S., et al. Calcinated Gold Nanoparticle Arrays for On-Chip, Multiplexed and Matrix-Free Mass Spectrometric Analysis of Peptides and Small Molecules. *Nanoscale* **2016**, 8, 1665-1675. The co-author listed in that publication, Dr. Chih-Yuan Chen, developed the fabrication protocol and performed the mass spectrometry measurements. The co-author listed in that publication, Dr. Jicheng Duan, provided assistance in the mass spectrometry data collection and

interpretation. The co-author listed in that publication, Prof. Quan Cheng, directed and supervised the research which forms the basis for Chapter 6 and Appendix E.

This dissertation is dedicated to my parents, Barbara and Timothy Hinman,  
for their constant love, support, and encouragement.

## ABSTRACT OF THE DISSERTATION

Plasmonic Interrogation of Biomimetic Systems for Enhanced Toxicity Assays

by

Samuel Stuart Hinman

Doctor of Philosophy, Graduate Program in Environmental Toxicology  
University of California, Riverside, June 2017  
Dr. Quan Cheng, Chairperson

In light of their escalating exposure to possible environmental toxicants, there are many biological systems that need to be evaluated in a resource and time efficient manner. Understanding how toxicants behave in relation to their physicochemical properties and within complex biological media is especially important toward developing a stronger scientific foundation of these systems so that adequate regulatory decisions may be made. While there are many emerging methods available for the detection and characterization of these chemicals, nanotechnology has presented itself as a promising alternative toward creating more efficient assays. In particular, metallic nanoparticles and thin films exhibit unique optical properties that allow for highly sensitive and multiplexed studies to be performed. These plasmonic materials often preclude the use of molecular tags and labels, enabling direct characterizations and enhancing the throughput of biomolecular studies. However, their lack of specificity toward certain targets and potential toxicity has thus far precluded their widespread use in toxicity testing.

The cell membrane, a natural signal transducer, represents one of the fundamental structures for biological recognition and communication. These interfaces principally function as a selective barrier to exogenous materials, including ions, signaling molecules, growth factors, and toxins; therefore, understanding interactions at membrane interfaces is a vital step in elucidating how biological responses are effected. Supported lipid bilayers, which may easily be tailored in composition and complexity, are ideal interfaces for coupling to plasmonic assays since they may be supported in close proximity to metallic nanoparticles and thin films, where measurements are most sensitive. This research will focus on the coupling of plasmonic materials and biomimetic interfaces to increase the sensitivity, efficiency, and throughput of conventional toxicity assays. The fabrication of new plasmonic materials for membrane-based assays is presented, as well as method developments in membrane array formation and opportunities for hyphenation with complementary analytical techniques.

## TABLE OF CONTENTS

Acknowledgements . . . . .	iv
Abstract of the Dissertation . . . . .	xii
List of Figures . . . . .	xvii
List of Tables . . . . .	xxii
<b>CHAPTER 1: Plasmonic Materials and Interfacial Recognition Schemes for Environmental Toxin Analysis . . . . .</b>	<b>1</b>
Introduction . . . . .	1
Lipid Membrane Models . . . . .	2
Surface Plasmon Resonance Biosensors . . . . .	11
Hyphenated Analysis with Mass Spectrometry . . . . .	22
Dissertation Scope . . . . .	26
<b>CHAPTER 2: Mix and Match – Coassembly of Amphiphilic Dendrimers and Phospholipids Creates Robust, Modular and Controllable Interfaces . . . . .</b>	<b>44</b>
Introduction . . . . .	44
Experimental Methods . . . . .	46
Results and Discussion . . . . .	51
Conclusions . . . . .	61
<b>CHAPTER 3: On-Demand Formation of Supported Lipid Membrane Arrays by Trehalose-Assisted Vesicle Delivery for SPR Imaging . . . . .</b>	<b>68</b>
Introduction . . . . .	68
Experimental Methods . . . . .	72

Results and Discussion . . . . .	77
Conclusions . . . . .	89
<b>CHAPTER 4: DNA Linkers and Diluents for Ultrastable Gold Nanoparticle</b>	
<b>Bioconjugates in Multiplexed Assay Development . . . . .</b>	<b>95</b>
Introduction . . . . .	95
Experimental Methods . . . . .	98
Results and Discussion . . . . .	101
Conclusions . . . . .	112
<b>CHAPTER 5: Nanoglassified, Monolayer Films of Gold Nanoparticles for <i>In Situ</i></b>	
<b>Orthogonal Detection by LSPR and SALDI-MS . . . . .</b>	<b>120</b>
Introduction . . . . .	120
Experimental Methods . . . . .	123
Results and Discussion . . . . .	127
Conclusions . . . . .	138
<b>CHAPTER 6: Calcinated Gold Nanoparticle Arrays for On-Chip, Multiplexed and</b>	
<b>Matrix-Free Mass Spectrometric Analysis of Peptides and Small Molecules . . . . .</b>	<b>146</b>
Introduction . . . . .	146
Experimental Methods . . . . .	148
Results and Discussion . . . . .	151
Conclusions . . . . .	167
<b>CHAPTER 7: 3D Printed Optical Biosensors . . . . .</b>	<b>175</b>
Introduction . . . . .	175

Experimental Methods	.	.	.	.	.	.	.	177
Results and Discussion	.	.	.	.	.	.	.	180
Conclusions	.	.	.	.	.	.	.	187
<b>CHAPTER 8: Future Biomaterial and Interface Directions</b>	.	.	.	.	.	.	.	193
Introduction	.	.	.	.	.	.	.	193
Lipid Membranes and Surface Plasmon Resonance	.	.	.	.	.	.	.	193
Expansion of Trehalose Mediated Preservation	.	.	.	.	.	.	.	196
Final Thoughts: Multifunctional Material Development	.	.	.	.	.	.	.	198
<b>APPENDIX A</b>	.	.	.	.	.	.	.	203
<b>APPENDIX B</b>	.	.	.	.	.	.	.	220
<b>APPENDIX C</b>	.	.	.	.	.	.	.	223
<b>APPENDIX D</b>	.	.	.	.	.	.	.	235
<b>APPENDIX E</b>	.	.	.	.	.	.	.	239

## LIST OF FIGURES

<b>Figure 1.1.</b> Lipid membrane assembly pathways for biosensor measurements . . . . .	3
<b>Figure 1.2.</b> Possible mechanisms of supported bilayer formation. . . . .	7
<b>Figure 1.3.</b> Schematic diagrams illustrating a surface plasmon polariton (or propagating plasmon) and a localized surface plasmon. . . . .	12
<b>Figure 1.4.</b> Schematic of real-time biointerface upon analyte binding to sensing surface. The reflectivity curve (lower left) shifts up analyte binding (displayed as AB) and can be monitored in real-time with a sensorgram (lower right). . . . .	17
<b>Figure 1.5.</b> Surface plasmon resonance instruments used throughout this dissertation research . . . . .	18
<b>Figure 2.1.</b> Molecular structures and supramolecular assembly pathways. . . . .	45
<b>Figure 2.2.</b> Co-assembly interaction studies. . . . .	52
<b>Figure 2.3.</b> Co-assembly structures. . . . .	55
<b>Figure 2.4.</b> Biophysical studies of co-assembled membranes. . . . .	57
<b>Figure 2.5.</b> In situ derivitization of hybrid 5% <b>2</b> /POPC membranes with biotin, followed by streptavidin recognition. . . . .	60
<b>Figure 3.1.</b> Schematic diagram exhibiting the processes of vesicle deposition, desiccation, and devitrification upon hydration of the trehalose matrix on the modified SPR sensor chips. . . . .	71
<b>Figure 3.2.</b> FRAP analysis of supported lipid bilayers formed using direct, traditional vesicle fusion and trehalose assisted deposition methods on microscope coverslips and SiO <sub>2</sub> modified SPR surfaces. . . . .	78
<b>Figure 3.3.</b> SPR studies of vesicle fusion upon devitrification of trehalose and preservation of embedded cargo activity. . . . .	81
<b>Figure 3.4.</b> SPR imaging study of membrane arrays formed using vesicles deposited, and preserved within, a trehalose matrix . . . . .	85
<b>Figure 3.5.</b> Hybrid bilayer membrane formation on SPR substrates using trehalose assisted vesicle delivery. . . . .	88

<b>Figure 4.1.</b> Gold nanoparticle conjugation schemes.	97
<b>Figure 4.2.</b> Surface plasmon resonance sensorgram depicting formation of a biotinylated supported lipid bilayer, followed by streptavidin and AuNP recognition.	102
<b>Figure 4.3.</b> Ionic strength stability assays.	104
<b>Figure 4.4.</b> Lyophilization of DNA/AuNPs.	107
<b>Figure 4.5.</b> Multistep conjugation of cT <sub>20</sub> /AuNPs with Protein A and anti-cholera toxin.	110
<b>Figure 5.1.</b> Fabrication scheme for the calcinated silicate nanofilm on a gold nanoparticle monolayer, supported by a glass slide.	122
<b>Figure 5.2.</b> Numerical finite-difference time-domain simulations and comparison to experimental results.	130
<b>Figure 5.3.</b> Characterization of LSPR performance with calcinated AuNP films.	132
<b>Figure 5.4.</b> Direct Raman spectroscopic analysis on the calcinated AuNP film, and comparison with planar substrates.	135
<b>Figure 5.5.</b> Laser desorption/ionization performance of the calcinated AuNP film and comparison to MALDI.	137
<b>Figure 6.1.</b> Fabrication of the calcinated AuNP array and analytical scheme.	152
<b>Figure 6.2.</b> Layer-by-layer modification of gold nanoparticles.	153
<b>Figure 6.3.</b> Scanning electron micrographs of arrayed and calcinated gold nanoparticles.	156
<b>Figure 6.4.</b> Ionization of [Sar <sup>1</sup> , Thr <sup>8</sup> ]-angiotensin II and neurotensin from various laser desorption/ionization substrates at laser fluence of 1900 a.u.	157
<b>Figure 6.5.</b> Ionization of cholesterol from various surfaces and matrices.	160
<b>Figure 6.6.</b> Reusability of the microarray.	162
<b>Figure 6.7.</b> Numerical simulations of plasmonic fields induced by $\lambda = 337$ nm light source for different nanoscale geometries.	165
<b>Figure 7.1.</b> 3D printed equilateral prisms in various stages of fabrication.	176

<b>Figure 7.2.</b> Effects of polishing treatments investigated by scanning electron microscopy and atomic force microscopy.	181
<b>Figure 7.3.</b> Optical characterizations.	182
<b>Figure 7.4.</b> Surface plasmon resonance activity of 3D printed prisms.	183
<b>Figure 7.5.</b> 3D printed prisms as surface plasmon resonance sensors.	184
<b>Figure 7.6.</b> Localized surface plasmon resonance (LSPR) sensing with 3D printed dove prisms.	186
<b>Scheme A.1.</b> Synthesis of amphiphilic dendrimers <b>1 – 3</b> .	209
<b>Figure A.1.</b> SPR study on fusion of POPC bilayer and transient adsorption of dendrimer <b>3</b> micelles with extended rinsing step.	210
<b>Figure A.2.</b> Simultaneous bleaching and recovery of labeled dendrimer micelles and POPC fused within the same membrane.	210
<b>Figure A.3.</b> TEM micrographs of dendrimers <b>1-3</b> alone assembled into nanomicelles.	211
<b>Figure A.4.</b> Bleaching and recovery of varying concentrations of dendrimer <b>1</b> within POPC membranes.	212
<b>Figure A.5.</b> Bleaching and recovery of varying concentrations of dendrimer <b>2</b> within POPC membranes.	213
<b>Figure A.6.</b> Bleaching and recovery of varying concentrations of dendrimer <b>3</b> within POPC membranes.	214
<b>Figure A.7.</b> SPR sensorgram depicting attempted derivitization of 100% POPC bilayer with biotin, and streptavidin recognition.	215
<b>Figure A.8.</b> <i>In situ</i> derivatization of a 5% <b>2</b> /POPC hybrid bilayer with NHS-AMCA.	215
<b>Figure A.9.</b> Schematic representation of the coarse-grained DPD models of dendrons <b>1, 2, and 3</b> .	216
<b>Figure A.10.</b> Diameter and potential energy as a function of simulation time ( $\tau$ ) for <b>3</b> /POPC system equilibration.	216
<b>Figure B.1.</b> Fabrication process of high-performance gold well SPR imaging substrate.	220

<b>Figure B.2.</b> Representative FRAP recovery curves for supported lipid bilayers formed using vesicle injection and devitrification processes on glass coverslips and modified SPR surfaces. . . . .	220
<b>Figure B.3.</b> Flow rate effects on devitrification of trehalose alone. . . . .	221
<b>Figure B.4.</b> Sensorgrams for cholera toxin binding to membranes obtained from devitrified vesicles that were stored between 1-4 weeks. . . . .	221
<b>Figure B.5.</b> FRAP results from devitrified hybrid bilayer membrane on C18 surface. . . . .	222
<b>Figure C.1.</b> Surface plasmon resonance sensorgram depicting formation of a ganglioside-impregnated supported lipid bilayer, followed by cholera toxin (CT), attempted AuNP recognition, then a biotinylated antibody specific for CT, streptavidin, and another attempt at AuNP recognition. . . . .	227
<b>Figure C.2.</b> Surface plasmon resonance sensorgram depicting formation of a biotinylated supported lipid bilayer, followed by streptavidin and biotin/MHDA/AuNP recognition. . . . .	227
<b>Figure C.3.</b> Ionic strength stability assays of bare AuNP (citrate capped), biotin/MHDA/AuNP, and bT <sub>20</sub> /AuNP exposures to varying concentrations of NaCl. . . . .	228
<b>Figure C.4.</b> Absorbance spectra of bT <sub>20</sub> /AuNPs in nanopure water, 4 M NaCl, 4 M MgCl <sub>2</sub> , 4 M NH <sub>4</sub> Cl, 4 M guanidinium chloride, 98% Los Angeles River water, and 98% human serum. . . . .	229
<b>Figure C.5.</b> Surface plasmon resonance sensorgram depicting formation of a biotinylated supported lipid bilayer, followed by streptavidin and 13 nm bT <sub>20</sub> /AuNP recognition (lyophilized and resuspended five times). . . . .	230
<b>Figure C.6.</b> 30 nm bT <sub>20</sub> /AuNP lyophilization studies. . . . .	230
<b>Figure C.7.</b> Lyophilization of free horseradish peroxidase (HRP). . . . .	231
<b>Figure C.8.</b> Lyophilization of HRP/cT <sub>20</sub> /AuNPs: absorbance spectra of the HRP/cT <sub>20</sub> /AuNPs before and after lyophilization. . . . .	232
<b>Figure C.9.</b> Representative transmission electron micrographs of as-prepared citrate capped 13 nm gold nanoparticles, and 30 nm gold nanoparticles. . . . .	232
<b>Figure D.1.</b> SEM characterization of the nanofilm substrates. . . . .	235
<b>Figure D.2.</b> Derivation of film thickness from atomic force microscopy (AFM). . . . .	236

<b>Figure D.3.</b> Fluorescence recovery after photobleaching (FRAP) of suspended lipid bilayer.	236
<b>Figure D.4.</b> MALDI spectrum of [Sar <sup>1</sup> , Thr <sup>8</sup> ]-angiotensin II (M1=956.1) and neurotensin (M2=1672) using CHCA as a matrix.	237
<b>Figure D.5.</b> Identification of intact protein by surface-assisted laser desorption/ionization mass spectrometry (SALDI-MS).	237
<b>Figure E.1.</b> Solution confinement of colloidal gold nanoparticle solutions on photocatalytically patterned glass microscope slides, exhibiting hydrophilic spots with hydrophobic surroundings.	240
<b>Figure E.2.</b> Contact angle measurements at various stages of material fabrication.	240
<b>Figure E.3.</b> SEM and AFM images of calcinated gold nanoparticles.	241
<b>Figure E.4.</b> Frequency distributions of diameters for individual nanoparticles.	242
<b>Figure E.5.</b> Deposited AuNP-(PAH-silicate) <sub>1</sub> calcination effects on ionization of N-acetyl tetradecapeptide renin substrate.	243
<b>Figure E.6.</b> Laser fluence threshold study for ionization of 20 pmol [Sar <sup>1</sup> , Thr <sup>8</sup> ]-angiotensin II and neurotensin.	244
<b>Figure E.7.</b> Detection of [Sar <sup>1</sup> , Thr <sup>8</sup> ]-angiotensin II in the low femtomole range.	245
<b>Figure E.8.</b> Numerical simulations of plasmonic fields induced by $\lambda = 520$ nm light source for different nanoscale geometries.	246

## LIST OF TABLES

<b>Table 4.1.</b> Functionalized DNA Oligonucleotide Sequences.	99
<b>Table A.1.</b> Physical properties of hybrid dendrimer/POPC vesicles.	217
<b>Table A.2.</b> Simulated average diameters, surface electrostatic potential ( $\Psi_s$ ), and zeta potential ( $\zeta$ ) for the three dendrimer/POPC vesicles.	217
<b>Table C.1.</b> Conjugated AuNP Zeta Potentials.	226
<b>Table D.1.</b> Identified peptide fragments from cytochrome c digest.	238

# CHAPTER 1: Plasmonic Materials and Interfacial Recognition

## Schemes for Environmental Toxin Analysis

### ■ INTRODUCTION

Human and animal populations have observed a dramatic increase in the number of chemicals they are exposed to through pharmaceutical drugs, commercial products, and toxic wastes. As chemical use escalates, there is an increasing demand for new technology to determine if their exposure leads to adverse effects, and if so, by what route so that appropriate treatments may be found. *In vivo* studies involving live animals have been broadly used for centuries in toxicity testing; however, they suffer from high cost, increased testing time, and animal sacrifice. In response to this, the National Academy of Sciences issued a report detailing a paradigm shift in toxicity screening.<sup>1</sup> This report called for the development of novel, *in vitro* assays not involving live animals, in which toxicity pathways could be specifically identified and as act an accurate prediction of *in vivo* responses. The vision itself encompasses multiple components, including: 1) chemical characterization; 2) toxicity testing, which includes the identification of use of toxicity pathways and targeted testing; 3) dose-response and extrapolation monitoring; and 4) evaluating the above with respect to population-based and human exposure data, while determining risk contexts for exposure. Biosensors represent an ideal technology amenable toward meeting the demands of the first and second components, as they pair biological recognition elements with signal transducers that are capable of translating biological processes into physical measurements.<sup>2</sup> While

the measurements they produce are generally targeted, biosensing materials are easily adaptable based on desired complexity and throughput of the assay at hand, essential for decreasing testing times and costs. The research conducted throughout this dissertation will focus on biosensor development toward identification and characterization of toxicity pathways as they relate to the cellular membrane, as this biological structure hosts many of the primary molecular recognition events that may lead to adverse, organismal effects.

## ■ LIPID MEMBRANE MODELS\*

While the plasma membrane is a naturally complex interface, a number of efforts have been made to simplify it into solid supported structures over the past several decades.<sup>3-5</sup> These have collectively allowed for biophysical studies of embedded biomolecules and membrane interactions in absence of potential interferents from the cellular matrix, in addition to exploitation of the interface for biologically inspired sensors.<sup>3</sup> Utilization of model lipid systems additionally carries the advantage of being able to alter and tune the composition of the membrane so that targeted biomolecular assays may be carried out, and if desired, with tailored biophysical properties (*e.g.* membrane stability and lipid fluidity).<sup>6</sup> For example, lipid vesicles can be formed from single phospholipids and receptors that have been commercially obtained, or isolated from cultured mammalian and bacterial cells for systems that more closely resemble their *in vivo* counterparts.<sup>7-9</sup> Any of these isolated systems may be used as-is, or assembled into various shapes and architectures.

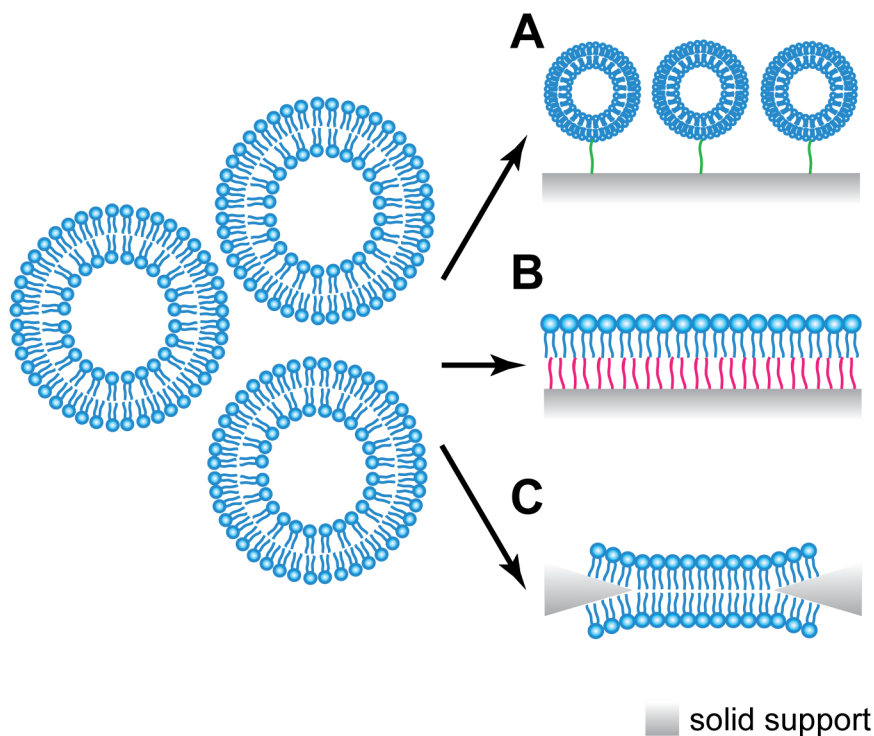


**Figure 1.1.** Lipid membrane assembly pathways for biosensor measurements. (a) Tethered lipid vesicles or micelles from the sensor surface. (b) Hybrid bilayer membranes, in which the lower leaflet is often a hydrophobic self- assembled monolayer. In supported lipid bilayers, the lower leaflet is another layer of lipids. (c) Black lipid membrane, suspended within a narrow aperture. Reprinted from *J. Electroanal. Chem.*, Vol. 781, Hinman, S. S. and Cheng, Q., *Bioinspired Assemblies and Plasmonic Interfaces for Electrochemical Biosensing*, 136-146, Copyright 2016, with permission from Elsevier.

There are many routes that may be taken to create a supported membrane structure for bioanalytical assays (Figure 1.1), which include: 1) tethering supramolecular lipid structures (*e.g.* bilayer vesicles, micelles, *etc.*) to a chemically modified surface; 2) fusing unilamellar vesicles into a planar membrane supported by a hydrophatically matching surface; or 3) suspending a bilayer membrane over a narrow aperture, which allows for direct measurement of current flow through membrane channels. While each of these have their own unique benefits for analytical characterizations, the biophysical properties will substantially vary, which must be considered in sensor and assay design.

***Tethered Lipid Nanostructures.*** Due to their amphiphilic nature, most phospholipids will spontaneously self-assemble into spherical structures in solution, which can be further shaped and sized using established techniques.<sup>10</sup> Direct conjugation of these functional structures to a support without further self-assembly schemes is an attractive avenue for decreasing sensor fabrication and preparation time. The incorporation of surface binding ligands into small, unilamellar vesicles (SUVs) for amperometric characterization of streptolysin O (SLO) was demonstrated by Xu and Cheng.<sup>11</sup> SUVs assembled from phosphatidylcholine, cholesterol, dicetyl phosphate, and 1-octadecanethiol were formed in a buffer containing the redox probe  $K_3Fe(CN)_6$ , which was encapsulated during the vesicle formation process. The alkanethiol constituent was evenly distributed with the other lipids, and allowed for direct attachment of the vesicles to gold disk electrodes. Upon introduction of the pore-forming toxin (SLO), the redox probe was released, resulting in a quantifiable change in the amperometric signal. Cheng et al. later applied similar methods for anchoring of polydiacetylene (PDA) lipid microstructures and voltammetric sensing of cholera toxin (CT).<sup>12</sup> The platelet lipid assemblies were incorporated with ferrocene and cysteine conjugated PDAs for electrochemical activity and gold surface attachment, respectively. With cell surface ligand  $GM_1$  co-assembled, these structures were capable of recognizing CT and producing a voltammetric response through blocking of the electron transport path, thus decreasing Faradaic current. While these are but a few examples of surface derivatization schemes, unilamellar lipid vesicles may be attached to the surface under a wide variety of techniques, including biotin-lipid/streptavidin recognition,<sup>13</sup> DNA-lipid/DNA base

pairing,<sup>14</sup> and supramolecular shape recognition.<sup>15</sup> Under more complex membrane environments, transmembrane proteins can also be reconstituted into liposomes, enabling their study through *ex situ* voltammetry and chronopotentiometry; in one instance, the method relied on the aspect that the proteins used were electroactive compared to the lipid bilayer, and allowed for studies of both Na<sup>+</sup>/K<sup>+</sup>-ATPase and mitochondrial uncoupling protein 1 in their native, folded states.<sup>16</sup>

While tethered vesicles have shown exceptional versatility for membrane characterization, their stability in solution and on-chip is often not amenable to long term storage, transport, or arraying schemes. The development of other tethered architectures has therefore received great attention. Nanodiscs, constructed from phospholipids and embedded receptors assembled onto a membrane protein scaffold (dia. 10 – 13 nm), have gained immense popularity since their introduction in 2002.<sup>17-18</sup> Demonstrating high versatility, these systems have been interfaced with surface plasmon resonance for cholera toxin analysis,<sup>19</sup> spectropotentiometry for cytochrome P450 characterization,<sup>20</sup> and silicon photonic microring resonators for high throughput screenings.<sup>21</sup> Larger discoidal structures have also been desired, leading to the development of lipodisks, which are *ca.* 100 nm in diameter and stabilized by a rim of poly(ethylene glycol) modified lipids.<sup>22-23</sup> While not as stable as nanodiscs due to lack of a scaffold support, these have also been applied for numerous biophysical studies.<sup>24-26</sup>

***Solid-Supported, Planar Lipid Architectures.*** Surface wettability plays an important role in further self-assembly processes of lipid vesicles. When exposed to a surface that is highly hydrophobic, free lipids or SUVs will fuse into a planar hybrid

bilayer membrane (HBM), where the upper leaflet of the membrane is composed of phospholipids and the lower leaflet is a chemically derivatized surface (often, a hydrophobic self-assembled monolayer).<sup>27</sup> Micropatterned HBMs have been used to quantify SLO on alkanethiol substrates through voltammetric responses of ferrocene carboxylic acid (FCA).<sup>28</sup> Formation of the HBM prevents access of FCA to the electrode surface, while pore formation by SLO restores redox response. This system was also found to be compatible with hexyl thiocetate and thiocetic acid tri(ethylene glycol) ester modified gold electrodes, which are capable of supporting HBMs and allow for more sensitive characterizations of pore forming toxins.<sup>29-30</sup> Hydrophobic SAM modified electrodes covalently bound to a Cu(I)/Cu(II) redox center have recently been used to characterize anion transport through hybrid bilayer membranes, and researchers were able to show transport to primarily follow a solubility-diffusion mechanism, rather than a pore translocation mechanism.<sup>31</sup>

On the other hand, if the solid support is rendered exceptionally clean and hydrophilic, SUVs will adsorb and fuse into a supported lipid bilayer (SLB).<sup>32</sup> Unlike HBMs, a 10 – 20 Å layer of water is trapped underneath the lower phospholipid leaflet of the SLB, lubricating the interface and allowing for embedded lipids to laterally diffuse, similar to their natural environments.<sup>33-34</sup> These have become an extremely popular interface due to their versatility and ease of fabrication, which is exhibited in Figure 1.2. The most common support for these systems is glass (fused silica),<sup>35</sup> though mica,<sup>36</sup> MgF<sub>2</sub>,<sup>36</sup> CaF<sub>2</sub>,<sup>36</sup> polydimethylsiloxane (PDMS),<sup>37</sup> and even gold nanogratings<sup>38</sup> have been used to induce vesicle fusion toward a fluid bilayer. Applications of SLBs are generally

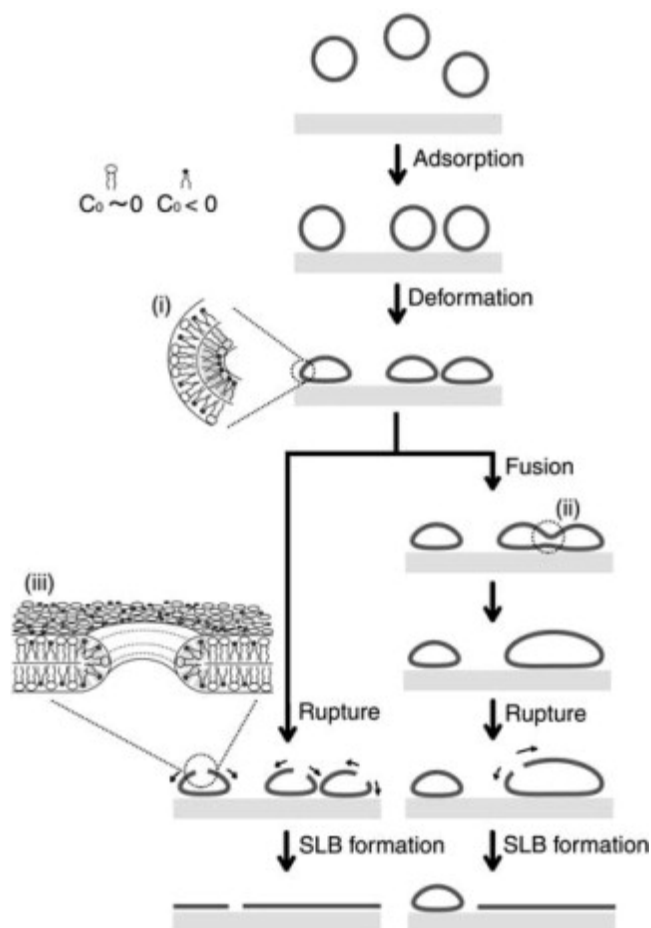


**Figure 1.2.** Possible mechanisms of supported bilayer formation. Vesicles adsorb, deform, and rupture to form an SLB. Under some conditions, vesicle-vesicle fusion occurs as an intermediate preceding vesicle rupture. Reprinted from Ref. 32, Copyright 2006, with permission from Elsevier.

similar to HBMs for biosensing, though can be especially useful for multivalent interaction characterizations<sup>39</sup> and viral fusion studies,<sup>40</sup> which are often dependent on membrane fluidity. Transmembrane proteins can hinder these properties, as they may electrostatically adsorb to the substrate underneath the bilayer, decreasing the lateral diffusion of surrounding lipids. To circumvent this, tethered lipid bilayers (TLBs), which are elevated from the solid support through a polymer or PEG chain, have also undergone rigorous investigation.<sup>41</sup> While not a perfect biological mimic due to the fact that PEG or

polymer derivatized lipids need to be integrated, full transmembrane mobility of embedded proteins and lipids may be preserved in both synthetic and cultured cell derived models.<sup>42-43</sup>

***Black Lipid Membranes and Nanopores.*** Black lipid membranes (BLMs) are lipid bilayers that have been formed over a narrow aperture (dia. < 1 mm), separating two distinct aqueous regions.<sup>3, 44</sup> BLMs are typically supported at their periphery by a hydrophobic support, which anchors the membrane in place through hydrophobic interactions with the phospholipid tails. Electrodes may then be placed on either side of the membrane for measurements of current, often accompanied by sensing across embedded channel proteins. While carrying the advantage of high transmembrane protein mobility, a feature often lacking in HBMs and most SLBs, BLMs are inherently less stable and many recent efforts have been made to improve the structural robustness of this class of materials. Polymerization of adjacent modified phospholipids is one popular option for improving stability, and has been tested using dienoyl- and sorbyl-modified phospholipids.<sup>45</sup> Each of the photopolymerized membranes exhibited significantly higher stability after UV exposure compared to diphytanoyl phosphocholine (DPhPC), extending the lifetime of these structures from hours to days. In addition to glass apertures coated with various monolayers, BLMs can be formed over polymer substrates (*e.g.* SU-8), for which the geometry can be precisely tuned and defined using standard photolithography techniques.<sup>46-47</sup>

Nanopore sensing is an exciting concept derived from biomimetic BLMs. Biological nanopores are typically constructed from transmembrane pore-forming

proteins, which result in pores with diameters of 10 – 30 Å that may be used for measuring the translocation of biomolecules based on their size or aggregation state.<sup>48</sup>  $\alpha$ -Hemolysin ( $\alpha$ -HL) is the most commonly used protein for these analyses, though alternative proteins such as aerolysin and SP1 are also being explored with promising results for peptide and DNA detection.<sup>49-51</sup> Biosensing is accomplished through measurements of current across the membrane, where binding or translocation events result in measurable step reductions in the presence of an applied potential. Accurate data processing is often crucial toward filtering electronic noise while discerning pore blockage dwell times and step magnitudes, which are indicative of binding affinity and molecular weight, respectively.<sup>52</sup> A plethora of bulk and single molecule applications exist for nanopore mediated biosensing, from peptide and protein interactions to nucleic acid sequencing.<sup>53</sup>

***Consequences of Embedded Lipid Mobility.*** While the formation of microscale structures, such as lipid rafts and cholesterol rich domains, is one of the most commonly considered consequences of a dynamic and fluid lipid membrane environment, fluidity also has important implications for biorecognition, particularly in multivalent binding schemes.<sup>54</sup> Certain proteins, such as cholera toxin (an AB<sub>5</sub> complex) and avidin (a homotetramer), are composed of multiple, identical subunits, each of which must bind to a separate receptor for highest affinity.<sup>55</sup> These receptors rearrange within the bilayer *via* random lateral diffusion for optimal binding sterics, which would not be possible in a static environment (*i.e.* a self-assembled monolayer platform or an immobile lipid membrane). With this in mind, concentration of the receptor or binding partner within the

lipid bilayer can be imperative for sensing purposes, as diffusive aggregation of receptors at higher concentrations can also adversely affect multivalent molecular binding. For instance, Shi et al. investigated the effect of GM<sub>1</sub> concentration within model phosphocholine SLBs using microfluidic devices, revealing a weakening of CT-GM<sub>1</sub> interaction strength when the GM<sub>1</sub> composition was raised from 0.02 to 10.0 % (n/n).<sup>39</sup> Atomic force microscopy analysis was used to confirm that GM<sub>1</sub> clustering was in fact occurring within these membranes, leading to a steric mismatch between CT and each of the ganglioside receptors. While potential electrostatic repulsion between GM<sub>1</sub> and CT was also considered, increasing the ionic strength of the assay buffer from 150 mM NaCl to 300 mM NaCl revealed no statistically significant change in dissociation constants. Therefore, while membrane fluidity is capable of substantially enhancing the recognition between membrane bound receptors and their respective ligands, one may need to consider whether tailoring membrane constituents toward highest biological accuracy or analytical sensitivity is of greater importance in assay design.

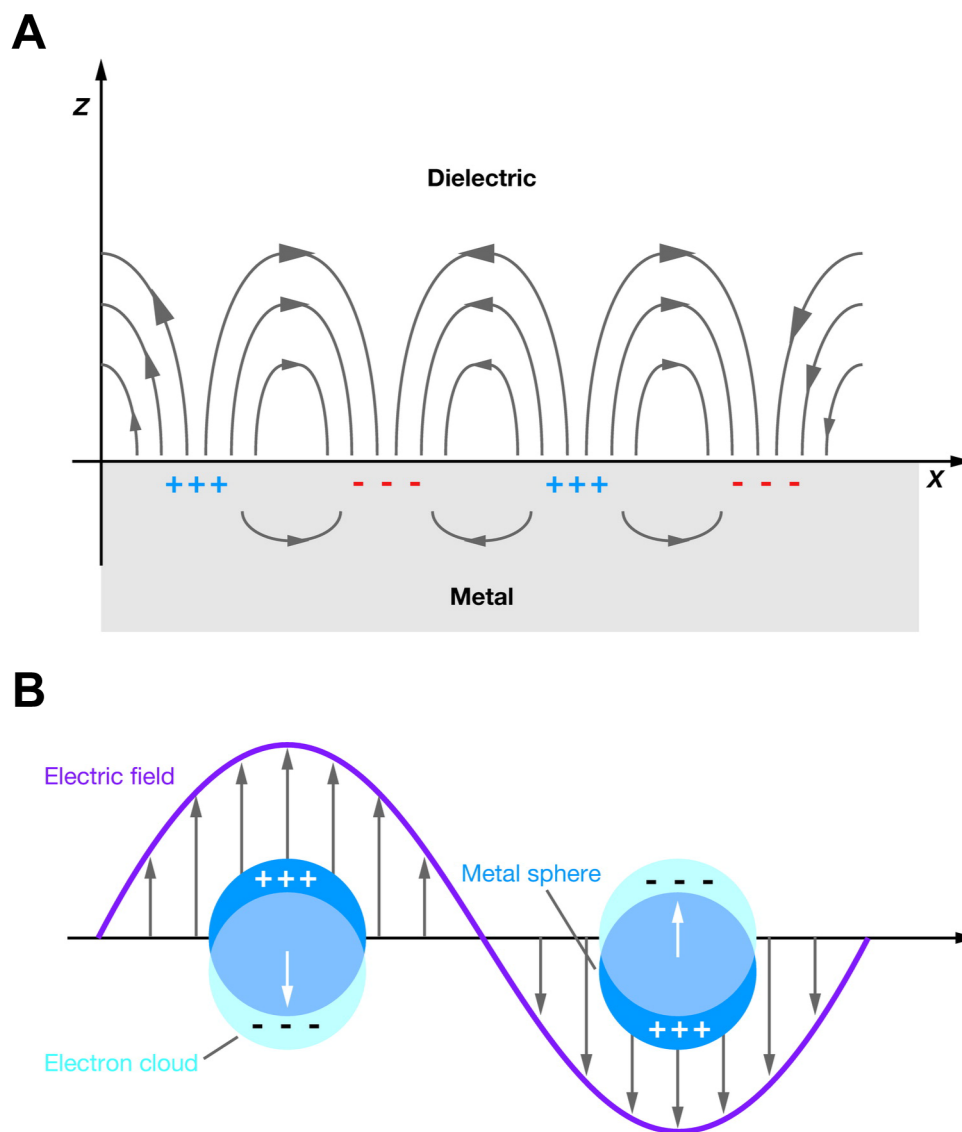
The mobility of lipids within different model membrane systems will vary, though in general follow the trend of SUVs ~ TLBs ~ BLMs > SLBs > HBMs > nanodiscs for diffusion rates (however, membrane composition and choice of solid support will also cause significant variations).<sup>3</sup> While single particle tracking is the most recent, and perhaps the most accurate, method of measuring mobility,<sup>56-58</sup> fluorescence recovery after photobleaching (FRAP, more accurately referred to as “fluorescence *redistribution* after photobleaching”), has remained the standard mobility measurement technique for many decades,<sup>59</sup> and is widely practiced for *in vitro* and *in vivo* systems.<sup>60-61</sup> Using the example


of a fluorescently tagged SLB observed under a confocal fluorescence microscope, mobility kinetics may be assessed by bleaching a region of interest under high laser intensity and monitoring the recovery of fluorescence within the bleached region over time as non-bleached lipids laterally redistribute within the membrane. The bleached region may take the form of a point,<sup>59, 62</sup> line,<sup>37</sup> or selected 2 dimensional shape,<sup>63</sup> for which the kinetic modeling and analyses will vary.<sup>61</sup>

## ■ SURFACE PLASMON RESONANCE BIOSENSORS

Surface plasmon resonance (SPR) is a nanomaterial enabled optical phenomenon that has revolutionized sensor development and analytical chemistry over the past several decades. Allowing for both direct, label-free analyses and a wide variety of sensitivity enhancement schemes, the techniques that have arisen from the SPR have substantially broadened the measurement toolkit available to researchers, clinical and field technicians, and untrained personnel in laboratory, home, and point-of-care settings. While this section is not intended to be an exhaustive review of the field, and included only to provide an introduction to the core techniques of this work, readers are encouraged to utilize the following published reviews on SPR for general biosensing,<sup>64-65</sup> sensor interface design,<sup>66-69</sup> SPR instrumentation,<sup>70-71</sup> and localized surface plasmon resonance (LSPR)<sup>72-73</sup> for more in-depth discussions on the above topics.

***Principle and Theory.*** Surface plasmon resonance (SPR) is the result of a momentum transfer from an oscillating, electromagnetic source (*e.g.* light) to the delocalized electrons of a bulk metal, thereby causing those electrons to oscillate in



 Willets KA, Van Duyne RP. 2007.  
Annu. Rev. Phys. Chem. 58:267–97

**Figure 1.3.** Schematic diagrams illustrating (A) a surface plasmon polariton (or propagating plasmon) and (B) a localized surface plasmon. Reprinted from Ref. 72.

resonance with the incident light at the metal:dielectric interface (Figure 1.3). The conditions under which this transfer is possible are dependent on a number of factors, including the shape/size/composition of the material, angular frequency of light, and dielectric constant(s) of the surrounding media.<sup>71</sup> While the optical effects of SPR had

been noted by scientists since the early 1900s, a physical interpretation of the phenomenon was not provided until 1968, when Otto developed a method of exciting non-radiative surface plasmon waves at a silver:vacuum interface and compared the obtained dispersion results with then-present metal optic theories.<sup>74</sup> Around the same time, Kretschmann and Raether were also successful in exciting surface plasmon waves at a silver:air interface, though under attenuated total reflection (ATR) geometry, which is still the most common experimental setup for modern SPR instrumentation.<sup>75</sup> These seminal research examples laid the groundwork for a modern understanding of surface plasmons (*i.e.* the electrons collectively oscillating in resonance with the incident light source) propagating at metal-dielectric interfaces, and dictated many of the conditions that must be met in order for SPR to occur. For instance, the coupling of incident light to a metal's conduction electrons is only possible when the wavevector of incident light ( $k_0$ ) is equal to the wavevector of the surface plasmon polaritons generated ( $k_{sp}$ ), as defined below:

$$k_{sp} = k_0 \sqrt{\frac{\epsilon_m(\lambda)\epsilon_s(\lambda)}{\epsilon_m(\lambda) + \epsilon_s(\lambda)}}$$

where  $\lambda$  is the wavelength of light,  $\epsilon_m$  is the dielectric constant of the metal, and  $\epsilon_s$  is the dielectric constant of the surrounding medium. The dielectric constant of the metal is a complex quantity with both real and imaginary components (*i.e.*  $\epsilon_m = \epsilon_m' + i\epsilon_m''$ ), thus preventing SPR from occurring unless the material possesses both a negative real ( $\epsilon_m'$ ) and small imaginary ( $\epsilon_m''$ ) dielectric constant.<sup>76</sup> It is important to note that by this equation, SPR is sensitive to changes in refractive index of the local environment, as  $\epsilon_s$

reduces to  $n^2$  ( $n$  = refractive index). These changes may be effected by large transfers of the bulk dielectric (*e.g.* flushing the surface with gas, water, buffer, *etc.*), or more subtle alterations, such as self-assembled monolayer adsorption to the metal surface, or (bio)molecular target binding, which is of great importance in sensor development. However, due to the dependency of  $k_{sp}$  on the dielectric constants,  $\epsilon_m$  and  $\epsilon_s$ ,  $k_{sp} \neq k_0$  when light is freely propagating through a vacuum, and the resonant conditions will not be satisfied. To make up for this “missing momentum,” a number of experimental setups have been utilized, though the most common is through coupling of light through a high refractive index prism under ATR geometry,<sup>75</sup> with the metal deposited on one face of the prism, thus increasing the effective wavevector of incident light ( $k_{eff}$ ) according to the equation below:

$$k_{eff} = k_0 n_D \sin(\theta) = \frac{2\pi}{\lambda} n_D \sin(\theta)$$

where  $n_D$  is the refractive index of the prism and  $\theta$  is the angle of incidence. Under this setup, not only may  $k_{sp}$  equal  $k_{eff}$ , allowing for surface plasmon polariton generation, but coupling conditions may also be tuned through variations in the wavelength or incident angle of the light source. The conditions under which SPR occurs manifests as a dip in the reflectance spectrum of the material, which will shift toward higher wavelengths or incident angles, respectively (dependent on the method of interrogation), in response to increases in  $n$  or  $\epsilon_s$ , and vice versa.

In regards to sensor design, one final parameter that must be taken into account is that surface plasmons do not extend infinitely in the  $z$ -direction from the surface, but exponentially decrease with increasing distance in the  $z$ -direction. Penetration depth ( $\delta_z$ )

is most commonly used to judge the distance from the substrate where measurements may still be taken from a practical standpoint. It is defined as the distance where the electromagnetic field of the surface plasmons decrease to  $1/e$  (*ca.* 37 %) of the maximal value, and is expressed as:

$$\delta_i = \frac{\lambda}{2\pi} \sqrt{\frac{\epsilon_m' + \epsilon_s}{\epsilon_s}}$$

Therefore, utilizing a 650 nm light source and 50 nm gold film immersed in water (*i.e.* the basic setup used throughout this dissertation),  $\delta_i$  is *ca.* 190 nm, and all SPR measurements should be carried out within this distance from the gold surface.<sup>70</sup>

It is worth mentioning that surface plasmons may also stay confined to discrete nanostructures (Figure 1.3B), as opposed to propagating as surface plasmon polaritons over planar films, in a process termed localized surface plasmon resonance (LSPR). In this case, light interacts with nanoparticles much smaller than the incident wavelength, generating localized surface plasmons that oscillate around the nanostructure itself. This results in strong absorbing and scattering properties of the nanomaterial, for which the extinction spectrum (of a metal sphere, as a simplified example) may be calculated as follows:

$$E(\lambda) = \frac{24\pi^2 N a^3 \epsilon_s^{3/2}}{\lambda \ln(10)} \left[ \frac{\epsilon''(\lambda)}{(\epsilon'(\lambda) + \chi \epsilon_s)^2 + \epsilon''(\lambda)^2} \right]$$

where  $N$  is the number of finite polarizable elements,  $a$  is the particle radius, and  $\chi$  is a coefficient that accounts for the particle aspect ratio ( $\chi = 2$  for a sphere).<sup>72</sup> With more exotic nanoparticle shapes (*e.g.* rods, stars, raspberries, cones, *etc.*) the equations

describing LSPR become incredibly complex, leading to the development of computational methods for descriptive modeling.<sup>77</sup> However, a general relationship between shifts in an LSPR absorbance peak wavelength and changes in the dielectric refractive index is provided below:

$$\Delta\lambda_{max} = m\Delta n \left[ 1 - \exp \left( \frac{-2d}{l_d} \right) \right]$$

where  $m$  is the bulk-refractive index response of the nanoparticle,  $d$  is the thickness of the layer being altered in the dielectric, and  $l_d$  is the characteristic decay length of the LSPR field (analogous to  $\delta_i$ ).<sup>72</sup> While there are many exceptions, in comparing LSPR to SPR the following general differences should be taken into account for assay design: 1)  $\delta_i$  is much lower for LSPR (< 15 nm), leading to greater consideration needed regarding thickness of supported elements in the dielectric medium; 2) LSPR is almost always interrogated under wavelength modulation, as the generation of localized surface plasmons from isotropic structures will be insensitive to the incident angle and anisotropic structures require exceptionally high precision to align; and 3) LSPR may be conducted as a solution or surface based assay, depending on whether the nanoparticles are suspended as a colloid or immobilized on a solid support.

**Measurement Versatility.** SPR may utilize a number of optical setups and configurations, making the technique accessible to a wide audience of researchers. The ATR setup used by Kretschmann and Raether,<sup>75</sup> also referred to as “Kretschmann configuration,” is the most common throughout commercial and homebuilt instruments, though other variations, including Otto configuration, long-range SPR (LRSPR), plasmon waveguide resonance (PWR), and waveguide-coupled SPR (WCSPR) are also seen,

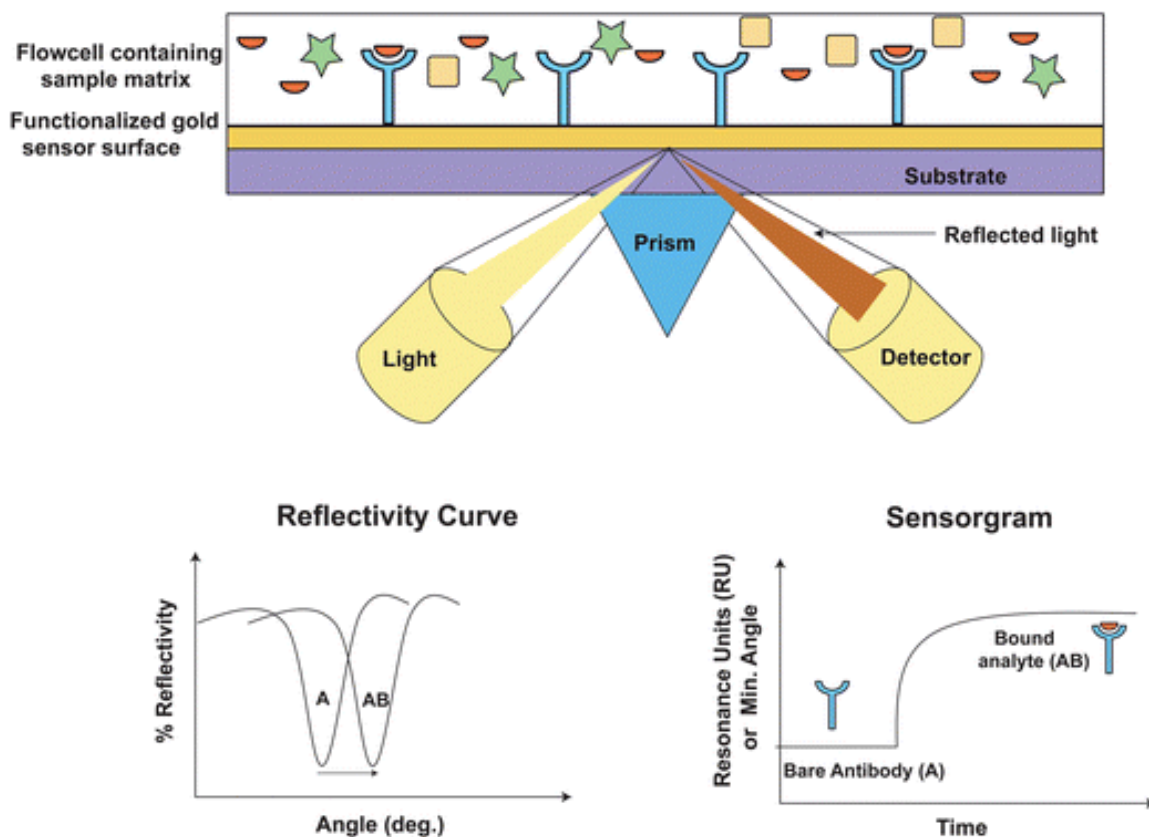


**Figure 1.4.** Schematic of real-time biointerface upon analyte binding to sensing surface. The reflectivity curve (lower left) shifts up analyte binding (displayed as AB) and can be monitored in real-time with a sensorgram (lower right). Reprinted from Ref. 67 with permission of Springer.

albeit less often, in modern sensing schemes.<sup>70</sup> An SPR instrumental diagram with components arranged in the Kretschmann configuration is provided in Figure 1.4, with the light source, coupling prism, gold film, and detector arranged in reflectance geometry. The majority of commercial SPR instruments utilize angular interrogation for measurements, in which the incident angle of light at a fixed wavelength (*e.g.*  $\lambda = 650$  nm) is scanned over a set range, resulting in a reflectivity spectrum (angle vs. reflectivity) that exhibits a sharp dip representing surface plasmon polariton excitation. Wavelength scanning instruments simplify the mechanics of these measurements, relying on a white light source fixed at an SPR-active angle, and a spectrometer utilized in place of a

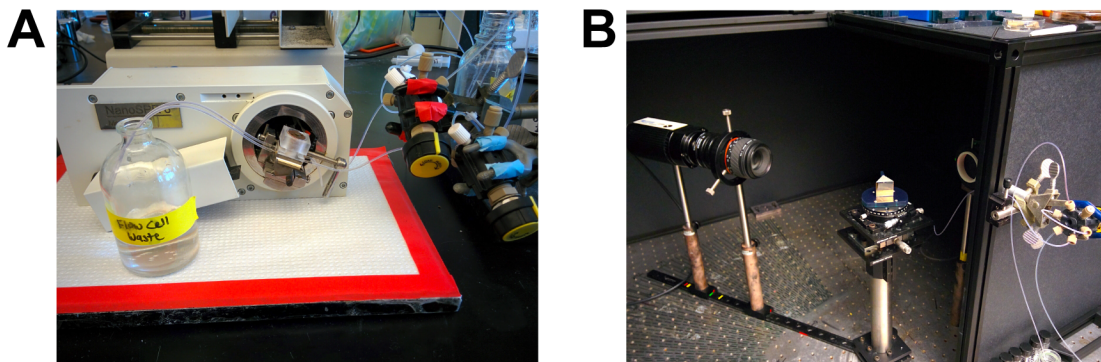


**Figure 1.5.** Surface plasmon resonance instruments used throughout this dissertation research. (A) NanoSPR 6-321 spectrometer from NanoSPR Devices. (B) Homebuilt SPR imager with CCD camera, sample stage, and fluidics shown. Dark box utilized to minimize fluctuations in ambient light intensity.

traditional CCD or CMOS detector. In either case, flow cells can be integrated with the sensing interface, allowing for precise sample handling and introduction to the surface. The measurements taken under these setups are heterogeneous, with recognition elements immobilized to the gold film, and respective binding partners flowed over to monitor concentration and/or binding kinetics. SPR carries the advantage of being refractive index sensitive by the wavevector equation for  $k_{sp}$ , and thus, label-free, precluding the need for external fluorescent tags or radiolabels which may complicate or interfere with measurements. Furthermore, data may be collected and interpreted in real-time, which provides a major advantage over traditionally used endpoint assays. While commercial instrumentation is often considered to be large and bulky, as is the case with the highly successful BIAcore<sup>®</sup> product line, portable instrumentation, such as that sold by NanoSPR Devices (Figure 1.5A)<sup>78</sup> and Affinité Instruments,<sup>79</sup> is becoming broadly validated and popular for laboratory and field use.

SPR imaging is a relatively new extension of SPR, and allows for multiplexed measurements to be taken across gold microarray films. SPR imaging also utilizes the

Kretschmann configuration, though with a fixed SPR-active incident angle and wavelength (Figure 1.5B). A CCD camera is used to image contrast changes across the entire surface, which can be defined and patterned according to research needs. While the dynamic range of measurements is lower than that of SPR spectroscopy, innovations in instrumentation (*e.g.* choice of light source, optical components), sample handling (*e.g.* arraying protocols, on-chip biosynthesis, material transfer), and data analysis have rendered the method highly sensitive and selective for high-throughput screenings.<sup>80</sup>

LSPR spectroscopy benefits from the simplest instrumentation, as nanoparticle substrates and solutions can be adapted to most standard UV/Vis spectrophotometers and transmission based setups. Colloids only require dilution to the desired concentration, followed by transfer to a standard cuvette for absorbance analysis. Solid supported substrates, on the other hand, require perpendicular mounting between the light source and spectrometer, along with fixation of a flow cell for sample introduction. One disadvantage of transmission analysis is the need for background correction of the solid support (*i.e.* glass, mica, quartz, acrylic) along with the solvent being introduced, as both of these will likely contribute to light absorbance and/or scattering, interfering with that taking place from LSPR. Reflectivity analysis utilizing nanoparticle-coated dove prisms is one recently introduced method that eliminates the need for solvent background correction while maintaining the placement of optical components along a single axis.<sup>81-83</sup> In this case, absorbance is only being measured within the penetration depth ( $\delta_i < 40$  nm) of the electromagnetic field generated from ATR.<sup>84</sup> While generally seen as a low throughput method, these setups can be scaled up for high throughput analysis, with some

research groups utilizing changes in contrast imaged with a CCD camera (similar to SPR imaging, low cost, yet less accurate for LSPR),<sup>85</sup> and others integrating liquid crystal tunable filters with a CCD camera for imaging shifts in peak wavelengths (high cost, yet more accurate for LSPR).<sup>86</sup>

***Nanoglassified Surface Functionalities.*** SPR and LSPR have been used for detecting and characterizing a broad range of biomolecular targets, including proteins, nucleic acids, carbohydrates, and whole cells.<sup>64, 68-69, 72</sup> However, integration of these sensors with lipid membranes has remained a challenge due to the their incompatibility with gold, and limited availability of surface tethering options. For over a decade, SPR characterizations were limited to structures such as HBMs and nanodiscs, which lack the lateral lipid mobility needed for native biomimicry. Tethered liposomes, which do exhibit membrane fluidity, have also been explored, yet require that synthetic lipids be incorporated for surface tethering.<sup>87-88</sup> In 2006, Phillips et al. demonstrated that nanoscale layers of silicate glass (2 – 15 nm) could be applied to gold surfaces through a layer-by-layer self-assembly/calcination process, providing a hydrophilic surface that allowed for vesicle rupture and fusion toward formation of a fluid SLB.<sup>89</sup> This work signaled a paradigm shift in the utility of SPR for the characterization of lipid membrane interactions, eventually exhibiting expanded utility for array screenings under SPR imaging<sup>90</sup> and compatibility with a diverse library of lipid species.<sup>91</sup> SLBs on calcinated silicate over gold were thereafter applied toward ultrasensitive detection of cholera toxin<sup>89, 92</sup> and biophysical characterizations of membrane-incorporated synthetic cavitands,<sup>93-97</sup> which have shown great promise as drug delivery tools.<sup>98</sup> Advances in the

nanoscale application of glass to gold surfaces have included development of a uniform spray-based method,<sup>99</sup> and cleanroom processing techniques, such as sputtering of fused silica<sup>100-101</sup> and plasma-enhanced chemical vapor deposition from SiH<sub>4</sub> and O<sub>2</sub> carrier gases.<sup>102-103</sup>

Thin layers of silica may also be applied to nanoparticle films through cleanroom sputtering processes, which have mainly been utilized within sensing schemes for gold nanodisc arrays (AuNDs) and LSPR.<sup>104-106</sup> Vesicles have been shown to adsorb to these nanofilms, as well as rupture and fuse into an SLB depending on the concentration of vesicles applied to the surface.<sup>106</sup> Similarly, silica sol gels may be spin coated over AuND surfaces down to 5 nm thicknesses, allowing for SLB formation and plasmonic sensing of membrane-binding proteins.<sup>107</sup> Among other solid supported LSPR structures are nanohole and nanovoid arrays, which consist of an elevated grid of gold or silver, and recessed holes lined with glass at each base.<sup>108</sup> Dahlin et al. demonstrated that these glass bases could be used to capture phospholipid vesicles and induce their fusion within each nanoaperture, allowing for LSPR based membrane studies.<sup>109</sup> While not directly applying nanoscale layers of glass to the particle, Galush et al. also noted that immobilized nanoparticles could be used for membrane studies, as long as there was glass accessible within the nanoparticle penetration depth for vesicle capture.<sup>110</sup> Membrane studies are not limited to solid-supported structures, however, and it has been demonstrated that dispersed nanoparticles coated with *ca.* 4 nm of silica through the Stöber method,<sup>111</sup> or adsorbed oleic acid<sup>112</sup> can also support lipid bilayers. While there is a clear drive for plasmonic (*i.e.* SPR and LSPR) characterizations of lipid membrane environments, and

feasibility has been broadly demonstrated, there have been very few examples of real-world applications or attempts to hyphenate these materials with complementary analytical techniques; therefore, the available toolkit of methods can benefit from expansion.

## ■ HYPHENATED ANALYSIS WITH MASS SPECTROMETRY

While creating selective and reproducible sensing surfaces is imperative toward extracting accurate quantitative information, it is often not possible to unambiguously identify ligands attached to the surface, especially through the use of label-free techniques (*i.e.* SPR or LSPR), for which any bound molecule, target or non-target, may induce a measurable signal. The addition of complementary analytical methods that are capable of molecular identification is therefore advantageous. Mass spectrometry (MS), which provides measurements based on the charge and molecular weight of ionized chemical species, is one tool that has been shown to substantially increase the informational power of biosensing materials. While comparatively costly and not capable of real-time measurements, mass spectrometric methods have shown great utility toward resolving complex biological structures, and are capable of sophisticated tasks such as protein and nucleic acid sequencing. With regard to SPR coupling, a number of methods are possible, which have been divided into two groups by Stigter et al: 1) MS analysis is performed directly on the SPR or LSPR sensor; or 2) SPR is used as an elution method, with the target removed from the sensor chip prior to MS analysis.<sup>113</sup> While using SPR as

an elution method has many advantages, performing MS directly on the sensing surface saves preparation time and material costs, and will therefore be the primary focus herein.

**MALDI-MS.** There are many surface based ionization methods for mass spectrometry, including matrix-assisted laser desorption/ionization (MALDI), laser ablation-inductively coupled plasma ionization (LA-ICP), desorption electrospray ionization (DESI), direct analysis in real time (DART), and electrostatic-spray ionization (ESTASI).<sup>114</sup> MALDI-MS is the most common of the above techniques, and has proven versatile for array screening, mapping, and imaging. In MALDI, an organic matrix capable of absorbing UV or IR radiation is mixed with the sample to be studied and dried on a specialized sample stage. The matrix serves as a mediator for absorption of laser energy, and may be capable of protonating/deprotonating or donating/accepting electrons from the sample, depending on the choice of matrix.<sup>115</sup> After laser irradiation, ionized species are formed from both the matrix and analyte, which are sent into the mass analyzer through a high voltage applied to the stage. When employing this as a coupled method to SPR, the only preparations that need to take place after SPR analysis are the addition of an organic matrix to the SPR surface, and insertion of the SPR sensor chip into an appropriately configured mass spectrometer. Krone et al. first reported the combination of SPR and MALDI-MS in 1997 for the confirmation of myotoxin *a* binding to sensor surfaces.<sup>116</sup> A commercial BIAcore<sup>®</sup> instrument and sensor chips were used for characterizations of toxin-antibody interactions within purified and crude (*i.e.* rattlesnake venom) samples, with MALDI-MS providing verification that SPR resonance shifts from the crude sample were not the result of nonspecific or non-target interactions. This

method of analysis is scalable toward array characterization, as exhibited by Nedelkov in 2007 for combined SPR imaging and MALDI-MS.<sup>117</sup> Utilizing a  $10 \times 10$  array substrate, five different antibodies to various human plasma proteins were applied across each array element, which were then introduced to their respective protein antigens and monitored under SPR imaging. After matrix application, MALDI-MS was used to assign  $m/z$  peaks to each spot, which matched with the intended binding partners. While these examples represent targeted approaches, untargeted analyses of complex samples have also been reported, including characterizations of nonspecific binding to monolayer surfaces through the Vroman cascade,<sup>118-119</sup> and analysis of thin tissue sections.<sup>120</sup>

In addition to organic matrices and planar SPR surfaces, nanoparticles have gained attention as both inorganic matrices and solid supports. Anker et al. demonstrated that LSPR substrates could function similarly to SPR substrates for hyphenated analysis, utilizing silver nanoprisms for LSPR and mass spectrometric studies of amyloid-beta derived diffusible ligands (ADDLs).<sup>121</sup> While an organic matrix was still used, normal and oxidized ADDLs could be distinguished on-chip using MALDI-MS, once relative amounts were determined by LSPR. Another possibility for coupled LSPR-MS analyses is to use plasmonic nanostructures themselves as the mediating matrix. This was first demonstrated in 2007 by McLean et al. with gold nanoparticles of varying diameter (2 – 10 nm).<sup>122</sup> All nanoparticles tested were mixed with the target analyte and spotted onto a MALDI plate, analogous to conventional MALDI-MS procedures. Peptide ionization with each nanoparticle size was possible under both positive and negative ion modes, though negative ion mode showed a higher abundance of gold clusters ablated from the

nanoparticle surface. Mechanistically, it was hypothesized that small nanoparticles (dia.  $\leq$  2 nm) ionize analytes through quantum confinement/electronic excitation, while larger nanoparticles (dia.  $\geq$  5 nm) ionize analytes through a thermally driven process. Duan et al. were later able to improve ionization efficiency and suppress gold cluster formation through covalent attachment of organic matrices to the gold nanoparticle surface.<sup>123</sup> Despite these advances, MALDI-MS still relies on optimal choice of matrix, organic or inorganic, as well as tuning of the analyte:matrix ratio for highest signal intensity and resolution. The design of substrates that circumvent these processes and streamline the transition from (L)SPR to MS instrumentation is therefore also under investigation.

**SALDI-MS.** Surface-assisted laser desorption/ionization mass spectrometry (SALDI-MS), a matrix-free approach, was sparked by the invention of desorption/ionization on silicon (DIOS) in 1999.<sup>124</sup> Galvanostatic etching was used to create a porous silicon surface, which was not only capable of trapping analytes, but also heat for thermally induced laser desorption and ionization within a standard MALDI-TOF mass spectrometer. While higher laser fluences were required for ionization in comparison to organic matrix use, DIOS benefitted from a lack of matrix ion interference in the low mass region, along with an increase in workflow efficiency since conventional matrix parameters no longer had to be finely tuned. Kawasaki et al. have been noted as pioneers in bridging measurements between SALDI-MS and LSPR since their introduction of multilayer gold nanoparticle films on which both plasmonic and mass spectrometric measurements were possible.<sup>125</sup> These nanofilms were fabricated through a layer-by-layer approach, alternately adsorbing negatively charged gold nanoparticles and

a cationic polymer to the surface. Variations in the fabrication technique toward different SALDI-active nanoscale architectures have included electrochemical deposition of gold nanostructures,<sup>126</sup> thermal annealing of gold nanoparticles to a solid support,<sup>127-128</sup> and microporous gold membrane fabrication,<sup>129</sup> each of which have exhibited modest increases in ionization efficiency. SALDI is also possible on gold thin films possessing no degree of nanostructuring, as demonstrated by Duan et al. with silicate coated SPR sensor chips.<sup>130</sup> The silicate nanofilms were fabricated under the same methods as Phillips et al. for SPR analysis of SLBs,<sup>89</sup> though in MS they also function as a thermal insulator for the gold surface, allowing for laser-generated heat to stay confined to localized hot spots from which desorption and ionization are possible. While this calcinated silicate substrate has not yet been utilized as an interface between SPR and MS, it does provide a clear example of how rational material design can influence and impart multimodal detection capabilities to fabricated sensors, and thus, is a frequently visited tool throughout this work.

## ■ DISSERTATION SCOPE

The goals of this thesis are to expand the efficiency and throughput of lipid membrane based biosensors toward their practical use within laboratories possessing varying levels of instrumentation. Surface plasmon resonance serves as the primary analytical tool for these studies, though integrations of nanotechnology and mass spectrometry have demonstrated noteworthy advances in the informational power of SPR, and are therefore also explored. Chapter 2 begins with a case study of how surface

analytical techniques, such as SPR and fluorescence microscopy, can be used to influence the development of new biological constructs with potential applications for targeted drug delivery. Within this chapter, the first hybrid bilayer systems coassembled from synthetic, amphiphilic dendrimers and naturally occurring phospholipids are reported. Both concentration and generation of the incorporated dendrimers have direct impacts on the biophysical properties of the coassemblies: raising the dendrimer concentration increases the hybrid bilayer stability, while changes in the generation and the concentration of the embedded dendrimers impact the fluidity of the coassembled systems. Multivalent dendrimer amine terminals allow for nondestructive *in situ* derivatization, providing a convenient approach to decorate and modulate the local environment of the hybrid bilayers, offering a unique platform for the creation of hybrid systems with modular and precisely controllable behavior.

Chapter 3 begins to explore method development for high-throughput analysis of SLB arrays. Their fabrication has traditionally been an arduous and complex task, primarily due to the need to maintain SLBs within an aqueous environment. We demonstrate the use of trehalose vitrified phospholipid vesicles that facilitate on-demand generation of microarrays, allowing each element a unique composition, for the label-free and high-throughput analysis of biomolecular interactions by SPR imaging. Small, unilamellar vesicles (SUVs) are suspended in trehalose, deposited in a spatially defined manner, with the trehalose vitrifying on either hydrophilic or hydrophobic SPR substrates. SLBs are subsequently formed on-demand simply by *in situ* hydration of the array in the SPR instrument flow cell. The resulting SLBs exhibit high lateral mobility,

characteristic of fluidic cellular lipid membranes, and preserve the biological function of embedded cell membrane receptors, as indicated by SPR affinity measurements.

Chapter 4 marks a shift from direct applications of SLBs toward the design of materials that enhance their measurement capabilities. Gold nanoparticles (AuNPs) have been used as measurement and enhancement tools within a wide variety of analytical methods, including SPR and SLB studies, and here we introduce a nanoparticle bioconjugation strategy that utilizes functionalized polythymine DNA in place of conventional alkane or PEG linkers and diluents. These nanoparticles remain a stable colloidal suspension under a wide range of buffers and ionic strengths, and can endure multiple rounds of lyophilization while retaining high biological activity. Furthermore, the high stability of the DNA/AuNPs allows for multiple reactions and conjugations to be performed within the colloidal suspensions (*i.e.*, Protein A and antibody binding) for tailored and specific recognition to take place. We demonstrate the applications of these DNA/AuNPs for colorimetric assays and microplate feasibility; additionally, SPR imaging analysis of a supported membrane microarray shows excellent results with DNA/AuNPs as the enhancing agent.

The potential for cross-platform analysis by LSPR and SALDI-MS is explored in Chapter 5. Gold nanoparticles are once again used, though bound to a solid glass support and protected by a nanoscale, calcinated silicate film. These proof-of-concept studies involve metrological and optical characterizations of the fabricated nanofilm, real-time monitoring of vesicle–surface interactions toward formation of a fluid lipid bilayer on the surface, and SALDI mass spectrometric analysis of peptides and cytochrome c. Yielding

complementary analytical information, a new tool is provided for comprehensive analysis of biomolecular samples, for which scalability and array applications are explored in Chapter 6. Photocatalytic patterning proved effective for defining isolated array elements of calcinated gold nanoparticles on glass, which demonstrated excellent capability as a reusable and matrix-free mass spectrometry array platform. Insights behind the high ionization efficiency in SALDI for the silicate-protected gold nanoparticles used throughout this work are also discussed.

The research undertaken concludes within Chapter 7, in which the potential of new fabrication technologies, such as 3D printing, are explored for optical biosensor construction. In the analytical field, 3D printing has largely been exploited for the prototyping of fluidic devices and custom mechanical parts, yet no effort has been made to create 3D printed optics. Using a proprietary transparent resin from Formlabs and stereolithography techniques, we 3D printed prisms for surface plasmon resonance biosensing. Following optimization of the polishing procedures, the material was modeled and characterized in regards to optical performance. Deposition of a nanoscale layer of gold and application of a self-assembled monolayer allowed for label-free biosensing of cholera toxin, utilizing a ganglioside receptor embedded in a biomimetic lipid membrane on the gold surface. This represents the first 3D printed optical device, and demonstrates the versatility of 3D printing for the rapid prototyping of field deployable optical equipment. Further developments of plasmonic materials and SLB platforms will be the focus of Chapter 8, with discussions of active research within similar and adjacent fields, and future directions that are open to innovation.

## ■ REFERENCES

- (1) National Research Council (U.S.). Committee on Toxicity Testing and Assessment of Environmental Agents., *Toxicity Testing in the 21st Century : A Vision and a Strategy*. National Academies Press: Washington, DC, **2007**; p 196.
- (2) Turner, A. P. F. Biosensors--Sense and Sensitivity. *Science* **2000**, *290*, 1315-1317.
- (3) Castellana, E. T.; Cremer, P. S. Solid Supported Lipid Bilayers: From Biophysical Studies to Sensor Design. *Surf. Sci. Rep.* **2006**, *61*, 429-444.
- (4) Bally, M.; Bailey, K.; Sugihara, K.; Grieshaber, D.; Voros, J.; Stadler, B. Liposome and Lipid Bilayer Arrays Towards Biosensing Applications. *Small* **2010**, *6*, 2481-2497.
- (5) Hsia, C. Y.; Richards, M. J.; Daniel, S. A Review of Traditional and Emerging Methods to Characterize Lipid-Protein Interactions in Biological Membranes. *Anal. Methods* **2015**, *7*, 7076-7094.
- (6) Schulz, M.; Binder, W. H. Mixed Hybrid Lipid/Polymer Vesicles as a Novel Membrane Platform. *Macromol. Rapid Commun.* **2015**, *36*, 2031-2041.
- (7) Scott, R. E. Plasma Membrane Vesiculation: A New Technique for Isolation of Plasma Membranes. *Science* **1976**, *194*, 743-745.
- (8) Sezgin, E.; Kaiser, H. J.; Baumgart, T.; Schwille, P.; Simons, K.; Levental, I. Elucidating Membrane Structure and Protein Behavior Using Giant Plasma Membrane Vesicles. *Nat. Protoc.* **2012**, *7*, 1042-1051.
- (9) Hsia, C. Y.; Chen, L. X.; Singh, R. R.; DeLisa, M. P.; Daniel, S. A Molecularly Complete Planar Bacterial Outer Membrane Platform. *Sci. Rep.* **2016**, *6*.
- (10) *Liposomes: Methods and Protocols, Volume 2: Biological Membrane Models*. 1 ed.; Humana Press: New York, NY, **2010**; Vol. 606, p XVI, 548.

- (11) Xu, D.; Cheng, Q. Surface-Bound Lipid Vesicles Encapsulating Redox Species for Amperometric Biosensing of Pore-Forming Bacterial Toxins. *J. Am. Chem. Soc.* **2002**, *124*, 14314-14315.
- (12) Cheng, Q.; Zhu, S.; Song, J.; Zhang, N. Functional Lipid Microstructures Immobilized on a Gold Electrode for Voltammetric Biosensing of Cholera Toxin. *Analyst* **2004**, *129*, 309-314.
- (13) Stamou, D.; Duschl, C.; Delamarche, E.; Vogel, H. Self-Assembled Microarrays of Attoliter Molecular Vessels. *Angew. Chem., Int. Ed.* **2003**, *42*, 5580-5583.
- (14) Dahlin, A. B.; Jonsson, M. P.; Hook, F. Specific Self-Assembly of Single Lipid Vesicles in Nanoplasmonic Apertures in Gold. *Adv. Mater.* **2008**, *20*, 1436-1442.
- (15) Wittenberg, N. J.; Im, H.; Johnson, T. W.; Xu, X. H.; Warrington, A. E.; Rodriguez, M.; Oh, S. H. Facile Assembly of Micro- and Nanoarrays for Sensing with Natural Cell Membranes. *ACS Nano* **2011**, *5*, 7555-7564.
- (16) Vacek, J.; Zatloukalova, M.; Geleticova, J.; Kubala, M.; Modriansky, M.; Fekete, L.; Masek, J.; Hubatka, F.; Turanek, J. Electrochemical Platform for the Detection of Transmembrane Proteins Reconstituted into Liposomes. *Anal. Chem.* **2016**, *88*, 4548-4556.
- (17) Bayburt, T. H.; Grinkova, Y. V.; Sligar, S. G. Self-Assembly of Discoidal Phospholipid Bilayer Nanoparticles with Membrane Scaffold Proteins. *Nano Lett.* **2002**, *2*, 853-856.
- (18) Denisov, I. G.; Sligari, S. G. Nanodiscs in Membrane Biochemistry and Biophysics. *Chem. Rev.* **2017**, *117*, 4669-4713.
- (19) Borch, J.; Torta, F.; Sligar, S. G.; Roepstorff, P. Nanodiscs for Immobilization of Lipid Bilayers and Membrane Receptors: Kinetic Analysis of Cholera Toxin Binding to a Glycolipid Receptor. *Anal. Chem.* **2008**, *80*, 6245-6252.
- (20) Das, A.; Sligar, S. G. Modulation of the Cytochrome P450 Reductase Redox Potential by the Phospholipid Bilayer. *Biochemistry* **2009**, *48*, 12104-12112.

- (21) Sloan, C. D. K.; Marty, M. T.; Sligar, S. G.; Bailey, R. C. Interfacing Lipid Bilayer Nanodiscs and Silicon Photonic Sensor Arrays for Multiplexed Protein-Lipid and Protein-Membrane Protein Interaction Screening. *Anal. Chem.* **2013**, *85*, 2970-2976.
- (22) Johnsson, M.; Edwards, K. Liposomes, Disks, and Spherical Micelles: Aggregate Structure in Mixtures of Gel Phase Phosphatidylcholines and Poly(Ethylene Glycol)-Phospholipids. *Biophys. J.* **2003**, *85*, 3839-3847.
- (23) Johansson, E.; Engvall, C.; Arfvidsson, M.; Lundahl, P.; Edwards, K. Development and Initial Evaluation of PEG-Stabilized Bilayer Disks as Novel Model Membranes. *Biophys. Chem.* **2005**, *113*, 183-192.
- (24) Hernandez, V. A.; Reijmar, K.; Edwards, K. Label-Free Characterization of Peptide-Lipid Interactions Using Immobilized Lipodisks. *Anal. Chem.* **2013**, *85*, 7377-7384.
- (25) Duong-Thi, M. D.; Bergstrom, M.; Edwards, K.; Eriksson, J.; Ohlson, S.; Ying, J. T. Y.; Torres, J.; Hernandez, V. A. Lipodisks Integrated with Weak Affinity Chromatography Enable Fragment Screening of Integral Membrane Proteins. *Analyst* **2016**, *141*, 981-988.
- (26) Reijmar, K.; Edwards, K.; Andersson, K.; Hernandez, V. A. Characterizing and Controlling the Loading and Release of Cationic Amphiphilic Peptides onto and from PEG-Stabilized Lipodisks. *Langmuir* **2016**, *32*, 12091-12099.
- (27) Plant, A. L. Supported Hybrid Bilayer Membranes as Rugged Cell Membrane Mimics. *Langmuir* **1999**, *15*, 5128-5135.
- (28) Wang, Z.; Wilkop, T.; Cheng, Q. Characterization of Micropatterned Lipid Membranes on a Gold Surface by Surface Plasmon Resonance Imaging and Electrochemical Signaling of a Pore-Forming Protein. *Langmuir* **2005**, *21*, 10292-10296.
- (29) Wilkop, T.; Xu, D.; Cheng, Q. Characterization of Pore Formation by Streptolysin O on Supported Lipid Membranes by Impedance Spectroscopy and Surface Plasmon Resonance Spectroscopy. *Langmuir* **2007**, *23*, 1403-1409.

- (30) Wilkop, T.; Xu, D.; Cheng, Q. Electrochemical Characterization of Pore Formation by Bacterial Protein Toxins on Hybrid Supported Membranes. *Langmuir* **2008**, *24*, 5615-5621.
- (31) Tse, E. C. M.; Barile, C. J.; Gewargis, J. P.; Li, Y.; Zimmerman, S. C.; Gewirth, A. A. Anion Transport through Lipids in a Hybrid Bilayer Membrane. *Anal. Chem.* **2015**, *87*, 2403-2409.
- (32) Hamai, C.; Yang, T. L.; Kataoka, S.; Cremer, P. S.; Musser, S. M. Effect of Average Phospholipid Curvature on Supported Bilayer Formation on Glass by Vesicle Fusion. *Biophys. J.* **2006**, *90*, 1241-1248.
- (33) Tamm, L. K.; McConnell, H. M. Supported Phospholipid-Bilayers. *Biophys. J.* **1985**, *47*, 105-113.
- (34) Johnson, S. J.; Bayerl, T. M.; Mcdermott, D. C.; Adam, G. W.; Rennie, A. R.; Thomas, R. K.; Sackmann, E. Structure of an Adsorbed Dimyristoylphosphatidylcholine Bilayer Measured with Specular Reflection of Neutrons. *Biophys. J.* **1991**, *59*, 289-294.
- (35) Groves, J. T.; Ulman, N.; Boxer, S. G. Micropatterning Fluid Lipid Bilayers on Solid Supports. *Science* **1997**, *275*, 651-653.
- (36) Sackmann, E. Supported Membranes: Scientific and Practical Applications. *Science* **1996**, *271*, 43-48.
- (37) Phillips, K. S.; Cheng, Q. Microfluidic Immunoassay for Bacterial Toxins with Supported Phospholipid Bilayer Membranes on Poly(Dimethylsiloxane). *Anal. Chem.* **2005**, *77*, 327-334.
- (38) Peng, P. Y.; Chiang, P. C.; Chao, L. Mobile Lipid Bilayers on Gold Surfaces through Structure-Induced Lipid Vesicle Rupture. *Langmuir* **2015**, *31*, 3904-3911.
- (39) Shi, J.; Yang, T.; Kataoka, S.; Zhang, Y.; Diaz, A. J.; Cremer, P. S. GM1 Clustering Inhibits Cholera Toxin Binding in Supported Phospholipid Membranes. *J. Am. Chem. Soc.* **2007**, *129*, 5954-5961.

- (40) Costello, D. A.; Whittaker, G. R.; Daniel, S. Variations in pH Sensitivity, Acid Stability, and Fusogenicity of Three Influenza Virus H3 Subtypes. *J. Virol.* **2015**, *89*, 350-360.
- (41) Taylor, J. D.; Linman, M. J.; Wilkop, T.; Cheng, Q. Regenerable Tethered Bilayer Lipid Membrane Arrays for Multiplexed Label-Free Analysis of Lipid-Protein Interactions on Poly(Dimethylsiloxane) Microchips Using SPR Imaging. *Anal. Chem.* **2009**, *81*, 1146-1153.
- (42) Pace, H.; Simonsson Nystrom, L.; Gunnarsson, A.; Eck, E.; Monson, C.; Geschwindner, S.; Snijder, A.; Hook, F. Preserved Transmembrane Protein Mobility in Polymer-Supported Lipid Bilayers Derived from Cell Membranes. *Anal. Chem.* **2015**, *87*, 9194-9203.
- (43) Richards, M. J.; Hsia, C. Y.; Singh, R. R.; Haider, H.; Kumpf, J.; Kawate, T.; Daniel, S. Membrane Protein Mobility and Orientation Preserved in Supported Bilayers Created Directly from Cell Plasma Membrane Blebs. *Langmuir* **2016**, *32*, 2963-2974.
- (44) Winterhalter, M. Black Lipid Membranes. *Curr. Opin. Colloid Interface Sci.* **2000**, *5*, 250-255.
- (45) Heitz, B. A.; Xu, J. H.; Jones, I. W.; Keogh, J. P.; Comi, T. J.; Hall, H. K.; Aspinwall, C. A.; Saavedra, S. S. Polymerized Planar Suspended Lipid Bilayers for Single Ion Channel Recordings: Comparison of Several Dienoyl Lipids. *Langmuir* **2011**, *27*, 1882-1890.
- (46) Baker, C. A.; Bright, L. K.; Aspinwall, C. A. Photolithographic Fabrication of Microapertures with Well-Defined, Three-Dimensional Geometries for Suspended Lipid Membrane Studies. *Anal. Chem.* **2013**, *85*, 9078-9086.
- (47) Baker, C. A.; Aspinwall, C. A. Emerging Trends in Precision Fabrication of Microapertures to Support Suspended Lipid Membranes for Sensors, Sequencing, and Beyond. *Anal. Bioanal. Chem.* **2015**, *407*, 647-652.
- (48) Schmidt, J. Membrane Platforms for Biological Nanopore Sensing and Sequencing. *Curr. Opin. Biotechnol.* **2016**, *39*, 17-27.

- (49) Stefureac, R.; Long, Y. T.; Kraatz, H. B.; Howard, P.; Lee, J. S. Transport of Alpha-Helical Peptides through Alpha-Hemolysin and Aerolysin Pores. *Biochemistry* **2006**, *45*, 9172-9179.
- (50) Wang, H. Y.; Li, Y.; Qin, L. X.; Heyman, A.; Shoseyov, O.; Willner, I.; Long, Y. T.; Tian, H. Single-Molecule DNA Detection Using a Novel SP1 Protein Nanopore. *Chem. Commun.* **2013**, *49*, 1741-1743.
- (51) Cao, C.; Ying, Y. L.; Hu, Z. L.; Liao, D. F.; Tian, H.; Long, Y. T. Discrimination of Oligonucleotides of Different Lengths with a Wild-Type Aerolysin Nanopore. *Nat. Nanotechnol.* **2016**, *11*, 713-718.
- (52) Gu, Z.; Ying, Y. L.; Cao, C.; He, P. G.; Long, Y. T. Accurate Data Process for Nanopore Analysis. *Anal. Chem.* **2015**, *87*, 907-913.
- (53) Ying, Y. L.; Cao, C.; Long, Y. T. Single Molecule Analysis by Biological Nanopore Sensors. *Analyst* **2014**, *139*, 3826-3835.
- (54) Kiessling, L. L.; Pohl, N. L. Strength in Numbers: Non-Natural Polyvalent Carbohydrate Derivatives. *Chem. Biol.* **1996**, *3*, 71-77.
- (55) Mammen, M.; Choi, S. K.; Whitesides, G. M. Polyvalent Interactions in Biological Systems: Implications for Design and Use of Multivalent Ligands and Inhibitors. *Angew. Chem., Int. Ed.* **1998**, *37*, 2755-2794.
- (56) Sagle, L. B.; Ruvuna, L. K.; Bingham, J. M.; Liu, C. M.; Cremer, P. S.; Van Duyne, R. P. Single Plasmonic Nanoparticle Tracking Studies of Solid Supported Bilayers with Ganglioside Lipids. *J. Am. Chem. Soc.* **2012**, *134*, 15832-15839.
- (57) Hsieh, C. L.; Spindler, S.; Ehrig, J.; Sandoghdar, V. Tracking Single Particles on Supported Lipid Membranes: Multimobility Diffusion and Nanoscopic Confinement. *J. Phys. Chem. B* **2014**, *118*, 1545-1554.
- (58) Spillane, K. M.; Ortega-Arroyo, J.; de Wit, G.; Eggeling, C.; Ewers, H.; Wallace, M. I.; Kukura, P. High-Speed Single-Particle Tracking of GM1 in Model Membranes Reveals Anomalous Diffusion Due to Interleaflet Coupling and Molecular Pinning. *Nano Lett.* **2014**, *14*, 5390-5397.

- (59) Axelrod, D.; Koppel, D. E.; Schlessinger, J.; Elson, E.; Webb, W. W. Mobility Measurement by Analysis of Fluorescence Photobleaching Recovery Kinetics. *Biophys. J.* **1976**, *16*, 1055-1069.
- (60) Reits, E. A. J.; Neefjes, J. J. From Fixed to FRAP: Measuring Protein Mobility and Activity in Living Cells. *Nat. Cell Biol.* **2001**, *3*, E145-E147.
- (61) Sprague, B. L.; McNally, J. G. FRAP Analysis of Binding: Proper and Fitting. *Trends Cell Biol.* **2005**, *15*, 84-91.
- (62) Soumpasis, D. M. Theoretical-Analysis of Fluorescence Photobleaching Recovery Experiments. *Biophys. J.* **1983**, *41*, 95-97.
- (63) Deschout, H.; Hagman, J.; Fransson, S.; Jonasson, J.; Rudemo, M.; Loren, N.; Braeckmans, K. Straightforward FRAP for Quantitative Diffusion Measurements with a Laser Scanning Microscope. *Opt. Express* **2010**, *18*, 22886-22905.
- (64) Homola, J. Surface Plasmon Resonance Sensors for Detection of Chemical and Biological Species. *Chem. Rev.* **2008**, *108*, 462-493.
- (65) Masson, J. F. Surface Plasmon Resonance Clinical Biosensors for Medical Diagnostics. *ACS Sensors* **2017**, *2*, 16-30.
- (66) Phillips, K. S.; Cheng, Q. Recent Advances in Surface Plasmon Resonance Based Techniques for Bioanalysis. *Anal. Bioanal. Chem.* **2007**, *387*, 1831-1840.
- (67) Linman, M. J.; Cheng, Q. J. Surface Plasmon Resonance: New Biointerface Designs and High-Throughput Affinity Screening. *Optical Guided-Wave Chemical and Biosensors I* **2010**, *7*, 133-153.
- (68) Linman, M. J.; Abbas, A.; Cheng, Q. A. Interface Design and Multiplexed Analysis with Surface Plasmon Resonance (SPR) Spectroscopy and SPR Imaging. *Analyst* **2010**, *135*, 2759-2767.
- (69) Fasoli, J. B.; Corn, R. M. Surface Enzyme Chemistries for Ultrasensitive Microarray Biosensing with SPR Imaging. *Langmuir* **2015**, *31*, 9527-9536.

- (70) Abbas, A.; Linman, M. J.; Cheng, Q. New Trends in Instrumental Design for Surface Plasmon Resonance-Based Biosensors. *Biosens. Bioelectron.* **2011**, *26*, 1815-1824.
- (71) Couture, M.; Zhao, S. S.; Masson, J. F. Modern Surface Plasmon Resonance for Bioanalytics and Biophysics. *Phys. Chem. Chem. Phys.* **2013**, *15*, 11190-11216.
- (72) Willets, K. A.; Van Duyne, R. P. Localized Surface Plasmon Resonance Spectroscopy and Sensing. *Annu. Rev. Phys. Chem.* **2007**, *58*, 267-297.
- (73) Unser, S.; Bruzas, I.; He, J.; Sagle, L. Localized Surface Plasmon Resonance Biosensing: Current Challenges and Approaches. *Sensors* **2015**, *15*, 15684-15716.
- (74) Otto, A. Excitation of Nonradiative Surface Plasma Waves in Silver by the Method of Frustrated Total Reflection. *Physik* **1968**, *216*, 398-410.
- (75) Kretschmann, E.; Raether, H. Radiative Decay of Non Radiative Surface Plasmons Excited by Light. *Naturforsch., A: Astrophys., Phys. Phys. Chem.* **1968**, *23*, 2135-2136.
- (76) Raether, H. Surface-Plasmons on Smooth and Rough Surfaces and on Gratings. *Springer Tracts in Modern Physics* **1988**, *111*, 1-133.
- (77) Wustholz, K. L.; Henry, A. I.; McMahon, J. M.; Freeman, R. G.; Valley, N.; Piotti, M. E.; Natan, M. J.; Schatz, G. C.; Van Duyne, R. P. Structure-Activity Relationships in Gold Nanoparticle Dimers and Trimers for Surface-Enhanced Raman Spectroscopy. *J. Am. Chem. Soc.* **2010**, *132*, 10903-10910.
- (78) NanoSPR - Devices and Glass Plates for Surface Plasmon Resonance. <http://nanospr.com/> (accessed May 17th, 2017).
- (79) Affinité Instruments - SPR Innovations. <http://affiniteinstruments.com/> (accessed May 17th, 2017).
- (80) Spoto, G.; Minunni, M. Surface Plasmon Resonance Imaging: What Next? *J. Phys. Chem. Lett.* **2012**, *3*, 2682-2691.

- (81) Yockell-Lelievre, H.; Bukar, N.; McKeating, K. S.; Arnaud, M.; Cosin, P.; Guo, Y.; Dupret-Carruel, J.; Mougin, B.; Masson, J. F. Plasmonic Sensors for the Competitive Detection of Testosterone. *Analyst* **2015**, *140*, 5105-5111.
- (82) Yockell-Lelievre, H.; Lussier, F.; Masson, J. F. Influence of the Particle Shape and Density of Self-Assembled Gold Nanoparticle Sensors on LSPR and SERS. *J. Phys. Chem. C* **2015**, *119*, 28577-28585.
- (83) Yockell-Lelievre, H.; Bukar, N.; Toulouse, J. L.; Pelletier, J. N.; Masson, J. F. Naked-Eye Nanobiosensor for Therapeutic Drug Monitoring of Methotrexate. *Analyst* **2016**, *141*, 697-703.
- (84) Ekgasit, S.; Thammacharoen, C.; Knoll, W. Surface Plasmon Resonance Spectroscopy Based on Evanescent Field Treatment. *Anal. Chem.* **2004**, *76*, 561-568.
- (85) Im, H.; Shao, H. L.; Park, Y. I.; Peterson, V. M.; Castro, C. M.; Weissleder, R.; Lee, H. Label-Free Detection and Molecular Profiling of Exosomes with a Nano-Plasmonic Sensor. *Nat. Biotechnol.* **2014**, *32*, 490-U219.
- (86) Ruemmele, J. A.; Hall, W. P.; Ruvuna, L. K.; Van Duyne, R. P. A Localized Surface Plasmon Resonance Imaging Instrument for Multiplexed Biosensing. *Anal. Chem.* **2013**, *85*, 4560-4566.
- (87) Fenzl, C.; Hirsch, T.; Baeumner, A. J. Liposomes with High Refractive Index Encapsulants as Tunable Signal Amplification Tools in Surface Plasmon Resonance Spectroscopy. *Anal. Chem.* **2015**, *87*, 11157-11163.
- (88) Fenzl, C.; Genslein, C.; Domonkos, C.; Edwards, K. A.; Hirsch, T.; Baeumner, A. J. Investigating Non-Specific Binding to Chemically Engineered Sensor Surfaces Using Liposomes as Models. *Analyst* **2016**, *141*, 5265-5273.
- (89) Phillips, K. S.; Han, J. H.; Martinez, M.; Wang, Z. Z.; Carter, D.; Cheng, Q. Nanoscale Glassification of Gold Substrates for Surface Plasmon Resonance Analysis of Protein Toxins with Supported Lipid Membranes. *Anal. Chem.* **2006**, *78*, 596-603.

- (90) Phillips, K. S.; Wilkop, T.; Wu, J. J.; Al-Kaysi, R. O.; Cheng, Q. Surface Plasmon Resonance Imaging Analysis of Protein-Receptor Binding in Supported Membrane Arrays on Gold Substrates with Calcinated Silicate Films. *J. Am. Chem. Soc.* **2006**, *128*, 9590-9591.
- (91) Han, J. H.; Taylor, J. D.; Phillips, K. S.; Wang, X.; Feng, P.; Cheng, Q. Characterizing Stability Properties of Supported Bilayer Membranes on Nanoglassified Substrates Using Surface Plasmon Resonance. *Langmuir* **2008**, *24*, 8127-8133.
- (92) Liu, Y.; Cheng, Q. Detection of Membrane-Binding Proteins by Surface Plasmon Resonance with an All-Aqueous Amplification Scheme. *Anal. Chem.* **2012**, *84*, 3179-3186.
- (93) Liu, Y.; Liao, P. H.; Cheng, Q. A.; Hooley, R. J. Protein and Small Molecule Recognition Properties of Deep Cavitands in a Supported Lipid Membrane Determined by Calcination-Enhanced SPR Spectroscopy. *J. Am. Chem. Soc.* **2010**, *132*, 10383-10390.
- (94) Liu, Y.; Young, M. C.; Moshe, O.; Cheng, Q.; Hooley, R. J. A Membrane-Bound Synthetic Receptor That Promotes Growth of a Polymeric Coating at the Bilayer-Water Interface. *Angew. Chem., Int. Ed.* **2012**, *51*, 7748-7751.
- (95) Ghang, Y. J.; Lloyd, J. J.; Moehlig, M. P.; Arguelles, J. K.; Mettry, M.; Zhang, X.; Julian, R. R.; Cheng, Q.; Hooley, R. J. Labeled Protein Recognition at a Membrane Bilayer Interface by Embedded Synthetic Receptors. *Langmuir* **2014**, *30*, 10161-10166.
- (96) Ghang, Y. J.; Perez, L.; Morgan, M. A.; Si, F.; Hamdy, O. M.; Beecher, C. N.; Larive, C. K.; Julian, R. R.; Zhong, W. W.; Cheng, Q.; Hooley, R. J. Anionic Deep Cavitands Enable the Adhesion of Unmodified Proteins at a Membrane Bilayer. *Soft Matter* **2014**, *10*, 9651-9656.
- (97) Perez, L.; Ghang, Y. J.; Williams, P. B.; Wang, Y.; Cheng, Q.; Hooley, R. J. Cell and Protein Recognition at a Supported Bilayer Interface Via in Situ Cavitand-Mediated Functional Polymer Growth. *Langmuir* **2015**, *31*, 11152-11157.

- (98) Ghang, Y. J.; Schramm, M. P.; Zhang, F.; Acey, R. A.; David, C. N.; Wilson, E. H.; Wang, Y. S.; Cheng, Q.; Hooley, R. J. Selective Cavitand-Mediated Endocytosis of Targeted Imaging Agents into Live Cells. *J. Am. Chem. Soc.* **2013**, *135*, 7090-7093.
- (99) Linman, M. J.; Culver, S. P.; Cheng, Q. Fabrication of Fracture-Free Nanoglassified Substrates by Layer-by-Layer Deposition with a Paint Gun Technique for Real-Time Monitoring of Protein-Lipid Interactions. *Langmuir* **2009**, *25*, 3075-3082.
- (100) Tawa, K.; Morigaki, K. Substrate-Supported Phospholipid Membranes Studied by Surface Plasmon Resonance and Surface Plasmon Fluorescence Spectroscopy. *Biophys. J.* **2005**, *89*, 2750-2758.
- (101) Morigaki, K.; Tawa, K. Vesicle Fusion Studied by Surface Plasmon Resonance and Surface Plasmon Fluorescence Spectroscopy. *Biophys. J.* **2006**, *91*, 1380-1387.
- (102) Abbas, A.; Linman, M. J.; Cheng, Q. Patterned Resonance Plasmonic Microarrays for High-Performance SPR Imaging. *Anal. Chem.* **2011**, *83*, 3147-3152.
- (103) Linman, M. J.; Abbas, A.; Roberts, C. C.; Cheng, Q. Etched Glass Microarrays with Differential Resonance for Enhanced Contrast and Sensitivity of Surface Plasmon Resonance Imaging Analysis. *Anal. Chem.* **2011**, *83*, 5936-5943.
- (104) Jose, J.; Jordan, L. R.; Johnson, T. W.; Lee, S. H.; Wittenberg, N. J.; Oh, S. H. Topographically Flat Substrates with Embedded Nanoplasmonic Devices for Biosensing. *Adv. Funct. Mater.* **2013**, *23*, 2812-2820.
- (105) Jackman, J. A.; Zhdanov, V. P.; Cho, N. J. Nanoplasmonic Biosensing for Soft Matter Adsorption: Kinetics of Lipid Vesicle Attachment and Shape Deformation. *Langmuir* **2014**, *30*, 9494-9503.
- (106) Zan, G. H.; Jackman, J. A.; Kim, S. O.; Cho, N. J. Controlling Lipid Membrane Architecture for Tunable Nanoplasmonic Biosensing. *Small* **2014**, *10*, 4828-4832.

- (107) Bruzas, I.; Unser, S.; Yazdi, S.; Ringe, E.; Sagle, L. Ultrasensitive Plasmonic Platform for Label-Free Detection of Membrane-Associated Species. *Anal. Chem.* **2016**, *88*, 7968-7974.
- (108) Genet, C.; Ebbesen, T. W. Light in Tiny Holes. *Nature* **2007**, *445*, 39-46.
- (109) Dahlin, A.; Zach, M.; Rindzevicius, T.; Kall, M.; Sutherland, D. S.; Hook, F. Localized Surface Plasmon Resonance Sensing of Lipid-Membrane-Mediated Biorecognition Events. *J. Am. Chem. Soc.* **2005**, *127*, 5043-5048.
- (110) Galush, W. J.; Shelby, S. A.; Mulvihill, M. J.; Tao, A.; Yang, P.; Groves, J. T. A Nanocube Plasmonic Sensor for Molecular Binding on Membrane Surfaces. *Nano Lett.* **2009**, *9*, 2077-82.
- (111) Wu, H. J.; Henzie, J.; Lin, W. C.; Rhodes, C.; Li, Z.; Sartorel, E.; Thorner, J.; Yang, P. D.; Groves, J. T. Membrane-Protein Binding Measured with Solution-Phase Plasmonic Nanocube Sensors. *Nat. Methods* **2012**, *9*, 1189-1191.
- (112) Matthews, J. R.; Payne, C. M.; Hafner, J. H. Analysis of Phospholipid Bilayers on Gold Nanorods by Plasmon Resonance Sensing and Surface-Enhanced Raman Scattering. *Langmuir* **2015**, *31*, 9893-9900.
- (113) Stigter, E. C. A.; de Jong, G. J.; van Bennekom, W. P. Coupling Surface-Plasmon Resonance and Mass Spectrometry to Quantify and to Identify Ligands. *TrAC, Trends Anal. Chem.* **2013**, *45*, 107-120.
- (114) Gross, J. H., *Mass Spectrometry*. 2nd ed.; Springer-Verlag Berlin Heidelberg: **2011**; p 753.
- (115) Karas, M.; Gluckmann, M.; Schafer, J. Ionization in Matrix-Assisted Laser Desorption/Ionization: Singly Charged Molecular Ions Are the Lucky Survivors. *J. Mass. Spectrom.* **2000**, *35*, 1-12.
- (116) Krone, J. R.; Nelson, R. W.; Dogruel, D.; Williams, P.; Granzow, R. BIA/MS: Interfacing Biomolecular Interaction Analysis with Mass Spectrometry. *Anal. Biochem.* **1997**, *244*, 124-132.

- (117) Nedelkov, D. Development of Surface Plasmon Resonance Mass Spectrometry Array Platform. *Anal. Chem.* **2007**, *79*, 5987-5990.
- (118) Aube, A.; Breault-Turcot, J.; Chaurand, P.; Pelletier, J. N.; Masson, J. F. Non-Specific Adsorption of Crude Cell Lysate on Surface Plasmon Resonance Sensors. *Langmuir* **2013**, *29*, 10141-10148.
- (119) Breault-Turcot, J.; Chaurand, P.; Masson, J. F. Unravelling Nonspecific Adsorption of Complex Protein Mixture on Surfaces with SPR and MS. *Anal. Chem.* **2014**, *86*, 9612-9619.
- (120) Forest, S.; Breault-Turcott, J.; Chaurand, P.; Masson, J. F. Surface Plasmon Resonance Imaging-MALDI-TOF Imaging Mass Spectrometry of Thin Tissue Sections. *Anal. Chem.* **2016**, *88*, 2072-2079.
- (121) Anker, J. N.; Hall, W. P.; Lambert, M. P.; Velasco, P. T.; Mrksich, M.; Klein, W. L.; Van Duyne, R. P. Detection and Identification of Bioanalytes with High Resolution LSPR Spectroscopy and MALDI Mass Spectrometry. *J. Phys. Chem., C* **2009**, *113*, 5891-5894.
- (122) McLean, J. A.; Stumpo, K. A.; Russell, D. H. Size-Selected (2-10 nm) Gold Nanoparticles for Matrix Assisted Laser Desorption Ionization of Peptides. *J. Am. Chem. Soc.* **2005**, *127*, 5304-5305.
- (123) Duan, J.; Linman, M.; Chen, C.-Y.; Cheng, Q. Chca-Modified Au Nanoparticles for Laser Desorption Ionization Mass Spectrometric Analysis of Peptides. *J. Am. Soc. Mass Spectrom.* **2009**, *20*, 1530-1539.
- (124) Buriak, J. M.; Wei, J.; Siuzdak, G. Desorption-Ionization Mass Spectrometry on Porous Silicon. *Nature* **1999**, *399*, 243-246.
- (125) Kawasaki, H.; Sugitani, T.; Watanabe, T.; Yonezawa, T.; Moriwaki, H.; Arakawa, R. Layer-by-Layer Self-Assembled Multilayer Films of Gold Nanoparticles for Surface-Assisted Laser Desorption/Ionization Mass Spectrometry. *Anal. Chem.* **2008**, *80*, 7524-7533.

- (126) Nayak, R.; Knapp, D. R. Matrix-Free Ldi Mass Spectrometry Platform Using Patterned Nanostructured Gold Thin Film. *Anal. Chem.* **2010**, *82*, 7772-7778.
- (127) Inuta, M.; Arakawa, R.; Kawasaki, H. Use of Thermally Annealed Multilayer Gold Nanoparticle Films in Combination Analysis of Localized Surface Plasmon Resonance Sensing and MALDI Mass Spectrometry. *Analyst* **2011**, *136*, 1167-1176.
- (128) Pilolli, R.; Ditaranto, N.; Di Franco, C.; Palmisano, F.; Cioffi, N. Thermally Annealed Gold Nanoparticles for Surface-Assisted Laser Desorption Ionisation-Mass Spectrometry of Low Molecular Weight Analytes. *Anal. Bioanal. Chem.* **2012**, *404*, 1703-11.
- (129) Liu, R.; Liu, J. F.; Zhou, X. X.; Jiang, G. B. Cysteine Modified Small Ligament Au Nanoporous Film: An Easy Fabricating and Highly Efficient Surface-Assisted Laser Desorption/Ionization Substrate. *Anal. Chem.* **2011**, *83*, 3668-3674.
- (130) Duan, J.; Linman, M. J.; Cheng, Q. Ultrathin Calcinated Films on a Gold Surface for Highly Effective Laser Desorption/Ionization of Biomolecules. *Anal. Chem.* **2010**, *82*, 5088-5094.

---

\*The section, "Lipid Membrane Models," was adapted from *J. Electroanal. Chem.*, Vol. 781, Hinman, S. S. and Cheng, Q., Bioinspired Assemblies and Plasmonic Interfaces for Electrochemical Biosensing, 136-146, Copyright **2016**, with permission from Elsevier.

## **CHAPTER 2: Mix and Match - Coassembly of Amphiphilic Dendrimers and Phospholipids Creates Robust, Modular and Controllable Interfaces<sup>\*</sup>**

### **■ INTRODUCTION**

Self-assembly of supramolecular complexes derived from biological and synthetic components is an important strategy to establish novel materials and interfaces.<sup>1-3</sup> These complexes include many classes, such as those derived from proteins, nucleic acids, lipids, polymers, or metal nanoparticles, and the interactions between them have many implications for their assembly pathways and dynamic geometries. One promising application of these constructs is based on their ability to sense, detect and transport biologically interesting agents, particularly in regards to self-assembled lipid and polymer nanostructures for drug delivery.<sup>4</sup> Both lipids and polymers are capable of assembling with the therapeutic agent to be delivered, providing protection from biodegrading physiological environments while improving bioavailability in order to bring the therapeutic cargo to the target site intact.

One specific type of synthetic polymer known as dendrimers are particularly appealing for drug delivery, by virtue of their well-defined structure with unique radial architecture, numerous terminal functionalities, and various interior cavities.<sup>5-7</sup> Polyamidoamine (PAMAM) dendrimers, originally developed by Tomalia as protein mimics with a large number of amide functionalities in the interior and primary amine

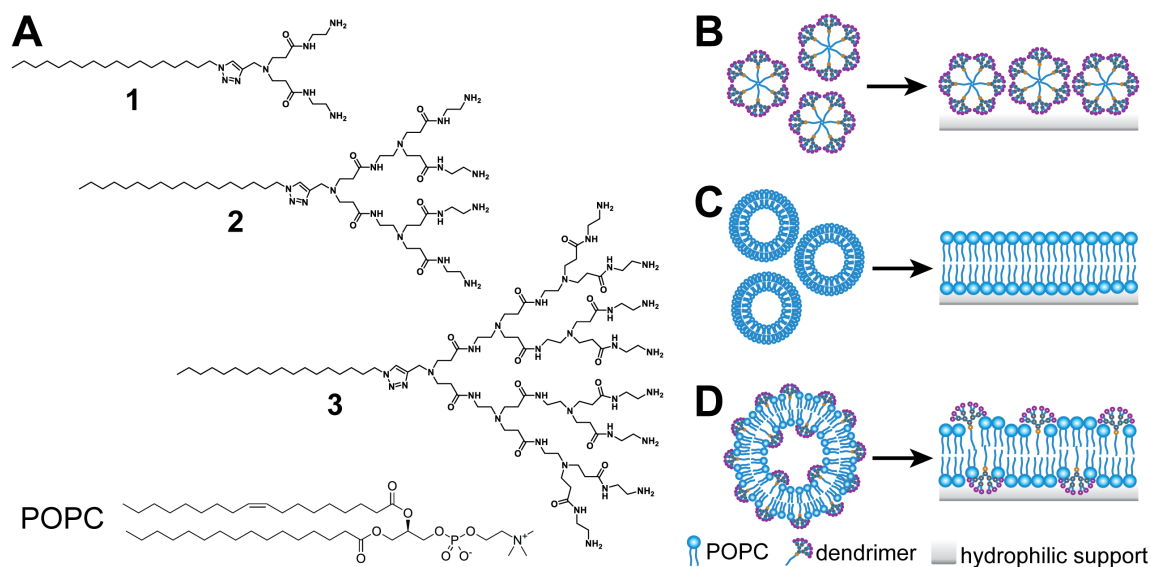


**Figure 2.1.** Molecular structures and supramolecular assembly pathways. (A) Molecular structures of amphiphilic dendrimers **1-3** and POPC used in this study. (B-D) Cartoon illustrations of (B) adsorption of amphiphilic dendrimer micelles onto a hydrophilic support, (C) fusion of phosphocholine vesicles on a hydrophilic support and (D) fusion of hybrid POPC/dendrimer liposomes on a hydrophilic support.

terminals on the surface,<sup>8-9</sup> have been the most extensively studied for biomedical applications.<sup>7</sup> Recently, amphiphilic dendrimers, constructed from long hydrophobic alkyl chains and PAMAM dendrons, have emerged as newcomers in the drug delivery field. These amphiphilic dendrimers are able to capitalize on the delivery features of lipid and polymer vectors while minimizing adverse toxic effects.<sup>10-12</sup> They can assemble into supramolecular nanostructures and can be loaded with therapeutic cargos, either through hydrophobic encapsulation within the interior of a dendrimer nanomicelle,<sup>11</sup> or via electrostatic interaction with the charged amine functionalities on the dendrimer surface.<sup>12-14</sup> While these assemblies have proved highly effective compared to traditional lipid or dendrimer vectors, interest is growing around the co-assembly of synthetic compounds with naturally occurring phospholipids for the assembled constructs' potential to demonstrate both natural and tunable biophysical properties.<sup>15-18</sup> In this line,

we investigated the co-assembly processes of amphiphilic dendrimers **1-3** with palmitoyl-oleoyl-phosphocholine (POPC), a major component of the plasma membrane (Figure 2.1). We used surface plasmon resonance (SPR) spectroscopy to characterize the dendrimer and lipid co-assembly processes on nanoglassified sensor chips,<sup>19-20</sup> and performed confocal fluorescence microscopy studies to inspect the spatial organization of embedded and tagged components. Our results demonstrate that the amphiphilic dendrimers and POPC are capable of co-assembling into uniform nanovesicles in solution, while also forming bilayer structures on hydrophilic glass supports. The hybrid membrane structures exhibit high lateral mobility - a trait common to natural lipid membranes - yet the bilayer stability and fluidity can be directly modulated by changing the dendrimer concentration and generation. In addition, *in situ* derivatization of the co-assembled system can be achieved through nondestructive tagging of the dendrimer terminals with a protein-recognizing ligand, demonstrating the promise of the hybrid interface to function towards an enhanced supramolecular sensor and/or targeting device.

## ■ EXPERIMENTAL METHODS

**Materials and Reagents.** Triton X-100 was from Sigma-Aldrich (St. Louis, MO). Sulfo-NHS-Biotin, NHS-AMCA, and Streptavidin were from Pierce Biotechnology (Rockford, IL). Octadecyl Rhodamine B chloride (R18) was from Biotium Inc. (Hayward, CA). 1-palmitoyl-2-oleoyl-*sn*-glycero-3-phosphocholine (POPC) and 1-palmitoyl-2-6-[(7-nitro-2-1,3-benzoxadiazol-4-yl)amino]hexanoyl-*sn*-glycero-3-phosphocholine (NBD-PC) were from Avanti Polar Lipids (Alabaster, AL). BK-7 glass substrates were from Corning

(Painted Post, NY). Chromium and gold used for electron-beam evaporation were acquired as pellets of 99.99% purity from Kurt J. Lesker (Jefferson Hills, PA).

**Instrumentation.** A dual-channel SPR spectrometer, NanoSPR5-321 (NanoSPR, Chicago, IL) with a GaAs semiconductor laser light source ( $\lambda_{\text{max}} = 670 \text{ nm}$ ) was used for all real-time binding measurements. SPR experiments were conducted at ambient temperature ( $\sim 23^\circ \text{C}$ ), with 1 $\times$ PBS (10 mM  $\text{Na}_2\text{HPO}_4$ , 1.8 mM  $\text{KH}_2\text{PO}_4$ , 137 mM  $\text{NaCl}$ , 2.7 mM  $\text{KCl}$ , pH 7.4) used as the running buffer set to a flow rate of  $5 \text{ mL h}^{-1}$  unless otherwise noted. The transmission electron microscope (TEM) used was a JEOL 3010 microscope operating at 300 kV and a pole piece ( $C_s = 1.4 \text{ mm}$ ) giving a resolution of 0.21 nm. All TEM images were recorded at low irradiation doses ( $< 3 \times 10^3 \text{ A} \cdot \text{m}^{-2}$ ). Dynamic and electrophoretic light scattering were conducted with a Delsa Nano C particle analyzer (Beckman Coulter, Brea, CA). Fluorescence microscopy was carried out on an inverted Leica TCS SP5 II (Leica Microsystems, Buffalo Point, IL) using the 405 nm diode laser (for AMCA), 488 nm Argon laser line (for NBD), or 543 nm HeNe laser (for R18) in conjunction with a  $40\times$  (NA 1.1) objective and Leica HyD hybrid detector.

**SPR Chip Fabrication.** BK-7 glass microscope slides were first cleaned using a boiling piranha solution (3:1 v/v  $\text{H}_2\text{SO}_4$  and 30%  $\text{H}_2\text{O}_2$ ) for 30 min, followed by rinsing with DI water and drying under compressed air. 2 nm of chromium ( $0.5 \text{ \AA s}^{-1}$ ), followed by 46 nm of gold ( $1.0 \text{ \AA s}^{-1}$ ) were then deposited using electron-beam evaporation (Temescal, Berkeley, CA) at  $5 \times 10^{-6}$  Torr in a Class 1000 cleanroom facility (UCR Center for Nanoscale Science & Engineering). To obtain a hydrophilic surface for lipid bilayer formation, *ca.* 4 nm of  $\text{SiO}_2$  was deposited on top of the gold layer using plasma

enhanced chemical vapor deposition (PECVD) with a Unaxis Plasmatherm 790 system (Santa Clara, CA).

**Synthesis and Characterization of Amphiphilic Dendrimers.** The amphiphilic dendrimers **1**, **2** and **3** were synthesized according to the previously reported method (Scheme A.1).<sup>10</sup> The chemical reagents used were purchased from Acros, Aldrich or Alfa Aesar. The <sup>1</sup>H NMR and <sup>13</sup>C NMR spectra were recorded at 300 MHz and 150 MHz respectively on Varian Mercury-VX300 and 600 spectrometers at room temperature. Coupling constants (*J*) are reported in Hertz, and chemical shifts are reported in parts per million (ppm) with TMS as an internal reference. FAB and ESI mass spectra were determined using ZAB-HF-3F or Finnigan LCQ Advantage mass respectively. MALDI-TOF mass spectra were recorded on a Voyager DE-STR. IR spectra were recorded with a Nicolet 380 spectrophotometer. Methyl acrylate, ethylenediamine, tetrahydrofuran were distilled before use. All other reagents and solvents were used without further purification from commercial sources. The dendron parts **G0.5**, **G1.5**, **G2.5**,<sup>10</sup> dendrimer parts **D1**, **D2**, **D3**<sup>10</sup> and alkyl azide compounds **C18**<sup>21</sup> were all synthesized according to the literature protocol.

**Vesicle Preparation.** An appropriate amount of POPC and/or dendrimer stock solution in chloroform was dried in a glass vial under nitrogen to form a thin lipid film. The vial containing lipids was then placed in a vacuum desiccator for at least 2 h to remove any residual solvent. The dried lipids were resuspended in 1×PBS to a lipid concentration of 1.0 mg mL<sup>-1</sup>. After vigorous vortexing to remove all lipid remnants from the vial wall, the solution was bath sonicated for 30 min. Thereafter, the supernatant was extruded

through a polycarbonate filter (Whatman, 100 nm) to produce small, unilamellar vesicles (SUVs) of uniform size. For fluorescence analysis, vesicle preparation followed the same procedure with the addition of 2% (w/w) NBD-PC, and dendrimer micelles were prepared with 1% (w/w) R18. All vesicle suspensions were used within one week and stored at 4 °C.

**Fluorescence Microscopy.** Fluidity of membranes incorporating the amphiphilic dendrimers was examined using fluorescence recovery after photobleaching (FRAP). Supported lipid bilayers were formed on clean glass coverslips (Fisher Scientific, Pittsburgh, PA) using vesicle suspensions deposited in 4.5 mm PDMS wells on the glass surface. These were incubated for 1 h prior rinsing with copious amounts of nanopure water. To assist with identification of the bilayer focal plane, a peripheral scratch in the bilayer was made. Photobleaching at 1.5 mW for 500 ms and fluorescence recovery monitoring were set up and performed using the LAS AF software package as described previously.<sup>20, 22-23</sup>

**FRAP Analysis.** The methods of Axelrod and Soumpasis were applied to derive diffusion coefficients for each membrane.<sup>22-23</sup> First, the fluorescence intensity of each bleach spot was normalized over a background area of the same size to account for background photobleaching. This normalized value ( $F_n$ ) was then used within the following formula to obtain the FRAP ratio ( $F_{FRAP}$ ), with  $F_0$  being the normalized intensity of the bleached area immediately after bleaching.

$$F_{FRAP} = \frac{F_n - F_0}{1 - F_0}$$

Thereafter,  $F_{\text{FRAP}}$  was plotted against time and fitted to a first order exponential function. The diffusion coefficient was calculated using the following equation, with  $D$  being the diffusion coefficient,  $\omega$  the full width at half maximum of the focused Gaussian laser profile,  $t_{1/2}$  the half-time recovery obtained from the exponential fit, and  $\gamma$  a correction factor accounting for the laser beam geometry.

$$D = \frac{\omega^2}{4t_{1/2}} \gamma$$

**TEM Imaging.** POPC and dendrimers were mixed from chloroform stocks, as in the other SUV procedures. 100  $\mu\text{L}$  of a POPC solution ( $10 \text{ mg mL}^{-1}$ ) was combined with 50  $\mu\text{L}$  of **1** ( $0.76 \text{ mg mL}^{-1}$ ), 50  $\mu\text{L}$  of **2** ( $1.36 \text{ mg mL}^{-1}$ ), or 100  $\mu\text{L}$  of **3** ( $1.28 \text{ mg mL}^{-1}$ ) and dried in a glass vial under nitrogen to form a thin lipid film. The vial containing the lipid/dendrimer mixture was then placed in a vacuum desiccator for at least 2 h to remove any residual solvent. Then, 1 mL D.I. water was added to the dried lipid/dendrimer film. After vigorous vortexing to remove all lipid remnants from the vial wall, the solution was bath sonicated for 30 min, then equilibrated 2 h at 277 K before being subjected to extrusion through a polycarbonate filter (Whatman, 200 nm). Thereafter, 100  $\mu\text{L}$  of this solution was withdrawn and diluted 40 $\times$  with D.I. water. After equilibration (15 min), 4  $\mu\text{L}$  of the diluted solution were dropped onto a standard carbon-coated copper TEM grid and allowed to dry in an oven set to 310 K for 30 min. The grid was stained with 3  $\mu\text{L}$  of uranyl acetate (2% in 50% EtOH) for 5 s, and the excess uranyl acetate was removed by filter paper. The dried specimens were observed with a JEOL 3010 transmission electron microscope operating at 300 kV. Data were analyzed with Digital Micrograph software.

## ■ RESULTS AND DISCUSSION

Amphiphilic compounds form different and distinct geometric assemblies that depend on both the molecular structure and the hydrophobic/hydrophilic balance.<sup>24</sup> Phosphocholine (PC) is a linear amphiphile capable of forming bilayer liposomes which, when exposed to a hydrophilic support, will rupture and fuse into a planar supported lipid bilayer (SLB) exhibiting high lateral mobility of the embedded lipids.<sup>25</sup> In contrast, dendrimer **3** is a conical amphiphilic molecule which readily self-assembles into nanomicelles.<sup>14</sup> We therefore performed our initial assessments on the interaction of micelles consisting solely of **3** with a POPC bilayer formed on nanoglassified sensor chips using SPR. As illustrated in Figure 2.2A, the first increase in the SPR sensorgram is due to POPC adsorption and fusion into a SLB (**I** in Figure 2.2A). Addition of dendrimer **3** micelles results in a notable increase in resonance angle ( $\Delta\theta_{\min} = 0.10^\circ$ , **III** and **IV** in Figure 2.2A), which then gradually decreases back to the baseline POPC value following the buffer rinse process (**V** in Figure 2.2A, and Figure A.1). This is indicative of weak and transient adsorption of dendrimer micelles onto the POPC membrane, and in agreement with the established macropinocytotic pathway for the internalization of dendrimer nanomicelles, *i.e.* amphiphilic dendrimers do not directly fuse or strongly interact with the biomembrane, but rather are internalized by energy-driven cellular processes, such as endocytosis.<sup>11</sup>

To further inspect the interaction of the dendrimer micelles with the POPC bilayer-covered glass support, we performed molecular simulations (see Appendix A for computational methods).<sup>11-12, 14, 26</sup> According to these calculations, the spherical micelle

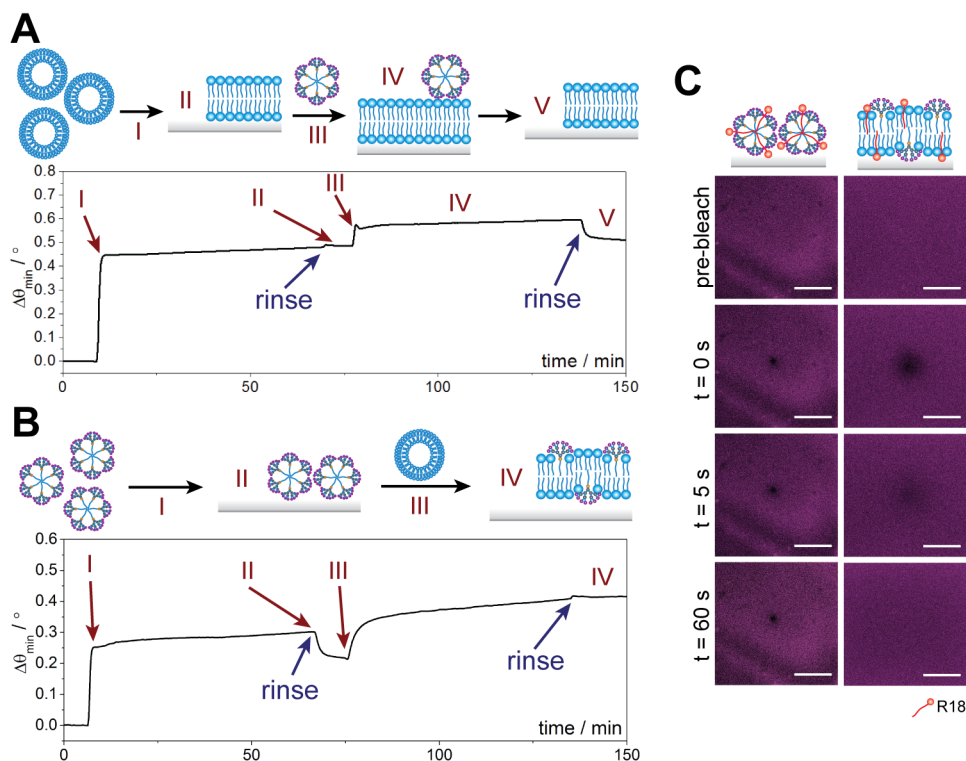


**Figure 2.2.** Co-assembly interaction studies. (A, B) SPR studies on (A) fusion of POPC bilayers and transient adsorption of dendrimer **3** micelles, and (B) adsorption of dendrimer **3** micelles and POPC-induced fusion. (C) FRAP studies on bleaching and recovery of dendrimer **3** micelles labeled with R18. Scale bars represent 30  $\mu\text{m}$ .

generated upon self-assembly of dendrimer **3** is able to land softly on the bilayer surface whereupon it preserves its shape throughout the entire simulated process (10  $\mu\text{s}$ ) of its adhesion with the glass-supported POPC bilayer. These results are in line with those obtained in SPR experiments, highlighting weak and transient adsorption of the dendrimer micelles to the POPC membrane.

Intriguingly, introducing dendrimer **3** to the silica-coated SPR chips results in a significantly smaller resonance angle change ( $\Delta\theta_{\min} = 0.20^\circ$ , **I** in Figure 2.2B) compared to POPC ( $\Delta\theta_{\min} \sim 0.45^\circ$ , **I** in Figure 2.2A). As SPR measures changes in the refractive index of the medium near the sensor interface,<sup>27</sup> the lower angular shift may be the result

of intact micelle adsorption, leaving nanoscale buffer voids between adjacent structures which exhibit a lower net refractive index change. Confocal fluorescence microscopy was employed to investigate the adsorption of dendrimer micelles containing R18 onto the glass-supported POPC bilayer (Figure 2.2C, upper panel). R18 is a molecular probe with the fluorophore at the aqueous interface and the alkyl tail protruding into the lipid membrane interior, which when contained within dendrimer nanomicelles allows inspection of their spatial distribution. The images in Figure 2.2C (upper panel) reveal an even distribution of the micelles that are immobile, as shown by the lack of fluorescence redistribution after photobleaching, suggesting their intact adsorption onto the glass support.

To induce fusion of the dendrimer micellar structures with a model membrane and investigate the properties using surface-based analytical techniques, we next added POPC liposomes to obtain hybrid SLBs (**III** in Figure 2.2B) using established protocols.<sup>28-29</sup> Contrary to the previous experiment in which we added the dendrimer micelles to a preformed POPC membrane with which they interacted weakly (Figure 2.2A), here we incubated POPC vesicles with dendrimer micelles already adsorbed to the silica-coated surface (Figure 2.2B). Remarkably, the SPR sensorgram shows a net increase in the resonance angle after addition of the POPC vesicles (**III** in Figure 2.2B), which remains constant even after rinsing with buffer (**IV** in Figure 2.2B), resulting in a final  $\Delta\theta_{\min}$  of  $0.41^\circ$ . This finding suggests the incorporation of POPC into a hybrid dendrimer/lipid structure. We further studied this hybrid system using confocal fluorescence microscopy, which showed an even distribution of R18 with tagged PC. In this instance, however,

fluorescence rapidly recovered after photobleaching, indicating a measurable lateral mobility in the membrane (lower panel in Figure 2.2C, and Figure A.2). To confirm that dendrimers were embedded in the POPC membrane and that we were not solely observing fusion of R18, we directly modified **2** with a fluorophore *in situ*, after fusion within the POPC bilayer, and also observed an even distribution of fluorescence (Figure A.8). The long-range diffusion of both R18 and NBD-tagged phosphocholine (Figure A.2) eliminate the possibility that the dendrimer micelles and phosphocholine vesicles remain adsorbed in their respective intact states, and provide evidence for a co-assembled lipid/dendrimer hybrid system with bilayer membrane fluidity.

Further investigations regarding the incorporation of amphiphilic dendrimers into fluid POPC bilayers required greater consistency among measurements, as well as the ability to control the relative concentrations of dendrimers and POPC. Throughout the rest of the studies, we therefore mixed the POPC and dendrimers in varying ratios prior to liposome formation, using a previously developed protocol.<sup>30</sup> To inspect how the dendrimers and POPC co-assemble in solution, we carried out dynamic light scattering (DLS) analysis and transmission electron microscopic (TEM) imaging on the mixed dendrimer/POPC assemblies. TEM imaging shows that the dendrimers alone form nanomicelles *ca.* 10 nm in diameter (Figure A.3), in agreement with data previously established for **3** alone.<sup>10</sup> However, the hybrid dendrimer/POPC systems form larger, unilamellar vesicles (Figure 2.3A). Furthermore, DLS analysis revealed that the incorporation of dendrimers **1-3** into POPC liposomes did not notably affect their

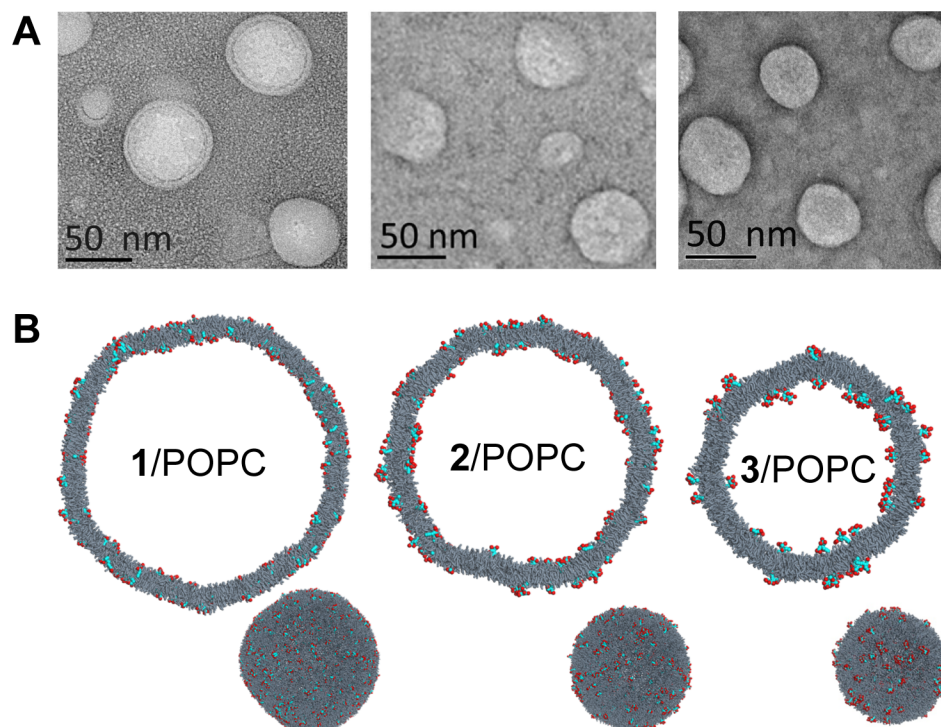


**Figure 2.3.** Co-assembly structures. (A) TEM images and (B) simulated mesoscale morphologies of the mixed vesicles obtained from POPC and dendrimer **1** (left), **2** (center) and **3** (right). The POPC molecules are shown as dark gray spheres whereas the dendrimer molecules are highlighted in red for the hydrophilic part and blue for the hydrophobic part. Water molecules, ions and counterions are not shown for clarity.

polydispersity, but had a considerable impact on their size, with a decreasing average hydrodynamic vesicle diameter observed with higher generation dendrimers (Table A.1). This decrease in size may be explained by considering the molecular geometry of POPC and dendrimers. POPC is a largely linear and cylindrical molecule, whereas dendrimers **1-3** are rather triangular and funnel-shaped. With increasing generation, the overall dendrimer shape becomes more conical, which likely produces some steric repulsion between the dendrimer terminals and adjacent POPC headgroups. Zeta potentials of the POPC vesicles were also affected by the dendrimers. Vesicles composed of POPC alone exhibited a near neutral zeta potential, whereas each of the hybrid lipid/dendrimer vesicle

suspensions had a zeta potential of *ca.* +20 mV. This can be reasonably ascribed to the positively charged terminal amines that are present in each dendrimer in physiological buffer. Altogether, these data indicate that the dendrimers produce a fairly stable colloid with POPC.

*In silico* experiments provided further support to these findings, with molecular simulations of mixed dendrimer/POPC systems yielding the stable unilamellar vesicles shown in Figure 2.3B. The calculated average dimensions of the vesicles and the corresponding zeta potential values (Table A.2) are in agreement with the DLS data (Table A.1). These snapshots extracted from the equilibrated simulation trajectories of the three mixed lipid/dendrimer vesicles revealed that dendrimers **1**, **2** and **3** are all uniformly dispersed within the POPC bilayer, with no evidence of clustering or other structural organization. The hydrophobic portion of each dendrimer is inserted into the bilayer, while the charged heads are exposed on the surface of the corresponding self-assembled structures (Figure 2.3B). The enhanced conical shape and the high total charge (+8) of dendrimer **3** is reflected in a mixed vesicle configuration in which, by virtue of both steric and electrostatic repulsions with the POPC positive charges, the large branched charged head of **3** sticks out of the lipid bilayer and protrudes into the solvent somewhat more than the heads of the other two dendrimers. This allows for a tighter compaction of the bilayer and, consequently, for smaller vesicle dimensions. In summary, the overall uniform dispersion of dendrimers **1**, **2** and **3** within the POPC bilayer

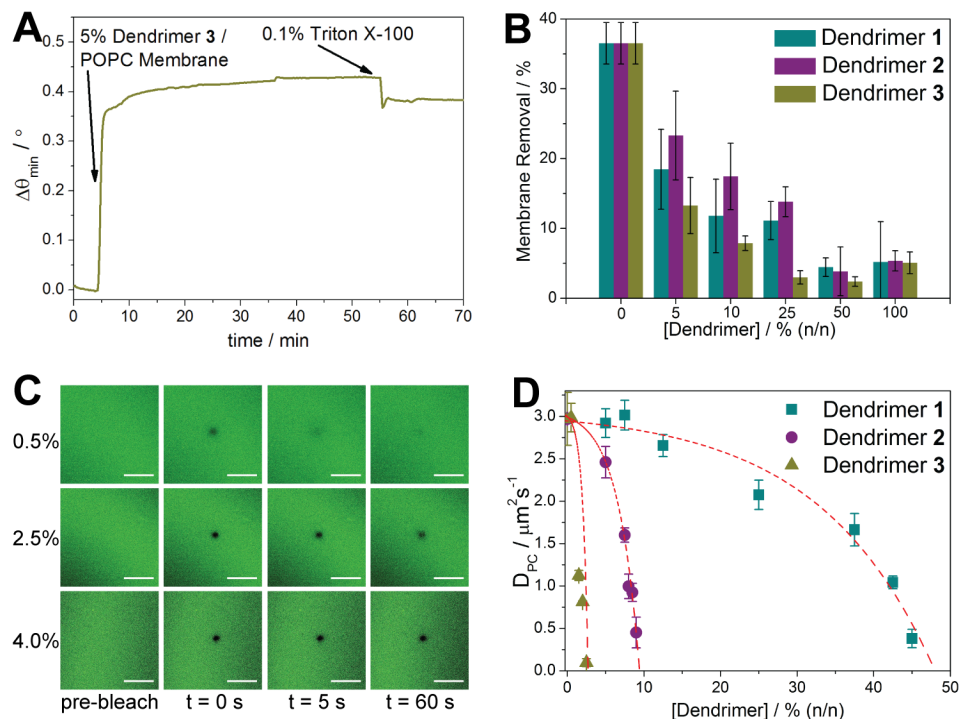


**Figure 2.4.** Biophysical studies of co-assembled membranes. (A) Fusion of 5% **3**/POPC vesicles into support lipid bilayers (SLBs) followed by surfactant rinsing. (B) Percentage membrane removal based on dendrimer generation and concentration. (C) FRAP images of POPC membranes with increasing concentrations of **3**. Scale bars represent 30  $\mu\text{m}$ . (D) Diffusion coefficients, indicative of POPC lateral mobility.

ultimately generates mixed vesicles with optimal size and zeta potential to ensure that the most stable nanoparticles are formed in accordance with the corresponding situation.

Fusion of the hybrid dendrimer/POPC vesicles into an SLB was carried out following the same procedure as for traditional POPC vesicles; that is, the hybrid vesicles were applied to the surface of the glass support and incubated in an aqueous environment. The stability of these lipid bilayer structures upon introduction of a chemical perturbant was investigated using established SPR methods.<sup>31</sup> After vesicle fusion and rinsing of the membrane under PBS flowing at 5  $\text{mL h}^{-1}$ , 0.1% (v/v) surfactant was introduced to the SPR flow cell at a rate of 20  $\text{mL h}^{-1}$ , and buffer was rinsed through at this rate for 5 min.

Upon return of the flow rate to 5 mL h<sup>-1</sup> for 10 min, relative membrane removal was quantified through percent change of the minimum resonance angle as shown below, where  $\Delta\theta_0$  represents the angular shift after vesicle fusion and  $\Delta\theta_f$  represents the final angular shift after surfactant rinsing.

$$\text{Membrane Removal} = \frac{\Delta\theta_0}{\Delta\theta_f} \times 100\%$$

A representative sensorgram for these processes is shown in Figure 2.4A, which illustrates bilayer formation from the co-assembled dendrimer/POPC vesicles, followed by rinsing with a mild surfactant to assess stability. All three dendrimers appeared to have a concentration-dependent effect on the overall bilayer stability (Figure 2.4B). POPC alone exhibited the lowest stability (>35% membrane removal) in the presence of a relatively low concentration of surfactant. Increasing the concentration of dendrimers within the membrane imparted greater levels of stability (<10% membrane removal) up to a 50% (n/n) composition of dendrimers and POPC.<sup>32</sup> The increased stability can be ascribed to the cooperative and multivalent interactions between the positively charged dendrimer amine terminals and the slightly negative glass support,<sup>33</sup> providing an *in situ* control of stability similar to previous findings with other fluidic membrane-embedded compounds.<sup>34</sup>

While the SPR stability studies provided us with an insight into the interactions between the hybrid co-assemblies and their underlying supports, we further examined changes in POPC fluidity in response to dendrimer concentration and generation using fluorescence recovery after photobleaching (FRAP). We noted a decrease in the lateral mobility of fluorophore-labeled PC with increasing concentration of each dendrimer in

the hybrid assemblies. This can be seen in the fluorescence images by the longer persistence of bleached areas with higher concentrations of the dendrimer (Figure 2.4C, also Figure A.4–A.6). Diffusion coefficients ( $D$ ) for POPC show distinct patterns with increasing concentrations of **1**, **2**, and **3** (Figure 2.4D). Dendrimer **1** causes a gradual decrease in fluidity as its concentration within the membrane increases, eventually resulting in a loss of measurable fluidity above the levels of 45% (n/n) **1**. Dendrimer **2** follows a similar pattern, with a loss of fluidity above 8% (n/n) **2**, while **3** has the greatest impact, causing a sharp decline in POPC mobility as soon as **3** is introduced. These results are intriguing, because they show that each of the dendrimers has a direct, concentration-dependent impact on the surrounding lipid environment. The orientation of the zwitterionic headgroups of POPC (Figure 2.1A) within the bilayer leaves the positively charged ammonium groups positioned away from the bilayer:water interface and the negatively charged phosphates slightly buried. As increasing the dendrimer generation leads to more laterally extending terminal amines, the positively charged terminals can therefore be placed in an ideal position for attractive electrostatic forces with the POPC phosphate groups to take effect. This is corroborated by the bilayer reinforcement exhibited in the SPR assays. Taken together, our results demonstrate how the amphiphilic dendrimers enable the fine-tuning of biophysical properties of the hybrid bilayer interfaces.

Membranes composed of PC exhibit low biofouling and strong protein-resistant properties owing to their unique headgroup structures.<sup>19, 35</sup> These are excellent

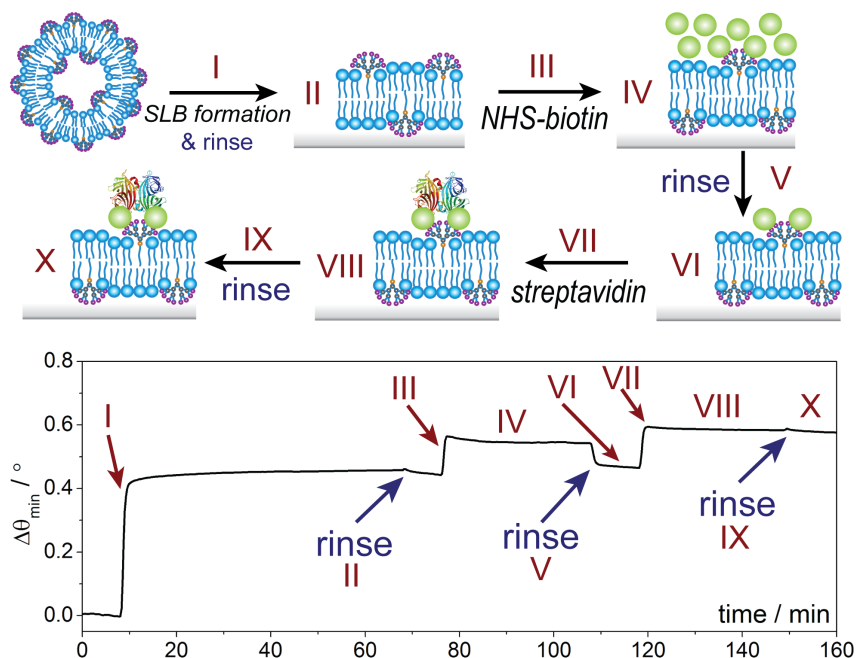


**Figure 2.5.** In situ derivitization of hybrid 5% **2**/POPC membranes with biotin, followed by streptavidin recognition.

characteristics for extending the detection limit in analytical sensors,<sup>19</sup> and preventing degradation of liposomal therapeutics.<sup>36</sup> However, modifying the interfacial surface in situ currently presents a challenge in the development of new sensors and drug delivery tools. In our hybrid interfaces, the presence of the amine terminals on the embedded amphiphilic dendrimers enables the easy conjugation of biological recognition ligands, and we exemplify this by tagging of the hybrid dendrimer/lipid membranes with biotin, followed by streptavidin recognition. The SPR sensorgram shows formation of a hybrid **2**/POPC bilayer, followed by derivatization and protein recognition (Figure 2.5). We chose 5% (n/n) of **2** in the POPC bilayer membrane, as it offered a sufficient availability of free amine terminals for conjugation with biotin, yet a good balance of increased stability and retention of lateral lipid mobility. Following formation of the hybrid

2/POPC bilayer (**I**, **II** in Figure 2.5), we added the NHS active form of biotin and incubated for 30 min. An increase in angular resonance ( $\Delta\theta_{\min}$  of  $0.02^\circ$ ) was observed, indicating successful attachment of biotin to the free amine terminals (**III**, **IV** in Figure 2.5). After rinsing with PBS to remove unbound biotin (**V** and **VI** in Figure 2.5), we added streptavidin ( $1\ \mu\text{M}$ ), which resulted in a significant increase in angular resonance ( $\Delta\theta_{\min} = 0.11^\circ$ ) (**VII** and **VIII** in Figure 2.5). This can be ascribed to the recognition and binding of biotin to streptavidin, which remained constant even after copious rinsing with buffer (**X** in Figure 2.5). The interaction here is strong and specific for the dendrimer-containing membranes, in contrast with a control experiment in which an SLB composed of 100% POPC, where both NHS-biotin tagging and streptavidin recognition were unsuccessful (Figure A.7). Verification of this process was also performed under fluorescence, in which a 5% 2/POPC SLB on glass was exposed to an amine-reactive fluorophore (NHS-AMCA). Coupling of AMCA with the dendrimer containing membranes revealed an even distribution of AMCA fluorescence, with no observable damage to the membrane itself (Figure A.8). The *in situ* derivatization exemplified here could be useful for developing high-performance sensors, in addition to designing drug delivery carriers where the protein corona surrounding the complex can be dynamically altered without damaging the supramolecular architecture.<sup>37-38</sup>

## ■ CONCLUSIONS

In summary, the dendrimer/lipid co-assembly processes investigated here have provided insights into the function and activity of the resulting biomimetic

supramolecular complexes and interfaces. Separate constructions of amphiphilic dendrimer micelles and phosphocholine bilayers alone yielded few measurable interactions between the two systems, while co-assembly of these materials into hybrid systems resulted in a new interface with tunable biophysical properties. Varying dendrimer generation and concentration allows modulating these hybrid interfaces with regards stability, fluidity, and availability of derivatization sites, enables the creation of enhanced supramolecular entities with potentially interesting interfacial applications. This is the first study of amphiphilic dendrimers co-assembled in a model membrane system. The potential directions to now be taken to gain further insight into additional assembly pathways and interfacial recognition schemes are multiple. Future studies will be geared towards accurately modulating and potentially controlling the behavior of this system towards tailored and specific applications.

## ■ REFERENCES

- (1) Lehn, J. M. Toward Self-Organization and Complex Matter. *Science* **2002**, 295, 2400-2403.
- (2) Aida, T.; Meijer, E. W.; Stupp, S. I. Functional Supramolecular Polymers. *Science* **2012**, 335, 813-817.
- (3) Webber, M. J.; Appel, E. A.; Meijer, E. W.; Langer, R. Supramolecular Biomaterials. *Nat. Mater.* **2016**, 15, 13-26.
- (4) Pamies, P.; Stoddart, A. Materials for Drug Delivery. *Nat. Mater.* **2013**, 12, 957.
- (5) Svenson, S. The Dendrimer Paradox--High Medical Expectations but Poor Clinical Translation. *Chem. Soc. Rev.* **2015**, 44, 4131-4144.
- (6) Mintzer, M. A.; Grinstaff, M. W. Biomedical Applications of Dendrimers: A Tutorial. *Chem. Soc. Rev.* **2011**, 40, 173-190.
- (7) Esfand, R.; Tomalia, D. A. Poly(Amidoamine) (PAMAM) Dendrimers: From Biomimicry to Drug Delivery and Biomedical Applications. *Drug Discovery Today* **2001**, 6, 427-436.
- (8) Tomalia, D. A.; Baker, H.; Dewald, J.; Hall, M.; Kallos, G.; Martin, S.; Roeck, J.; Ryder, J.; Smith, P. A New Class of Polymers - Starburst-Dendritic Macromolecules. *Polym. J.* **1985**, 17, 117-132.
- (9) Tomalia, D. A.; Naylor, A. M.; Goddard, W. A. Starburst Dendrimers - Molecular-Level Control of Size, Shape, Surface-Chemistry, Topology, and Flexibility from Atoms to Macroscopic Matter. *Angew. Chem., Int. Ed.* **1990**, 29, 138-175.
- (10) Yu, T. Z.; Liu, X. X.; Bolcato-Bellemin, A. L.; Wang, Y.; Liu, C.; Erbacher, P.; Qu, F. Q.; Rocchi, P.; Behr, J. P.; Peng, L. An Amphiphilic Dendrimer for Effective Delivery of Small Interfering RNA and Gene Silencing in Vitro and in Vivo. *Angew. Chem., Int. Ed.* **2012**, 51, 8478-8484.

- (11) Wei, T.; Chen, C.; Liu, J.; Liu, C.; Posocco, P.; Liu, X.; Cheng, Q.; Huo, S.; Liang, Z.; Fermeglia, M.; Pricl, S.; Liang, X. J.; Rocchi, P.; Peng, L. Anticancer Drug Nanomicelles Formed by Self-Assembling Amphiphilic Dendrimer to Combat Cancer Drug Resistance. *Proc. Natl. Acad. Sci. U. S. A.* **2015**, *112*, 2978-2983.
- (12) Liu, X. X.; Zhou, J. H.; Yu, T. Z.; Chen, C.; Cheng, Q.; Sengupta, K.; Huang, Y. Y.; Li, H. T.; Liu, C.; Wang, Y.; Posocco, P.; Wang, M. H.; Cui, Q.; Giorgio, S.; Fermeglia, M.; Qu, F. Q.; Pricl, S.; Shi, Y. H.; Liang, Z. C.; Rocchi, P.; Rossi, J. J.; Peng, L. Adaptive Amphiphilic Dendrimer-Based Nanoassemblies as Robust and Versatile siRNA Delivery Systems. *Angew. Chem., Int. Ed.* **2014**, *53*, 11822-11827.
- (13) Liu, X. X.; Liu, C.; Zhou, J. H.; Chen, C.; Qu, F. Q.; Rossi, J. J.; Rocchi, P.; Peng, L. Promoting siRNA Delivery Via Enhanced Cellular Uptake Using an Arginine-Decorated Amphiphilic Dendrimer. *Nanoscale* **2015**, *7*, 3867-3875.
- (14) Chen, C.; Posocco, P.; Liu, X.; Cheng, Q.; Laurini, E.; Zhou, J. H.; Liu, C.; Wang, Y.; Tang, J.; Dal Col, V.; Yu, T. Z.; Giorgio, S.; Fermeglia, M.; Qu, F. Q.; Liang, Z.; Rossi, J. J.; Liu, M.; Rocchi, P.; Pricl, S.; Peng, L. Mastering Dendrimer Self-Assembly for Efficient siRNA Delivery: From Conceptual Design to in Vivo Efficient Gene Silencing. *Small* **2016**, *12*, 3667-3676.
- (15) Ruyschaert, T.; Sonnen, A. F. P.; Haelele, T.; Meier, W.; Winterhalt, M.; Fournier, D. Hybrid Nanocapsules: Interactions of ABA Block Copolymers with Liposomes. *J. Am. Chem. Soc.* **2005**, *127*, 6242-6247.
- (16) Le Meins, J. F.; Schatz, C.; Lecommandoux, S.; Sandre, O. Hybrid Polymer/Lipid Vesicles: State of the Art and Future Perspectives. *Mater. Today* **2013**, *16*, 397-402.
- (17) Schulz, M.; Binder, W. H. Mixed Hybrid Lipid/Polymer Vesicles as a Novel Membrane Platform. *Macromol. Rapid Commun.* **2015**, *36*, 2031-2041.
- (18) Xiao, Q.; Yadavalli, S. S.; Zhang, S.; Sherman, S. E.; Fiorin, E.; da Silva, L.; Wilson, D. A.; Hammer, D. A.; Andre, S.; Gabius, H. J.; Klein, M. L.; Goulian, M.; Percec, V. Bioactive Cell-Like Hybrids Coassembled from (Glyco)Dendrimersomes with Bacterial Membranes. *Proc. Natl. Acad. Sci. U. S. A.* **2016**, *113*, E1134-E1141.

- (19) Phillips, K. S.; Han, J. H.; Martinez, M.; Wang, Z. Z.; Carter, D.; Cheng, Q. Nanoscale Glassification of Gold Substrates for Surface Plasmon Resonance Analysis of Protein Toxins with Supported Lipid Membranes. *Anal. Chem.* **2006**, *78*, 596-603.
- (20) Hinman, S. S.; Ruiz, C. J.; Drakakaki, G.; Wilkop, T. E.; Cheng, Q. On-Demand Formation of Supported Lipid Membrane Arrays by Trehalose-Assisted Vesicle Delivery for SPR Imaging. *ACS Appl. Mater. Interfaces* **2015**, *7*, 17122-17130.
- (21) Goddard-Borger, E. D.; Stick, R. V. An Efficient, Inexpensive, and Shelf-Stable Diazotransfer Reagent: Imidazole-1-Sulfonyl Azide Hydrochloride. *Org. Lett.* **2007**, *9*, 3797-3800.
- (22) Axelrod, D.; Koppel, D. E.; Schlessinger, J.; Elson, E.; Webb, W. W. Mobility Measurement by Analysis of Fluorescence Photobleaching Recovery Kinetics. *Biophys. J.* **1976**, *16*, 1055-1069.
- (23) Soumpasis, D. M. Theoretical-Analysis of Fluorescence Photobleaching Recovery Experiments. *Biophys. J.* **1983**, *41*, 95-97.
- (24) Lu, J. R.; Zhao, X. B.; Yaseen, M. Biomimetic Amphiphiles: Biosurfactants. *Curr. Opin. Colloid Interface Sci.* **2007**, *12*, 60-67.
- (25) Castellana, E. T.; Cremer, P. S. Solid Supported Lipid Bilayers: From Biophysical Studies to Sensor Design. *Surf. Sci. Rep.* **2006**, *61*, 429-444.
- (26) Welsh, D. J.; Posocco, P.; Pricl, S.; Smith, D. K. Self-Assembled Multivalent Rgd-Peptide Arrays - Morphological Control and Integrin Binding. *Org. Biomol. Chem.* **2013**, *11*, 3177-3186.
- (27) Couture, M.; Zhao, S. S.; Masson, J. F. Modern Surface Plasmon Resonance for Bioanalytics and Biophysics. *Phys. Chem. Chem. Phys.* **2013**, *15*, 11190-11216.
- (28) Dodd, C. E.; Johnson, B. R. G.; Jeuken, L. J. C.; Bugg, T. D. H.; Bushby, R. J.; Evans, S. D. Native E. Coli Inner Membrane Incorporation in Solid-Supported Lipid Bilayer Membranes. *Biointerphases* **2008**, *3*, FA59-FA67.

- (29) Costello, D. A.; Hsia, C. Y.; Millet, J. K.; Porri, T.; Daniel, S. Membrane Fusion-Competent Virus-Like Proteoliposomes and Proteinaceous Supported Bilayers Made Directly from Cell Plasma Membranes. *Langmuir* **2013**, *29*, 6409-6419.
- (30) Ghang, Y. J.; Lloyd, J. J.; Moehlig, M. P.; Arguelles, J. K.; Mettry, M.; Zhang, X.; Julian, R. R.; Cheng, Q.; Hooley, R. J. Labeled Protein Recognition at a Membrane Bilayer Interface by Embedded Synthetic Receptors. *Langmuir* **2014**, *30*, 10161-10166.
- (31) Han, J. H.; Taylor, J. D.; Phillips, K. S.; Wang, X.; Feng, P.; Cheng, Q. Characterizing Stability Properties of Supported Bilayer Membranes on Nanoglassified Substrates Using Surface Plasmon Resonance. *Langmuir* **2008**, *24*, 8127-33.
- (32) Interestingly, there is a slightly higher amount of material removed when dendrimer micelles are applied alone, though this may be due to a lack of adsorbed supramolecular fusion. It should also be noted that higher concentrations of surfactant, ca. 1% or 5% Triton X-100, resulted in near complete or complete removal of material for all compositions.
- (33) Behrens, S. H.; Grier, D. G. The Charge of Glass and Silica Surfaces. *J. Chem. Phys.* **2001**, *115*, 6716-6721.
- (34) Holden, M. A.; Jung, S. Y.; Yang, T. L.; Castellana, E. T.; Cremer, P. S. Creating Fluid and Air-Stable Solid Supported Lipid Bilayers. *J. Am. Chem. Soc.* **2004**, *126*, 6512-6513.
- (35) Groves, J. T.; Mahal, L. K.; Bertozzi, C. R. Control of Cell Adhesion and Growth with Micropatterned Supported Lipid Membranes. *Langmuir* **2001**, *17*, 5129-5133.
- (36) Farhood, H.; Serbina, N.; Huang, L. The Role of Dioleoyl Phosphatidylethanolamine in Cationic Liposome Mediated Gene Transfer. *Biochim. Biophys. Acta* **1995**, *1235*, 289-295.
- (37) Cedervall, T.; Lynch, I.; Foy, M.; Berggard, T.; Donnelly, S. C.; Cagney, G.; Linse, S.; Dawson, K. A. Detailed Identification of Plasma Proteins Adsorbed on Copolymer Nanoparticles. *Angew. Chem., Int. Ed.* **2007**, *46*, 5754-5756.

- (38) Lundqvist, M.; Stigler, J.; Elia, G.; Lynch, I.; Cedervall, T.; Dawson, K. A. Nanoparticle Size and Surface Properties Determine the Protein Corona with Possible Implications for Biological Impacts. *Proc. Natl. Acad. Sci. U. S. A.* **2008**, *105*, 14265-14270.

---

\* Adapted with permission from: Hinman, S. S., et al. Mix and Match: Coassembly of Amphiphilic Dendrimers and Phospholipids Creates Robust, Modular and Controllable Interfaces. *ACS Appl. Mater. Interfaces* **2017**, *9*, 1029-1035. Copyright 2017 American Chemical Society.

# **CHAPTER 3: On-Demand Formation of Supported Lipid Membrane Arrays by Trehalose-Assisted Vesicle Delivery for SPR Imaging<sup>\*</sup>**

## **■ INTRODUCTION**

The cell membrane is a fundamental structure of living organisms, separating exterior and interior content, with embedded receptors and structures facilitating communication and regulated active and passive material exchange.<sup>1</sup> This interface principally serves as a selective barrier for a range of exogenous materials, including ions, metabolites, growth factors and toxins. As a plethora of recognition sites in the membrane translates biotic and abiotic environmental stimuli across the membrane, these are primary targets in studies towards a better understanding of signaling pathways and how biological responses are effected on the cellular level.<sup>2</sup> Supported lipid bilayer (SLB) systems, typically formed on glass<sup>3</sup> or PDMS,<sup>4</sup> have proven to be a convenient platform for these studies, as the isolated lipid environment eliminates complexities and interferences from other cellular activities. These SLBs are easily tunable with a broad spectrum of compositional complexities ranging from single phospholipids to mixtures of lipids with embedded proteins and natural receptors.<sup>5-6</sup> To date, SLB systems have been used for a variety of applications, including gaining insight to biophysical processes,<sup>7-8</sup> enhancing drug delivery through incorporation of synthetic receptors,<sup>9</sup> and in designing sensors that bind molecules to their natural targets.<sup>10-12</sup>

Despite the potential and flexibility of SLBs, microarray applications of these systems have been scant. This is in large part due to the complexity and limited scalability of generating and maintaining SLBs in an aqueous environment in a way that ensures membrane integrity and unaltered activity of embedded components. Currently, common methods of creating patterned lipid bilayer microarrays include utilizing lipid corrals<sup>13</sup>, non-contact printing through confined films,<sup>14</sup> and injecting single-composition vesicle suspensions over multi-element array substrates.<sup>15</sup> Each of these methods crucially depends on constant hydration of the fabricated array, as exposure to air results in a loss of structural integrity of the SLB. This translates to required on site fabrication of SLBs, with severe limits for even short term storage and transport of SLB array substrates, facts that make commercialization and widespread adaption very challenging. However, a unique fabrication method was recently introduced that allows for the spatially defined deposition of matrix encapsulated lipid vesicles, followed by on-demand formation of solid-supported lipid bilayers once hydrated.<sup>16</sup> By adding a low molecular weight, non-reducing disaccharide, trehalose, to preformed vesicle suspensions, a strategy that mimics the natural preservation mechanisms encountered in drought-tolerant and anhydrobiotic organisms,<sup>17-18</sup> vesicles remain intact during the vitrification of trehalose. Hydration leads to a devitrification of trehalose, removal of the sugar, and a concurrent release of the vesicles followed by their fusion into SLBs on fusogenic surfaces. Resulting lipid bilayers on glass were studied by fluorescence microscopy, and were shown to have fluidity comparable to conventional SLBs, as well as being capable

of maintaining embedded ligands and receptors in their active state throughout the trehalose vitrification and devitrification processes.<sup>16</sup>

Compared to fluorescence, label-free analytical methods such as surface plasmon resonance (SPR) allow for the characterization of molecular interactions in a highly efficient fashion without extra labeling or tagging steps, thereby eliminating potential interference and labor.<sup>19</sup> SPR assays have successfully been applied toward studying a large variety of chemical and biological samples,<sup>20</sup> and are user-friendly enough to be conducted in clinical settings.<sup>21</sup> Many early studies utilizing SPR for investigating lipid membrane systems made use of hybrid bilayer membranes,<sup>10, 22</sup> where the hydrophobic tails of phospholipids adsorb to long-chain alkanethiol monolayers assembled on gold substrates. In previous work, we demonstrated that by creating nanoscale layers of glass on gold surfaces,<sup>23</sup> formation and characterization of stable bilayer membranes is also possible for SPR. Recently, a number of high-performance SPR imaging (SPRi) substrates have been developed that allow for ultrasensitive screenings of SLB systems in a high-throughput manner.<sup>24-25</sup> These substrates were featured thin coatings of silica, applied through advanced cleanroom techniques, attenuated background evanescent fields to yield higher dynamic response ranges, and allowed for the detection of proteinaceous toxins binding to receptor-containing SLBs at low nanomolar concentrations.

In this work, we report an approach that combines trehalose-assisted phospholipid vesicle deposition with SPRi for on-demand and label-free analysis of biomolecular interactions in an arrayed SLB system. Vesicle suspensions in trehalose were deposited

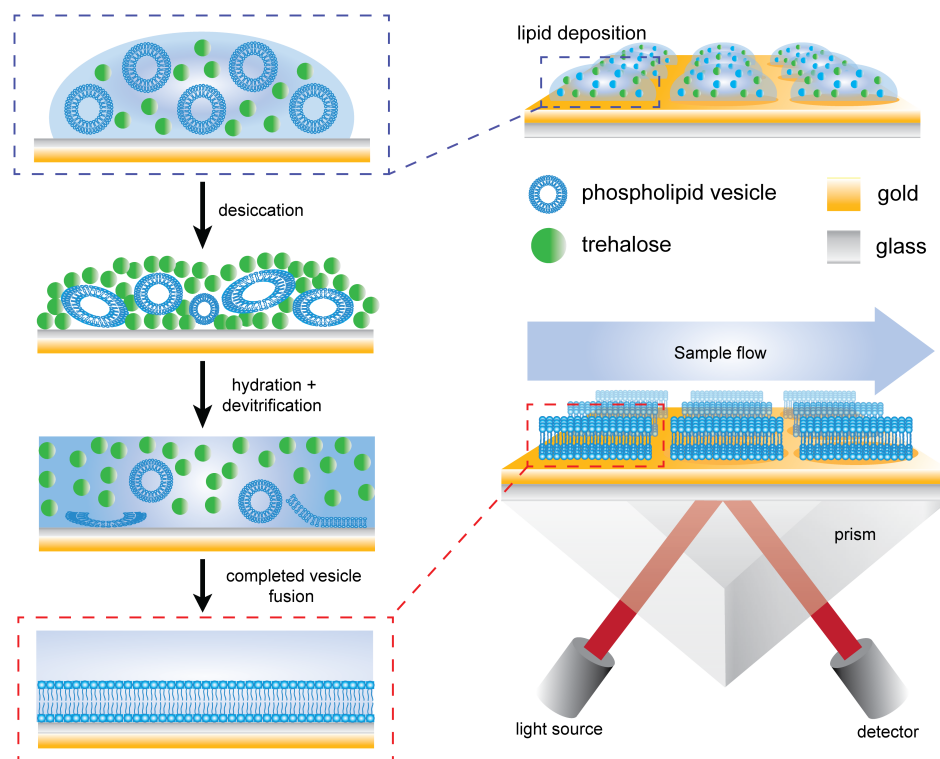


**Figure 3.1.** Schematic diagram exhibiting the processes of vesicle deposition, desiccation, and devitrification upon hydration of the trehalose matrix on the modified SPR sensor chips. Each SPR chip is modified with *ca.* 4 nm of silica, applied by plasma-enhanced chemical vapor deposition to increase hydrophilicity and provide a fusogenic surface for the SUVs. The devitrification process releasing the SUVs takes place in the SPR flow cell environment.

on ultrathin (<10 nm) layers of engineered glass deposited on gold substrates, desiccated, and directly used for analytical characterization once rehydrated (Figure 3.1). Lateral mobility properties of traditionally formed bilayers and those that stem from rehydrated lipids released from trehalose were compared on a variety of substrate surfaces, including Au/SiO<sub>2</sub> glass coverslips and alkanethiol modified gold. After empirically optimizing the flow rate conditions for the rehydration within the SPR flow cell, we studied the behavior of the generated lipid membranes by SPR in terms of the effective refractive index changes compared to traditionally formed membranes. Furthermore, affinity studies were carried out with cell membrane receptors, namely gangliosides GM<sub>1</sub>, GM<sub>2</sub> and GM<sub>3</sub>, in

which the response signals for the binding of cholera toxin to differently prepared bilayers were found to be virtually identical. SPRi experiments showed no crosstalk between adjacent array elements. Individual binding responses of multiple monosialogangliosides across a multi-element array were compared and exhibited excellent coherence, underscoring the utility of this versatile methodology for large-scale arrays. In addition to the fluid SLB arrays on Au/SiO<sub>2</sub> substrates, we also show on-demand bilayer formation on hydrophobic surfaces resulting in hybrid bilayers and their characterization.

## ■ EXPERIMENTAL METHODS

**Materials and Reagents.** Cholera toxin (CT) from *Vibrio cholerae*, Triton X-100, 1-octadecanethiol (98%), and *n*-octadecyltrichlorosilane (OTS, 90+%) were from Sigma-Aldrich (St. Louis, MO). Trehalose was from Swanson Health Products (Fargo, ND). 1-palmitoyl-2-oleoyl-*sn*-glycero-3-phosphocholine (POPC) and 1-palmitoyl-2-6-[(7-nitro-2-1,3-benzoxadiazol-4-yl)amino]hexanoyl-*sn*-glycero-3-phosphocholine (NBD-PC) were from Avanti Polar Lipids (Alabaster, AL). Monosialoganglioside GM<sub>1</sub> (NH<sub>4</sub><sup>+</sup> salt) and Monosialoganglioside GM<sub>2</sub> (NH<sub>4</sub><sup>+</sup> salt) were from Matreya (Pleasant Gap, PA). Monosialoganglioside GM<sub>3</sub> was from EMD Biosciences (La Jolla, CA). BK-7 glass substrates were from Corning (Painted Post, NY). Chromium and gold used for electron-beam evaporation were acquired as pellets of 99.99% purity from Kurt J. Lesker (Jefferson Hills, PA).

**Vesicle Preparation.** An appropriate amount of lipid stock solution containing 95% (w/w) POPC and 5% (w/w) monosialoganglioside (GM<sub>1</sub>, GM<sub>2</sub>, or GM<sub>3</sub>) in chloroform was dried in a glass vial under nitrogen to form a thin lipid film. The vial containing lipids was then placed in a vacuum desiccator for at least 2 h to remove any residual solvent. The dried lipids were resuspended in 1×PBS (10 mM Na<sub>2</sub>HPO<sub>4</sub>, 1.8 mM KH<sub>2</sub>PO<sub>4</sub>, 137 mM NaCl, 2.7 mM KCl, pH 7.4) to a lipid concentration of 2.0 mg mL<sup>-1</sup>. After vigorous vortexing to remove all lipid remnants from the vial wall, the solution was probe sonicated for 20 min. The resuspended lipids were then centrifuged at 8000 rpm for 15 min to remove titanium particles expelled from the sonicator probe tip. Thereafter, the supernatant was extruded through a polycarbonate filter (100 nm) to produce small, unilamellar vesicles (SUVs) of uniform size. If the vesicles were suspended in trehalose, the solution was diluted to a final concentration of 1.0 mg mL<sup>-1</sup> PC in 50 mM trehalose using a trehalose/1×PBS mixture. If not, the solution was diluted to 1.0 mg mL<sup>-1</sup> PC using 1×PBS. For fluorescence analysis, the vesicle preparation followed the same procedure with the addition of 2% (w/w) NBD-PC. All vesicle suspensions were applied within a week and stored at 4 °C before use.

**SPR Chip Fabrication.** SPR and SPRi chips were fabricated using BK-7 glass microscope slides. BK-7 glass microscope slides were first cleaned using a boiling piranha solution (3:1 v/v H<sub>2</sub>SO<sub>4</sub> and 30% H<sub>2</sub>O<sub>2</sub>) for 30 min, followed by rinsing with DI water and drying under compressed air. 2 nm of chromium (0.5 Å s<sup>-1</sup>), followed by 46 nm of gold (1.0 Å s<sup>-1</sup>) were then deposited using electron-beam evaporation (Temescal, Berkeley, CA) at 5×10<sup>-6</sup> Torr in a Class 1000 cleanroom facility (UCR Center for

Nanoscale Science & Engineering). To obtain a hydrophilic surface for lipid bilayer formation, *ca.* 4 nm of SiO<sub>2</sub> was deposited on top of the gold layer using plasma enhanced chemical vapor deposition (PECVD) with a Unaxis Plasmatherm 790 system (Santa Clara, CA).

High-performance gold well SPRi chips were fabricated using previously developed methods<sup>24</sup> (Figure B.1). Using the above protocol, 2 nm of chromium and 51 nm of gold were deposited onto cleaned BK-7 glass substrates. The surface was then rendered hydrophilic with *ca.* 4 nm of SiO<sub>2</sub> by PECVD. Subsequently, photoresist AZ5214E was spin coated on the surface at 4000 rpm, which was patterned into mesas representing the final array spots using standard image reversal photolithographic methods. After a second electron beam evaporation of 100 nm of gold, the photoresist was lifted off with acetone, leaving an elevated gold grid behind, defining the array elements on the SiO<sub>2</sub>.

**SPR Instrumentation.** A dual-channel SPR spectrometer, NanoSPR5-321 (NanoSPR, Chicago, IL) with a GaAs semiconductor laser light source ( $\lambda_{\text{max}} = 670$  nm) was used for all real-time binding measurements. SPR experiments were conducted at ambient temperature (*ca.* 23 °C), with 1×PBS (10 mM Na<sub>2</sub>HPO<sub>4</sub>, 1.8 mM KH<sub>2</sub>PO<sub>4</sub>, 137 mM NaCl, 2.7 mM KCl, pH 7.4) used as the running buffer set to a flow rate of 6 mL h<sup>-1</sup> unless otherwise noted. A detailed description of the SPR imaging instrumentation setup has been provided in previous work.<sup>26</sup> In brief, each SPRi array was mounted onto an optical stage containing a 300  $\mu$ L flow cell. Each array was put in contact with an equilateral SF2 prism ( $n = 1.616$ , Surplus Shed, Fleetwood, PA) using refractive index

matching fluid ( $n = 1.616$ , Cargille Laboratories, Cedar Grove, NJ). The optical stage was fixed to a goniometer allowing manual selection of the incident light angle. An incoherent light source (LED,  $\lambda = 648$  nm) was used for SPR excitation and the reflected images were captured by a cooled 12-bit CCD camera, Retiga 1300 (QImaging, Surrey, BC, Canada) with a resolution of 1.3 MP ( $1280 \times 1024$  pixels) and  $6.7 \mu\text{m} \times 6.7 \mu\text{m}$  pixel size. Injections of sample solutions into the flow cell were monitored in real time by recording changes in the reflectance every 300 ms inside the gold array wells and for reference purpose on the surroundings. Sensorgrams were obtained by averaging reflected light intensity over each array element using a home-built LabView program.

**Desiccation of Vesicle Suspensions.** An appropriate amount of preformed SUVs in 50 mM trehalose and 1×PBS (50  $\mu\text{L}$  for SPR channels, 20  $\mu\text{L}$  for fluorescence wells, 200 nL for SPRi array spots) was deposited on the chosen substrate surface and dried overnight in a vacuum desiccator, substrates were typically left under vacuum until use. In the case of the long-term storage assessment, substrates were moved from vacuum to ambient conditions after 12 h.

**Devitrification of Trehalose Coatings.** The substrates with trehalose suspended vesicles were placed directly into the SPR or SPRi instruments and rehydrated within the flow cell environment. Once a stable signal was obtained, indicating completion of the membrane formation and removal of excess material, the lipid bilayers were used for analytical studies.

**Fluorescence Microscopy and FRAP Analysis.** Fluidity of membranes from traditional fusion of POPC vesicles and those from hydrated trehalose encapsulated POPC vesicles

on different surfaces was examined using fluorescence recovery after photobleaching (FRAP). Supported lipid bilayers were formed on bare glass coverslips (Fisher Scientific, Pittsburgh, PA), glass coverslips covered with 10 nm of SiO<sub>2</sub>, and C18-modified glass coverslips. For the trehalose derived membranes, 20  $\mu$ L of 2% (w/w) NBD-PC/98% (w/w) POPC in 50 mM trehalose and 1 $\times$ PBS was deposited into 4.5 mm PDMS wells on top of the glass/modified Au substrates. Following an overnight dehydration in vacuum the vesicle suspension was rehydrated in 1 $\times$ PBS buffer *in situ* the following day and rinsed thoroughly with DI water to remove unfused vesicles. For traditional membranes, 20  $\mu$ L of 2% (w/w) NBD-PC/98% (w/w) POPC in 1 $\times$ PBS was deposited into the PDMS wells and allowed to incubate for 1 h prior to rinsing with water. To assist with the identification of the focal plane for the bilayer under the microscope, a peripheral scratch on the membrane was made. Fluorescence microscopy was carried out on an inverted Leica TCS SP5 II (Leica Microsystems, Buffalo Point, IL) using the 488 nm Argon laser line and a 40 $\times$  (NA 1.1) objective. Photobleaching at 1.5 mW for 500 ms and fluorescence recovery monitoring were set up and performed using the LAS AF software package (Leica Microsystems, Buffalo Point, IL).

The methods of Axelrod and Soumpasis were applied to derive diffusion coefficients for each membrane.<sup>27-28</sup> First, the fluorescence intensity of each bleach spot was normalized over a background area of the same size to account for background photobleaching. This normalized value ( $F_n$ ) was then used within the following formula to obtain the FRAP ratio ( $F_{FRAP}$ ), with  $F_0$  being the normalized intensity of the bleached area immediately after bleaching.

$$F_{FRAP} = \frac{F_n - F_0}{1 - F_0}$$

Thereafter,  $F_{FRAP}$  was plotted against time and fitted to a first order exponential function. The diffusion coefficient was calculated using the following equation, with  $D$  being the diffusion coefficient,  $\omega$  the full width at half maximum of the focused Gaussian laser profile,  $t_{1/2}$  the half-time recovery obtained from the exponential fit, and  $\gamma$  a correction factor accounting for the laser beam geometry.

$$D = \frac{\omega^2}{4t_{1/2}} \gamma$$

## ■ RESULTS AND DISCUSSION

***Diffusion Kinetics of Devitrified Membranes on SPR Surfaces.*** Glass has been used as a standard substrate for SLB studies, as it offers robust solid support for membrane formation from vesicle fusion, and the resulting membranes exhibit fluidic properties comparable to that of native cell membranes.<sup>29</sup> In order to be compatible with SPR detection, while maintaining acceptable sensitivity, glass layers must be as thin as possible (ideally on the nanometer scale) since the SPR evanescent field decays exponentially with distance from the gold surface. As noted in previous work, the layer-by-layer assembly of polyelectrolytes and sodium silicate followed by high-temperature calcination is an effective and low cost way to produce glassy silicate films of uniform, nanoscale thickness.<sup>23, 30</sup> Here we chose to explore membrane formation on SPR substrates on which silica ( $\text{SiO}_2$ ) is deposited by plasma-enhanced chemical vapor deposition (PECVD). This method offers the advantages of short process times (<10 min)

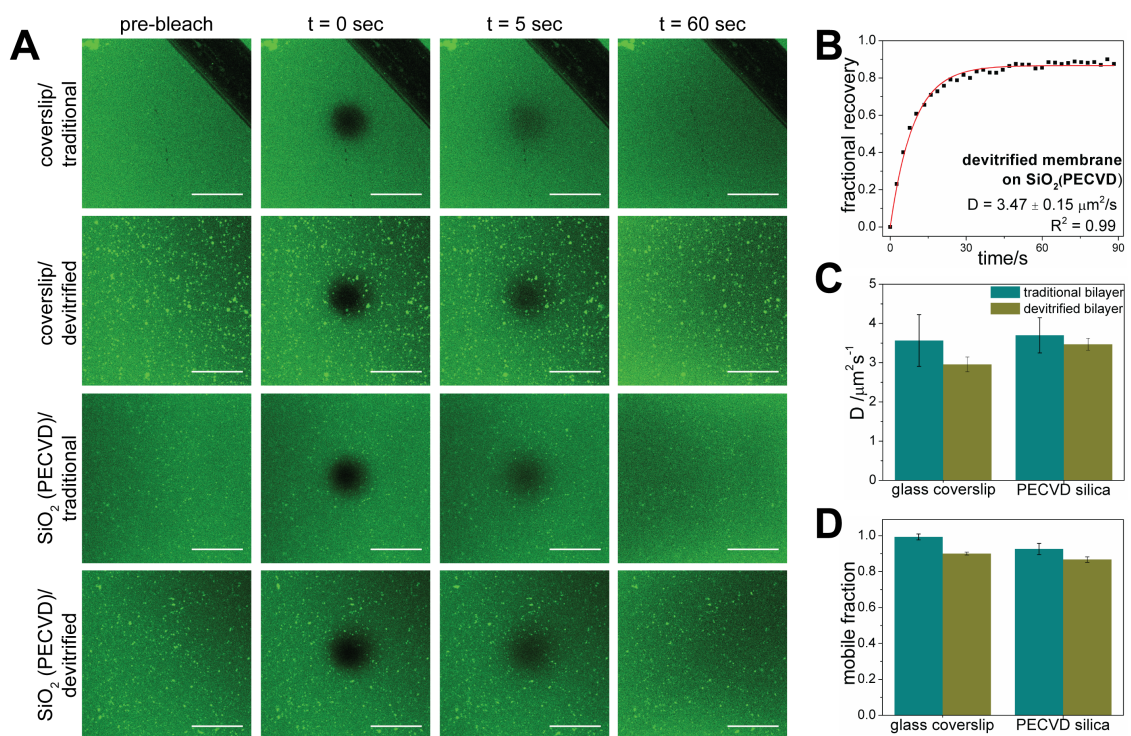


**Figure 3.2.** FRAP analysis of supported lipid bilayers formed using direct, traditional vesicle fusion and trehalose assisted deposition methods on microscope coverslips and SiO<sub>2</sub> modified SPR surfaces. Calculated values are the result of  $n = 3$  experiments. (A) Fluorescence microscopy images showing bleaching and recovery of fluorescence due to redistribution of lipids over time. Scale bars represent 20  $\mu\text{m}$ . (B) FRAP recovery curve of the devitrified membrane on modified SPR surface. (C) Diffusion coefficients. (D) Mobile fractions.

and remarkably smooth surfaces, which benefits lipid bilayer fluidity and minimizes optical scattering. Previous studies have established that these surfaces are characterized by low surface roughness values ( $\text{rms} < 1.5 \text{ nm}$ )<sup>31-32</sup> and high stability in buffer conditions compared to silica deposited using thermal evaporation.<sup>33</sup> However, the properties of SLBs on PECVD grown silica have not been fully investigated to determine if their diffusion kinetics match those on other glass-supported bilayers.

FRAP was performed to verify that the bilayers formed by traditional vesicle injection and through trehalose assisted delivery methods on glass coverslips (*i.e.* a standard solid support) and silica surfaces deposited using PECVD (Figure 3.2) were

contiguous, uniform, and fluidic. The fluorescence images (Figure 3.2A) show that all bilayers uniformly cover their respective surfaces, without defects or voids that would be indicative of a lack of membrane fusion. One minor difference to be noted when comparing the traditional versus devitrified membranes is that membranes originating from vesicles released from the devitrified trehalose showed a stronger abundance of small, higher fluorescence intensity patches across the membrane surface on the SiO<sub>2</sub> covered SPR substrates. This may be attributed to the rehydrating conditions used for the devitrification of trehalose with some rehydrated lipids only partially fusing and remaining as aggregates at the glass:lipid interface. However, this only appears to have a minimal impact on the diffusion kinetics of lipids within the bilayer, as seen when comparing the fractional recovery profiles and their associated kinetic values (Figure 3.2B-D, also see Figure B.2). It should be noted that the fractional recovery profile for membranes from trehalose released vesicles on PECVD silica is relatively smooth and fits the lateral diffusion curve well ( $R^2 = 0.99$ ), strongly indicating a natural and uniform bilayer (Figure 3.2B). While the lateral mobilities of traditional membranes (Figure 3.2B) are slightly higher, all diffusion coefficients ( $D$ ) are between  $2 - 4 \mu\text{m}^2 \text{s}^{-1}$  (Figure 3.2C). The slightly lower lateral mobilities of trehalose formed membranes may be due to trace amounts of trehalose remaining under the bilayer, affecting the short-range interactions between the lipids and glass support. However, all values still compare favorably with previous studies of phosphatidylcholine based SLBs on glass surfaces, where diffusion coefficients ranged between  $1 - 4 \mu\text{m}^2 \text{s}^{-1}$ .<sup>29</sup>

Another interesting observation is that mobile fractions ( $\beta$ ) differ slightly when comparing membranes on glass coverslips and silica deposited using PECVD (Figure 3.2D). In general, mobile fractions were higher for bilayers on glass coverslips, 99% and 90% for traditional and devitrified trehalose respectively, than for bilayers on the PECVD surface, with 92% and 86%, respectively. Lower mobile fractions have previously been attributed to higher surface roughness of the underlying material,<sup>34</sup> though PECVD surfaces are known to be quite smooth.<sup>31-32</sup> These lower mobile fractions are more likely to be due to the different levels of hydrogen bonding observed in PECVD grown dielectrics, thereby changing the affinity for phospholipids at the surface,<sup>35</sup> or to remnants of trehalose remaining under the bilayer. Nevertheless, all mobile fraction values are quite high, and taken together with the high diffusion coefficients and continuous fluorescence signal, the data suggests that a fluid and natural membrane is formed using trehalose preserved vesicles on PECVD grown silica, resulting in a SLB that is capable of full biological functionality<sup>36-37</sup> and suitable for SPR imaging and spectroscopic studies.

***SPR Monitoring of SLB Formation from Trehalose Encapsulated Vesicles and Toxin Binding.*** SPR has been established as a universal tool for monitoring interactions at membrane interfaces,<sup>10, 15</sup> as the probing evanescent field of SPR is most sensitive directly near the gold surface on which lipid bilayers are supported. Vesicles were deposited by spotting an appropriate amount of small, unilamellar vesicles (SUVs) suspended in 50 mM trehalose onto the silica coated SPR chips, followed by drying overnight in vacuum. These SUVs in vitrified trehalose were rehydrated in the SPR flow cell, and the trehalose devitrification and vesicle fusion processes leading to on-demand

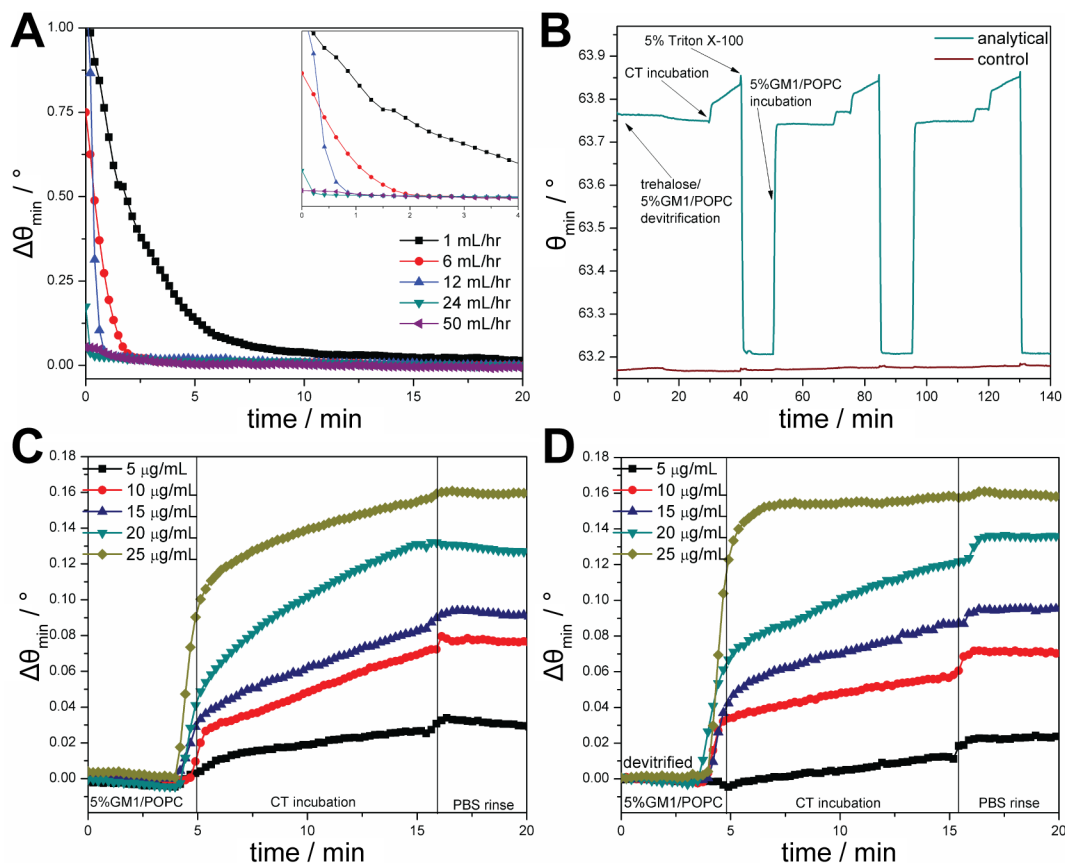


**Figure 3.3.** SPR studies of vesicle fusion upon devitrification of trehalose and preservation of embedded cargo activity. (A) Flow rate effects on devitrification of trehalose, release of SUVs, and formation of supported lipid bilayers. (B) Formation of supported lipid bilayer from trehalose released SUVs containing GM<sub>1</sub> and subsequent CT binding response, followed by a comparative study of the same system generated by traditional vesicle fusion. (C) Responses of membranes formed by vesicle injection methods to cholera toxin injections. (D) Responses of membranes formed by vesicle preservation and devitrification methods to cholera toxin injections.

lipid bilayer formation were monitored in real time. Rehydration of the SUVs was carried out over a range of flow rates, set between 1 – 50 mL h<sup>-1</sup> (Figure 3.3A). There are a number of processes occurring at the substrate surface during rehydration, which include devitrification of trehalose, diffusion of trehalose into solution, diffusion of SUVs into solution, and fusion of SUVs to the adjacent substrate surface.<sup>16</sup> Given the flow cell arrangement employed in our studies, the flow rate is a vital parameter to ensure that upon devitrification of the trehalose the release of vesicles ensures formation of a

contiguous membrane before mass transport away from the surface leads to SUV depletion. For lower flow rates in the range of 1 – 6 mL h<sup>-1</sup>, a substantial amount of time was required for SPR sensorgrams to reach a flat baseline, which we interpret as a stable bilayer. It is possible that SUVs remain adsorbed to the bilayer interface and are only gradually removed in the flowing buffer. Given the high solubility of trehalose in water, it is unlikely that gradual trehalose removal can fully account for the observed behavior. This was confirmed by a control where only trehalose was desiccated and rehydrated, resulting in only a partial resonance angle decrease compared to when both vesicles and trehalose were rehydrated (Figure B.3). The former is in agreement with the observation of small phospholipid aggregates in the fluorescence images (Figure 3.2A). Higher flow rates between 12 – 50 mL h<sup>-1</sup> allowed for complete vesicle fusion and excess removal without an extended equilibration period; therefore all further assays used an initial rapid flow rate of 24 mL h<sup>-1</sup> for rehydration, followed by a lower flow rate of 6 mL h<sup>-1</sup> during affinity measurements to minimize laminar shear forces on the bilayer.

The binding properties of embedded receptors in the SLBs formed on-demand by this method were compared to SLBs containing the same receptors but formed by the traditional vesicle injection method on the identical substrate. For this evaluation, it was first established that SLBs originating from the two methods yield similar membrane thicknesses. For this, equilibrated SLBs formed with trehalose assistance on the SPR chips were stripped away with buffer containing 5% Triton X-100, and new SLBs were generated by incubating the identical substrate with a fresh SUV suspension. The observed resonance angle shifts of the SPR chip match precisely for both methods each

time a new lipid bilayer is formed on the surface (Figure 3.3B). SPR is a refractive index sensitive method, in which the observed signal change for SLBs is determined by their unique bulk refractive index and geometry, and in this case the SLB thickness;<sup>19</sup> here, the observed similarities in resonance angles between the two types of bilayers strongly suggest that their thicknesses and effective masses are identical. The above evaluation strategy was also explored in the context of biointeraction analyses, using the model system of cholera toxin (CT) binding to the membrane-bound GM<sub>1</sub> receptor. Over a range of concentrations, the response signals at equilibrium for CT-GM<sub>1</sub> interactions are very similar (Figure 3.3C,D), indicating that throughout the vitrification, rehydration, and fusion processes, receptors embedded in the preserved vesicles retain biological activity and respective ligand affinities comparable to those not undergoing desiccation and rehydration. This was further evaluated over a period of four weeks, in which measurements of CT binding to different GM<sub>1</sub>/POPC membranes, deposited at the same time, were taken at regular intervals. Response signals remained nearly unchanged over the 28 days, exhibiting only a 4.3% relative standard deviation at a CT concentration of 20  $\mu\text{g mL}^{-1}$  (Figure B.4). It should be noted that each of these substrates were left in ambient conditions over the month, not requiring continuous desiccation or refrigeration. Given that this involves humidity and temperature fluctuations, the sub 5% standard deviation in the response is excellent and could possibly be even more improved in a more controlled environment. Preservation of biological function during medium and long-term storage is essential for a practical, expanded deployment of this methodology.

***SPR Imaging of Multi-Element SLB Arrays.*** SPR imaging is a powerful tool for real-time and label-free microarray analysis, expanding the throughput of assays and minimizing artifacts from sequential measurements. Analyzing SLB microarrays with varying bilayer compositions remains a challenging task, mainly due to the requirement of maintaining constant hydration of the substrate during the arraying, handling, and assaying processes. One option to generate membrane arrays of varying compositions is to utilize multiple microfluidic channels during the formation and analysis of supported lipid bilayers.<sup>38</sup> While this approach is promising for analyzing multiple “lanes” in real-time, fluidics with an open chamber design offer the advantage of exposing all array elements to the same analyte and flow conditions. To demonstrate the feasibility of using trehalose mediated lipid array generation for SPR imaging, a number of assays were conducted using a home-built SPRi instrument in the Kretschmann configuration.<sup>26</sup>

Membrane confinement was initially investigated in order to establish that supported membranes remain localized to the area of deposition during and after the hydration-fusion step. An array pattern on a planar SiO<sub>2</sub> covered gold surface was hand spotted with vesicles suspended in trehalose, desiccated, and SPR difference images were taken before, during, and after hydration in the flow cell environment (Figure 3.4A). The initial SPR difference image of the as deposited spots was recorded at a lower angle allowing SPR resonance in air compared to the rehydrated substrate difference images that were imaged in buffer. Post hydration and under a maintained flow rate of 6 mL h<sup>-1</sup>, the resulting SLBs stay confined to their areas of deposition and fusion, as seen in Figure 3.4A. The observed spatial confinement is in agreement with the previous study

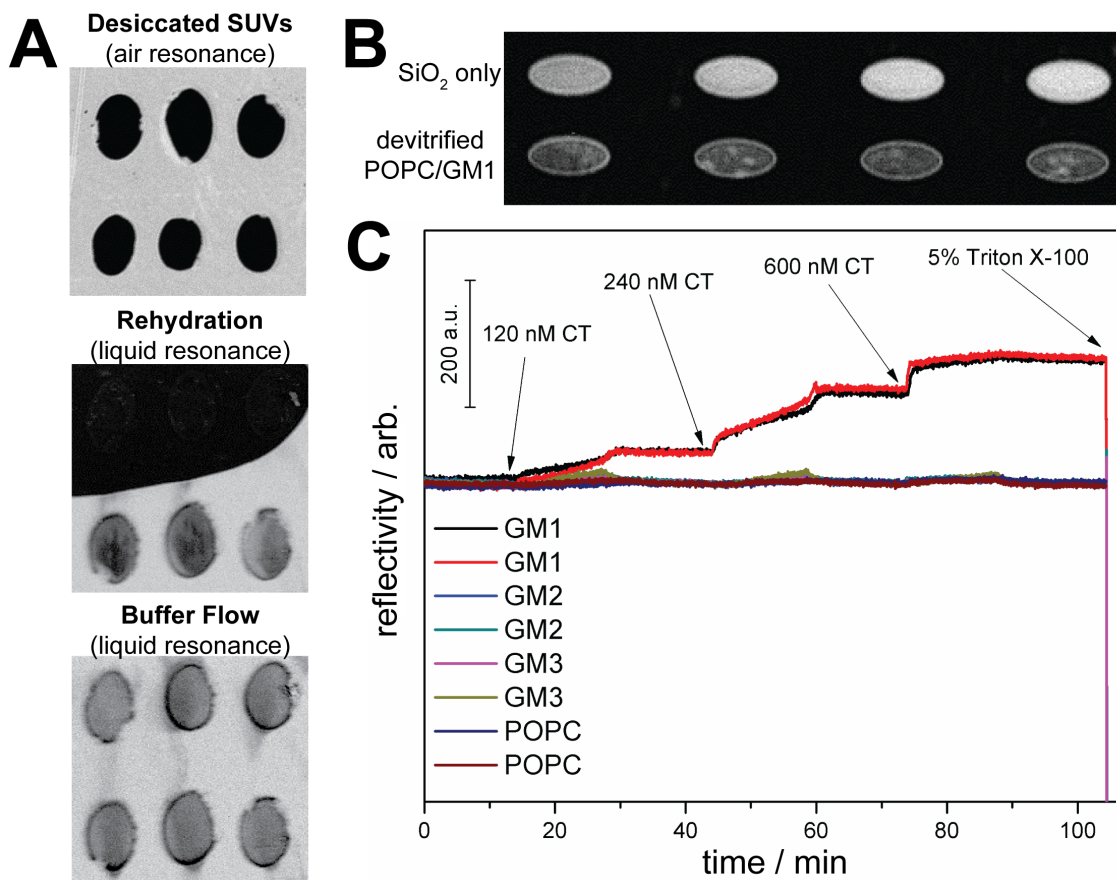


**Figure 3.4.** SPR imaging study of membrane arrays formed using vesicles deposited, and preserved within, a trehalose matrix. (A) Spatial confinement of lipids before, during, and after rehydration. The middle image exhibits the buffer front. (B) SPR difference image comparing bare silica surface and membrane-covered surface. (C) SPR imaging sensorgrams comparing cholera toxin binding to SLBs of various compositions on the same SPR imaging substrate.

involving fluorescence,<sup>16</sup> but extends this to a laminar flow regime, providing an additional measure of assurance that there is no cross talk between adjacent spots. An understanding of the mechanism behind membrane formation during the devitrification process is critical toward evaluating the utility of this scheme for SPR microarray analysis, as one outstanding question is what the limiting factor would be for printing arrays of high density. During the vitrification of trehalose and removal of water from the environment, embedded SUVs undergo significant shape deformation, which is restored

once water is added back to the system.<sup>16</sup> This shape deformation likely plays an important role in determining minimum distances for eliminating cross talk of adjacent populations, as this may cause the bulk deposited vesicle surface area to laterally stretch from the arrayed spot. While this would need to be taken into account in determining the limits for printing density, within the context of experiments conducted so far, this process has not seemed to impart any negative impact on results, even with spacings less than 100  $\mu\text{m}$ .<sup>16</sup>

This was further explored by spotting a microarray substrate for biological recognition, that on hydration resulted in  $800 \times 800 \mu\text{m}$  POPC membranes containing either GM<sub>1</sub>, GM<sub>2</sub>, GM<sub>3</sub>, or no receptors, as a negative control. Previous work has shown that cholera toxin has a very low affinity toward GM<sub>2</sub> and GM<sub>3</sub> compared to GM<sub>1</sub>, and no affinity toward POPC alone.<sup>10</sup> Figure 3.4B shows an SPR difference image comparing bare silica and devitrified SLB array spots on a patterned SPR imaging array substrate, where the high contrast between each row together with the sharp boundaries is indicative of bilayer formation in orderly rows, without migration of elements into adjacent ones. Assaying the array on the SPR imager with various concentrations of cholera toxin in the range of 120 – 600 nM revealed that only SLBs containing the GM<sub>1</sub> receptor yielded measurable signals, while in array elements containing GM<sub>2</sub> and GM<sub>3</sub> the signal remained at baseline values. This clearly demonstrates that vesicles released from trehalose during the devitrification and bilayer fusion processes do not mix with those in adjacent array spots, resulting in a lack of cross talk between array elements. To

the best of our knowledge, this represents the first direct assaying of these three receptors side by side within their natural lipid environments in a microarray format.

***Beyond SLBs: Trehalose-Mediated Hybrid Bilayer Membranes.*** Hybrid bilayer membranes (HBMs) are a classic model of biomimetic systems<sup>22</sup> and an active research area for investigating biophysical processes.<sup>39-40</sup> In hybrid membranes, the lower leaflet of the bilayer membrane is composed of hydrophobic molecules covalently bound to the substrate surface, whereas the upper leaflet is composed of phospholipids. The rigidity of the hydrophobic lower leaflet reduces the lateral mobility of the lipid leaflet; however their high mechanical stability and ease of integration with many optical and electrochemical techniques are heavily exploited in current sensor design. Since the formation of HBMs essentially follows similar steps as the formation of SLBs, we explored the extent to which our trehalose-assisted methodology for on-demand lipid membrane generation in SPRi analysis would also be applicable toward HBMs (Figure 3.5A). Fluorescence images (Figure B.5) show that the fused phospholipids uniformly, across all observed length scales, cover the hydrophobic octadecanethiol-modified gold surface. FRAP analysis of the lipids mobility in the hybrid bilayer showed that these are far less mobile than both traditional and trehalose mediated SLBs, with a diffusion coefficient of  $0.48 \mu\text{m}^2 \text{s}^{-1}$  and mobile fraction of 51%. This is to be expected, as the affinity of phospholipid tails for the underlying hydrophobic monolayer is much stronger than the hydrophilic reactions supporting lipid bilayers,<sup>41</sup> limiting lateral movement of these lipids. SPRi assaying of the system followed the same procedures as for the SLB system. Formed HBMs remain confined under buffer flow to locations where the arrays

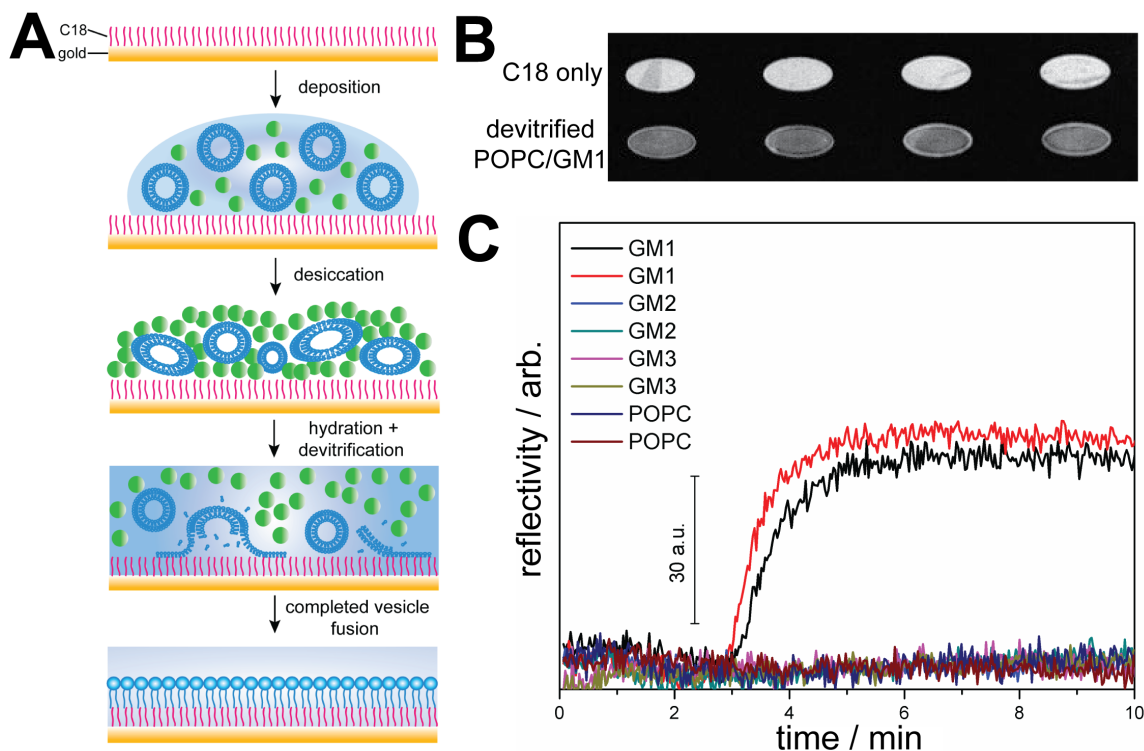


**Figure 3.5.** Hybrid bilayer membrane formation on SPR substrates using trehalose assisted vesicle delivery. (A) Scheme of deposition, desiccation, and hydration on hydrophobic rendered SPR surface. (B) SPR difference image comparing bare C18 surface and membrane-covered surface. (C) SPR imaging sensorgrams comparing cholera toxin binding to HBMs of various compositions on the same SPR imaging substrate.

were originally spotted and vitrified, as seen in the SPR difference image (Figure 3.5B). In addition, the hydrophobic SPR substrate was spotted with arrays of SUVs incorporating GM<sub>1</sub>, GM<sub>2</sub>, GM<sub>3</sub> or no additional receptors. The sensorgrams (Figure 3.5C) during the injection of 120 nM cholera toxin across this array confirm that protein binding only occurs to the HBMs containing GM<sub>1</sub>. These results align well with those obtained for the hydrophilic SLB arrays and demonstrate that the methods developed in this work are applicable to various surfaces and membrane geometries.

## ■ CONCLUSIONS

The combination of trehalose-mediated phospholipid vesicle deposition and their on-demand fusion into SLBs combined with SPR spectroscopy and imaging is an efficient, powerful, and easily scalable tool for label-free assaying of molecular interactions with SLBs. Supported lipid bilayers produced by this method are of high quality and nearly indistinguishable from those generated by traditional vesicle fusion methods. Fluorescence microscopy and FRAP analysis showed that the membranes on our engineered SPR chips are uniform and exhibit high lateral mobility, similar to native membrane environments. SPR spectroscopic studies show the bilayers from trehalose released vesicles are equivalent to conventionally generated bilayers in terms of effective refractive index values, and hence, membrane geometry and packing density. Incorporation of the GM<sub>1</sub> receptor into these systems resulted in binding of its natural ligand, cholera toxin, similar to that for traditionally prepared membranes. Furthermore, deposited lipids were stored in their vitrified state for up to one month while maintaining excellent ligand binding affinity upon hydration. Newly formed membranes stayed confined to their deposited spots upon hydration on both hydrophilic and hydrophobic SPR substrates, without crosstalk, which allows for the high-throughput screening of multiple SLBs with varying constituents. Taken together, these results represent a substantial step forward in the advancement of label-free lipid membrane arrays. We expect the methods reported here to inspire more widespread adaption of supported membrane systems, as the on-demand and label-free nature of this scheme is highly efficient, scalable, and convenient.

## ■ REFERENCES

- (1) van Meer, G.; Voelker, D. R.; Feigenson, G. W. Membrane Lipids: Where They Are and How They Behave. *Nat. Rev. Mol. Cell Biol.* **2008**, *9*, 112-124.
- (2) Cuatrecasas, P. Membrane Receptors. *Annu. Rev. Biochem.* **1974**, *43*, 169-214.
- (3) Brian, A. A.; McConnell, H. M. Allogeneic Stimulation of Cytotoxic T Cells by Supported Planar Membranes. *Proc. Natl. Acad. Sci. U. S. A.* **1984**, *81*, 6159-6163.
- (4) Phillips, K. S.; Cheng, Q. Microfluidic Immunoassay for Bacterial Toxins with Supported Phospholipid Bilayer Membranes on Poly(Dimethylsiloxane). *Anal. Chem.* **2005**, *77*, 327-334.
- (5) Costello, D. A.; Hsia, C. Y.; Millet, J. K.; Porri, T.; Daniel, S. Membrane Fusion-Competent Virus-Like Proteoliposomes and Proteinaceous Supported Bilayers Made Directly from Cell Plasma Membranes. *Langmuir* **2013**, *29*, 6409-6419.
- (6) Costello, D. A.; Millet, J. K.; Hsia, C. Y.; Whittaker, G. R.; Daniel, S. Single Particle Assay of Coronavirus Membrane Fusion with Proteinaceous Receptor-Embedded Supported Bilayers. *Biomaterials* **2013**, *34*, 7895-7904.
- (7) Grakoui, A.; Bromley, S. K.; Sumen, C.; Davis, M. M.; Shaw, A. S.; Allen, P. M.; Dustin, M. L. The Immunological Synapse: A Molecular Machine Controlling T Cell Activation. *Science* **1999**, *285*, 221-227.
- (8) Mossman, K. D.; Campi, G.; Groves, J. T.; Dustin, M. L. Altered Tcr Signaling from Geometrically Repatterned Immunological Synapses. *Science* **2005**, *310*, 1191-1193.
- (9) Ghang, Y. J.; Schramm, M. P.; Zhang, F.; Acey, R. A.; David, C. N.; Wilson, E. H.; Wang, Y. S.; Cheng, Q.; Hooley, R. J. Selective Cavitand-Mediated Endocytosis of Targeted Imaging Agents into Live Cells. *J. Am. Chem. Soc.* **2013**, *135*, 7090-7093.

- (10) Kuziemko, G. M.; Stroh, M.; Stevens, R. C. Cholera Toxin Binding Affinity and Specificity for Gangliosides Determined by Surface Plasmon Resonance. *Biochemistry* **1996**, *35*, 6375-6384.
- (11) Cornell, B. A.; BraachMaksvytis, V. L. B.; King, L. G.; Osman, P. D. J.; Raguse, B.; Wieczorek, L.; Pace, R. J. A Biosensor That Uses Ion-Channel Switches. *Nature* **1997**, *387*, 580-583.
- (12) Bayley, H.; Cremer, P. S. Stochastic Sensors Inspired by Biology. *Nature* **2001**, *413*, 226-230.
- (13) Groves, J. T.; Boxer, S. G. Micropattern Formation in Supported Lipid Membranes. *Acc. Chem. Res.* **2002**, *35*, 149-157.
- (14) Kaufmann, S.; Sobek, J.; Textor, M.; Reimhult, E. Supported Lipid Bilayer Microarrays Created by Non-Contact Printing. *Lab Chip* **2011**, *11*, 2403-2410.
- (15) Phillips, K. S.; Wilkop, T.; Wu, J. J.; Al-Kaysi, R. O.; Cheng, Q. Surface Plasmon Resonance Imaging Analysis of Protein-Receptor Binding in Supported Membrane Arrays on Gold Substrates with Calcinated Silicate Films. *J. Am. Chem. Soc.* **2006**, *128*, 9590-9591.
- (16) Wilkop, T. E.; Sanborn, J.; Oliver, A. E.; Hanson, J. M.; Parikh, A. N. On-Demand Self-Assembly of Supported Membranes Using Sacrificial, Anhydrobiotic Sugar Coats. *J. Am. Chem. Soc.* **2014**, *136*, 60-63.
- (17) Crowe, J. H.; Hoekstra, F. A.; Crowe, L. M. Anhydrobiosis. *Annu. Rev. Physiol.* **1992**, *54*, 579-599.
- (18) Crowe, L. M.; Crowe, J. H. Stabilization of Dry Liposomes by Carbohydrates. *Dev. Biol. Stand.* **1992**, *74*, 285-294.
- (19) Homola, J.; Yee, S. S.; Gauglitz, G. Surface Plasmon Resonance Sensors: Review. *Sens. Actuators, B* **1999**, *54*, 3-15.

- (20) Homola, J. Surface Plasmon Resonance Sensors for Detection of Chemical and Biological Species. *Chem. Rev.* **2008**, *108*, 462-493.
- (21) Zhao, S. S.; Bukar, N.; Toulouse, J. L.; Pelechacz, D.; Robitaille, R.; Pelletier, J. N.; Masson, J. F. Miniature Multi-Channel SPR Instrument for Methotrexate Monitoring in Clinical Samples. *Biosens. Bioelectron.* **2015**, *64*, 664-670.
- (22) Plant, A. L. Supported Hybrid Bilayer Membranes as Rugged Cell Membrane Mimics. *Langmuir* **1999**, *15*, 5128-5135.
- (23) Phillips, K. S.; Han, J. H.; Martinez, M.; Wang, Z. Z.; Carter, D.; Cheng, Q. Nanoscale Glassification of Gold Substrates for Surface Plasmon Resonance Analysis of Protein Toxins with Supported Lipid Membranes. *Anal. Chem.* **2006**, *78*, 596-603.
- (24) Abbas, A.; Linman, M. J.; Cheng, Q. Patterned Resonance Plasmonic Microarrays for High-Performance SPR Imaging. *Anal. Chem.* **2011**, *83*, 3147-3152.
- (25) Linman, M. J.; Abbas, A.; Roberts, C. C.; Cheng, Q. Etched Glass Microarrays with Differential Resonance for Enhanced Contrast and Sensitivity of Surface Plasmon Resonance Imaging Analysis. *Anal. Chem.* **2011**, *83*, 5936-5943.
- (26) Wilkop, T.; Wang, Z. Z.; Cheng, Q. Analysis of Mu-Contact Printed Protein Patterns by SPR Imaging with a LED Light Source. *Langmuir* **2004**, *20*, 11141-11148.
- (27) Axelrod, D.; Koppel, D. E.; Schlessinger, J.; Elson, E.; Webb, W. W. Mobility Measurement by Analysis of Fluorescence Photobleaching Recovery Kinetics. *Biophys. J.* **1976**, *16*, 1055-1069.
- (28) Soumpasis, D. M. Theoretical-Analysis of Fluorescence Photobleaching Recovery Experiments. *Biophys. J.* **1983**, *41*, 95-97.
- (29) Stelzle, M.; Miehllich, R.; Sackmann, E. 2-Dimensional Microelectrophoresis in Supported Lipid Bilayers. *Biophys. J.* **1992**, *63*, 1346-1354.

- (30) Linman, M. J.; Culver, S. P.; Cheng, Q. Fabrication of Fracture-Free Nanoglassified Substrates by Layer-by-Layer Deposition with a Paint Gun Technique for Real-Time Monitoring of Protein-Lipid Interactions. *Langmuir* **2009**, *25*, 3075-3082.
- (31) Szunerits, S.; Coffinier, Y.; Janel, S.; Boukherroub, R. Stability of the Gold/Silica Thin Film Interface: Electrochemical and Surface Plasmon Resonance Studies. *Langmuir* **2006**, *22*, 10716-10722.
- (32) Szunerits, S.; Boukherroub, R. Electrochemical Investigation of Gold/Silica Thin Film Interfaces for Electrochemical Surface Plasmon Resonance Studies. *Electrochem. Commun.* **2006**, *8*, 439-444.
- (33) Kambhampati, D. K.; Jakob, T. A. M.; Robertson, J. W.; Cai, M.; Pemberton, J. E.; Knoll, W. Novel Silicon Dioxide Sol-Gel Films for Potential Sensor Applications: A Surface Plasmon Resonance Study. *Langmuir* **2001**, *17*, 1169-1175.
- (34) Chen, C.-Y.; Hinman, S. S.; Duan, J.; Cheng, Q. Nanoglassified, Optically-Active Monolayer Films of Gold Nanoparticles for in Situ Orthogonal Detection by Localized Surface Plasmon Resonance and Surface-Assisted Laser Desorption/Ionization-Ms. *Anal. Chem.* **2014**, *86*, 11942-11945.
- (35) Ay, F.; Aydinli, A. Comparative Investigation of Hydrogen Bonding in Silicon Based PECVD Grown Dielectrics for Optical Waveguides. *Opt. Mater.* **2004**, *26*, 33-46.
- (36) Reits, E. A. J.; Neeffjes, J. J. From Fixed to FRAP: Measuring Protein Mobility and Activity in Living Cells. *Nat. Cell Biol.* **2001**, *3*, E145-E147.
- (37) Sprague, B. L.; McNally, J. G. FRAP Analysis of Binding: Proper and Fitting. *Trends Cell Biol.* **2005**, *15*, 84-91.
- (38) Taylor, J. D.; Phillips, K. S.; Cheng, Q. Microfluidic Fabrication of Addressable Tethered Lipid Bilayer Arrays and Optimization Using SPR with Silane-Derivatized Nanoglassy Substrates. *Lab Chip* **2007**, *7*, 927-930.

- (39) Ma, W.; Ying, Y. L.; Qin, L. X.; Gu, Z.; Zhou, H.; Li, D. W.; Sutherland, T. C.; Chen, H. Y.; Long, Y. T. Investigating Electron-Transfer Processes Using a Biomimetic Hybrid Bilayer Membrane System. *Nat. Protoc.* **2013**, *8*, 439-450.
- (40) Tse, E. C. M.; Barile, C. J.; Gewargis, J. P.; Li, Y.; Zimmerman, S. C.; Gewirth, A. A. Anion Transport through Lipids in a Hybrid Bilayer Membrane. *Anal. Chem.* **2015**, *87*, 2403-2409.
- (41) Castellana, E. T.; Cremer, P. S. Solid Supported Lipid Bilayers: From Biophysical Studies to Sensor Design. *Surf. Sci. Rep.* **2006**, *61*, 429-444.

---

\* Adapted with permission from: Hinman, S. S., et al. On-Demand Formation of Supported Lipid Membrane Arrays by Trehalose-Assisted Vesicle Delivery for SPR Imaging. *ACS Appl. Mater. Interfaces* **2014**, *7*, 17122-17130. Copyright 2014 American Chemical Society.

## **CHAPTER 4: DNA Linkers and Diluents for Ultrastable Gold Nanoparticle Bioconjugates in Multiplexed Assay Development\***

### **■ INTRODUCTION**

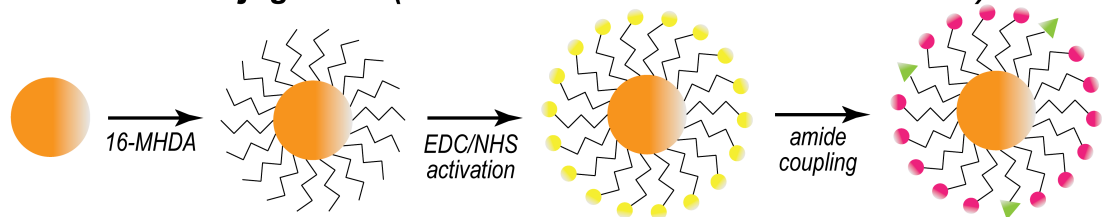
Gold nanoparticles have been established as ideal signaling agents and enhancement tools for a wide variety of sensing schemes and detection modalities,<sup>1-4</sup> yet their practical use can be limited by low colloidal stabilities, especially within high salt media, complex biological samples, and through extreme storage conditions.<sup>5</sup> While the gold cores are resistant to oxidation, even after being aerosolized or heated,<sup>6</sup> shielding of surface charges or application of mechanical forces may lead to irreversible aggregation into larger clusters, followed by their eventual precipitation from solution. Thiolated monolayers have been broadly used for functionalization of AuNPs and to impart some measure of stability, as they leave the cores coated with, and relatively protected by, a covalently bound alkane or PEG chain.<sup>7</sup> However, a systematic investigation conducted by Gao et al. of commonly used thiolated monolayers, including a nonionic PEG-thiol, glutathione, mercaptopropionic acid, cysteine, cysteamine, and dihydrolipoic acid, has revealed that all the monolayers studied, with the exception of the PEG-thiol, resulted in AuNP conjugates that exhibited very little tolerance to pH or ionic strength,<sup>8</sup> both of which may vary substantially in analytical samples. While PEG-thiols are clearly preferable for their increased tolerance to these conditions, they are not infallible; nonionic PEG-thiols have been shown to leave AuNPs subject to aggregation following

freezing and lyophilization, both of which have been established as common, and sometimes necessary, storage techniques.<sup>9</sup>

Various biologically inspired and synthetic coatings have been utilized for the stabilization of gold nanoparticles against exposure to high ionic strengths and freeze-drying. Direct adsorption of proteins to the nanoparticle surface represents one of the most straightforward methods to functionalize and stabilize AuNPs, and takes place *via* electrostatic interactions between the protein and the gold surface.<sup>10-11</sup> Human serum albumin, for example, has been shown to stabilize AuNPs in up to 0.3 M NaCl,<sup>11</sup> though control of protein orientation on the surface can be problematic, as are further ligand derivatizations. Simpler pentapeptide capping ligands, terminated with a functional carboxyl group, have been shown to have sequence dependent effects on stability, producing colloids that are stable in up to 1 M NaCl and capable of being redispersed after lyophilization.<sup>12</sup> Lipid bilayers, while not tested for their ability to shield against high ionic strengths, were also shown to protect AuNPs from the freezing process.<sup>13</sup> Some of the most successful protective ligands are synthetic compounds, with large polymers and zwitterionic terminals conferring exceptionally high stability to gold colloids (up to 5 M NaCl, and capable of being lyophilized).<sup>9, 14-16</sup> However, each of these has required in-house synthesis and purification of the ligands prior to attachment, thereby limiting accessibility.

The attachment of thiolated DNA to gold nanoparticles has been extensively explored for drug delivery and sensing, and the fabrication process has undergone multiple iterations to be made widely accessible and controllable.<sup>17-20</sup> Similar to peptide

### Conventional Conjugations (Alkanethiol/PEG Linkers and Diluents)



### Functional DNA Conjugations (DNA Linkers and Diluents)

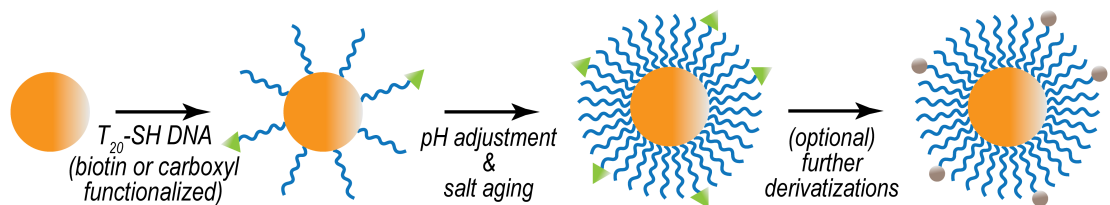


**Figure 4.1.** Gold nanoparticle conjugation schemes. (Top) Alkanethiol (16-MHDA) attachment, and amide coupling through carbodiimide crosslinking. (Bottom) DNA ( $T_{20}$ ) attachment, facilitated through pH adjustment and salt aging. Further derivatizations may follow DNA attachment.

capping ligands,<sup>12</sup> the stability they confer is also sequence dependent,<sup>21</sup> with thymine polynucleotides providing AuNPs that are stable in up to 6.1 M NaCl.<sup>22</sup> Moreover, thiolated oligonucleotides, terminated with a wide variety of functional groups, are commercially available from a number of sources. With the above in mind, we set out to utilize DNA linkers and diluents as an alternative to alkane and PEG linkers, for the conjugation of proteins and small molecules to gold nanoparticle surfaces. Herein, we have fabricated DNA/AuNPs conjugated to biorecognition molecules that are exceptionally stable in high ionic strength solutions and complex media (Figure 4.1). Additionally, they can be lyophilized and resuspended multiple times with retention of biological activity. The DNA/AuNPs are shown to function well for surface plasmon resonance signal enhancement, are capable of being utilized within colorimetric microplate assays, and are robust enough to remain a stable colloid after multiple derivatizations at the nanoparticle surface toward orientation-controlled antibody loading.

Taken together, the stability and versatility that this DNA interface offers for effective nanoparticle bioconjugation pathways are unparalleled by most conventional ligands.

## ■ EXPERIMENTAL METHODS

**Materials and Reagents.** Gold (III) chloride trihydrate, trisodium citrate dihydrate, N-hydroxysuccinimide (NHS), 1-(3-dimethylaminopropyl)-3-ethylcarbodiimide hydrochloride (EDC), 2-(2'-aminoethoxy) ethanol (AEE), Tween 20, 16-mercaptohexadecanoic acid (16-MHDA), 3,3',5,5'-tetramethylbenzidine (TMB), horseradish peroxidase (HRP, Type VI), cholera toxin from *Vibrio cholerae* (CT), anti-cholera toxin antibody from rabbit (whole antiserum), and Protein A from *Staphylococcus aureus* were from Sigma Aldrich (St. Louis, MO). Streptavidin and (+)-Biotinyl-3,6,9-trioxaundecanediamine (BA) were from Thermo Scientific (Rockford, IL). 1-oleoyl-2-palmitoyl-*sn*-glycero-3-phosphocholine (POPC) and 1,2-dipalmitoyl-*sn*-glycero-3-phosphoethanolamine-N-(biotinyl) sodium salt (biotin-PE) were from Avanti Polar Lipids (Alabaster, AL). Monosialoganglioside receptor GM<sub>1</sub> was from Matreya (Pleasant Gap, PA). Functionalized oligonucleotides were obtained from Integrated DNA Technologies (Coralville, IA), and their sequences are provided in Table 4.1. Detailed compositions of all buffers used (1×PBS, PBT, PCB, and MES) may be found in Appendix C. Nanopure water ( $\geq 18 \text{ M}\Omega\cdot\text{cm}$ ), purified through a Barnstead E-Pure filtration system (Thermo Scientific, Rockford, IL), was used for all reagent preparations.

**Table 4.1.** Functionalized DNA Oligonucleotide Sequences

Name	5' Modification	Sequence
<b>T<sub>20</sub></b>	none	5' – T <sub>20</sub> – (CH <sub>2</sub> ) <sub>3</sub> – SH – 3'
<b>bT<sub>20</sub></b>	biotin	5' – biotin-NH <sub>2</sub> -(CH <sub>2</sub> ) <sub>2</sub> O(CH <sub>2</sub> ) <sub>2</sub> -PO <sub>4</sub> – T <sub>20</sub> – (CH <sub>2</sub> ) <sub>3</sub> – SH – 3'
<b>cT<sub>20</sub></b>	carboxyl	5' – COOH-T – T <sub>20</sub> – (CH <sub>2</sub> ) <sub>3</sub> – SH – 3'

**Instrumentation.** Absorbance spectra were obtained using a Cary 50 UV-Vis spectrophotometer (Agilent Technologies, Santa Clara, CA), and microplate data was acquired through a PowerWave X-340 (Biotek Instruments, Winooski, VT). Transmission electron microscopy (TEM) was conducted on a Phillips FEI Tecnai 12 TEM (Andover, MA) in UCR CFAMM. Zeta potential analysis was performed using a Delsa Nano C particle analyzer (Beckman Coulter, Brea, CA). Surface plasmon resonance (SPR) spectroscopy and imaging were conducted at room temperature (*ca.* 23 °C) on a NanoSPR6-321 (NanoSPR, Addison, IL) and a homebuilt SPR imaging setup,<sup>23</sup> respectively, both using 1×PBS as the running buffer set to a flow rate of 5 mL h<sup>-1</sup> (*ca.* 83 μL min<sup>-1</sup>). Nanoglassified gold sensor chips were fabricated in a Class 1000 cleanroom facility (UCR Center for Nanoscale Science & Engineering) according to established methods.<sup>24-25</sup>

**Gold Nanoparticle Functionalization.** Citrate stabilized gold nanoparticles were fabricated by standard citrate reduction and stored in amber bottles at room temperature. Regarding sample handling for all functionalization and cleanup procedures, smaller

nanoparticles were separated via centrifugation at 14,000 rpm, and larger nanoparticles at 8,000 rpm. Biotin functionalization via 16-MHDA monolayer coupling to produce biotin/MHDA/AuNPs was performed according the procedure outlined by Aslan et al.,<sup>26</sup> and is detailed in Appendix C. Functionalization of AuNPs with thiolated oligonucleotides followed the methods of Hurst and Zhang.<sup>18-19</sup> In brief, 2.5 nmol of thiolated DNA (100  $\mu$ M, H<sub>2</sub>O) was added to 1 mL of as-prepared 13 nm AuNPs (*ca.* 11 nM). For larger AuNPs (*ca.* 0.5 nM), 10 nmol of DNA was added.<sup>20</sup> Immediately, 20  $\mu$ L citrate-HCl (500 mM, pH 3.0) was mixed into the solution, which was thoroughly stirred, sonicated for 20 s, and allowed to rest for 20 min. Thereafter, the ionic strength was adjusted to 1 M NaCl in one step to ensure maximum surface coverage of DNA, and again, stirred and sonicated for 20 s. After incubating at 4 °C overnight, the functionalized AuNPs were cleaned up from excess salts and oligonucleotides through centrifugal filtration (Amicon, MWCO 50 kDa).

Amide coupling of proteins to the **cT<sub>20</sub>**/AuNP surfaces was facilitated through carbodiimide crosslinking. The **cT<sub>20</sub>**/AuNPs were suspended in 1 mL of a 50 mM NHS/200 mM EDC mixture in MES for 20 min, after which, the nanoparticles were centrifuged, resuspended in 1.5 mL of PBT, and centrifuged again. The supernatant was discarded, and 50  $\mu$ g protein (*i.e.* HRP or Protein A) was added directly to the pellet and incubated for 2 h at room temperature. Thereafter, the AuNPs were cleaned up from excess protein through centrifugal filtration (Amicon, MWCO 50 or 100 kDa). For the attachment of anti-CT to the Protein A/**cT<sub>20</sub>**/AuNP surface, the Protein A-conjugated **cT<sub>20</sub>**/AuNPs were centrifuged down, and 50  $\mu$ g anti-CT was added to directly to the

pellet, which was incubated for 4 h at room temperature. Excess antibody was removed from the mixture through multiple cycles ( $n \geq 3$ ) of centrifugation/resuspension of the AuNPs in PBT or 1×PBS.

## ■ RESULTS AND DISCUSSION

Traditionally, alkane- or PEG-thiols are used in the preparation of gold nanoparticle bioconjugates. These ligands carry the advantages of commercial availability from a large number of sources, and their end terminals can be specifically tailored by the supplier for further desired chemical attachment schemes. Their attachment to gold or silver nanoparticles is met with relative ease, as these compounds exhibit a high packing density upon self-assembly onto gold and silver surfaces. Thiolated DNA, on the other hand, natively exhibits a much lower packing density on these surfaces, owing to high electrostatic repulsion of the phosphate backbone between adjacent strands.<sup>17</sup> However, recent innovations in fabrication have rendered the quantitative attachment of DNA to nanoparticles fast and convenient.<sup>18-19</sup> Here, we utilize a pH-assisted approach coupled with high salt incubation and sonication to ensure maximal loading of thiolated DNA onto the AuNP surfaces (Figure 4.1). Given that multiple strands can be attached at user designated ratios in this manner,<sup>19</sup> we have decided to exploit this feature toward their use as both a chemical linker and diluent (dependent on their end terminal groups), analogous to how alkane- and PEG-thiols have been used.

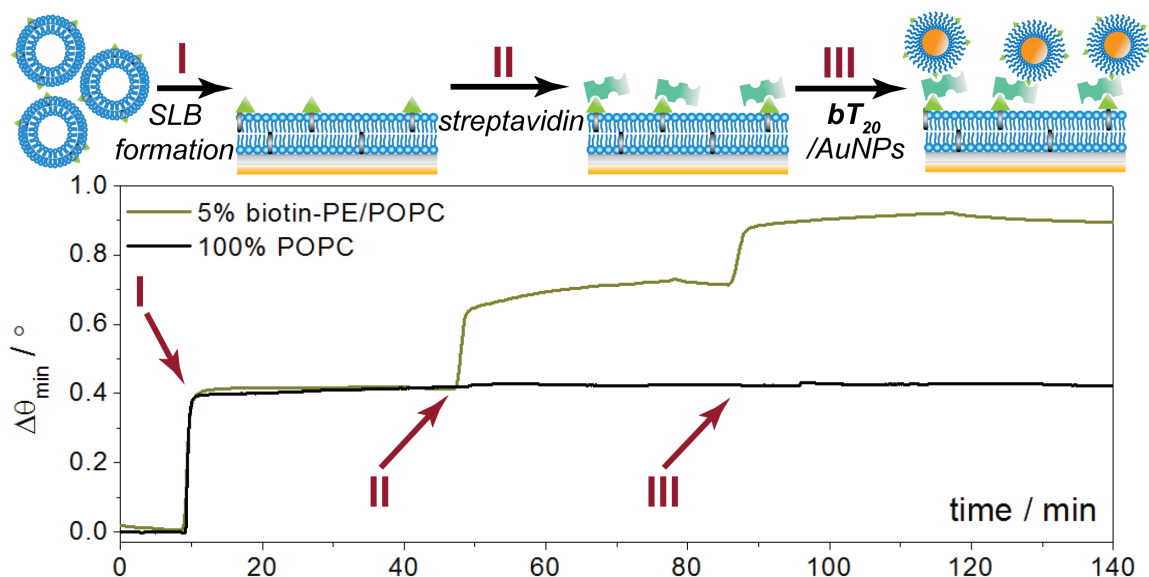


**Figure 4.2.** Surface plasmon resonance sensorgram depicting formation of a biotinylated supported lipid bilayer, followed by streptavidin and AuNP recognition. A 100% POPC bilayer is formed in the reference channel and exposed to streptavidin and AuNPs for control purposes.

Our initial studies targeted the incorporation of a biotin-terminus on the DNA linkers (**bT**<sub>20</sub>) with a 1:1 ratio of **T**<sub>20</sub> diluent strands, allowing for a universal nanoparticle probe in multiplexed analysis.<sup>27</sup> Previous work has demonstrated that biotin may be attached to silver nanoparticles through a short DNA linker;<sup>28</sup> here we utilize a 20-nucleotide polythymine linker for maximum colloidal stability,<sup>21-22</sup> and attach biotin in conjunction with a diluent strand for improved binding sterics, as previously exemplified.<sup>26</sup> The capacity of this nanoparticle conjugate to specifically bind its intended target, streptavidin, is demonstrated through the surface plasmon resonance (SPR) results in Figure 4.2. A supported lipid bilayer (SLB) platform was chosen for this analysis due to its ability to incorporate specific recognition elements while minimizing nonspecific binding.<sup>29</sup> Phosphocholine (POPC) SUVs incorporating 5% (n/n) biotin-PE were flowed over nanoglassified gold sensor chips to form a biotinylated SLB in the analytical

channel, while 100% POPC bilayers were formed in the reference channel (**I** in Figure 4.2). Thereafter, streptavidin ( $250\ \mu\text{g mL}^{-1}$ ) was added to both channels (**II** in Figure 4.2), followed by the **bT**<sub>20</sub>/AuNPs (5 nM, **III** in Figure 4.2). Each injection and incubation was followed by a 10 min rinse with 1×PBS to remove any unbound molecules. The streptavidin and **bT**<sub>20</sub>/AuNPs bind specifically to the biotinylated membrane, whereas the signal changes from either of these complexes binding to the 100% POPC membrane are negligible, thus confirming that the **bT**<sub>20</sub> attachment chemistry was successful and rendered the AuNP recognition specific toward streptavidin. This specificity is not only applicable to streptavidin over the POPC lipids, but also over other proteins, as demonstrated in a toxin assay in which the **bT**<sub>20</sub>/AuNPs would not bind to the cholera toxin protein until a streptavidin linker was introduced (Figure C.1). The results match those obtained from biotin/MHDA/AuNPs fabricated through traditional alkanethiol SAM attachment,<sup>26</sup> for which the binding patterns to streptavidin were comparable (Figure C.2).

***Stability Against High Salt Concentrations.*** The significant advantage of utilizing DNA linkers and diluents in place of conventional monolayers is the enhanced colloidal stability they append to gold nanoparticles. We used a modified protocol of previously established methods to compare the colorimetric shift, indicative of aggregation, of bare nanoparticles (with adsorbed citrate), biotin/MHDA/AuNPs, and **bT**<sub>20</sub>/AuNPs when exposed to increasing concentrations of NaCl.<sup>9, 12, 21-22</sup> For each solution, the AuNP concentration was set to 1.5 nM, and designated concentrations of NaCl were added immediately before monitoring the absorbance at 620 nm over the

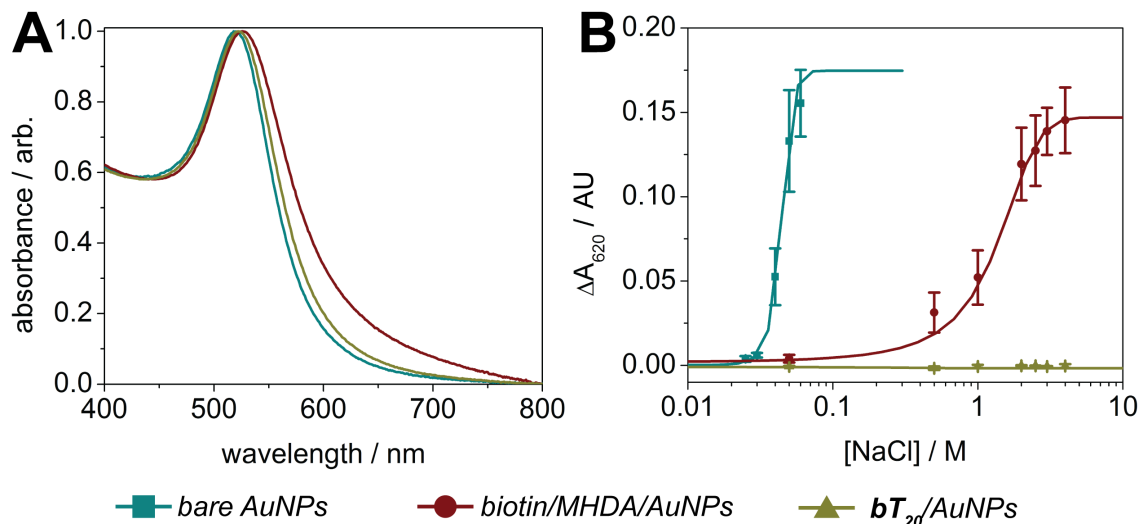


**Figure 4.3.** Ionic strength stability assays. (A) Absorbance spectra of AuNPs with various surface functionalizations in nanopure water. (B) Aggregation induced changes in nanoparticle absorbance at 620 nm resulting from varying ionic strength ( $\pm$  SEM,  $n = 5$ ).

course of 5 min (see Appendix C for assay details, also Figure C.3). The absorbance spectra for each of these nanoparticles in nanopure water are shown in Figure 4.3A, while their aggregation-induced changes in absorbance at 620 nm ( $\Delta A_{620}$ ) are shown in Figure 4.3B. There is a minor increase in the full width at half maximum (FWHM) for the absorbance peak of the biotin/MHDA/AuNPs in nanopure water compared to the other nanoparticles (Figure 4.3A), which is likely due to inhomogeneity from the MHDA coupling procedure. As expected, bare nanoparticles exhibited the lowest tolerance to NaCl, with a critical ionic strength parameter ( $\mu_c$ ), defined as the midpoint between the minimum and maximum  $\Delta A_{620}$ ,<sup>21</sup> of *ca.* 35 mM NaCl. The biotin/MHDA/AuNPs fared significantly better than the bare AuNPs ( $\mu_c \sim 1.5$  M NaCl), though the  $bT_{20}$ /AuNPs performed best, exhibiting no observable aggregation even when suspended in 4 M NaCl (Figure 4.3B).

The highly enhanced stability of the **bT<sub>20</sub>**/AuNPs is likely due to the high density of negative charge along the DNA phosphate backbone, in line with the high electronegativity of thymine compared to other nucleobases,<sup>30</sup> and increased steric repulsion when comparing **T<sub>20</sub>** and hexadecanethiol (lengths measure approximately 6.8 nm and 2 nm, respectively).<sup>31</sup> The correlation between surface charge and colloidal stability is further evidenced in the measured  $\zeta$ -potentials of these nanoparticles, with the **T<sub>20</sub>**/AuNPs exhibiting the most negative value (−53 mV) of the conjugated nanoparticles investigated (Table C.1). To further understand how the **bT<sub>20</sub>**/AuNPs would tolerate a range of electrolytes over longer periods of time, these nanoparticles were separately incubated for 1 h with representative cations from the Hofmeister series (each 4 M, with Cl<sup>−</sup> as counterion), ranked for their ability to salt out proteins from aqueous solutions.<sup>32</sup> The monovalent cations studied appeared to follow standard Hofmeister trends, with the kosmotropes (*i.e.* Na<sup>+</sup> and NH<sub>4</sub><sup>+</sup>) causing no change in **bT<sub>20</sub>**/AuNP absorbance over 1 h, and the representative chaotrope, guanidinium, resulting in a slight change in  $\Delta A_{620}$  of ~0.025 AU (Figure C.4). The divalent cation, Mg<sup>2+</sup>, exhibited a larger  $\Delta A_{620}$  (~0.05 AU), indicating moderate aggregation of the **bT<sub>20</sub>**/AuNPs. This is in fact expected as Mg<sup>2+</sup> is an effective chelator of the phosphate backbone, and the aggregation effect has been reported in other studies of DNA/AuNPs within extreme levels of Mg<sup>2+</sup>.<sup>21</sup> Pooled human serum and waste water samples sourced from the Los Angeles River, representing clinical and environmental matrices, were also investigated for their impact on stability and aggregation of the **bT<sub>20</sub>**/AuNPs, though neither caused any significant change in the AuNP absorbance over 1 h (Figure C.4). Altogether, these data indicate that a remarkably

stable and biofunctionalized nanoparticle conjugate can be formed after quantitative attachment of selective DNA strands to the AuNP surface, which in turn can be utilized within a wide variety of matrices and environments.

***Lyophilization Endurance.*** Freeze-drying of biological materials has been established as an ideal method to preserve structure and activity during long-term storage and transport. While lyophilization of native proteins may be met with some batch variability,<sup>33</sup> the technique has overall proved robust enough for clinical and point-of-care applications where stable storage conditions are not guaranteed. Unfortunately, it is significantly challenging to preserve nanoparticles through lyophilization as they exhibit a strong tendency to irreversibly aggregate and precipitate during freezing.<sup>34</sup> While the use of cryoprotective matrices (*e.g.* sucrose, trehalose) has been presented as one method to preserve the colloidal stability of nanoparticles throughout the process,<sup>13, 35</sup> direct protection by the nanoparticle's capping ligand is more desirable as it lends to simplified assay constituents, and has been explored with varied degrees of success.<sup>9, 12, 14, 35</sup> As the cryoprotectant capacity of conjugated DNA has not been investigated for metal nanoparticles, the **bT<sub>20</sub>/AuNPs** and **HRP/cT<sub>20</sub>/AuNPs** fabricated here were chosen to study for their ability to be resuspended and utilized post-lyophilization.

As expected, bare gold nanoparticles (5 nM) could not be effectively reconstituted in a monodisperse manner, exhibiting a massive decrease in absorbance and a colorimetric shift from red to pale blue after lyophilization overnight and resuspension in nanopure water (Figure 4.4A). The **bT<sub>20</sub>/AuNPs** (5 nM), on the other hand, were capable of being lyophilized and resuspended multiple times with minimal or no change in their

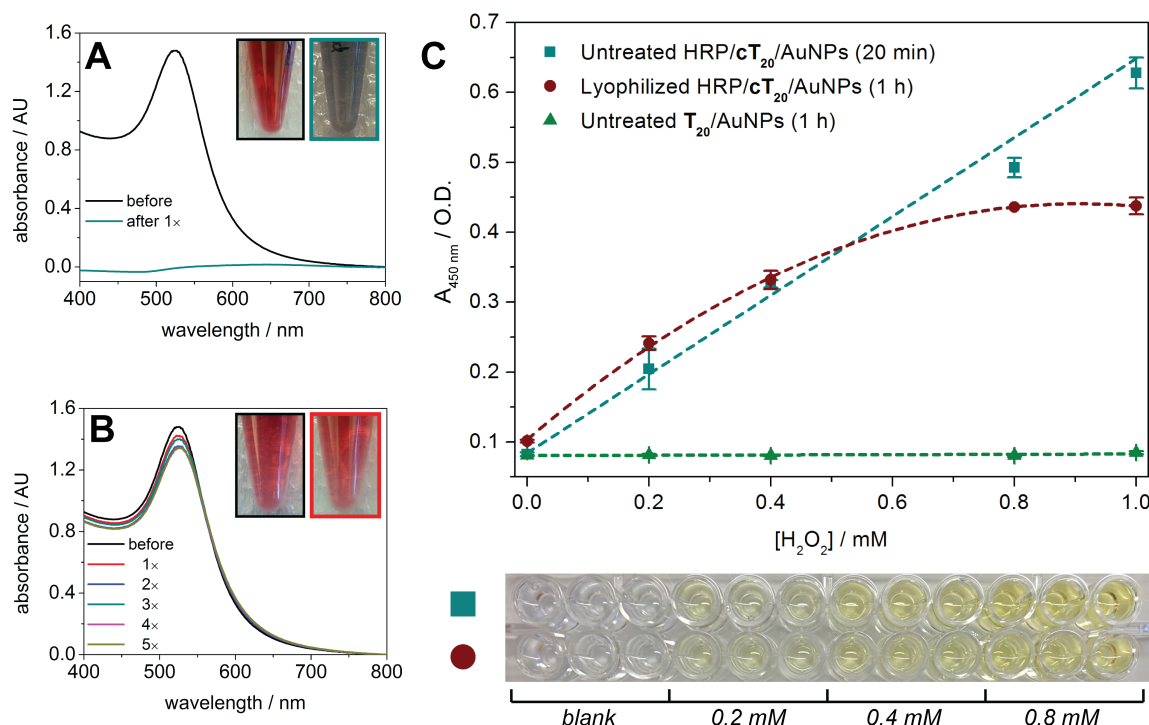


**Figure 4.4.** Lyophilization of DNA/AuNPs. (A) Absorbance spectra of bare AuNPs (citrate-capped) before and after lyophilization. (B) Absorbance spectra of **bT**<sub>20</sub>/AuNPs before and after five lyophilization cycles. (C) Hydrogen peroxide assay utilizing TMB and HRP/cT<sub>20</sub>/AuNPs ( $\pm$  SEM,  $n = 3$ ).

absorbance (Figure 4.4B). Moreover, their streptavidin binding capability was left intact post-lyophilization, resulting in specific SPR angular shifts that match those of the non-lyophilized **bT**<sub>20</sub>/AuNPs (Figure C.5). This was not only possible for the smaller nanoparticles ( $d_a \sim 13$  nm), but also could be accomplished for larger nanoparticles ( $d_a \sim 30$  nm), which are inherently less stable in solution (Figure C.6).

Gupta et al. recently demonstrated that the avidin protein could be covalently attached to a custom-synthesized zwitterionic PEG linker on the AuNP surface, which in turn could be lyophilized and functionally resuspended.<sup>9</sup> However, retention of enzymatic activity on a nanoparticle surface after lyophilization has yet to be explored. We chose to investigate the conjugation of horseradish peroxidase (HRP), an enzyme that has

previously been attached to AuNPs and utilized for ELISA, increasing target sensitivities by multiple orders of magnitude compared to free HRP.<sup>36-39</sup> Toward this end, HRP/cT<sub>20</sub>/AuNPs were fabricated and applied to an enzyme-linked colorimetric microplate assay (see Appendix C for protocol). The HRP/cT<sub>20</sub>/AuNPs (~333 pM, d<sub>a</sub> ~13 nm) exhibited a hydrogen peroxide concentration-dependent response in their ability to generate the oxidized form of TMB (Figure 4.4C), consistent with results obtained for free HRP (Figure C.7). While the nanoparticles remained stable in solution post-lyophilization (Figure C.8), the enzymatic activity of conjugated HRP was slightly compromised, with the turnover of TMB taking a 3-fold greater length of time, and the maximum signal plateauing at a lower substrate concentration (Figure 4.4C). Interestingly, when free HRP was lyophilized, its activity was affected to a far greater extent than the AuNP-conjugated HRP, generating almost no colorimetric signal over the greater length of time, even for the highest concentrations (0.8 – 1 mM) of hydrogen peroxide tested (Figure C.7). To confirm whether nanozyme activity (*i.e.* the inherent property of metal nanoparticles to exhibit peroxidase-mimicking characteristics) could explain the post-lyophilization activity of the HRP/cT<sub>20</sub>/AuNPs,<sup>40-41</sup> untreated T<sub>20</sub>/AuNPs were tested. No signal was generated for any substrate concentration (Figure 4.4C), thus excluding any nanozyme contribution from the observation. This is likely due to inaccessibility of TMB or hydrogen peroxide to the metal surface, as the HRP/cT<sub>20</sub>/AuNPs and T<sub>20</sub>/AuNPs were fully coated with DNA from the attachment procedure used.

The results suggest that while AuNP-conjugated proteins are still subject to some degree of secondary structural changes that may lead to altered activity after freeze-drying,<sup>42-43</sup> some level of protection resulting from the surface conjugation is imparted. The presence of covalently attached HRP or biotin does not appear to negatively affect the stability of the nanoparticles themselves, as evidenced from their ability to be lyophilized and resuspended with no colorimetric shift, providing a unique system to study the biological stability effects of ligand attachment. Beyond this proof-of-concept study indicating that **bT<sub>20</sub>/AuNPs** and **HRP/cT<sub>20</sub>/AuNPs** may be lyophilized and used thereafter, we believe the DNA conjugated particles reported here could potentially find broad applications in enzymatic assays where long term storage of nanoparticle/enzyme conjugates is critical.

***Enhanced SPR Imaging Analysis with Multistep Conjugation Products.*** Control of protein orientation during surface attachment has attracted great attention for nanoparticle bioconjugates. Most attachment schemes may result in undesired or highly variable orientations, as covalent couplings are dependent upon accessible functional groups on protein surface (*e.g.* free primary amines, carboxyls, thiols), and electrostatic adsorption depends on the localized areas of charge on the surface. In a worst-case scenario for antibodies, these complexes may be bound through the Fab region, blocking the antigen recognition site and rendering the nanoparticle nonselective toward the intended target. Various solutions for controlling the orientation have included altering the surface density of protein,<sup>44</sup> reversing the surface charge of the nanoparticle,<sup>45</sup> and attachment of antibodies through Protein G,<sup>46</sup> which binds to the Fc region of antibodies.

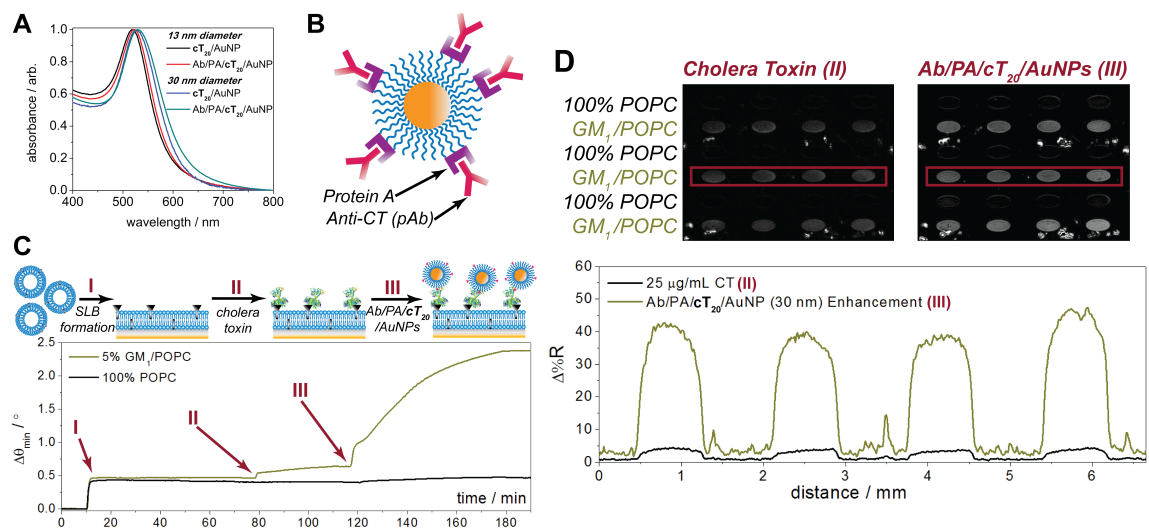


**Figure 4.5.** Multistep conjugation of  $cT_{20}$ /AuNPs with Protein A and anti-cholera toxin. (A) Absorbance spectra of 13 nm and 30 nm  $cT_{20}$ /AuNPs before and after Protein A and antibody conjugation. (B) Cartoon illustration of final anti-CT/PA/ $cT_{20}$ /AuNP bioconjugate. (C) Surface plasmon resonance sensorgram depicting formation of a ganglioside-impregnated supported lipid bilayer, followed by cholera toxin and AuNP recognition, with a 100% POPC bilayer in the reference channel. (D) SPR imaging results of cholera toxin and AuNP recognition across a lipid membrane array.

In the study in which Protein G was used, the protein had to be engineered to express a cysteine residue at the n-terminus, which was attached to an aminated DNA linker offline and bound to the gold surface through complementary DNA base pairing. Due to the high stability of the  $cT_{20}$ /AuNPs, we were able to directly attach unmodified Protein A (PA), which also specifically targets antibody Fc regions, to the DNA/AuNP interface, and subsequently bind an antibody of choice. Both 13 nm and 30 nm  $cT_{20}$ /AuNPs remained stable through multiple rounds of derivatization and cleanup, as exhibited through the absorbance spectra in Figure 4.5. Indicative of surface attachment and consistent with the LSPR mechanism, the absorbance peaks also shifted toward higher wavelengths as Protein A and anti-cholera toxin (anti-CT) were immobilized to the  $cT_{20}$ /AuNPs.

We tested the use of anti-CT/PA/ $cT_{20}$ /AuNP toward the nanoparticle-enhanced detection of cholera toxin by SPR (Figure 4.5C) and SPR imaging (Figure 4.5D) in a

standard sandwich assay format. Similar to the **bT<sub>20</sub>**/AuNP SPR binding assays, a supported lipid bilayer was used to host a membrane-bound ganglioside receptor, GM<sub>1</sub>, which is specific to cholera toxin. Following the formation of a POPC bilayer containing 5% (n/n) GM<sub>1</sub> in the analytical channel, and 100% POPC in the reference channel (**I** in Figure 4.5C), 20  $\mu\text{g mL}^{-1}$  of cholera toxin was incubated for 30 min on both membrane surfaces (**II** in Figure 4.5C). After a 10 min rinse with 1×PBS, 2 nM of anti-CT/PA/**cT<sub>20</sub>**/AuNPs ( $d_a \sim 30$  nm) were introduced to both channels (**III** in Figure 4.5C), which were incubated for 1 h before a final rinse with 1×PBS. The enhancement seen here is strong and specific for the GM<sub>1</sub> impregnated membranes, with no binding of cholera toxin or the anti-CT/PA/**cT<sub>20</sub>**/AuNPs exhibited in the reference channel. This high level of signal amplification for cholera toxin is in line with those reported previously from our group,<sup>47-48</sup> though here could be achieved in far fewer assay steps due to the majority of the constituents (*i.e.* antibodies and linkers) being pre-conjugated to the AuNP surface. Furthermore, the use of these nanoparticles was scalable toward their specific enhancement in a microarray format. For SPR imaging analysis, the difference images of a 4 × 6 SLB array are presented in Figure 4.5D. The individual array elements were formed through trehalose-assisted vesicle deposition, with alternating rows of 5% (n/n) GM<sub>1</sub>/POPC SUVs and 100% POPC SUVs protected from intermixing and the effects of desiccation through a sacrificial, anhydrobiotic trehalose matrix.<sup>25, 49</sup> Upon rehydration, the array was rinsed under a 1×PBS flow for 30 min to remove the trehalose and form spatially defined SLBs, prior to conducting the same SPR sandwich assay for cholera toxin as described above. The difference images, obtained by digitally subtracting

a pre-binding image from a post-binding image, show similar patterns to the SPR sensorgrams in Figure 4.5C, with a significant increase in contrast between the 5% (n/n) GM<sub>1</sub>/POPC and 100% POPC array elements after the anti-CT/PA/cT<sub>20</sub>/AuNPs were introduced (corresponding line profiles shown in the lower panel of Figure 4.5D). The nanoparticle enhanced signals for the GM<sub>1</sub>/POPC array elements exhibited >10-fold amplification, consistent with previous CT signal amplification work from our group,<sup>48</sup> with values of  $3.8 \pm 0.5 \Delta\%R$  prior to nanoparticle enhancement, and  $41.8 \pm 6.4 \Delta\%R$  after nanoparticle enhancement. By combining this level of amplification with trehalose-mediated vesicle preservation, the large-scale analysis and signal enhancement across an entire array of varied constituents can take place in  $\sim 2$  h. Moreover, the specificity exhibited in this nanoparticle-enhanced microarray platform may be generally applied beyond the cholera toxin/GM<sub>1</sub> system, as Protein A conjugated to the cT<sub>20</sub>/AuNPs can bind most antibodies of choice for tailored, high-throughput, and ultrasensitive assay development.

## ■ CONCLUSIONS

In summary, we have shown that 20-nucleotide polythymine DNA sequences function effectively as a linker and diluent for preparing gold nanoparticle bioconjugates for analytical applications. The stability they append toward high ionic strengths and complex media is exceptional, exhibiting no traceable aggregation of nanoparticles in a number of testing media including 4 M NaCl, 4 M NH<sub>4</sub>Cl, Los Angeles River water, and human serum. Only slight change in absorbance in 4M guanidinium chloride and 4M

MgCl<sub>2</sub> was noted, suggesting the DNA/AuNP suspensions are generally stable in these harsh conditions and only mild aggregation had occurred. Lyophilization and resuspension of the DNA/AuNPs was possible, with retention of activity for horseradish peroxidase, offering a method of preservation that is not accessible for most nanoparticle conjugates. While there seems to be a protective effect provided by the nanoparticles to the conjugated enzyme during lyophilization, further studies need to be undertaken to understand this mechanism and its amenability to other proteins. Nevertheless, both this observation and the line of study are only made possible as a result of the high stability offered by the unique interface we have developed. Additionally, the **cT<sub>20</sub>**/AuNPs proved successful for microplate and microarray assays, two standard techniques for high-throughput detection and characterization, demonstrating the versatility and selectivity of this material. We envision wide adoption of this interface toward stable and specific nanoparticle bioconjugates throughout multiplexed assay development for clinical, environmental, and point-of-care settings, given the unparalleled sensitivity offered by nanoparticle enhancement, and the convenience of these commercially available and accessible DNA ligands.

## ■ REFERENCES

- (1) Zhou, W.; Gao, X.; Liu, D. B.; Chen, X. Y. Gold Nanoparticles for in Vitro Diagnostics. *Chem. Rev.* **2015**, *115*, 10575-10636.
- (2) Kumar, A.; Kim, S.; Nam, J. M. Plasmonically Engineered Nanoprobes for Biomedical Applications. *J. Am. Chem. Soc.* **2016**, *138*, 14509-14525.
- (3) Li, T.; Wu, X.; Liu, F.; Li, N. Analytical Methods Based on the Light-Scattering of Plasmonic Nanoparticles at the Single Particle Level with Dark-Field Microscopy Imaging. *Analyst* **2016**, *142*, 248-256.
- (4) Syedmoradi, L.; Daneshpour, M.; Alvandipour, M.; Gomez, F. A.; Hajghassem, H.; Omidfar, K. Point of Care Testing: The Impact of Nanotechnology. *Biosens. Bioelectron.* **2017**, *87*, 373-387.
- (5) Zhou, J. F.; Ralston, J.; Sedev, R.; Beattie, D. A. Functionalized Gold Nanoparticles: Synthesis, Structure and Colloid Stability. *J. Colloid Interface Sci.* **2009**, *331*, 251-262.
- (6) Balasubramanian, S. K.; Yang, L. M.; Yung, L. Y. L.; Ong, C. N.; Ong, W. Y.; Yu, L. E. Characterization, Purification, and Stability of Gold Nanoparticles. *Biomaterials* **2010**, *31*, 9023-9030.
- (7) Zeng, S. W.; Yong, K. T.; Roy, I.; Dinh, X. Q.; Yu, X.; Luan, F. A Review on Functionalized Gold Nanoparticles for Biosensing Applications. *Plasmonics* **2011**, *6*, 491-506.
- (8) Gao, J.; Huang, X. Y.; Liu, H.; Zan, F.; Ren, J. C. Colloidal Stability of Gold Nanoparticles Modified with Thiol Compounds: Bioconjugation and Application in Cancer Cell Imaging. *Langmuir* **2012**, *28*, 4464-4471.
- (9) Gupta, A.; Moyano, D. F.; Parnsubsakul, A.; Papadopoulos, A.; Wang, L. S.; Landis, R. F.; Das, R.; Rotello, V. M. Ultrastable and Biofunctionalizable Gold Nanoparticles. *ACS Appl. Mater. Interfaces* **2016**, *8*, 14096-14101.

- (10) Shang, L.; Wang, Y. Z.; Jiang, J. G.; Dong, S. J. Ph-Dependent Protein Conformational Changes in Albumin : Gold Nanoparticle Bioconjugates: A Spectroscopic Study. *Langmuir* **2007**, *23*, 2714-2721.
- (11) Canaveras, F.; Madueno, R.; Sevilla, J. M.; Blazquez, M.; Pineda, T. Role of the Functionalization of the Gold Nanoparticle Surface on the Formation of Bioconjugates with Human Serum Albumin. *J. Phys. Chem. C* **2012**, *116*, 10430-10437.
- (12) Levy, R.; Thanh, N. T. K.; Doty, R. C.; Hussain, I.; Nichols, R. J.; Schiffrin, D. J.; Brust, M.; Fernig, D. G. Rational and Combinatorial Design of Peptide Capping Ligands for Gold Nanoparticles. *J. Am. Chem. Soc.* **2004**, *126*, 10076-10084.
- (13) Zhang, L.; Li, P.; Li, D.; Guo, S.; Wang, E. Effect of Freeze-Thawing on Lipid Bilayer-Protected Gold Nanoparticles. *Langmuir* **2008**, *24*, 3407-3411.
- (14) Mangeney, C.; Ferrage, F.; Aujard, I.; Marchi-Artzner, V.; Jullien, L.; Ouari, O.; Rekaï, E. D.; Laschewsky, A.; Vikholm, I.; Sadowski, J. W. Synthesis and Properties of Water-Soluble Gold Colloids Covalently Derivatized with Neutral Polymer Monolayers. *J. Am. Chem. Soc.* **2002**, *124*, 5811-5821.
- (15) Rouhana, L. L.; Jaber, J. A.; Schlenoff, J. B. Aggregation-Resistant Water-Soluble Gold Nanoparticles. *Langmuir* **2007**, *23*, 12799-12801.
- (16) Yang, W.; Zhang, L.; Wang, S. L.; White, A. D.; Jiang, S. Y. Functionalizable and Ultra Stable Nanoparticles Coated with Zwitterionic Poly(Carboxybetaine) in Undiluted Blood Serum. *Biomaterials* **2009**, *30*, 5617-5621.
- (17) Mirkin, C. A.; Letsinger, R. L.; Mucic, R. C.; Storhoff, J. J. A DNA-Based Method for Rationally Assembling Nanoparticles into Macroscopic Materials. *Nature* **1996**, *382*, 607-609.
- (18) Hurst, S. J.; Lytton-Jean, A. K. R.; Mirkin, C. A. Maximizing DNA Loading on a Range of Gold Nanoparticle Sizes. *Anal. Chem.* **2006**, *78*, 8313-8318.

- (19) Zhang, X.; Servos, M. R.; Liu, J. W. Instantaneous and Quantitative Functionalization of Gold Nanoparticles with Thiolated DNA Using a Ph-Assisted and Surfactant-Free Route. *J. Am. Chem. Soc.* **2012**, *134*, 7266-7269.
- (20) Zhang, X.; Gouriye, T.; Goeken, K.; Servos, M. R.; Gill, R.; Liu, J. W. Toward Fast and Quantitative Modification of Large Gold Nanoparticles by Thiolated DNA: Scaling of Nanoscale Forces, Kinetics, and the Need for Thiol Reduction. *J. Phys. Chem. C* **2013**, *117*, 15677-15684.
- (21) Storhoff, J. J.; Elghanian, R.; Mirkin, C. A.; Letsinger, R. L. Sequence-Dependent Stability of DNA-Modified Gold Nanoparticles. *Langmuir* **2002**, *18*, 6666-6670.
- (22) Heo, J. H.; Cho, H. H.; Lee, J. H. Surfactant-Free Nanoparticle DNA Complexes with Ultrahigh Stability against Salt for Environmental and Biological Sensing. *Analyst* **2014**, *139*, 5936-5944.
- (23) Wilkop, T.; Wang, Z. Z.; Cheng, Q. Analysis of Mu-Contact Printed Protein Patterns by SPR Imaging with a LED Light Source. *Langmuir* **2004**, *20*, 11141-11148.
- (24) Abbas, A.; Linman, M. J.; Cheng, Q. Patterned Resonance Plasmonic Microarrays for High-Performance SPR Imaging. *Anal. Chem.* **2011**, *83*, 3147-3152.
- (25) Hinman, S. S.; Ruiz, C. J.; Drakakaki, G.; Wilkop, T. E.; Cheng, Q. On-Demand Formation of Supported Lipid Membrane Arrays by Trehalose-Assisted Vesicle Delivery for SPR Imaging. *ACS Appl. Mater. Interfaces* **2015**, *7*, 17122-17130.
- (26) Aslan, K.; Luhrs, C. C.; Perez-Luna, V. H. Controlled and Reversible Aggregation of Biotinylated Gold Nanoparticles with Streptavidin. *J. Phys. Chem. B* **2004**, *108*, 15631-15639.
- (27) Scott, A. W.; Garimella, V.; Calabrese, C. M.; Mirkin, C. A. Universal Biotin-Peg-Linked Gold Nanoparticle Probes for the Simultaneous Detection of Nucleic Acids and Proteins. *Bioconjugate Chem.* **2017**, *28*, 203-211.

- (28) Cunningham, J. C.; Kogan, M. R.; Tsai, Y. J.; Luo, L.; Richards, I.; Crooks, R. M. Paper-Based Sensor for Electrochemical Detection of Silver Nanoparticle Labels by Galvanic Exchange. *ACS Sensors* **2016**, *1*, 40-47.
- (29) Phillips, K. S.; Han, J. H.; Martinez, M.; Wang, Z. Z.; Carter, D.; Cheng, Q. Nanoscale Glassification of Gold Substrates for Surface Plasmon Resonance Analysis of Protein Toxins with Supported Lipid Membranes. *Anal. Chem.* **2006**, *78*, 596-603.
- (30) Zhang, Q.; Chen, E. C. M. The Experimental Hardness and Electronegativity of the Purines and Pyrimidines in DNA and RNA Supported by the Am1 Calculation of the Electron Affinities and Ionization Potentials. *Biochem. Biophys. Res. Commun.* **1995**, *217*, 755-760.
- (31) Malinsky, M. D.; Kelly, K. L.; Schatz, G. C.; Van Duyne, R. P. Chain Length Dependence and Sensing Capabilities of the Localized Surface Plasmon Resonance of Silver Nanoparticles Chemically Modified with Alkanethiol Self-Assembled Monolayers. *J. Am. Chem. Soc.* **2001**, *123*, 1471-1482.
- (32) Xie, W. J.; Gao, Y. Q. A Simple Theory for the Hofmeister Series. *J. Phys. Chem. Lett.* **2013**, *4*, 4247-4252.
- (33) Wahl, V.; Khinast, J.; Paudel, A. Lyophilized Protein Powders: A Review of Analytical Tools for Root Cause Analysis of Lot-to-Lot Variability. *TrAC, Trends Anal. Chem.* **2016**, *82*, 468-491.
- (34) Abdelwahed, W.; Degobert, G.; Stainmesse, S.; Fessi, H. Freeze-Drying of Nanoparticles: Formulation, Process and Storage Considerations. *Adv. Drug Delivery Rev.* **2006**, *58*, 1688-1713.
- (35) Alkilany, A. M.; Abulateefeh, S. R.; Mills, K. K.; Yaseen, A. I. B.; Hamaly, M. A.; Alkhatib, H. S.; Aiedeh, K. M.; Stone, J. W. Colloidal Stability of Citrate and Mercaptoacetic Acid Capped Gold Nanoparticles Upon Lyophilization: Effect of Capping Ligand Attachment and Type of Cryoprotectants. *Langmuir* **2014**, *30*, 13799-13808.
- (36) Ambrosi, A.; Airo, F.; Merkoci, A. Enhanced Gold Nanoparticle Based ELISA for a Breast Cancer Biomarker. *Anal. Chem.* **2010**, *82*, 1151-1156.

- (37) Zhou, Y.; Tian, X. L.; Li, Y. S.; Pan, F. G.; Zhang, Y. Y.; Zhang, J. H.; Yang, L.; Wang, X. R.; Ren, H. L.; Lu, S. Y.; Li, Z. H.; Chen, Q. J.; Liu, Z. S.; Liu, J. Q. An Enhanced ELISA Based on Modified Colloidal Gold Nanoparticles for the Detection of Pb(II). *Biosens. Bioelectron.* **2011**, *26*, 3700-3704.
- (38) Zhan, L.; Wu, W. B.; Yang, X. X.; Huang, C. Z. Gold Nanoparticle-Based Enhanced ELISA for Respiratory Syncytial Virus. *New J. Chem.* **2014**, *38*, 2935-2940.
- (39) Guo, Q.; Han, J. J.; Shan, S.; Liu, D. F.; Wu, S. S.; Xiong, Y. H.; Lai, W. H. DNA-Based Hybridization Chain Reaction and Biotin-Streptavidin Signal Amplification for Sensitive Detection of Escherichia Coli O157:H7 through ELISA. *Biosens. Bioelectron.* **2016**, *86*, 990-995.
- (40) McKeating, K. S.; Sloan-Dennison, S.; Graham, D.; Faulds, K. An Investigation into the Simultaneous Enzymatic and Serrs Properties of Silver Nanoparticles. *Analyst* **2013**, *138*, 6347-6353.
- (41) Wang, X. Y.; Hu, Y. H.; Wei, H. Nanozymes in Bionanotechnology: From Sensing to Therapeutics and Beyond. *Inorg. Chem. Front.* **2016**, *3*, 41-60.
- (42) Griebenow, K.; Klibanov, A. M. Lyophilization-Induced Reversible Changes in the Secondary Structure of Proteins. *Proc. Natl. Acad. Sci. U. S. A.* **1995**, *92*, 10969-10976.
- (43) Roy, I.; Gupta, M. N. Freeze-Drying of Proteins: Some Emerging Concerns. *Biotechnol. Appl. Biochem.* **2004**, *39*, 165-177.
- (44) Liu, F.; Wang, L.; Wang, H. W.; Yuan, L.; Li, J. W.; Brash, J. L.; Chen, H. Modulating the Activity of Protein Conjugated to Gold Nanoparticles by Site-Directed Orientation and Surface Density of Bound Protein. *ACS Appl. Mater. Interfaces* **2015**, *7*, 3717-3724.
- (45) Lin, W.; Insley, T.; Tuttle, M. D.; Zhu, L. Y.; Berthold, D. A.; Kral, P.; Rienstra, C. M.; Murphy, C. J. Control of Protein Orientation on Gold Nanoparticles. *J. Phys. Chem. C* **2015**, *119*, 21035-21043.

- (46) Jung, Y.; Lee, J. M.; Jung, H.; Chung, B. H. Self-Directed and Self-Oriented Immobilization of Antibody by Protein G-DNA Conjugate. *Anal. Chem.* **2007**, *79*, 6534-6541.
- (47) Liu, Y.; Dong, Y.; Jauw, J.; Linman, M. J.; Cheng, Q. Highly Sensitive Detection of Protein Toxins by Surface Plasmon Resonance with Biotinylation-Based Inline Atom Transfer Radical Polymerization Amplification. *Anal. Chem.* **2010**, *82*, 3679-3685.
- (48) Liu, Y.; Cheng, Q. Detection of Membrane-Binding Proteins by Surface Plasmon Resonance with an All-Aqueous Amplification Scheme. *Anal. Chem.* **2012**, *84*, 3179-3186.
- (49) Wilkop, T. E.; Sanborn, J.; Oliver, A. E.; Hanson, J. M.; Parikh, A. N. On-Demand Self-Assembly of Supported Membranes Using Sacrificial, Anhydrobiotic Sugar Coats. *J. Am. Chem. Soc.* **2014**, *136*, 60-63.

---

\*Adapted with permission from: Hinman, S. S., et al. DNA Linkers and Diluents for Ultrastable Gold Nanoparticle Bioconjugates in Multiplexed Assay Development. *Anal. Chem.* **2017**, *89*, 4272-4279. Copyright 2017 American Chemical Society.

# **CHAPTER 5: Nanoglassified, Monolayer Films of Gold**

## **Nanoparticles for *In Situ* Orthogonal Detection by LSPR and SALDI-MS\***

### **■ INTRODUCTION**

The development of highly integrated, multifunctional biosensing platforms is of great importance to the fields of environmental monitoring, toxicity screenings, proteomics, and drug discovery.<sup>1</sup> In particular, localized surface plasmon resonance (LSPR) has gained considerable attention as an effective signal transducer due to its sensitivity and versatility.<sup>2</sup> LSPR is an optical phenomenon associated with nanomaterials and is typically monitored by changes in the extinction spectra, as LSPR results in strong light absorbing and scattering properties. These properties are influenced by the shape, size, and composition of the nanostructure, making LSPR materials highly tunable.<sup>3-4</sup> Compared to the vast literature of solution-based detection, solid-state LSPR sensing comprises only a small portion, yet the fabrication processes remain an active research topic. These processes include top down techniques such as e-beam lithography,<sup>5</sup> focused ion beam lithography,<sup>6</sup> nanosphere lithography,<sup>7</sup> and colloidal lithography,<sup>8-9</sup> in addition to bottom up methods, largely dominated by layer-by-layer (LbL) deposition from colloidal solutions.<sup>10-11</sup> The LbL method is attractive toward fabricating LSPR substrates, as it allows for nanometer scale control of the substrate without the need of expensive cleanroom equipment, making reproducible substrates accessible to a large audience.<sup>12</sup>

However, despite its versatility in material fabrication and inherent sensitivity, LSPR as a label-free method faces the challenge of distinguishing nonspecific binding from true analyte signals in its measurements of biomolecular interactions.

Adding another dimension of measurement to these nanomaterials would significantly improve interaction studies, especially with methods that yield chemical and structural information. Mass spectrometry, capable of sophisticated tasks such as DNA and protein sequencing,<sup>13</sup> is one such method that carries the potential for cross-platform analysis in conjunction with LSPR substrates. Metallic nanostructures such as gold nanoparticles (AuNPs) may directly absorb UV laser light and function in place of an organic matrix during laser desorption/ionization mass spectrometry (LDI-MS).<sup>14</sup> Therefore, considerable effort has been placed on preparing nanostructure assemblies that function as surface-assisted laser desorption/ionization (SALDI) platforms.<sup>15-17</sup> SALDI is advantageous as it reduces sample preparation for MS and is more amenable to small molecule and drug screening analyses, where matrix-related ions may convolute experimental spectra. However, formation of gold structures that promote laser desorption/ionization generally compromises the optical properties of the nanoparticles intrinsic in their dispersed states, and little success has been made in performing LSPR biosensing and *in situ* SALDI-MS on the same substrate.

Herein we report the use of the LbL method combined with a previously established calcination process<sup>18-19</sup> (Figure 5.1) to generate a glass-coated and optically active monolayer film of gold nanoparticles for the detection and identification of biomolecules, as well as characterizations of biophysical processes. Incorporation of an

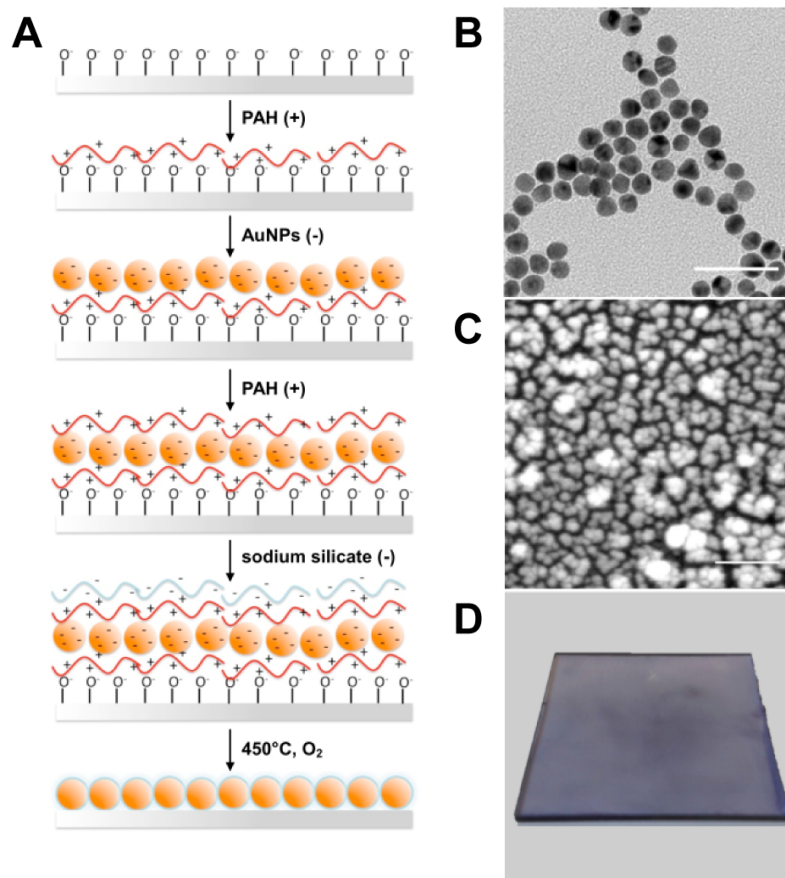


**Figure 5.1.** Fabrication scheme for the calcinated silicate nanofilm on a gold nanoparticle monolayer, supported by a glass slide. (A) Workflow of the LbL and calcination steps on a PAH-coated glass slide. (B) TEM image of 13 nm AuNPs from solution, scale bar represents 50 nm. (C) SEM image of immobilized and calcinated AuNPs, scale bar represents 200 nm. (D) Photograph of the nanofilm substrate.

inorganic precursor into LbL self-assembly has previously allowed for the nanoscale fabrication of inorganic oxide films once treated by a high temperature calcination step on both silica and gold supports.<sup>18-20</sup> By combining an inorganic precursor, such as sodium silicate, layered with gold nanoparticles, a unique, nanoglassified, nanoparticle substrate may be obtained, with applicable functionality toward multiple detection modalities. We provide evidence that a controllable nanoscale structure may be obtained under the proposed fabrication scheme, with electron microscopy revealing a regular

pattern of aggregation and porosity. Finite-difference time-domain simulations suggest that the fabricated nanostructures are optically active, which we confirm through localized surface plasmon resonance assays of bulk and surface refractive index sensitivity, resulting in label-free studies of lipid vesicle interactions with the calcinated AuNP surface. While not suitable at present for optical identification techniques such as Raman spectroscopy, the calcinated AuNPs function excellently for SALDI-MS, eliminating the need for application of an external organic matrix, and offering comparable performance to traditional MALDI techniques for small and medium sized biomolecules. This multifunction-enabling surface material can therefore yield complementary analytical information, providing a new tool for comprehensive analysis of biomolecular samples.

## ■ EXPERIMENTAL METHODS

**Materials and Reagents.** Gold (III) chloride trihydrate, trisodium citrate dihydrate, poly(allylamine hydrochloride) (PAH, MW ~56 kDa),  $\alpha$ -Cyano-4-hydroxycinnamic acid (CHCA), trifluoroacetic acid (TFA), trypsin from bovine pancreas, cytochrome c, [Sar<sup>1</sup>, Thr<sup>8</sup>]-angiotensin II, and neurotensin were from Sigma-Aldrich (St. Louis, MO). Sodium silicate (37%) and acetonitrile were from Fisher Scientific (Pittsburgh, PA). L- $\alpha$ -phosphatidylcholine from egg (egg PC) and 1-palmitoyl-2-6-[(7-nitro-2-1,3-benzoxadiazol-4-yl)amino]hexanoyl-*sn*-glycero-3-phosphocholine (NBD-PC) were from Avanti Polar Lipids (Alabaster, AL). BK-7 glass microscope slides were from Corning (Painted Post, NY).

**Instrumentation.** Absorbance spectra were recorded on a Cary 50 UV-Vis spectrophotometer. Raman spectra were obtained using a Labram HR 800 confocal system (Horiba Jobin Yvon, France), equipped with a 532 nm frequency-doubled Nd:YAG laser (Laser Quantum, Santa Clara, CA). The accumulation time was 60 s, and the incident power at the sample position was 60 mW. Atomic force microscopy (AFM) images were obtained using a Veeco Dimension 5000 atomic force microscope (Santa Barbara, CA) with manufacturer-provided hardware. All images were obtained in tapping mode at a scan rate of 1 Hz. Scanning electron microscopy was conducted on a Philips FEI XL30 scanning electron microscope (SEM), and synthesized nanoparticle sizes were verified using a Philips Tecnai 12 transmission electron microscope (TEM) in UCR CFAMM. Fluorescence microscopy was performed on a Meridian Insight confocal laser scanning microscope (CLSM) with 488 nm Argon laser excitation, SPOT Pursuit CCD, and a fluorescein emission filter used in conjunction with a 40× (NA 0.75) Achroplan dipping objective. Mass spectra were collected on a Voyager-DE STR MALDI-TOF mass spectrometer (Applied Biosystems, Framingham, MA). The instrument was set in positive reflector mode at accelerating voltage of 20 kV. The spectrometer is equipped with a pulsed nitrogen laser operating at 337 nm with 3 ns duration pulses, and each reported mass spectrum was acquired as an average of 60 laser shots.

**Gold Nanoparticle Synthesis.** AuNPs (*ca.* 13 nm diameter) were prepared by standard citrate reduction and stored in amber bottles at 4 °C. In brief, a round bottom flask containing 500 mL of 1 mM gold (III) chloride trihydrate was heated until boiling, after which, 50 mL of 38.8 mM trisodium citrate dihydrate was added. The solution was

continuously stirred and boiled until a deep red color was obtained. Nanoparticle formation and size distribution were verified using UV-Vis absorption and TEM.

**Layer-by-Layer/Calcination of Nanoparticle Films.** Standard BK-7 glass microscope slides were first cleaned in a piranha solution (3:1 v/v H<sub>2</sub>SO<sub>4</sub> and 30% H<sub>2</sub>O<sub>2</sub>) for 30 min to ensure hydroxyl group coverage across the surface, then rinsed with nanopure water, followed by drying under nitrogen. The cleaned glass slides were immersed for 2 h in 1.0 mg mL<sup>-1</sup> PAH (pH 8.0). The PAH coated slides were incubated with as-prepared AuNP solution overnight with gentle agitation. After being immersed in another PAH solution (1.0 mg mL<sup>-1</sup>, pH 8.0), the modified glass slides were dipped into a 22 mg mL<sup>-1</sup> sodium silicate solution (pH 9.5) for 1 min. Finally, the slides were dried with nitrogen and heated in a furnace to 450 °C for four hours at a rate of 17 °C min<sup>-1</sup>.

**Vesicle Preparation.** An appropriate amount of lipid stock solution containing egg PC in chloroform was dried under nitrogen to form a thin lipid film. The vial containing lipids was then placed in a vacuum desiccator for 4 h in order to completely remove all residual solvent. Thereafter, the lipids were resuspended in nanopure water to a lipid concentration of 1.0 mg mL<sup>-1</sup>. After vigorous vortexing to remove all lipid remnants from the vial wall, the solution was probe sonicated for 20 min. The resuspended lipids were centrifuged at 8000 rpm for 15 min to remove any titanium particles ejected from the probe tip during sonication. The supernatant was collected and extruded through a polycarbonate filter (Whatman, 100 nm) to produce small, unilamellar vesicles of uniform size. All suspensions were stored at 4 °C before use, and discarded after 1 week.

For fluorescence studies, vesicle preparation followed the same procedure with 2% (w/w) NBD-PC.

**Fluorescence Microscopy.** Mobility of embedded lipids within membranes supported by the calcinated gold nanoparticle surface was examined using fluorescence recovery after photobleaching (FRAP). Supported lipid bilayers were formed on each surface by incubating the material for 1 h under a vesicle suspension within a plastic petri dish. Prior to analysis, the petri dishes were repeatedly drained and refilled with nanopure water ( $\geq 5\times$ ) to remove unbound vesicles, with exceptional care given toward not exposing the lipid-coated nanoparticle surface to air. To assist with identification of the bilayer focal plane, a peripheral scratch in the bilayer was made. Photobleaching was performed manually on the CLSM by stopping the laser line scan for 1 s to obtain a bleach profile, and images were thereafter captured by the CCD camera in 1 s intervals.

**FRAP Analysis.** The methods of Axelrod and Phillips were applied to derive mobility coefficients from the linear bleach profiles.<sup>21-22</sup> First, the fluorescence intensity of each bleached line (*i.e.* minimum intensity at  $t = 0$  s) was averaged over the entire y-axis and normalized over a background area of the same size to account for background photobleaching. This normalized value, here designated  $F_n$ , was plotted against time ( $t$ ) and fitted to the equation below, where  $\alpha = (1 - F_0)$ ,  $F_0$  is the first measured  $F_n$  immediately after photobleaching,  $\beta$  is the mobile fraction,  $\omega$  is the radius ( $\mu\text{m}$ ) of the bleach profile at  $[(1 - (1/e^2)) \times \text{bleach profile height}]$ , and  $D$  is the diffusion coefficient.

$$F_n = 1 - \alpha_0(1 - \beta) - \sqrt{\frac{\alpha_0\beta}{1 + 4Dt/\omega^2}}$$

**Sample Preparation for MS Analysis.** Two peptides, [Sar<sup>1</sup>, Thr<sup>8</sup>]-angiotensin II (956.1 Da) and neurotensin (1672 Da) were prepared in 50% acetonitrile containing 0.1% TFA and 10 mM citric acid to a final concentration of 2  $\mu$ M, respectively. Cytochrome c (5 mg mL<sup>-1</sup> stock in 25 mM NH<sub>4</sub>CO<sub>3</sub>) was digested with trypsin (0.4 mg mL<sup>-1</sup> stock in 1 mM HCl) overnight at 37 °C. The final cytochrome c concentration was set to 1 mg mL<sup>-1</sup> with a substrate:enzyme ratio of 50:1 (w/w). After completion of the digest, 2  $\mu$ L of 100% formic acid was added to the mixture to stop the enzymatic reaction. The sample was then diluted to the desired experimental concentration with 50% acetonitrile containing 0.1% TFA and 10 mM citric acid, analogous to the peptide samples.

Matrix-assisted samples were prepared by spotting 0.5  $\mu$ L aliquots onto a stainless steel MALDI plate. A CHCA stock solution was prepared at 10 mg mL<sup>-1</sup> in a solvent of 50% acetonitrile, 49.95% water, and 0.05% trifluoroacetic acid. When used with a matrix, samples were prepared in a 1:10 ratio of peptide solution to CHCA. Matrix-free samples on the calcinated film were dissolved in 50% acetonitrile, 49.95% water, and 0.05% trifluoroacetic acid, containing 10 mM citric acid, then spotted in 0.5  $\mu$ L aliquots onto the calcinated AuNP film. All substrates were fixed onto a custom stainless steel sample stage with conductive (5 – 10 m $\Omega$ ) copper foil 1181 tape (3M, USA) for MS analysis.

## ■ RESULTS AND DISCUSSION

*Design and Morphological Characterizations.* Developing cross-platform sensing materials poses many challenges in that different techniques require varying optimized conditions in their respective substrates. Figure 5.1 shows the scheme we used

for fabricating an ultrathin film for dual-mode LSPR and SALDI-MS analysis. Three parameters were principally optimized during the fabrication process: a) number of layers of AuNPs, b) conditions leading to dense packing, and c) realization of an ultrathin silicate coating. We chose a monolayer configuration of AuNPs for the nanofilm due to the fact that single layer films show fewer nanoscale inconsistencies across the surface.<sup>10,</sup>  
<sup>19</sup> These nanoparticles needed to be densely packed with an organized porosity in order to generate small nanogaps and crevices where heat would concentrate during the LD/I process.<sup>23</sup> In order to create a densely packed structure, we used a long-chain polyelectrolyte to aggregate multiple nanoparticles via a bridging flocculation effect.<sup>24</sup> In addition, a water-rinsing step was omitted before deposition of nanoparticles, as this has been shown to generate a randomized porosity across the substrate.<sup>25</sup> Finally, the entire film was coated with an ultrathin layer of silicate glass which not only appends functionality not traditionally accessible to gold,<sup>18</sup> but also thermally insulates the nanoparticles, which is ideal for heat confinement and promoting desorption/ionization in SALDI-MS.<sup>19</sup> The substrate was subjected to a 450 °C calcination process, during which the high temperature combusts sacrificial polymer layers (*i.e.* PAH) used to electrostatically immobilize the nanoparticles, and creates a dense nanoscale coating of silicate-like glass. While the thickness of this silicate film may be tuned by altering the number of PAH/silicate layers, we chose to add only one layer of silicate for a final thickness of *ca.* 2 nm,<sup>18</sup> as this would still allow for plasmonic sensing to occur beyond the ultrathin silicate nanofilm.<sup>2,26</sup>

Scanning electron microscopic (SEM) characterization confirms a monolayer structure with AuNPs aggregating in different states, consisting mostly of dimer and trimer morphologies, with occasional larger aggregates (Figure D.1). From a side profile view, these aggregates appear to arrange themselves in a monolayer fashion, with very few larger clusters forming from Ostwald ripening (Figure D.1A,B).<sup>27-28</sup> We attribute the dimer and trimer clustering to the intended PAH-induced bridging flocculation, and the limited amount of larger aggregates post-calcination to the silicate protection. Atomic force microscopy (AFM) reveals an average thickness of  $26.1 \pm 5.7$  nm ( $n = 5$  height profiles), consistent with the monolayer arrangement of aggregates, and proving that a precisely controlled self-assembled nanoparticle substrate can be obtained using the LbL/calcination approach (Figures D.2). SEM images also confirm the increased robustness offered by the nano-silicate coating, as calcination of AuNP film without the protective silicate layer resulted in destructive thermal annealing of nanoparticles and complete loss of plasmonic activity (Figure D.1D).

One concern of the LbL process for the fabrication of plasmonic substrates is that the self-assembly process does not allow for precise control of the placement and orientation of individual nanoparticles, leading to less homogeneity across the surface. Since the structural properties of single nanoparticles may have a large impact on a substrate's bulk optical characteristics,<sup>29-30</sup> any inconsistencies between structures have the potential to impact the sensing performance. Since all optical measurements taken on this film are treated as an ensemble of a larger area of varying structures, numerical finite-difference time domain (FDTD) simulations were employed to investigate how the

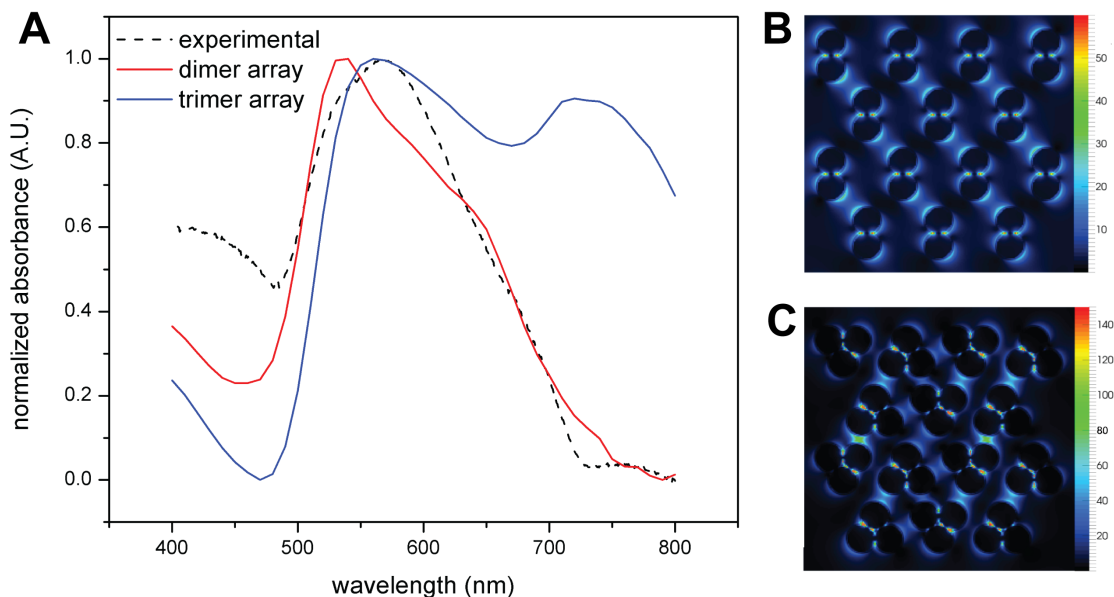


**Figure 5.2.** Numerical finite-difference time-domain simulations and comparison to experimental results. (A) Experimental spectrum of calcinated AuNPs compared to those of simulated arrays. (B) Electric field intensity map for simulated dimer array at  $\lambda = 540$  nm. (C) Electric field intensity map for simulated trimer array at  $\lambda = 560$  nm.

optical properties of ordered, monodisperse nanoparticle arrays compared to those of the calcinated AuNP film. Different geometries were chosen that correlated with the possible aggregation states that could be achieved using 60 kDa PAH and 13 nm dia. AuNPs, which include monomer, dimer, and trimer nanoparticle aggregation states.<sup>24</sup> These shapes were then respectively organized into patterned arrays within their simulation domains. Simulation results indicate that the optical properties of this film are largely reflective of arrayed dimer and trimer morphologies (Figure 5.2). For instance, the primary peak of the simulated dimer array closely matches with the left shoulder peak of the experimental substrate (at  $\lambda = 530$  nm), in addition to the primary peak of both the trimer array and experimental substrate (both at  $\lambda = 560 - 570$  nm). It appears that the LbL self-assembly promotes reproducible structures (*i.e.* dimer and trimer morphologies)

that will in turn manifest in consistent experimental results (*i.e.* similar extinction bands and RI sensitivities). In addition, the strong electromagnetic coupling between neighboring nanostructures unique in the solid state leads to plasmonic properties that may be useful for sensitivity enhancement and heat confinement.<sup>31-32</sup>

***Plasmonic Activity for Optical Detection Modalities.*** The calcinated AuNP film exhibits a well-defined absorption band with reasonable LSPR sensitivity for spherical AuNPs. To establish the bulk sensitivity of the calcinated AuNP film, the changes in extinction spectrum of the film immersed in different solvents with varying refractive indices (RI) were monitored. Water, ethanol, n-propanol, ethylene glycol, and benzene were used, with a refractive index range of 1.33 – 1.50 RIU. Consistent with Maxwell-Garnett effective medium theory,<sup>33</sup> the LSPR extinction peaks exhibited a red shift and increase in intensity as the refractive index of the solution in which the AuNP film was immersed increased. Repeating this for multiple ( $n = 3$ ) substrates, a bulk RI sensitivity of  $84 \pm 10$  nm RIU<sup>-1</sup> was obtained (Figure 5.3A). This is slightly higher than another study which evaluated the refractive index sensitivity of a monolayer of AuNPs without any protective layer,<sup>34</sup> and while other self-assembled AuNP films with thin silica layers exist, their bulk refractive index sensitivities were not calculated for comparison.<sup>35-36</sup> The differential extinction spectrum approach was also employed for data analysis so that refractive index sensitivities may be evaluated across the entire measured spectrum, rather than being limited to only extinction peaks or valleys.<sup>37</sup> These are obtained by subtracting the normalized extinction spectrum of the film in water from a normalized extinction spectrum of the film in each solvent. Using this approach for the calcinated

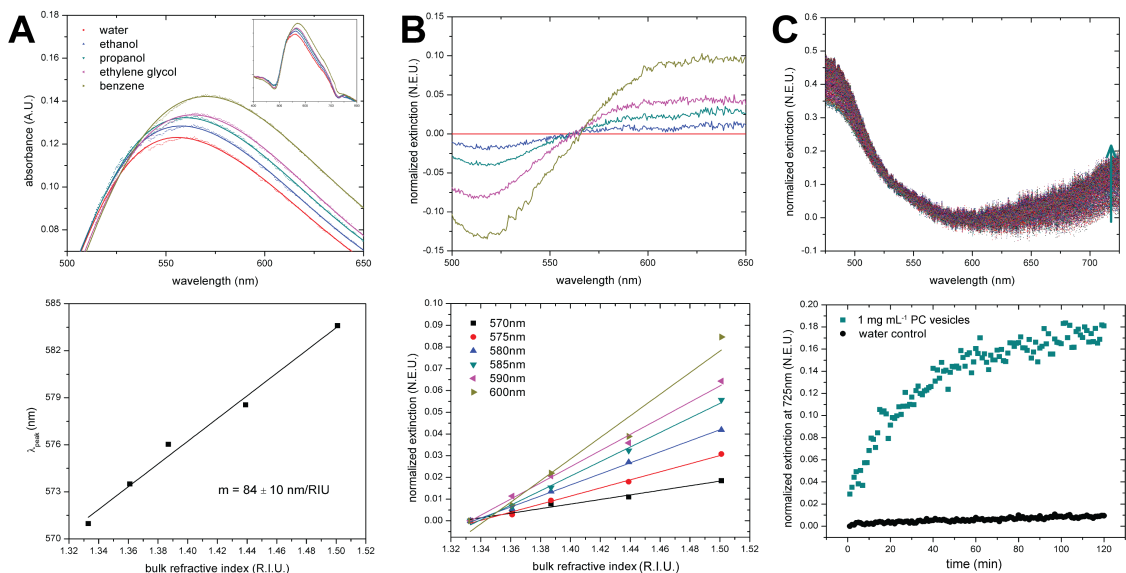


**Figure 5.3.** Characterization of LSPR performance with calcinated AuNP films. (A) Absorption spectra near the peak wavelength in solutions with varying refractive index (RI), and evaluation of RI sensitivity at peak wavelength. (B) Differential spectra and evaluation of RI sensitivity at multiple wavelengths. (C) Differential spectra of the film in PC vesicle suspension over time and change in normalized extinction at 725 nm indicating lipid bilayer formation.

monolayer of AuNPs, we observed that wavelengths higher than the maximum absorbance displayed higher bulk refractive index sensitivities, with the sensitivity of  $0.106 \text{ NEU RIU}^{-1}$  at 570 nm increasing to  $0.497 \text{ NEU RIU}^{-1}$  at 600 nm (Figure 5.3B).

Addition of the nano-silicate coating via LbL/calcination appends new functionality not typically seen in LSPR substrates. Different from metal substrates that generally suppress bilayer formation,<sup>38-39</sup> lipid membranes are readily formed over silicate glass, which provides a hydrophilic surface allowing for phospholipid vesicles to rupture, fuse, and self-assemble into a continuous supported lipid bilayer (SLB).<sup>18</sup> To demonstrate this feature and assess LSPR surface sensitivity, interactions of phosphatidylcholine vesicles and formation of a lipid bilayer on the surface from a bulk vesicle suspension were investigated. The differential extinction spectra in Figure 5.3C show that this

surface interaction shifts the AuNP film absorbance to the greatest extent at higher wavelengths, in line with the bulk RI sensitivity assays. There is no change across the entire spectrum when immersed only in water, thereby leading to the conclusion that these LSPR shifts can be specifically attributed to adsorption of lipid vesicles, and not to a temperature or instrument related drift. By plotting the normalized extinction at 725 nm against time, a kinetic curve was obtained, showing that the adsorption process reaches a plateau in about 1 h. This is slower than previous studies of bilayer formation on calcinated silicate over evaporated gold films, suggesting that the formation process is slightly hindered and may not result in a pristine SLB.<sup>18,40</sup> Here, we attribute this to the relatively higher surface roughness of the nanoparticle film vs. planar, evaporated gold, though further characterizations were needed to assess the final structure(s) of adsorbed lipids.

Fluorescence microscopy and the FRAP technique were performed to investigate the spatial distribution of the surface bound lipid structures, in addition to assessing whether long-range lateral lipid mobility is possible on the calcinated AuNP surface. Fluorescence images show that supported bilayer membrane covers the entire nanofilm surface, with scattered areas of higher fluorescence intensity indicative of defect spots (Figure D.3). Using previously established methods for line FRAP,<sup>21</sup> a diffusion coefficient of  $2.95 \mu\text{m}^2 \text{s}^{-1}$  was obtained, along with a mobile fraction of 86%. While the mobile fraction was lower than the expected value of 100%, the diffusion coefficient agrees with those of other lipid bilayers supported by glassy surfaces, which range from  $1 - 4 \mu\text{m}^2 \text{s}^{-1}$ .<sup>41</sup> These data suggest that the slow formation may be the result of a poor

fusion process of lipid vesicles on the rough nanoparticle substrate, yielding a complex bilayer structure with lipid aggregates trapped between adjacent nanostructures. The mobility of lipids in these defect spots would thereby be restricted, yielding the slightly lower mobile fraction. However, given that the high lateral mobility after extensive incubation is comparable to those of more uniform glass surfaces, the calcinated nanofilm proves suitable for studies where a natural lipid membrane environment is necessary for function.

Once it was established that this substrate proved effective for refractive index based LSPR sensing, the potential for other plasmonic techniques was explored. Surface-enhanced Raman spectroscopy takes advantage of the electromagnetic field generated from LSPR nanostructures, effectively increasing the incident light intensity by several orders of magnitude at the nanoparticle surface.<sup>26</sup> This in turn yields ultrasensitive levels of detection for adsorbed or trapped species, even down to the single molecule level, with the ability to obtain structural information from the vibrational signals of many analytes.<sup>42</sup> The SERS effect is highly dependent on distance of the analyte from the substrate,<sup>26</sup> and for practical purposes, the analyte should be within 5 nm of the surface in order to see plasmon-mediated Raman signal enhancement.<sup>43</sup> While the silicate glass layer does act as a nanoscale spacer between the AuNP surface and the analyte, enhanced Raman signals are still seen for 1 mM rhodamine 6G (R6G, Figure 5.4A). A flat, evaporated gold surface (46 nm Au, on glass) offered the best comparison with the highest resolution peaks among the planar substrates studied, which also included 46 nm gold with a 2 nm silica spacer (comparable to the silicate layer on the calcinated AuNPs)

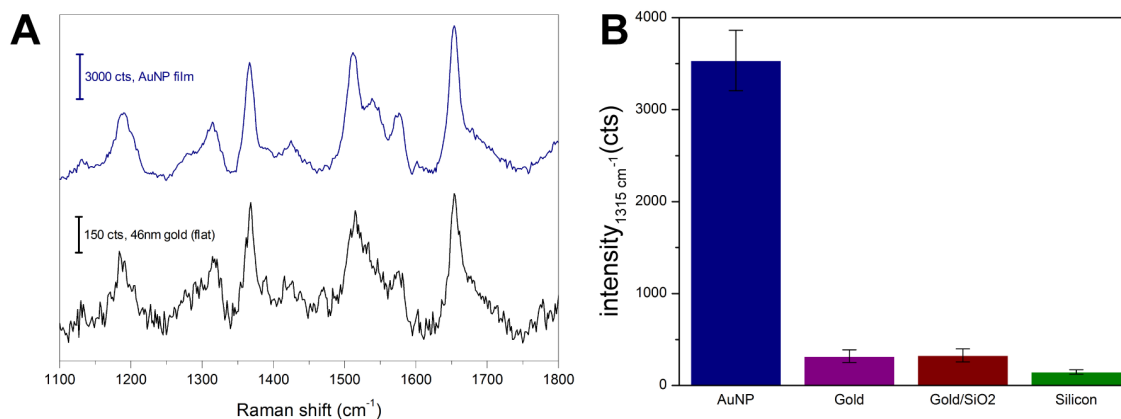


**Figure 5.4.** Direct Raman spectroscopic analysis on the calcinated AuNP film, and comparison with planar substrates. (A) Raman spectra of rhodamine 6G (R6G) on calcinated AuNP film (blue) and evaporated gold film (black). (B) Intensity of the 1315 cm<sup>-1</sup> peak of R6G drop deposited and dried on various substrates.

and a P type <111> silicon wafer (Figure 5.4B). In the spectra for R6G on both the calcinated AuNP film and evaporated gold, the vibrational bands for C-C stretching at 1368 cm<sup>-1</sup>, 1518 cm<sup>-1</sup>, and 1662 cm<sup>-1</sup> can be easily distinguished. In addition, the peaks for N-H planar bends at 1315 cm<sup>-1</sup> and 1587 cm<sup>-1</sup>, and those for aromatic C-H planar bends at 1128 cm<sup>-1</sup> and 1186 cm<sup>-1</sup> are clearly noted.<sup>44</sup> These signals are reproducible throughout varying regions of the AuNP film, and relative standard deviations of the signal intensities for all substrates are <8% (Figure 5.4B). However, while the Raman signals on the calcinated AuNP film are generally higher than on the other substrates, with *ca.* 20 fold enhancement in the peak intensity at 1315 cm<sup>-1</sup> as an example, the contribution of a true SERS mechanism is unlikely. Expected enhancement factors are often at least 5 orders of magnitude greater than a SERS-inactive surface, with some high performance materials reaching 10<sup>10</sup> fold enhancement.<sup>26</sup> Since the generated EM fields from the AuNP film only extend an additional 2 – 3 nm beyond the silicate coating and exponentially decay with increasing distance from the gold surface, they may simply not be of a high enough intensity for effective Raman excitation and scattering. This may be

partially improved through the use of higher wavelength lasers ( $>\lambda_{\text{peak}}$ ), generating increased plasmonic resonance and sensitivity for gold (as noted in the LSPR experiments), which were inaccessible for the above studies. The modest enhancement exhibited here can likely be attributed to a combination of the AuNP film providing a higher surface area for R6G to adsorb, and to a resonance Raman effect, given that R6G strongly absorbs light at the instrument's excitation wavelength of 532 nm.<sup>45</sup>

***SALDI-MS Performance.*** Gold nanoparticles have exhibited excellent performance in place of traditional LD/I matrices due to their broad absorption, which ranges from the UV to visible regions of the electromagnetic spectrum.<sup>14</sup> To demonstrate the potential for matrix-free SALDI-MS analysis with the calcinated AuNP film, ionization of two peptides, [Sar<sup>1</sup>, Thr<sup>8</sup>]-angiotensin II and neurotensin was investigated (Figure 5.5A). These peptides were applied as a mixture in the amount of 2 pmol and ionization was carried out at the same arbitrary laser fluence (1850 a.u.). 10 mM citric acid was incorporated into the experimental solutions as it does not absorb UV light, but does act as an external proton donor to promote the formation of protonated ions over alkali-adducted ions.<sup>46</sup> SALDI experiments were performed alongside MALDI using CHCA as a matrix, with samples deposited on a commercial, stainless steel plate, and comparable results were obtained (Figure D.4A). The  $[M+H]^+$  peaks can be readily distinguished in both spectra, and background noise is very low. There are also no gold clusters evident in the SALDI spectra, which has been an issue for similar work using AuNPs in place of traditional ionization matrices.<sup>14-16</sup> This can be attributed to the calcinated silicate layer, which offers protection of the AuNPs and anchors them to the

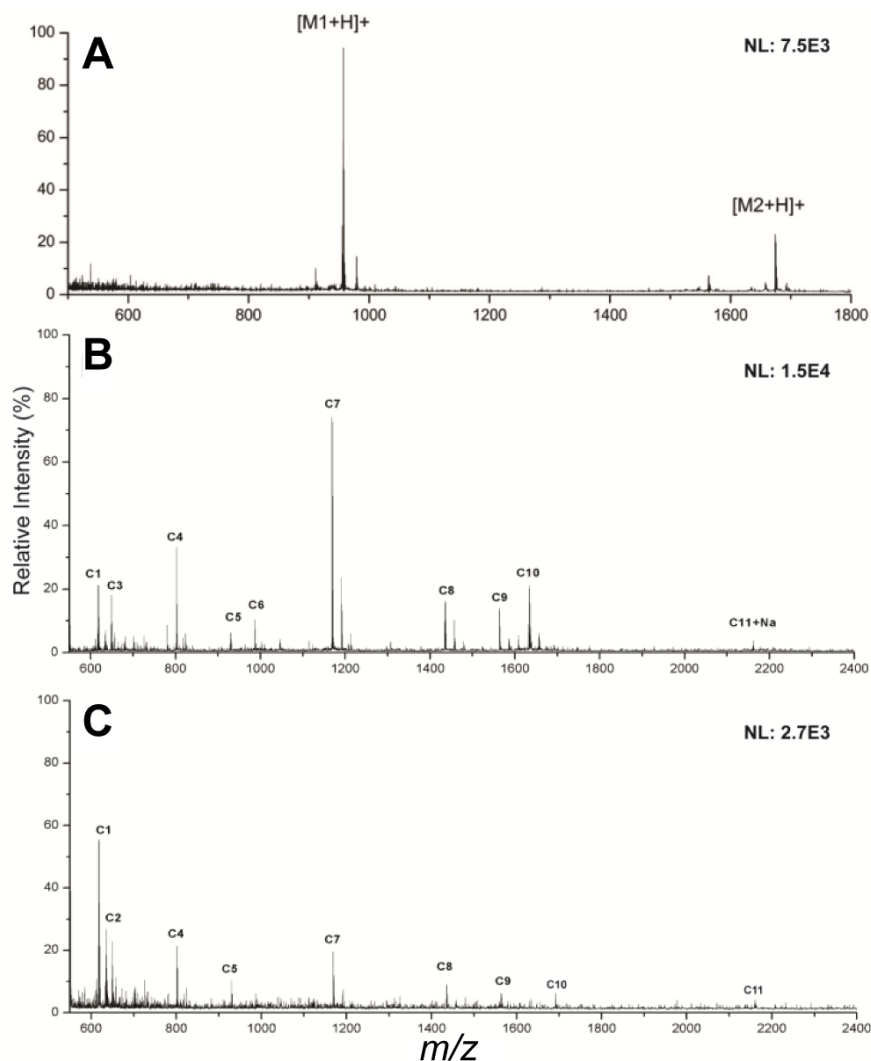


**Figure 5.5.** Laser desorption/ionization performance of the calcinated AuNP film and comparison to MALDI. (A) SALDI mass spectrum of [Sar<sup>1</sup>, Thr<sup>8</sup>]-angiotensin II (M1 = 956.1 Da) and Neurotensin (M2 = 1672 Da). (B) SALDI mass spectrum of a cytochrome c digest. (C) MALDI mass spectrum of the same cytochrome c digest using CHCA as the ionization matrix.

surface during the LD/I process. Beyond protection from the laser source, the calcinated silicate film also exhibits low thermal conductivity, which assists in confining heat to localized hot spots, promoting desorption from the surface and increasing ionization performance.<sup>19</sup>

Further MS characterization was carried out with a tryptic digest of cytochrome c, which yields more information about the nanofilm performance for proteomic studies (Figure 5.5B). Comparable results for 80 pmol of cytochrome c digest are obtained between SALDI and MALDI, though the SALDI experiments detected one less peptide (Table D.1). The loss of this peptide in the SALDI mass spectrum could be due to a number of factors, though most likely is a result of hydrophathy mismatch between the C2 peptide and the silicate surface, given that C2 is relatively hydrophobic compared to the other fragments (with calcinated silicate being hydrophilic).<sup>25</sup> On the other hand, the CHCA matrix yielded abundant background noise in comparison to the AuNP film (Figure 5.5C), and *S/N* ratios for many peaks were lower, possibly due to LD/I suppression of target analytes by matrix ions. This is clearly shown in the higher relative intensities of C6, C7, and C10 peaks at *m/z* 965, 1169, and 1634, respectively, in the calcinated AuNP spectrum. Intact cytochrome c was also detectable on the calcinated AuNP film (Figure D.5), albeit with higher noise and lower resolution, though nonetheless showing that the calcinated nanofilm of AuNPs enables mass spectrometric measurement of a reasonable mass range of substrates, from peptides to small proteins, and is thus applicable to broad analysis beyond only small molecules.

## ■ CONCLUSIONS

Using the AuNP film fabricated by LbL self-assembly and calcination, we have demonstrated a multi-functional surface that is compatible with several developing and important analytical methods. The intended properties of a monolayer of AuNPs, dense

packing structure, and calcinated silicate coating were each realized, contributing to the dual-mode sensing functionality. Furthermore, the LbL process allows for these properties to be easily tailored in a consistent and reproducible fashion. The substrate exhibits the capability for LSPR spectroscopy studies, and the ability to track the immobilization of a lipid bilayer in real-time was demonstrated. Significantly, these supported lipid bilayer membranes may be further used for studies that involve biomimetic systems and characterization of ligand/receptor interactions. While LSPR sensing may play a powerful role in the detection and characterization of biomolecules and interactions, it does not allow for absolute identification without the use of specific binding strategies. SALDI-MS was therefore performed directly on this substrate, for the analysis of multiple peptides and a protein digest, exhibiting that complementary identification based on charge and molecular weight is possible with minimal interference compared to traditional MALDI techniques. These results clearly demonstrate the potential of this unique nanofilm substrate on which multiple, *in situ* measurements are possible and thus an array of complementary information, quantitative and structural, is obtainable. Given that LSPR and SALDI-MS are label-free techniques, the combined function of multiple detections may lead to highly efficient bioassays that rely on orthogonal methods using the same sample on the same chip, vastly decreasing time and cost in the characterization of biological systems and environmental samples.

## ■ REFERENCES

- (1) Turner, A. P. F. Biosensors: Sense and Sensibility. *Chem. Soc. Rev.* **2013**, *42*, 3184-3196.
- (2) Willets, K. A.; Van Duyne, R. P. Localized Surface Plasmon Resonance Spectroscopy and Sensing. *Annu. Rev. Phys. Chem.* **2007**, *58*, 267-297.
- (3) Anker, J. N.; Hall, W. P.; Lyandres, O.; Shah, N. C.; Zhao, J.; Van Duyne, R. P. Biosensing with Plasmonic Nanosensors. *Nat. Mater.* **2008**, *7*, 442-453.
- (4) Sepulveda, B.; Angelome, P. C.; Lechuga, L. M.; Liz-Marzan, L. M. LSPR-Based Nanobiosensors. *Nano Today* **2009**, *4*, 244-251.
- (5) Gunnarsson, L.; Rindzevicius, T.; Prikulis, J.; Kasemo, B.; Kall, M.; Zou, S. L.; Schatz, G. C. Confined Plasmons in Nanofabricated Single Silver Particle Pairs: Experimental Observations of Strong Interparticle Interactions. *J. Phys. Chem. B* **2005**, *109*, 1079-1087.
- (6) Ebbesen, T. W.; Lezec, H. J.; Ghaemi, H. F.; Thio, T.; Wolff, P. A. Extraordinary Optical Transmission through Sub-Wavelength Hole Arrays. *Nature* **1998**, *391*, 667-669.
- (7) Hulsteen, J. C.; Vanduyne, R. P. Nanosphere Lithography - a Materials General Fabrication Process for Periodic Particle Array Surfaces. *J. Vac. Sci. Technol.* **1995**, *13*, 1553-1558.
- (8) Fredriksson, H.; Alaverdyan, Y.; Dmitriev, A.; Langhammer, C.; Sutherland, D. S.; Zaech, M.; Kasemo, B. Hole-Mask Colloidal Lithography. *Adv. Mater.* **2007**, *19*, 4297-4302.
- (9) Dahlin, A.; Zach, M.; Rindzevicius, T.; Kall, M.; Sutherland, D. S.; Hook, F. Localized Surface Plasmon Resonance Sensing of Lipid-Membrane-Mediated Biorecognition Events. *J. Am. Chem. Soc.* **2005**, *127*, 5043-8.

- (10) Brust, M.; Bethell, D.; Kiely, C. J.; Schiffrin, D. J. Self-Assembled Gold Nanoparticle Thin Films with Nonmetallic Optical and Electronic Properties. *Langmuir* **1998**, *14*, 5425-5429.
- (11) Mayya, K. S.; Schoeler, B.; Caruso, F. Preparation and Organization of Nanoscale Polyelectrolyte-Coated Gold Nanoparticles. *Adv. Funct. Mater.* **2003**, *13*, 183-188.
- (12) Decher, G. Fuzzy Nanoassemblies: Toward Layered Polymeric Multicomposites. *Science* **1997**, *277*, 1232-1237.
- (13) Stigter, E. C. A.; de Jong, G. J.; van Bennekom, W. P. Coupling Surface-Plasmon Resonance and Mass Spectrometry to Quantify and to Identify Ligands. *TrAC, Trends Anal. Chem.* **2013**, *45*, 107-120.
- (14) McLean, J. A.; Stumpo, K. A.; Russell, D. H. Size-Selected (2-10 Nm) Gold Nanoparticles for Matrix Assisted Laser Desorption Ionization of Peptides. *J. Am. Chem. Soc.* **2005**, *127*, 5304-5305.
- (15) Kawasaki, H.; Sugitani, T.; Watanabe, T.; Yonezawa, T.; Moriwaki, H.; Arakawa, R. Layer-by-Layer Self-Assembled Multilayer Films of Gold Nanoparticles for Surface-Assisted Laser Desorption/Ionization Mass Spectrometry. *Anal. Chem.* **2008**, *80*, 7524-7533.
- (16) Nayak, R.; Knapp, D. R. Matrix-Free Ldi Mass Spectrometry Platform Using Patterned Nanostructured Gold Thin Film. *Anal. Chem.* **2010**, *82*, 7772-7778.
- (17) Pilolli, R.; Ditaranto, N.; Di Franco, C.; Palmisano, F.; Cioffi, N. Thermally Annealed Gold Nanoparticles for Surface-Assisted Laser Desorption Ionisation-Mass Spectrometry of Low Molecular Weight Analytes. *Anal. Bioanal. Chem.* **2012**, *404*, 1703-11.
- (18) Phillips, K. S.; Han, J. H.; Martinez, M.; Wang, Z. Z.; Carter, D.; Cheng, Q. Nanoscale Glassification of Gold Substrates for Surface Plasmon Resonance Analysis of Protein Toxins with Supported Lipid Membranes. *Anal. Chem.* **2006**, *78*, 596-603.

- (19) Duan, J.; Linman, M. J.; Cheng, Q. Ultrathin Calcinated Films on a Gold Surface for Highly Effective Laser Desorption/Ionization of Biomolecules. *Anal. Chem.* **2010**, *82*, 5088-5094.
- (20) Wang, H.; Duan, J. C.; Cheng, Q. Photocatalytically Patterned Tio<sub>2</sub> Arrays for on-Plate Selective Enrichment of Phosphopeptides and Direct Maldi Ms Analysis. *Anal. Chem.* **2011**, *83*, 1624-1631.
- (21) Phillips, K. S.; Cheng, Q. Microfluidic Immunoassay for Bacterial Toxins with Supported Phospholipid Bilayer Membranes on Poly(Dimethylsiloxane). *Anal. Chem.* **2005**, *77*, 327-334.
- (22) Axelrod, D.; Koppel, D. E.; Schlessinger, J.; Elson, E.; Webb, W. W. Mobility Measurement by Analysis of Fluorescence Photobleaching Recovery Kinetics. *Biophys. J.* **1976**, *16*, 1055-1069.
- (23) Chen, Y.; Vertes, A. Adjustable Fragmentation in Laser Desorption/Ionization from Laser-Induced Silicon Microcolumn Arrays. *Anal. Chem.* **2006**, *78*, 5835-5844.
- (24) Schneider, G.; Decher, G. Functional Core/Shell Nanoparticles Via Layer-by-Layer Assembly. Investigation of the Experimental Parameters for Controlling Particle Aggregation and for Enhancing Dispersion Stability. *Langmuir* **2008**, *24*, 1778-89.
- (25) Duan, J. C.; Wang, H.; Cheng, Q. On-Plate Desalting and Saldi-Ms Analysis of Peptides with Hydrophobic Silicate Nanofilms on a Gold Substrate. *Anal. Chem.* **2010**, *82*, 9211-9220.
- (26) Stiles, P. L.; Dieringer, J. A.; Shah, N. C.; Van Duyne, R. P. Surface-Enhanced Raman Spectroscopy. *Annu. Rev. Anal. Chem.* **2008**, *1*, 601-626.
- (27) Krost, A.; Christen, J.; Oleynik, N.; Dadgar, A.; Deiter, S.; Blasing, J.; Krtischil, A.; Forster, D.; Bertram, F.; Diez, A. Ostwald Ripening and Flattening of Epitaxial ZnO Layers During in Situ Annealing in Metalorganic Vapor Phase Epitaxy. *Appl. Phys. Lett.* **2004**, *85*, 1496-1498.

- (28) Thiel, P. A.; Shen, M.; Liu, D. J.; Evans, J. W. Coarsening of Two-Dimensional Nanoclusters on Metal Surfaces. *J. Phys. Chem. C* **2009**, *113*, 5047-5067.
- (29) McMahon, J.; Henry, A.-I.; Wustholz, K.; Natan, M.; Freeman, R. G.; Duyne, R.; Schatz, G. Gold Nanoparticle Dimer Plasmonics: Finite Element Method Calculations of the Electromagnetic Enhancement to Surface-Enhanced Raman Spectroscopy. *Anal. Bioanal. Chem.* **2009**, *394*, 1819-1825.
- (30) Wustholz, K. L.; Henry, A. I.; McMahon, J. M.; Freeman, R. G.; Valley, N.; Piotti, M. E.; Natan, M. J.; Schatz, G. C.; Van Duyne, R. P. Structure-Activity Relationships in Gold Nanoparticle Dimers and Trimers for Surface-Enhanced Raman Spectroscopy. *J. Am. Chem. Soc.* **2010**, *132*, 10903-10910.
- (31) Hogan, N. J.; Urban, A. S.; Ayala-Orozco, C.; Pimpinelli, A.; Nordlander, P.; Halas, N. J. Nanoparticles Heat through Light Localization. *Nano Lett.* **2014**, *14*, 4640-4645.
- (32) Brongersma, M. L.; Halas, N. J.; Nordlander, P. Plasmon-Induced Hot Carrier Science and Technology. *Nat. Nanotechnol.* **2015**, *10*, 25-34.
- (33) Maxwell-Garnett, J. C. Colours in Metal Glasses, in Metallic Films, and in Metallic Solutions. Ii. *Philos. Trans. R. Soc., A* **1906**, *205*, 237-288.
- (34) Inuta, M.; Arakawa, R.; Kawasaki, H. Use of Thermally Annealed Multilayer Gold Nanoparticle Films in Combination Analysis of Localized Surface Plasmon Resonance Sensing and Maldi Mass Spectrometry. *Analyst* **2011**, *136*, 1167-1176.
- (35) Ruach-Nir, I.; Bendikov, T. A.; Doron-Mor, I.; Barkay, Z.; Vaskevich, A.; Rubinstein, I. Silica-Stabilized Gold Island Films for Transmission Localized Surface Plasmon Sensing. *J. Am. Chem. Soc.* **2006**, *129*, 84-92.
- (36) Chaikin, Y.; Kedem, O.; Raz, J.; Vaskevich, A.; Rubinstein, I. Stabilization of Metal Nanoparticle Films on Glass Surfaces Using Ultrathin Silica Coating. *Anal. Chem.* **2013**, *85*, 10022-10027.

- (37) Raschke, G.; Kowarik, S.; Franzl, T.; Sönnichsen, C.; Klar, T. A.; Feldmann, J.; Nichtl, A.; Kürzinger, K. Biomolecular Recognition Based on Single Gold Nanoparticle Light Scattering. *Nano Lett.* **2003**, *3*, 935-938.
- (38) Groves, J. T.; Ulman, N.; Boxer, S. G. Micropatterning Fluid Lipid Bilayers on Solid Supports. *Science* **1997**, *275*, 651-653.
- (39) Groves, J. T.; Ulman, N.; Cremer, P. S.; Boxer, S. G. Substrate–Membrane Interactions: Mechanisms for Imposing Patterns on a Fluid Bilayer Membrane. *Langmuir* **1998**, *14*, 3347-3350.
- (40) Han, J. H.; Taylor, J. D.; Phillips, K. S.; Wang, X.; Feng, P.; Cheng, Q. Characterizing Stability Properties of Supported Bilayer Membranes on Nanoglassified Substrates Using Surface Plasmon Resonance. *Langmuir* **2008**, *24*, 8127-33.
- (41) Stelzle, M.; Miehlisch, R.; Sackmann, E. 2-Dimensional Microelectrophoresis in Supported Lipid Bilayers. *Biophys. J.* **1992**, *63*, 1346-1354.
- (42) Jamieson, L. E.; Asiala, S. M.; Gracie, K.; Faulds, K.; Graham, D. Bioanalytical Measurements Enabled by Surface-Enhanced Raman Scattering (SERS) Probes. *Annu. Rev. Anal. Chem.* **2017**.
- (43) Bantz, K. C.; Haynes, C. L. Surface-Enhanced Raman Scattering Detection and Discrimination of Polychlorinated Biphenyls. *Vib. Spectrosc.* **2009**, *50*, 29-35.
- (44) Chang, C.-C.; Yang, K.-H.; Liu, Y.-C.; Yu, C.-C.; Wu, Y.-H. Surface-Enhanced Raman Scattering-Active Gold Nanoparticles Modified with a Monolayer of Silver Film. *Analyst* **2012**, *137*, 4943-4950.
- (45) Kim, N. H.; Kim, K. Surface-Enhanced Resonance Raman Scattering of Rhodamine 6g on Pt Nanoaggregates. *J. Raman Spectrosc.* **2005**, *36*, 623-628.
- (46) Chen, C. T.; Chen, Y. C. Desorption/Ionization Mass Spectrometry on Nanocrystalline Titania Sol-Gel-Deposited Films. *Rapid Commun. Mass Spectrom.* **2004**, *18*, 1956-1964.

---

\*Adapted with permission from: Hinman, S. S., et al. Nanoglassified, Optically-Active Monolayer Films of Gold Nanoparticles for *in Situ* Orthogonal Detection by Localized Surface Plasmon Resonance and Surface-Assisted Laser Desorption/Ionization-MS. *Anal. Chem.* **2014**, 86, 11942-11945. Copyright 2014 American Chemical Society.

# **CHAPTER 6: Calcinated Gold Nanoparticle Arrays for On-Chip, Multiplexed and Matrix-Free Mass Spectrometric Analysis of Peptides and Small Molecules\***

## **■ INTRODUCTION**

The characterization of proteome, genome, and metabolome wide patterns represents a difficult and complex task in the face of a myriad of toxicants and stressors that affect living systems.<sup>1</sup> While biosensors have served as effective tools for the detection of biomolecules and characterization of biophysical processes,<sup>2</sup> higher throughput in the performance is constantly demanded. The combination of biosensing and microarray technologies offers robust, multiplex detection strategies to meet this demand for a variety of target analytes.<sup>3-5</sup> Different from optical detection, various mass spectrometric techniques, capable of sophisticated tasks such as DNA and protein sequencing,<sup>6-7</sup> are often difficult to integrate with chip-based samples, with the exception of matrix-assisted laser desorption/ionization mass spectrometry (MALDI-MS) which has shown great promise as a powerful surface-based method.<sup>8</sup> MALDI arrays utilize an organic matrix to assist in the ionization of target analytes, and with appropriate functionalization of the array chip, may be used for profiling global cellular activities.<sup>9</sup> However, due to the presence of matrix related ions, MALDI-MS is rarely applied to low molecular weight samples, hindering its application in clinical and industry settings where small molecule detection and identification is greatly needed.

To circumvent this issue, the field of surface-assisted laser desorption/ionization mass spectrometry (SALDI-MS) has undergone rigorous development and is gaining considerable attention for low molecular weight analytes.<sup>10</sup> SALDI-MS relies on the properties of the underlying material, rather than those of a separate organic matrix, to assist in analyte desorption and ionization from the substrate surface. Naturally, this results in minimized sample preparation and little to no interference in the low mass region, as an external matrix no longer needs to be applied or incorporated into the samples. Porous silicon (also known as desorption/ionization on silicon, or DIOS) is one of the most established SALDI materials, and its ionization performance benefits from strong UV absorption and heat transfer properties.<sup>11-13</sup> Gold nanomaterials share many of the same performance benefits as DIOS for SALDI-MS, both in colloid<sup>14-17</sup> and thin film<sup>18-19</sup> formats. This class of materials has the benefit of being relatively inert compared to DIOS, which is prone to oxidation, leading to a decline or even loss of performance. While effective, gold nanoparticles for SALDI have certain weaknesses; gold clusters may ionize with the target analyte and introduce contaminating peaks into mass spectra.<sup>14, 16</sup> Furthermore, little attempt has been made to create patterned microarrays of these materials, likely due to the high expense of sophisticated cleanroom and lithography techniques, or to coffee ring formation effects in arrayed, drop-deposited colloids.<sup>20</sup>

Herein we demonstrate the layer-by-layer modification of gold nanoparticles, coupled with an inexpensive photocatalytic patterning process for the development of a highly effective, inexpensive, and reusable microarray substrate that is optimized for SALDI-MS. Gold nanoparticle modification is realized by a method our group developed

for localized surface plasmon resonance (LSPR) and SALDI.<sup>17</sup> Using photocatalytic patterning to create hydrophilic deposition areas with hydrophobic surroundings, we are able to alleviate the inhomogeneous sample spreading issue during formation of our AuNP array spots, and during deposition of target analytes. Calcination of the substrate before sample deposition permanently fixes these features in place, leaving robust films of AuNPs protected by ultrathin layers of silicate. In this work, performance-contributing factors of this material will be discussed. The calcinated AuNP microarray is found to be more efficient than many developed SALDI materials, while exhibiting comparable performance to other MS methods using organic matrices for small to medium sized molecules. In addition, the microarray can be regenerated under mild conditions with no deterioration of performance over many cycles. The sensitive and multiplexed measurements achieved here with minimized sample preparation and in a reusable format may lead to a large reduction in material and reagent costs for chip-based detection and screening.

## ■ EXPERIMENTAL METHODS

**Materials and Reagents.** Gold (III) chloride trihydrate, trisodium citrate dihydrate, poly(allylamine hydrochloride) (PAH, MW ~56 kDa), *n*-octadecyltrichlorosilane (OTS, 90+%),  $\alpha$ -Cyano-4-hydroxycinnamic acid (CHCA), 2,5-Dihydroxybenzoic acid (DHB), trifluoroacetic acid (TFA), titanium (IV) chloride, [Sar<sup>1</sup>, Thr<sup>8</sup>]-angiotensin II, and neurotensin were from Sigma-Aldrich (St. Louis, MO). Citric acid, sodium silicate (37%), ethanol, toluene, and chloroform were from Fisher Scientific (Pittsburgh, PA). Acetyl-

tetradecapeptide renin substrate was from AnaSpec (San Jose, CA). BK-7 glass microscope slides were from Corning (Painted Post, NY).

**Instrumentation.** All extinction spectra were obtained using a Cary 50 UV-Vis spectrophotometer (Agilent Technologies, Santa Clara, CA). Scanning electron microscopy (SEM) was conducted with a Hitachi TM-1000 Tabletop SEM (Tokyo, Japan). Transmission electron microscopy (TEM) was conducted with a Philips FEI Tecnai 12 TEM (Andover, MA) in UCR CFAMM.

Mass spectra were collected using a Voyager-DE STR MALDI-TOF mass spectrometer (Applied Biosystems, Framingham, MA) set in positive reflector mode at an accelerating voltage of 20 kV. The spectrometer is equipped with a pulsed nitrogen laser operating at 337 nm, with each spectrum acquired as an average of 60 laser shots.

**Sample Preparation.** The peptides, [Sar<sup>1</sup>, Thr<sup>8</sup>]-angiotensin II, neurotensin, and acetyl-tetradecapeptide renin substrate, were prepared in stock solutions of 50% acetonitrile containing 0.1% TFA and 10 mM citric acid to a final concentration of 20  $\mu$ M. Cholesterol was dissolved in chloroform to a concentration of 2.59 mM (1 mg mL<sup>-1</sup>). These solutions were diluted to desired experimental concentrations, and aliquots of 1  $\mu$ L were spotted onto the AuNP array, followed by drying under vacuum. The array was then attached to a custom stainless steel MALDI plate using polyimide tape. When matrices were utilized in ionization, the analyte and matrix were set to a volume ratio of 1:10, respectively, and 1  $\mu$ L aliquots were spotted onto a commercial stainless steel MALDI plate.

**Synthesis and Modification of Gold Nanoparticles.** Gold nanoparticles (AuNPs), *ca.* 13 nm in diameter, were prepared using previously established methods.<sup>21</sup> In short, a round bottom flask containing 500 mL of 1 mM gold (III) chloride trihydrate was heated until boiling, after which, 50 mL of 38.8 mM trisodium citrate dihydrate was added. The solution was continuously boiled and stirred until a deep red color was obtained. Nanoparticle formation and size distribution were verified using the LSPR band measured by UV-Vis absorption, and transmission electron microscopy.

AuNPs were modified using layer-by-layer immobilization of polyelectrolytes at the nanoparticle surface.<sup>22</sup> To modify AuNPs for immobilization and calcination on glass slides, an aliquot (1.5 mL) of as-prepared citrate-capped AuNP solution was first centrifuged at 10,000 rpm for 15 min, and the supernatant was discarded. Thereafter, an aqueous solution of 1 mg mL<sup>-1</sup> PAH (1.5 mL, pH 8.0) was added to the AuNP pellet. The mixture was bath sonicated for 5 min to disperse the AuNPs and immobilize PAH at the AuNP surface. The AuNP-PAH solution was centrifuged again followed by removal of the supernatant. The addition of an aqueous solution of 22 mg mL<sup>-1</sup> sodium silicate (1.5 mL, pH 9.5) to the AuNP-PAH pellet was followed by sonication for 5 min to immobilize silicate ions and yield AuNP-(PAH-silicate)<sub>1</sub>. This process was repeated to yield the desired number of (PAH-silicate) layers on the AuNPs. The resulting solution was concentrated 15-fold before arraying.

**Microarray Patterning of Glass Substrates.** A photocatalytic method to prepare alternating hydrophobic and hydrophilic areas on glass microscope slides was used with modification.<sup>23</sup> BK-7 glass microscope slides were cleaned using a boiling piranha

solution (3:1 v/v H<sub>2</sub>SO<sub>4</sub> and 30% H<sub>2</sub>O<sub>2</sub>) for 30 min, followed by rinsing with DI water and drying under a stream of nitrogen gas. Glass slides were then immersed in 10 mM titanium (IV) chloride in toluene with 0.1% (v/v) water for 15 min, in order to hydrolyze TiCl<sub>4</sub> and obtain a photocatalytic nanofilm of TiO<sub>2</sub> on the glass surface.<sup>24</sup> The TiO<sub>2</sub> coated microscope slides were then rinsed alternately with toluene and ethanol three times. Thereafter, the slides were immersed in 10 mM OTS in toluene to generate a hydrophobic C18 layer, then rinsed alternately with toluene and ethanol three more times before drying under a stream of nitrogen gas. The entire glass/TiO<sub>2</sub>/C18 substrate was covered by a photomask and irradiated under a 450 mW cm<sup>-2</sup>,  $\lambda = 254$  nm, light source (CL-1000, UVP Inc., Upland, CA) for one hour to cleave C18 from the exposed areas, and obtain a pattern of hydrophilic spots with hydrophobic surroundings. The photomask was perforated with holes representing the final array, separated into areas of 2 mm dia. spots with 3 mm pitch, 1 mm dia. spots with 3 mm pitch, and 800  $\mu$ m dia. spots with 1.5 mm pitch. After UV irradiation, 1  $\mu$ L of prepared AuNP-(PAH-silicate)<sub>n</sub> solution was deposited on each hydrophilic array spot and dried. The number of deposited and dried droplets per spot was varied to determine optimal performance. Finally, all slides were heated in a furnace to 450 °C for 4 h at a rate of 17 °C min<sup>-1</sup>. Each slide was thoroughly rinsed with ethanol and DI water before use.

## ■ RESULTS AND DISCUSSION

*Photocatalytic Patterning of Arrayed Calcinated AuNPs.* The layer-by-layer (LbL) assembly technique is a versatile and cost-effective strategy for creating

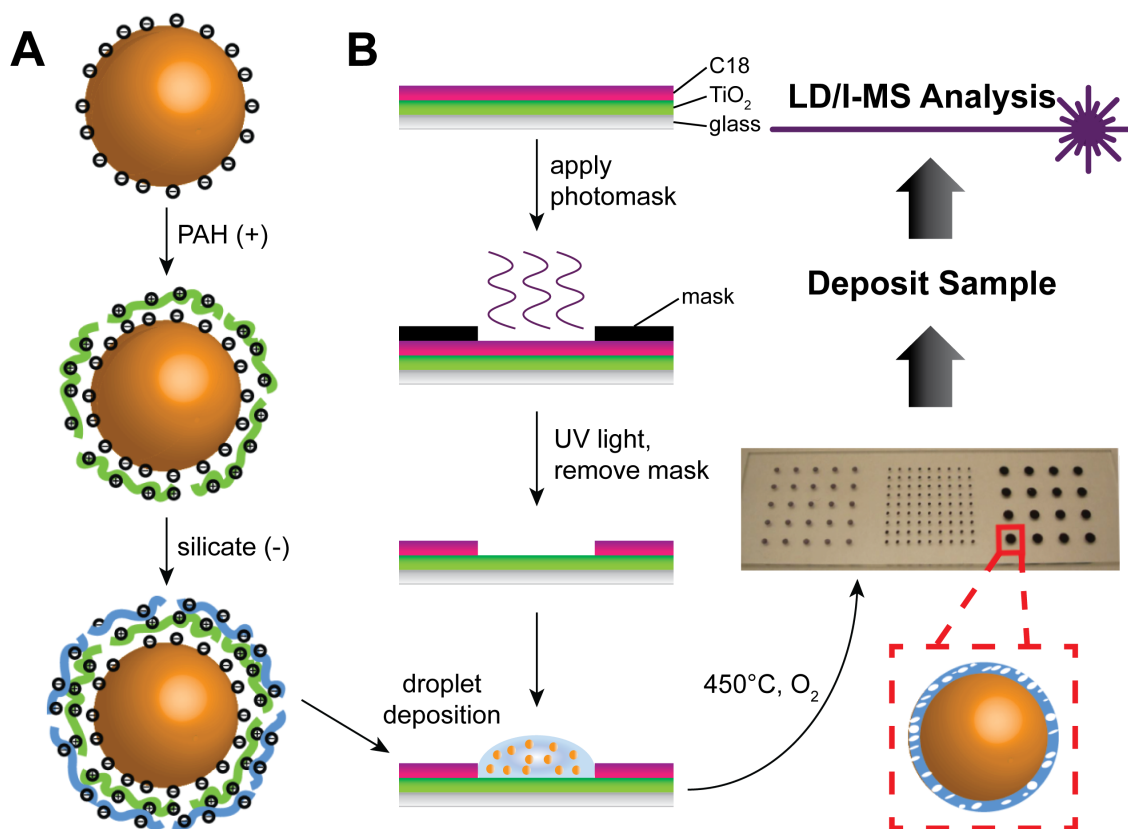


**Figure 6.1.** Fabrication of the calcinated AuNP array and analytical scheme. (A) Layer-by-layer modification of gold nanoparticle surface in solution. (B) Photocatalytic method for creating a hydrophilic spot pattern with hydrophobic surroundings on glass microscope slides.

nanostructures possessing specifically tailored compositions and morphologies.<sup>25</sup> In this work, we applied the LbL technique to gold nanoparticles in solution, followed by high temperature calcination, to generate dense coatings of silicate with tunable, nanoscale thicknesses around individual nanoparticles (Figure 6.1). The calcination step took place on BK-7 glass microscope slides, patterned with hydrophilic spots and hydrophobic surroundings, to assist in generating a well-defined microarray of the silicate-coated product (Figure 6.1B). Each step of this fabrication was optimized for high SALDI-MS performance.

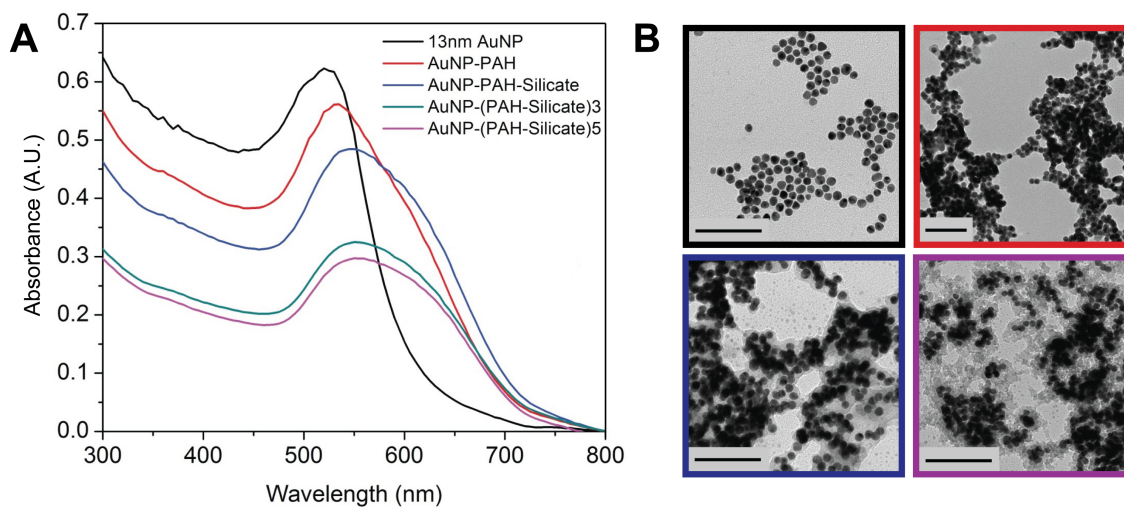


**Figure 6.2.** Layer-by-layer modification of gold nanoparticles. (A) Monitoring of polymer and silicate depositions using localized surface plasmon resonance absorbance bands. (B) Corresponding transmission electron micrographs. Scale bars represent 100 nm.

The deposition of alternately charged polyelectrolytes at the nanoparticle surface was monitored using changes in the localized surface plasmon resonance (LSPR) band of the colloidal nanoparticle solutions, with transmission electron microscopy (TEM) providing additional verification of the results (Figure 6.2). Due to the LSPR phenomenon, gold nanoparticles may function as optical nanoantennae, capable of absorbing light at discrete wavelengths and generating localized, oscillating electromagnetic fields from the delocalized electrons of the bulk material.<sup>26</sup> In response to changes in the local dielectric environment, the wavelength at which these nanoparticles absorb light shifts as a function of the surrounding refractive index, allowing for a unique sensing modality that has been broadly exploited.<sup>17, 27-33</sup> Here, as each layer of polyelectrolyte is added to the gold nanoparticle surface, the absorbance peak shifts to a higher wavelength (Figure 6.2A), in agreement with the underlying mechanism of LSPR.<sup>27</sup> Starting with the citrate capped and negatively charged AuNP

surface (AuNP,  $\lambda_{\text{peak}} = 520 \text{ nm}$ ), the first layer of positively charged polyallylamine hydrochloride (PAH) results in a red shift of the absorbance band (AuNP-PAH,  $\lambda_{\text{peak}} = 535 \text{ nm}$ ), followed by a further red shift once a layer of negatively charged silicate is added to the surface (AuNP-(PAH-silicate)<sub>1</sub>,  $\lambda_{\text{peak}} = 545 \text{ nm}$ ). Further increases in the number of (PAH-silicate)<sub>n</sub> layers result in additional red shifts of the absorbance band ( $\lambda_{\text{peak}} = 550 \text{ nm}$ ). The decrease in LSPR sensitivity in the higher layer number samples is due to the short decay length of the plasmonic sensing field, which only extends *ca.* 10 nm and decreases with distance from the nanoparticle surface. TEM analysis agrees with the LSPR results, showing increasing thicknesses shell around the AuNPs as more layers are added (Figure 6.2B).

Fabricating a precisely defined microarray from a colloidal suspension presents a challenge, as liquid droplets deposited on solid surfaces often do not dry uniformly, which can adversely affect microarray patterning and performance.<sup>34</sup> Capillary flow from the center of a liquid drop with a pinned contact line (*e.g.* a deposited nanoparticle suspension) results in dissolved particles migrating outwardly from the center of the droplet toward the contact line in order to replenish evaporating solvent at this location.<sup>20,</sup>  
<sup>35</sup> The formation of a ring-like deposit and heterogeneous sample spreading is often unavoidable, but properties of this deposit may be controlled by altering the deposition environment.<sup>36</sup> Lubrication theory shows that if the evaporative flux of solvent can be driven away from the contact line, a uniform deposition can be achieved,<sup>37</sup> and this was successfully realized for fluorescence based proteomic arrays in which fixed, hydrophobic patterns were used to confine aqueous solutions and create uniform drying

profiles.<sup>38</sup> We used a modification of previously established methods<sup>23-24</sup> to photocatalytically pattern hydrophilic deposition areas with hydrophobic surroundings on BK-7 glass microscope slides and achieve even drying profiles of deposited AuNPs within each array spot (Figure E.1). While hydrophobic C18 layers may be applied directly to glass, the thin film of TiO<sub>2</sub> utilized in this and prior work is applied for its photocatalytic acceleration of C18 breakdown during UV treatment, decreasing fabrication time for this material.<sup>23-24</sup> The OTS monolayer, with a thickness of 2 – 3 nm,<sup>39-41</sup> functions as a hydrophobic corral for the nanoparticle suspensions, and is removed during the calcination step (Figure E.2). After deposition of the modified AuNP solutions, followed by heating of the entire microarray substrate in a furnace set at 450 °C, the physical properties were examined using scanning electron microscopy (SEM).

SEM images in Figure 3 reveal that the nanoparticles are remarkably evenly distributed throughout the entire array spot (dia. 800  $\mu$ m shown), and no ring-like deposit is observed along the defined spot edge. Increasing magnification of the arrayed AuNPs reveals a regular pattern of porosity, with a relatively high roughness across the surface of the material (Figure E.3). These features are beneficial; high surface area increases sample-loading capacity within smaller areas for MS analysis, and may confine heat to promote higher laser desorption/ionization performance.<sup>11, 15, 19, 23, 42</sup> For this microarray, we accomplished this through the addition of a high molecular weight (56 kDa) polyelectrolyte during AuNP modification, and by utilizing multiple ( $n = 9$ ), consecutive droplet depositions on the patterned glass slides. The high molecular weight PAH induces

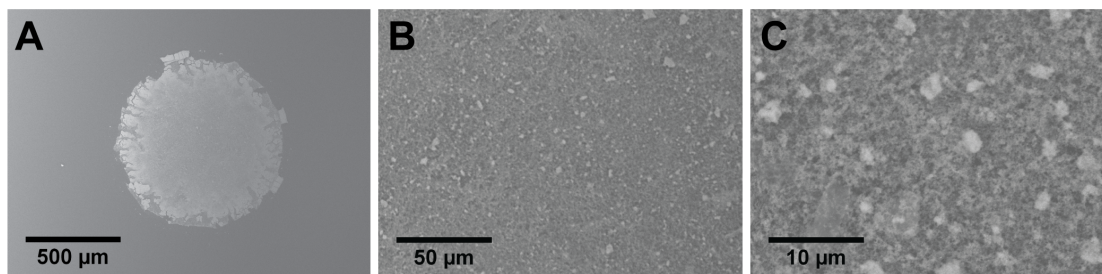


**Figure 6.3.** Scanning electron micrographs of arrayed and calcinated gold nanoparticles. (A) 100× magnification. (B) 1000× magnification. (C) 5000× magnification.

bridging flocculation of neighboring AuNPs, producing a regular pattern of AuNP clusters, or “flocs”, when deposited on the solid surface.<sup>22</sup> The resulting roughness and porosity are controllable, which is advantageous for high shot-to-shot reproducibility in mass spectra. Calcination permanently fixes these nanoscale (floc) and microscale (array spot) patterns in place on the glass slides, as the high temperature combusts the sacrificial polymer layers used for immobilization (PAH) and forms a dense network of silicate glass covering the AuNPs. Each (PAH-silicate)<sub>n</sub> layer results in *ca.* 2 nm of glass coating<sup>43</sup> and protects the nanoparticle morphologies during the calcination process, with individual diameters of *ca.* 13 nm retained after calcination and with varying layer numbers (Figure E.4). In addition to increasing the structural robustness of the nanoparticles, this nanoscale coating also confines heat at the AuNP surface for highly effective SALDI-MS performance.<sup>17</sup>

***Characterization of Arrayed AuNPs by SALDI-MS.*** Ionization of two peptides, [Sar<sup>1</sup>, Thr<sup>8</sup>]-angiotensin II (M1 = 956.1 Da) and neurotensin (M2 = 1672 Da) was carried out to demonstrate how the calcinated AuNP array performs for matrix-free laser desorption/ionization (LD/I) mass spectrometry. These peptides were applied as a mixture in the amount of 20 pmol and ionization was carried out at the same arbitrary

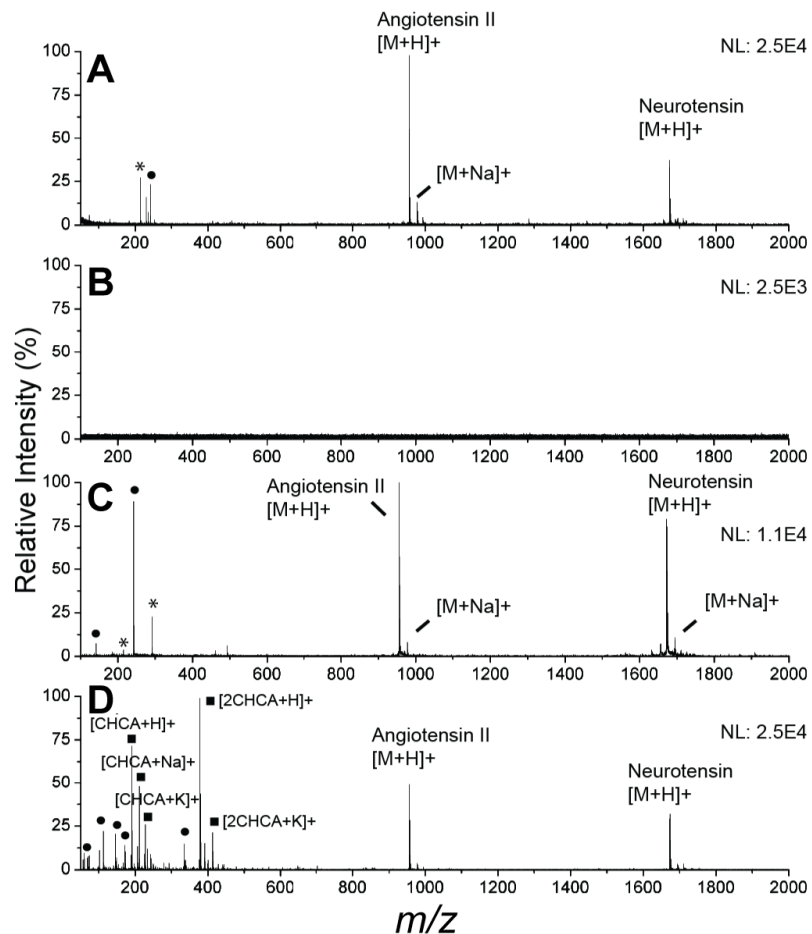


**Figure 6.4.** Ionization of [Sar<sup>1</sup>, Thr<sup>8</sup>]-angiotensin II and neurotensin from various laser desorption/ionization substrates at laser fluence of 1900 a.u. *S/N* ratios are given for the angiotensin II [ $M+H$ ]<sup>+</sup> peak. (A) Calcinated AuNP microarray (*S/N* = 72.0). (B) Bare AuNPs, with no silicate protection or calcination (no analyte signal). (C) Evaporated gold substrate with ca. 20 nm of silicate (*S/N* = 74.0). (D) CHCA matrix (*S/N* = 37.0).

laser fluence (1900 a.u.). The solutions are deposited on the calcinated AuNP array, along with several surfaces for comparison that include a bare AuNP array (bearing no silicate), an established SALDI material (46 nm evaporated Au, 20 nm silicate, see Appendix E for fabrication),<sup>19</sup> and a commercial, stainless steel MALDI plate. The mass spectra are shown in Figure 6.4. Only the peptides deposited on the commercial MALDI plate required an organic matrix for ionization, and in this study, CHCA proved suitable. While

the peptide solution was diluted in CHCA matrix for optimal signal, the amount of analyte applied to the plate remained constant (fixed 20 pmol peptides per 1  $\mu$ L spot). In the other substrates, which did not utilize a matrix, 10 mM citric acid was incorporated into the experimental solutions as an external proton donor to promote the formation of protonated ions over alkali-adducted ions.<sup>44</sup> Three peaks are prominent in each spectrum: the signals at  $m/z$  957, 978, and 1673 correspond to  $[M1+H]^+$ ,  $[M1+Na]^+$ , and  $[M2+H]^+$ , respectively, and all exhibit signal intensities that are within the same order of magnitude. The sodium adducted peak,  $[M1+Na]^+$ , appears in the spectra from the calcinated substrates (Figure 6.4A,C), which we have attributed to the sodium silicate precursor used during the array fabrication process. However, these were largely suppressed through competition of protons donated from citric acid, resulting in an ion intensity ratio of protonated ions to single sodium adducted ions greater than 7.5. Furthermore, all substrates tested showed little fragmentation of target analytes, indicating that the calcinated AuNP substrate functions effectively as a soft ionization source, with mass spectra that are simplified and easy to interpret.

AuNPs alone have served as an effective matrix for the desorption and ionization of biomolecules.<sup>14</sup> However, the nanoglassification process used in this work further improves the efficiency of LD/I and renders the material superior for chip-based, mass spectrometric characterizations. This is clearly demonstrated in comparing Figures 6.4A and 6.4B, in which the ultrathin silicate layer is present, and not present, respectively. In the absence of silicate (Figure 6.4B), no effective ionization of either peptide was achieved at the laser fluence used (1900 a.u.). While ionization is still possible on the

bare AuNP substrate, higher laser fluences are required. For all SALDI experiments involving the AuNPs, we used only one layer of silicate, as this demonstrated the best ionization performance compared to other silicate thicknesses. Further increases in thickness attenuated signal intensity, suggesting that heat generated at the nanoparticle surface is gradually subjected to insulation with thicker silicate layers. These findings were also supported by investigating the ionization of N-acetyl-tetradecapeptide renin substrate from AuNP-(PAH-silicate)<sub>1</sub> constructs before (Figure E.5A) and after calcination (Figure E.5B), where the calcinated substrate displayed a much higher ionization intensity and signal-to-noise (*S/N*) ratio (*S/N* of 5.5 and 60 in the uncalcinated and calcinated substrates, respectively). PAH has been shown to potentially act as an insulator during the LD/I process,<sup>15</sup> and will therefore further confine heat when left deposited with silicate. As PAH is removed during the calcination step, the overall insulation thickness is decreased by several nanometers, and tuned to optimal experimental conditions.

***Performance Toward Small Biomolecules and Reusability.*** Cholesterol and its oxidation products are important small molecules of broad interest, mainly due to their roles in atherosclerosis,<sup>45</sup> participation in a number of biosynthetic pathways,<sup>46</sup> and unique biophysical trafficking mechanisms.<sup>47</sup> Traditionally, one major drawback of MALDI-MS has been the presence of matrix-related ions at *m/z* <600, which convolute the spectra and make it difficult to discern meaningful data when ionizing small molecules in this mass range (*e.g.* sterols, hormones, amino acids, nucleic acids, and short chain carbohydrates). While sputtered silver films have successfully been used in

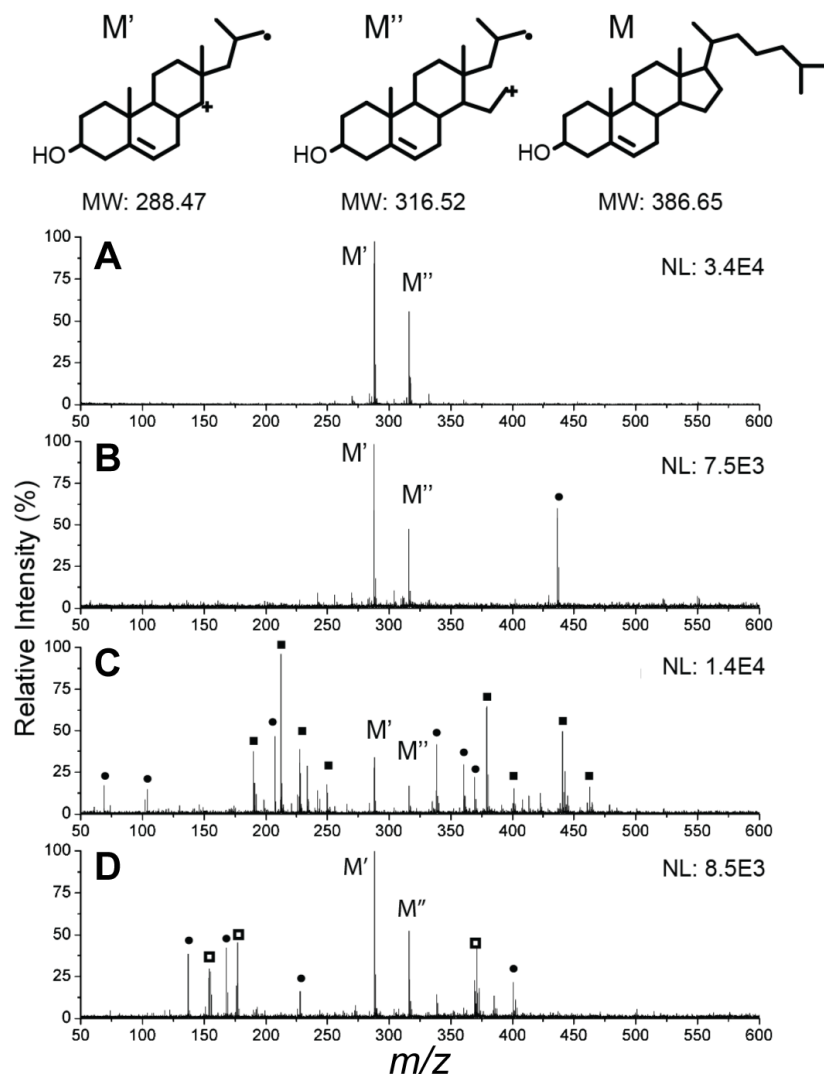


**Figure 6.5.** Ionization of cholesterol from various surfaces and matrices.  $S/N$  ratios are given for the M' peak. (A) Calcinated gold nanoparticle array ( $S/N = 70.0$ ). (B) Uncalcinated AuNP-(PAH-silicate)<sub>1</sub> construct ( $S/N = 35.5$ ). (C) CHCA matrix ( $S/N = 12.5$ ). (D) DHB matrix ( $S/N = 36.0$ ).

MALDI imaging for high resolution spatial mapping of cholesterol in tissues,<sup>48</sup> little success has been seen in ionizing cholesterol with gold nanomaterials, and with no matrix present. We have tested the ionization of cholesterol using the calcinated AuNP array and compared the results to those obtained from two common organic matrices to demonstrate the versatility of the calcinated film for small molecule detection and identification (Figure 6.5). Cholesterol is known to oxidize under LD/I mass

spectrometric methods, generating unique fragments and providing additional information for structural analysis and elucidation of various oxidation mechanisms.<sup>49-51</sup> The laser-induced oxidation products for cholesterol show distinct peaks in each spectrum at  $m/z$  288 and 316. The peaks in Figure 6.5A, corresponding to products ionized from the calcinated AuNP film, have a very clean background compared to those obtained from CHCA (Figure 6.5C) and DHB (Figure 6.5D) matrices. The uncalcinated AuNP-(PAH-silicate)<sub>1</sub> construct is also capable of generating a clean spectrum, albeit with slightly more background noise and lower absolute signal intensity (Figure 6.5B). It is clear that in the matrix-assisted ionization analyte detection is overwhelmed by CHCA fragments and clusters (Figure 6.5C), and while DHB seems to fare better for detection below  $m/z$  600, many interfering ions still remain which may prohibit a comprehensive analysis (Figure 6.5D).

Aside from the lack of matrix interference, one of the advantages of using chip-assisted ionization is the ability to reuse the substrate for repeated measurements, saving costs in materials. The microarray presented in this work is no exception, and was tested for reusability. We applied 2 pmol of [Sar<sup>1</sup>, Thr<sup>8</sup>]-angiotensin II to each array spot, and after a mass spectrum was obtained, the chip was rinsed with 0.1 M ammonia and DI water (Figure 6.6). Each time the surface is rinsed, no trace of the analyte remains, yet the signal can be regenerated within the same order of magnitude for subsequent measurements. The resulting signal abundance exhibits only an 8.4% relative standard deviation ( $n = 3$  surface regenerations), with no observable damage to the substrate induced by the source laser. This is vastly different from many SALDI structures that are

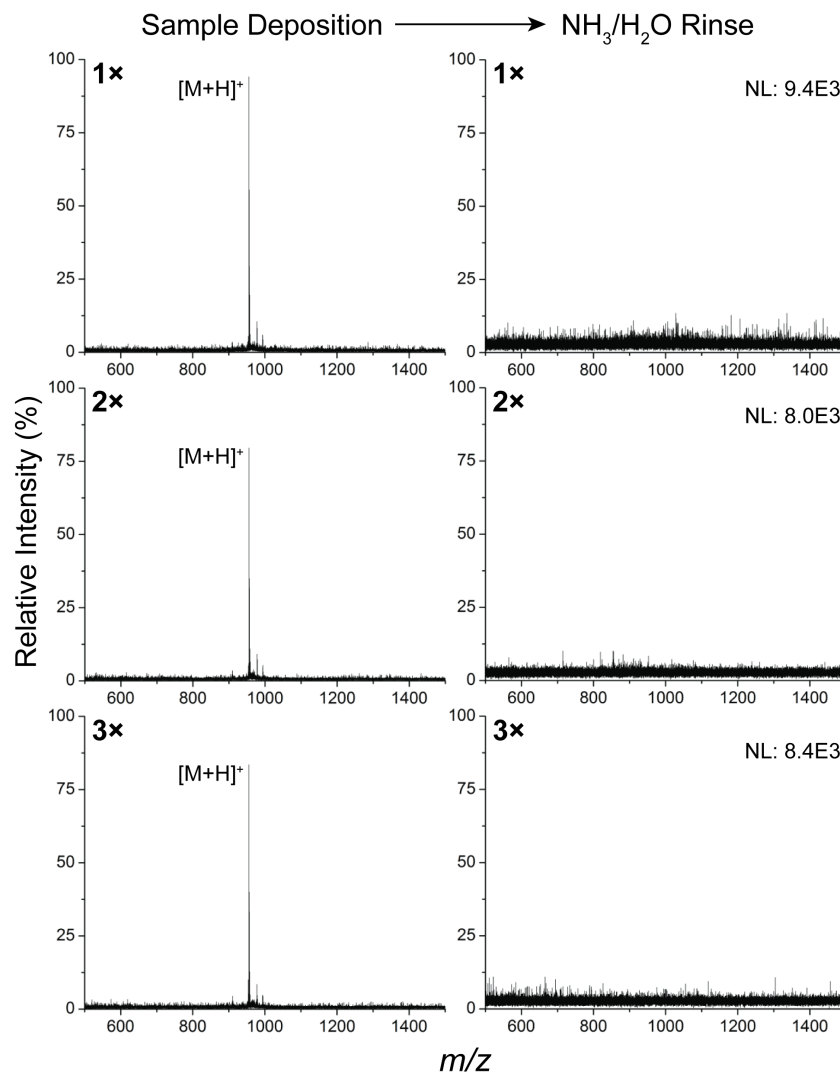


**Figure 6.6.** Reusability of the microarray. Ionization and rinsing of [Sar<sup>1</sup>, Thr<sup>8</sup>]-angiotensin II was repeated three times on the substrate, and the mass spectra for each deposition and rinse step is shown above. *S/N* is >35 for each deposition and regeneration.

often subjected to surface damage over repeated use, resulting in a decline of ionization performance.<sup>52-53</sup> The improved reusability is likely due to the fact that we require a much lower laser power for ionization compared to other SALDI materials, and due to the additional durability appended by the nano-silicate coating. The robust silicate coatings installed through the calcination process can in fact withstand significantly higher laser fluences than used here (up to 2500 a.u.), as we demonstrated in the previous

work<sup>18</sup>. Furthermore, the durability can be further increased through the application of long-chain monolayer coatings.<sup>18</sup>

The effect of laser fluence on the analyte signal abundance has previously been used to investigate LD/I efficiency from various SALDI materials,<sup>19, 54</sup> and we have applied this method to evaluate the performance of the calcinated AuNP array against CHCA. The laser fluence threshold for detecting measurable peptide signals on the calcinated AuNP array was determined to be 1450 a.u. (Figure E.6), which is 150 units lower than analytes ionized from CHCA, and 470 units lower than those ionized from our previously developed evaporated gold SALDI material.<sup>19</sup> In contrast, other SALDI structures, including porous silicon (DIOS) and porous alumina, possess much higher threshold laser fluences than CHCA.<sup>54</sup> This shows that the calcinated AuNP array developed here has a clear advantage compared to other nano- and micro-sized structures. In addition, this array exhibits comparable performance to common organic matrices for small and medium sized molecules. This is reflected in its sensitivity for [Sar<sup>1</sup>, Thr<sup>8</sup>]-angiotensin II, which exhibits a limit of detection in the low femtomole range on a Voyager-DE STR MALDI-TOF mass spectrometer. Ionization of this analyte at 20 fmol gives a *S/N* ratio of 12.8, and a discernable signal for 2 fmol of peptide can still be achieved without any pre-enrichment or concentration steps (Figure E.7).

***Mechanistic Investigations and Simulations.*** We have demonstrated that the calcinated AuNP array is capable of achieving sensitive mass spectrometric measurements for small molecular mass compounds. While the mechanism of LD/I on the calcinated AuNP microarray could be very complex, here we discuss some of the

factors that may contribute to the high LD/I efficiency observed. DIOS remains one of the most well studied systems for SALDI-MS, and it has been shown that DIOS performance benefits from the following features: confinement of heat within submicron sized gaps, crevices, and pores; effective heat transfer to analytes for desorption/ionization; and strong UV laser light absorption.<sup>12-13, 54-56</sup> Many of these properties align well with those of gold nanoparticle films, and Kawasaki et al. propose that during UV illumination, energy is absorbed by the interband transition of gold and converted to heat confined to the nanoparticle surface, causing analytes to thermally desorb from the material.<sup>15</sup> Here, due to polymer induced bridging flocculation of neighboring AuNPs, a high number of nanoscale gaps and crevices have been created to further confine heat generated during the LD/I process (Figure E.3), similar to other AuNP based SALDI materials.<sup>15-17</sup> The ultrathin silicate layer also provides heat confinement, mostly to individual AuNP clusters, so that this energy is not dissipated throughout the entire gold substrate but instead turned into localized “hot spots” for analytes to desorb from.<sup>19</sup> A fine balance appears to exist in heat confinement at the AuNP surface and total insulation, however. Increasing the thickness of this silicate layer beyond optimized conditions leads to lower LD/I efficiency, possibly due to isolation of heat transfer between the gold surface and the surrounding analyte medium, which has been seen in this and other work.<sup>19</sup>

In regards to absorption of UV light to produce heat, gold nanoparticles exhibit a reasonably high absorption coefficient in the UV range (Figure 6.2A) and it has been shown this is mainly due to interband transition of d-orbital electrons.<sup>57</sup> Following their

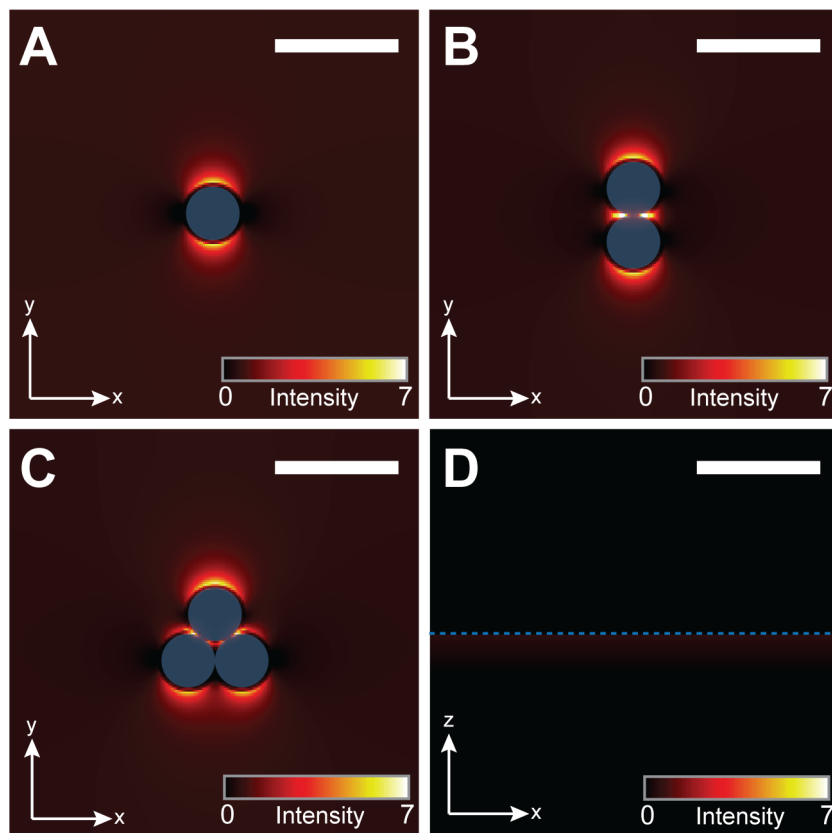


**Figure 6.7.** Numerical simulations of plasmonic fields induced by  $\lambda = 337$  nm light source for different nanoscale geometries. Scale bars represent 30 nm and blue represents the gold surface. (A) Single gold nanoparticle. (B) Gold nanoparticle dimer. (C) Gold nanoparticle trimer. (D) Planar gold film.

photoexcitation, these electrons undergo quick (picoseconds) relaxation back to ground state through electron-electron and electron-phonon collisions, generating heat at the nanoparticle surface.<sup>15, 57</sup> This photoexcitation/relaxation mechanism is not only applicable to gold nanoparticles, but also to gold thin films, which function as effective SALDI substrates when properly insulated.<sup>19</sup> Recently, the field of plasmon-induced hot carriers and engineered heating from metallic nanostructures has gained attention.<sup>58-59</sup> Following the excitation of a localized surface plasmon, resulting in a nanoparticle-localized, oscillating electromagnetic field, this resonance is non-radiatively damped by the creation of hot electron-hole pairs *via* a process termed Landau damping.<sup>60</sup> After

carrier relaxation, in which the hot electrons redistribute energy *via* electron-electron interactions within the metal, heat is generated and transferred from the nanoparticle to the surroundings, resulting in an overall process that ranges from 100 ps to 10 ns.<sup>58</sup> Given that the laser pulse width from our instrument is 3 ns, plasmon-induced excitation and heating may be allowed for within the provided timeframe, and in conjunction with the interband transition process. To test whether any plasmonic field exists for calcinated AuNP array structure at  $\lambda = 337$  nm (operating wavelength of the instrument's pulsed nitrogen laser), finite-difference time-domain (FDTD) simulations were conducted for various nanoparticle geometries consistent with the material developed here (Figure 6.7). While the electromagnetic fields are in general weaker than those excited at  $\lambda = 520$  nm (Figure E.8), there appear to be localized surface plasmons at  $\lambda = 337$  nm (Figure 6.7A-C) and the intensities vary according to cluster geometry. It is interesting to note that plasmonic fields at  $\lambda = 337$  nm are absent for the planar gold film (Figure 6.7D). These results suggest that for both isolated gold nanoparticles and their aggregated states, plasmonic fields are generated under UV illumination, which may subsequently undergo Landau damping and produce heat. While the interband transition proposed by Kawasaki et. al<sup>15</sup> for SALDI is likely the main source for localized heating, we speculate that the LSPR character of the AuNPs may also contribute, thereby enhancing ionization performance in comparison to planar thin film structures (as seen in Figure 6.4A,C).

## ■ CONCLUSIONS

The calcinated AuNP microarray represents an attractive tool for multiplexed analysis of biomolecules by SALDI-MS. The fabrication method is simple, and thus accessible to a wide audience, as no sophisticated cleanroom equipment is required. Layer-by-layer modification of the nanoparticles allows for nanoscale features that are easily tailored in a consistent fashion. This includes the formation of small AuNP clusters through selection of a suitable polyelectrolyte, and formation of a nanoscale layer of glass on the material surface. Performance was found to be better than many existing SALDI structures, and comparable to that of commonly used organic matrices. We attribute this to the rational design in the nanoscale morphology of the material, which has resulted in efficient heat transfer from the surface to the analyte. The more significant benefits this material has are less sample preparation and reusability of the substrate. As the accessibility of silane chemistry to the glassy surface allows for easy derivitization, the material may be further modified for on-chip enrichment, purification, and detection,<sup>18</sup> providing a multi-faceted and multifunctional substrate. The high performance reported here should inspire more widespread use of SALDI microarrays for higher throughput detection and characterization.

## ■ REFERENCES

- (1) National Research Council (U.S.). Committee on Toxicity Testing and Assessment of Environmental Agents., *Toxicity Testing in the 21st Century : A Vision and a Strategy*. National Academies Press: Washington, DC, **2007**; p 196.
- (2) Turner, A. P. F. Biosensors: Sense and Sensibility. *Chem. Soc. Rev.* **2013**, *42*, 3184-3196.
- (3) Zhu, H.; Bilgin, M.; Bangham, R.; Hall, D.; Casamayor, A.; Bertone, P.; Lan, N.; Jansen, R.; Bidlingmaier, S.; Houfek, T.; Mitchell, T.; Miller, P.; Dean, R. A.; Gerstein, M.; Snyder, M. Global Analysis of Protein Activities Using Proteome Chips. *Science* **2001**, *293*, 2101-2105.
- (4) Hoheisel, J. D. Microarray Technology: Beyond Transcript Profiling and Genotype Analysis. *Nat. Rev. Genet.* **2006**, *7*, 200-210.
- (5) Miller, M. B.; Tang, Y. W. Basic Concepts of Microarrays and Potential Applications in Clinical Microbiology. *Clin. Microbiol. Rev.* **2009**, *22*, 611-633.
- (6) Aebersold, R.; Goodlett, D. R. Mass Spectrometry in Proteomics. *Chem. Rev.* **2001**, *101*, 269-295.
- (7) Edwards, J. R.; Ruparel, H.; Ju, J. Y. Mass-Spectrometry DNA Sequencing. *Mutat. Res., Fundam. Mol. Mech. Mutagen.* **2005**, *573*, 3-12.
- (8) Clark, A. E.; Kaleta, E. J.; Arora, A.; Wolk, D. M. Matrix-Assisted Laser Desorption Ionization-Time of Flight Mass Spectrometry: A Fundamental Shift in the Routine Practice of Clinical Microbiology. *Clin. Microbiol. Rev.* **2013**, *26*, 547-603.
- (9) Kuo, H. Y.; DeLuca, T. A.; Miller, W. M.; Mrksich, M. Profiling Deacetylase Activities in Cell Lysates with Peptide Arrays and Samdi Mass Spectrometry. *Anal. Chem.* **2013**, *85*, 10635-10642.
- (10) Cohen, L. H.; Gusev, A. I. Small Molecule Analysis by Maldi Mass Spectrometry. *Anal. Bioanal. Chem.* **2002**, *373*, 571-586.

- (11) Buriak, J. M.; Wei, J.; Siuzdak, G. Desorption-Ionization Mass Spectrometry on Porous Silicon. *Nature* **1999**, *399*, 243-246.
- (12) Shen, Z. X.; Thomas, J. J.; Averbuj, C.; Broo, K. M.; Engelhard, M.; Crowell, J. E.; Finn, M. G.; Siuzdak, G. Porous Silicon as a Versatile Platform for Laser Desorption/Ionization Mass Spectrometry. *Anal. Chem.* **2001**, *73*, 612-619.
- (13) Xiao, Y. S.; Retterer, S. T.; Thomas, D. K.; Tao, J. Y.; He, L. Impacts of Surface Morphology on Ion Desorption and Ionization in Desorption Ionization on Porous Silicon (Dios) Mass Spectrometry. *J. Phys. Chem. C* **2009**, *113*, 3076-3083.
- (14) McLean, J. A.; Stumpo, K. A.; Russell, D. H. Size-Selected (2-10 Nm) Gold Nanoparticles for Matrix Assisted Laser Desorption Ionization of Peptides. *J. Am. Chem. Soc.* **2005**, *127*, 5304-5305.
- (15) Kawasaki, H.; Sugitani, T.; Watanabe, T.; Yonezawa, T.; Moriwaki, H.; Arakawa, R. Layer-by-Layer Self-Assembled Multilayer Films of Gold Nanoparticles for Surface-Assisted Laser Desorption/Ionization Mass Spectrometry. *Anal. Chem.* **2008**, *80*, 7524-7533.
- (16) Pilolli, R.; Ditaranto, N.; Di Franco, C.; Palmisano, F.; Cioffi, N. Thermally Annealed Gold Nanoparticles for Surface-Assisted Laser Desorption Ionisation-Mass Spectrometry of Low Molecular Weight Analytes. *Anal. Bioanal. Chem.* **2012**, *404*, 1703-11.
- (17) Chen, C.-Y.; Hinman, S. S.; Duan, J.; Cheng, Q. Nanoglassified, Optically-Active Monolayer Films of Gold Nanoparticles for in Situ Orthogonal Detection by Localized Surface Plasmon Resonance and Surface-Assisted Laser Desorption/Ionization-Ms. *Anal. Chem.* **2014**, *86*, 11942-11945.
- (18) Duan, J. C.; Wang, H.; Cheng, Q. On-Plate Desalting and Saldi-Ms Analysis of Peptides with Hydrophobic Silicate Nanofilms on a Gold Substrate. *Anal. Chem.* **2010**, *82*, 9211-9220.
- (19) Duan, J.; Linman, M. J.; Cheng, Q. Ultrathin Calcinated Films on a Gold Surface for Highly Effective Laser Desorption/Ionization of Biomolecules. *Anal. Chem.* **2010**, *82*, 5088-5094.

- (20) Deegan, R. D.; Bakajin, O.; Dupont, T. F.; Huber, G.; Nagel, S. R.; Witten, T. A. Capillary Flow as the Cause of Ring Stains from Dried Liquid Drops. *Nature* **1997**, *389*, 827-829.
- (21) Frens, G. Controlled Nucleation for the Regulation of the Particle Size in Monodisperse Gold Suspensions. *Nature* **1973**, *241*, 20-22.
- (22) Schneider, G.; Decher, G. Functional Core/Shell Nanoparticles Via Layer-by-Layer Assembly. Investigation of the Experimental Parameters for Controlling Particle Aggregation and for Enhancing Dispersion Stability. *Langmuir* **2008**, *24*, 1778-89.
- (23) Wang, H.; Duan, J. C.; Cheng, Q. Photocatalytically Patterned Tio<sub>2</sub> Arrays for on-Plate Selective Enrichment of Phosphopeptides and Direct Maldi Ms Analysis. *Anal. Chem.* **2011**, *83*, 1624-1631.
- (24) Addamo, M.; Augugliaro, V.; Di Paola, A.; Garcia-Lopez, E.; Loddo, V.; Marci, G.; Palmisano, L. Preparation and Photoactivity of Nanostructured Tio(2) Particles Obtained by Hydrolysis of Ticl(4). *Colloids Surf., A* **2005**, *265*, 23-31.
- (25) Decher, G. Fuzzy Nanoassemblies: Toward Layered Polymeric Multicomposites. *Science* **1997**, *277*, 1232-1237.
- (26) Willets, K. A.; Van Duyne, R. P. Localized Surface Plasmon Resonance Spectroscopy and Sensing. *Annu. Rev. Phys. Chem.* **2007**, *58*, 267-297.
- (27) Jensen, T. R.; Duval, M. L.; Kelly, K. L.; Lazarides, A. A.; Schatz, G. C.; Van Duyne, R. P. Nanosphere Lithography: Effect of the External Dielectric Medium on the Surface Plasmon Resonance Spectrum of a Periodic Array of Silver Nanoparticles. *J. Phys. Chem. B* **1999**, *103*, 9846-9853.
- (28) Haes, A. J.; Van Duyne, R. P. A Nanoscale Optical Biosensor: Sensitivity and Selectivity of an Approach Based on the Localized Surface Plasmon Resonance Spectroscopy of Triangular Silver Nanoparticles. *J. Am. Chem. Soc.* **2002**, *124*, 10596-10604.

- (29) Raschke, G.; Kowarik, S.; Franzl, T.; Sönnichsen, C.; Klar, T. A.; Feldmann, J.; Nichtl, A.; Kürzinger, K. Biomolecular Recognition Based on Single Gold Nanoparticle Light Scattering. *Nano Lett.* **2003**, *3*, 935-938.
- (30) Dahlin, A. B.; Jonsson, M. P.; Hook, F. Specific Self-Assembly of Single Lipid Vesicles in Nanoplasmonic Apertures in Gold. *Adv. Mater.* **2008**, *20*, 1436-1442.
- (31) Zhao, S. S.; Bichelberger, M. A.; Colin, D. Y.; Robitaille, R.; Pelletier, J. N.; Masson, J. F. Monitoring Methotrexate in Clinical Samples from Cancer Patients During Chemotherapy with a LSPR-Based Competitive Sensor. *Analyst* **2012**, *137*, 4742-4750.
- (32) Jackman, J. A.; Zhdanov, V. P.; Cho, N. J. Nanoplasmonic Biosensing for Soft Matter Adsorption: Kinetics of Lipid Vesicle Attachment and Shape Deformation. *Langmuir* **2014**, *30*, 9494-9503.
- (33) Yockell-Lelievre, H.; Bukar, N.; McKeating, K. S.; Arnaud, M.; Cosin, P.; Guo, Y.; Dupret-Carruel, J.; Mougin, B.; Masson, J. F. Plasmonic Sensors for the Competitive Detection of Testosterone. *Analyst* **2015**, *140*, 5105-5111.
- (34) Hu, J. B.; Chen, Y. C.; Urban, P. L. Coffee-Ring Effects in Laser Desorption/Ionization Mass Spectrometry. *Anal. Chim. Acta* **2013**, *766*, 77-82.
- (35) Deegan, R. D. Pattern Formation in Drying Drops. *Phys. Rev. E: Stat. Phys., Plasmas, Fluids, Relat. Interdiscip. Top.* **2000**, *61*, 475-485.
- (36) Deegan, R. D.; Bakajin, O.; Dupont, T. F.; Huber, G.; Nagel, S. R.; Witten, T. A. Contact Line Deposits in an Evaporating Drop. *Phys. Rev. E: Stat. Phys., Plasmas, Fluids, Relat. Interdiscip. Top.* **2000**, *62*, 756-765.
- (37) Fischer, B. J. Particle Convection in an Evaporating Colloidal Droplet. *Langmuir* **2002**, *18*, 60-67.
- (38) Li, Y.; McKenna, E. O.; Parkes, W.; Pitt, A. R.; Walton, A. J. The Application of Fixed Hydrophobic Patterns for Confinement of Aqueous Solutions in Proteomic Microarrays. *Appl. Phys. Lett.* **2011**, *99*.

- (39) Tillman, N.; Ulman, A.; Schildkraut, J. S.; Penner, T. L. Incorporation of Phenoxy Groups in Self-Assembled Monolayers of Trichlorosilane Derivatives - Effects on Film Thickness, Wettability, and Molecular-Orientation. *J. Am. Chem. Soc.* **1988**, *110*, 6136-6144.
- (40) Wasserman, S. R.; Tao, Y. T.; Whitesides, G. M. Structure and Reactivity of Alkylsiloxane Monolayers Formed by Reaction of Alkyltrichlorosilanes on Silicon Substrates. *Langmuir* **1989**, *5*, 1074-1087.
- (41) Vallant, T.; Brunner, H.; Mayer, U.; Hoffmann, H.; Leitner, T.; Resch, R.; Friedbacher, G. Formation of Self-Assembled Octadecylsiloxane Monolayers on Mica and Silicon Surfaces Studied by Atomic Force Microscopy and Infrared Spectroscopy. *J. Phys. Chem. B* **1998**, *102*, 7190-7197.
- (42) Nayak, R.; Knapp, D. R. Matrix-Free Ldi Mass Spectrometry Platform Using Patterned Nanostructured Gold Thin Film. *Anal. Chem.* **2010**, *82*, 7772-7778.
- (43) Phillips, K. S.; Han, J. H.; Martinez, M.; Wang, Z. Z.; Carter, D.; Cheng, Q. Nanoscale Glassification of Gold Substrates for Surface Plasmon Resonance Analysis of Protein Toxins with Supported Lipid Membranes. *Anal. Chem.* **2006**, *78*, 596-603.
- (44) Chen, C. T.; Chen, Y. C. Desorption/Ionization Mass Spectrometry on Nanocrystalline Titania Sol-Gel-Deposited Films. *Rapid Commun. Mass Spectrom.* **2004**, *18*, 1956-1964.
- (45) Kumar, N.; Singhal, O. P. Cholesterol Oxides and Atherosclerosis - a Review. *J. Sci. Food Agric.* **1991**, *55*, 497-510.
- (46) Rao, K. N. The Significance of the Cholesterol Biosynthetic-Pathway in Cell-Growth and Carcinogenesis (Review). *Anticancer Res.* **1995**, *15*, 309-314.
- (47) Ikonen, E. Cellular Cholesterol Trafficking and Compartmentalization. *Nat. Rev. Mol. Cell Biol.* **2008**, *9*, 125-138.
- (48) Dufresne, M.; Thomas, A.; Breault-Turcot, J.; Masson, J. F.; Chaurand, P. Silver-Assisted Laser Desorption Ionization for High Spatial Resolution Imaging Mass

Spectrometry of Olefins from Thin Tissue Sections. *Anal. Chem.* **2013**, 85, 3318-3324.

- (49) Andreu, I.; Bosca, F.; Sanchez, L.; Morera, I. M.; Camps, P.; Miranda, M. A. Efficient and Selective Photogeneration of Cholesterol-Derived Radicals by Intramolecular Hydrogen Abstraction in Model Dyads. *Org. Lett.* **2006**, 8, 4596-4600.
- (50) van den Brink, O. F.; Ferreira, E. S. B.; van der Horst, J.; Boon, J. J. A Direct Temperature-Resolved Tandem Mass Spectrometry Study of Cholesterol Oxidation Products in Light-Aged Egg Tempera Paints with Examples from Works of Art. *Int. J. Mass Spectrom.* **2009**, 284, 12-21.
- (51) McAvey, K. M.; Guan, B.; Fortier, C. A.; Tarr, M. A.; Cole, R. B. Laser-Induced Oxidation of Cholesterol Observed During Maldi-Tof Mass Spectrometry. *J. Am. Soc. Mass Spectrom.* **2011**, 22, 659-669.
- (52) Wada, Y.; Yanagishita, T.; Masudata, H. Ordered Porous Alumina Geometries and Surface Metals for Surface-Assisted Laser Desorption/Ionization of Biomolecules: Possible Mechanistic Implications of Metal Surface Melting. *Anal. Chem.* **2007**, 79, 9122-9127.
- (53) Alimpiev, S.; Grechnikov, A.; Sunner, J.; Karavanskii, V.; Simanovsky, Y.; Zhabin, S.; Nikiforov, S. On the Role of Defects and Surface Chemistry for Surface-Assisted Laser Desorption Ionization from Silicon. *J. Chem. Phys.* **2008**, 128.
- (54) Okuno, S.; Arakawa, R.; Okamoto, K.; Matsui, Y.; Seki, S.; Kozawa, T.; Tagawa, S.; Wada, Y. Requirements for Laser-Induced Desorption/Ionization on Submicrometer Structures. *Anal. Chem.* **2005**, 77, 5364-5369.
- (55) Li, J.; Lipson, R. H. Insights into Desorption Ionization on Silicon (Dios). *J. Phys. Chem. C* **2013**, 117, 27114-27119.
- (56) Alhmoud, H. Z.; Guinan, T. M.; Elnathan, R.; Kobus, H.; Voelcker, N. H. Surface-Assisted Laser Desorption/Ionization Mass Spectrometry Using Ordered Silicon Nanopillar Arrays. *Analyst* **2014**, 139, 5999-6009.

- (57) Shoji, M.; Miyajima, K.; Mafune, F. Ionization of Gold Nanoparticles in Solution by Pulse Laser Excitation as Studied by Mass Spectrometric Detection of Gold Cluster Ions. *J. Phys. Chem. C* **2008**, *112*, 1929-1932.
- (58) Brongersma, M. L.; Halas, N. J.; Nordlander, P. Plasmon-Induced Hot Carrier Science and Technology. *Nat. Nanotechnol.* **2015**, *10*, 25-34.
- (59) Govorov, A. O.; Richardson, H. H. Generating Heat with Metal Nanoparticles. *Nano Today* **2007**, *2*, 30-38.
- (60) Li, X. G.; Xiao, D.; Zhang, Z. Y. Landau Damping of Quantum Plasmons in Metal Nanostructures. *New J. Phys.* **2013**, *15*.

---

\*Reproduced from: Hinman, S. S., et al. Calcinated Gold Nanoparticle Arrays for On-Chip, Multiplexed and Matrix-Free Mass Spectrometric Analysis of Peptides and Small Molecules. *Nanoscale* **2016**, *8*, 1665-1675, with permission from the Royal Society of Chemistry.

## CHAPTER 7: 3D Printed Optical Biosensors

### ■ INTRODUCTION

Three-dimensional (3D) printing has revolutionized material production in many facets of society, from industry to consumer levels, as the technology enables the rapid translation of original ideas into physical objects, with minimal training or expertise required on behalf of the end user. Also termed additive manufacturing, 3D printing encompasses a variety of techniques capable of assembling 3D objects from digital files. These techniques may be divided into seven categories, which include: binder jetting, directed energy deposition, material extrusion, material jetting, powder bed fusion, sheet lamination, and vat photopolymerization.<sup>1</sup> Vat photopolymerization techniques, such as stereolithography, have been commercially available for the greatest amount of time,<sup>2</sup> and are competitive in terms of resolution and price (based on a laboratory budget). In stereolithography, a liquid resin consisting of photoactive monomers and oligomers is exposed to a focused light source, which polymerizes the final product in a controlled manner. This photopolymerization is most often catalyzed by a UV laser light source, and occurs one layer at a time to build up the final model. One disadvantage of the method is that only plastics can be assembled, while other methods, such as fused deposition modeling, are capable of utilizing plastics, ceramic, paper, and metal as the source material. However, recent developments in nanoparticle-integrated photopolymers are rendering stereolithographic printing of glass and metal embedded models possible.<sup>3</sup>

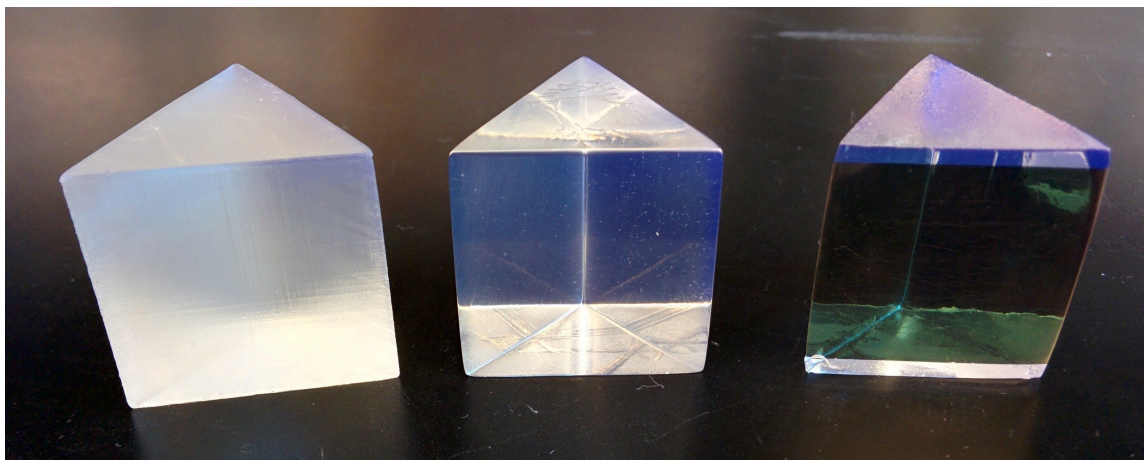


**Figure 7.1.** 3D printed equilateral prisms in various stages of fabrication. (Left) Prism has been printed and post-cured within a UV crosslinker. (Middle) Prism has been polished to optical clarity. (Right) After polishing, prism has been subjected to gold deposition via electron-beam evaporation.

In the analytical field, 3D printing has largely been exploited for the prototyping of fluidic devices and custom mechanical parts, which has been recently reviewed by several groups.<sup>4-6</sup> Sample handling has remained a common motif in analytical 3D printing, with the manufacturing of silica gel patterns for chromatography,<sup>7</sup> bacterial incubators,<sup>8</sup> solid phase extraction devices,<sup>9-10</sup> microfluidic sample preconcentrators,<sup>11</sup> and microchannel chips<sup>12-15</sup> previously demonstrated. There have been limited attempts to fabricate integrated biosensors and biorecognition elements into 3D printed devices,<sup>16</sup> with the majority of signal transduction being electrochemical.<sup>15, 17-18</sup> While optical detection within 3D printed devices has been noted, including chemiluminescence for detection of lactate<sup>19</sup> and cancer proteins,<sup>14</sup> a magnetic nanoparticle-embedded microplate with peroxidase mimicking characteristics,<sup>20</sup> and a low-volume cuvette with temperature control,<sup>21</sup> the act of guiding and manipulating light through 3D printed optics has evaded investigation.

Within this chapter, a stereolithographic approach for the manufacturing of optical components, notably high-quality, custom prisms, is presented. While direct 3D printing of equilateral prisms results in highly variable surface roughness, the application of affordable and accessible benchtop polishing procedures renders the photoplastic surface amenable to optical techniques requiring high precision, which we demonstrate in their use for surface plasmon resonance (SPR) biosensing (Figure 7.1). This approach not only allows for optics with individually dictatable geometry, but also negates the high costs that can be associated with many high refractive index glass components.

## ■ EXPERIMENTAL METHODS

**Materials and Reagents.** Gold (III) chloride trihydrate, *N*-(2-Hydroxyethyl)piperazine-*N'*-(2-ethanesulfonic acid) sodium salt (HEPES), poly(allylamine hydrochloride) (PAH, MW ~17.5 kDa), 3-mercaptopropanol (MPO), and cholera toxin from *Vibrio cholerae* (CT) were from Sigma Aldrich (St. Louis, MO). 1-oleoyl-2-palmitoyl-*sn*-glycero-3-phosphocholine (POPC) was from Avanti Polar Lipids (Alabaster, AL). Monosialoganglioside receptor GM<sub>1</sub> was from Matreya (Pleasant Gap, PA). Clear photoactive resin (GPCL02) was from Formlabs, Inc. (Somerville, MA). NOVUS 2 Fine Scratch Remover was from NOVUS Plastic Polish (St. Paul, MN). Glossy acrylic spray was from Rust-Oleum (Vernon Hills, IL). BK-7 ( $n = 1.517$ ) and SF2 ( $n = 1.648$ ) equilateral prisms were from Surplus Shed (Fleetwood, PA). Chromium and gold used for electron-beam evaporation were acquired as pellets of 99.99% purity from Kurt J. Lesker (Jefferson Hills, PA). 1×PBS was composed of 10 mM Na<sub>2</sub>HPO<sub>4</sub>, 1.8 mM

KH<sub>2</sub>PO<sub>4</sub>, 137 mM NaCl, 2.7 mM KCl, and titrated to pH 7.4. Nanopure water ( $\geq 18$  M $\Omega$ •cm), purified through a Barnstead E-Pure filtration system (Thermo Scientific, Rockford, IL), was used for all reagent preparations.

**Instrumentation.** Surface plasmon resonance (SPR) spectroscopy and imaging were conducted at room temperature (*ca.* 23 °C) on a homebuilt SPR imaging setup,<sup>22</sup> using nanopure water or 1×PBS as the running buffer set to a flow rate of 5 mL h<sup>-1</sup> (*ca.* 83  $\mu$ L min<sup>-1</sup>) unless otherwise noted. For real-time binding measurements, the incident angle was set to the position where the starting SPR reflectivity curve measured 30 %R, as the slope is highest at this location and changes in image contrast are greatest.<sup>23</sup> Absorbance spectra were collected using a USB 2000+ UV-Vis spectrometer with illumination from a HL-2000 Tungsten-Halogen light source guided through 200  $\mu$ m optical fibers (Ocean Optics, Dunedin, FL). FT-IR analysis was performed on a Nicolet 6700 spectrometer (Thermo Scientific, Rockville, IL), and ellipsometry was performed on a UVISEL M200 (Horiba Jobin Yvon, France). Scanning electron microscopy (SEM) was conducted on an FEI NNS450 SEM (Hillsboro, OR) in CFAMM at UC Riverside. Atomic force microscopy was conducted on a Veeco Dimension 5000 (Santa Barbara, CA) under tapping mode at a scan rate of 1 Hz.

**Stereolithography.** Prisms were designed in SketchUp (Trimble, Inc., Sunnyvale, CA), and uploaded to a commercial stereolithography printer, a Formlabs Form 2 (Somerville, MA), through manufacturer provided software. The Form 2 includes a 250 mW UV laser with 140  $\mu$ m spot size, and layer thickness was set to the highest resolution (25  $\mu$ m). When the automated process was complete, the cured prisms were washed in an

isopropanol bath, dried under compressed air, and subjected to a 1 h post-cure in a CL-1000 UV crosslinker (UVP Inc., Upland, CA). Final polishing was performed through a combination of wet sanding and buffer wheel/polishing compound treatment (Central Machinery, USA).

**Gold Nanofilm Preparation.** SPR active prisms were fabricated from BK-7, SF2, or 3D printed equilateral prisms ( $25 \times 25 \times 25$  mm). The prisms were first cleaned through copious rinsing with ethanol and isopropanol, and dried under compressed air. 2 nm of chromium ( $0.5 \text{ \AA s}^{-1}$ ), followed by 50 nm of gold ( $1.0 \text{ \AA s}^{-1}$ ) were then deposited on one face using electron-beam evaporation (Temescal, Berkeley, CA) at  $5 \times 10^{-6}$  Torr in a Class 1000 cleanroom facility (UCR Center for Nanoscale Science & Engineering). For supported lipid bilayer analysis, the 3D printed prisms were subsequently immersed in a 5 mM MPO solution (10% v/v ethanol) for 4 h, followed by rinsing with nanopure water and drying under a nitrogen stream.

**Gold Nanoraspberry Functionalization.** Gold nanoraspberries were synthesized using the method of Xie et al.<sup>24</sup> In brief, 500 mL of a 0.5 mM gold chloride solution was mixed with 25 mL of 0.1 M HEPES (pH 7.4), which was stirred for 1 h, then stored in amber bottles at 4 °C until use. 3D printed prisms were modified with the nanoraspberries using a modified layer-by-layer method.<sup>25</sup> The prism surface was rendered hydrophilic through a 2 min plasma treatment in a Harrick PDC-32G source set to an RF power of 18 W, then immediately placed in a  $2 \text{ mg mL}^{-1}$  PAH solution (pH 8.0) for 1 min. Thereafter, the surface was rinsed with nanopure water for 1 min and dried under a nitrogen stream. The nanoraspberries were applied to each surface and incubated in a humidity chamber for 4 h,

after which, excess nanoparticles were rinsed away with nanopure water and the prisms were once more dried under nitrogen.

## ■ RESULTS AND DISCUSSION

***Material Characterizations.*** A commercial, clear photoactive resin was used for prism fabrication, which consists of a proprietary mixture of methacrylated oligomers, a methacrylated monomer, and photoinitiator(s) according to the manufacturer.<sup>26</sup> Once cured, the material presumably resembles poly(methyl methacrylate) (PMMA) and is relatively transparent, as exhibited in Figure 7.1. Direct printing of equilateral prisms ( $25 \times 25 \times 25$  mm) resulted in a highly variable surface roughness, causing significant scattering of light passing through each face. Therefore, polishing methods that would reduce both surface roughness and optical scattering were explored. As the major constituent of the 3D printed prisms is plastic, and not glass, methods of shaping the surface are easily affordable and accessible. We thereby tested a commercial plastic polish, glossy acrylic spray, and benchtop polishing wheel for their efficacy in rendering each face optically smooth after an initial wet sanding (Figure 7.2). Each method was effective in reducing the surface roughness (rms,  $20 \times 20$   $\mu\text{m}$  areas,  $n = 3$ ) from the initial untreated value of 326 nm (Figure 7.2A), though to varying degrees. The plastic polish left a significant number of microscale scratches, blemishes, and defects in the surface, giving an average roughness of 55 nm (Figure 7.2B). While both the acrylic spray and polishing wheel methods resulted in much better appearances under naked eye and scanning electron microscopy, the polishing wheel fared best, giving the lowest

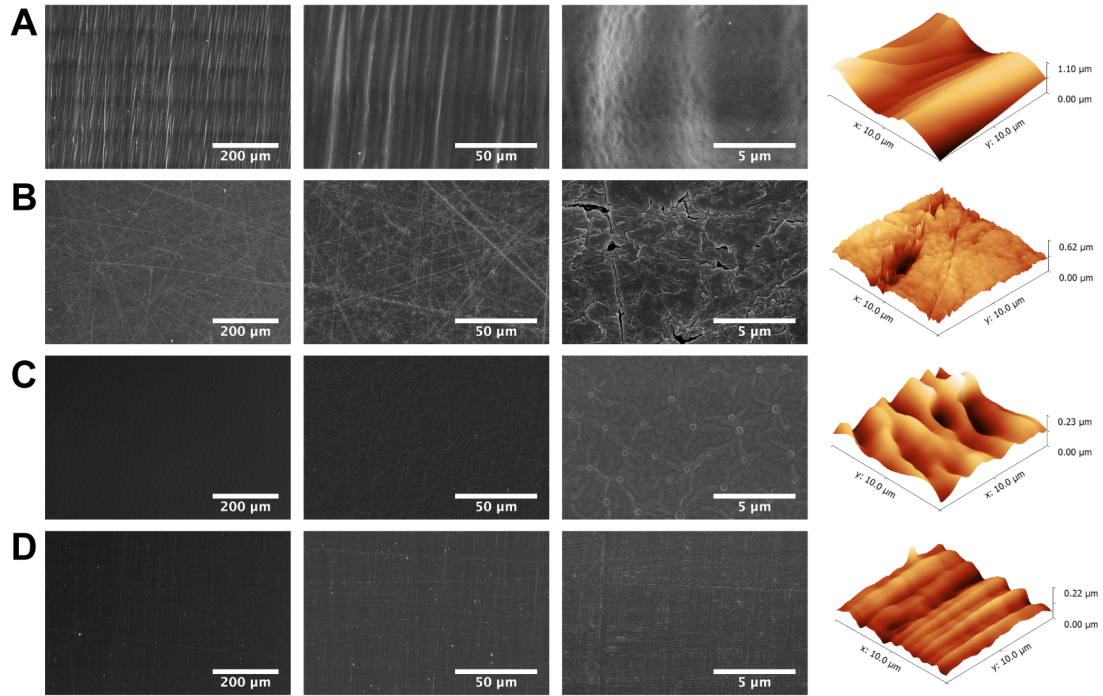


**Figure 7.2.** Effects of polishing treatments investigated by scanning electron microscopy and atomic force microscopy. (A) Untreated prism surface. (B-C) Wet sanding, followed by commercially obtained plastic polish (B), glossy acrylic spray (C), and benchtop polishing wheel (D).

roughness of 23 nm, and the acrylic spray, 41 nm. Beyond these attributes, the polishing wheel was the least labor intensive and circumvented the application of additional material layers, as was the case for the acrylic spray, and was therefore chosen as optimal.

Optical characterizations confirmed the similarity of the cured substrate to PMMA, which were performed through ellipsometry and fourier transform-infrared (FT-IR) spectroscopy. The complex refractive index ( $n$ ) and extinction coefficient ( $k$ ), determined through reflection ellipsometry, are exhibited in Figure 7.3A. Both curves follow standard Cauchy or Sellmeier distributions, albeit with increased noise, which we attribute to residual surface roughness from our polishing process. The obtained values match closely with those obtained for PMMA from other research groups, with the

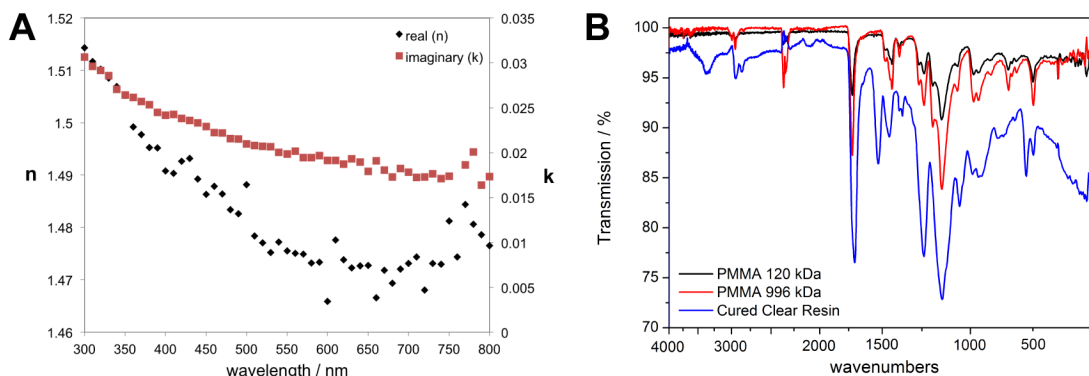


**Figure 7.3.** Optical characterizations. (A) Ellipsometry measurements of complex refractive index ( $n$ ) and extinction coefficient ( $k$ ). (B) FT-IR spectra of cured resin and PMMA standards.

refractive index at  $\lambda = 650$  nm (common for SPR) of the 3D printed material being 1.475, and other groups reporting a refractive indices in the range of 1.48 – 1.49.<sup>27-28</sup> The small discrepancy in  $n$  could be explained by slight variations in the chemical composition of PMMA and the clear photopolymer. While not an exhaustive method, FT-IR is capable of shedding some light on the chemical bonds present. The FT-IR spectra of the cured resin and two PMMA standards of varying molecular weight are provided in Figure 7.3B. While there are multiple overlapping bands, particularly within the 500 – 2000  $\text{cm}^{-1}$  region, there is also a modest amount of discrepancies that do not overlap. These are most likely manifesting from vibrationally active functional groups attached to the photoinitiator that are not present in the native PMMA polymer.

**3D Printed Surface Plasmon Resonance Sensors.** Sensing with light guiding materials is commonplace, and we demonstrate the ability of the 3D printed prisms to do so through surface plasmon resonance (SPR) assays. The basis of SPR is the surface plasmon polariton (SPP), which propagates along a planar, nanoscale gold surface in resonance with an incident light source of matching angular frequency.<sup>29</sup> High-refractive

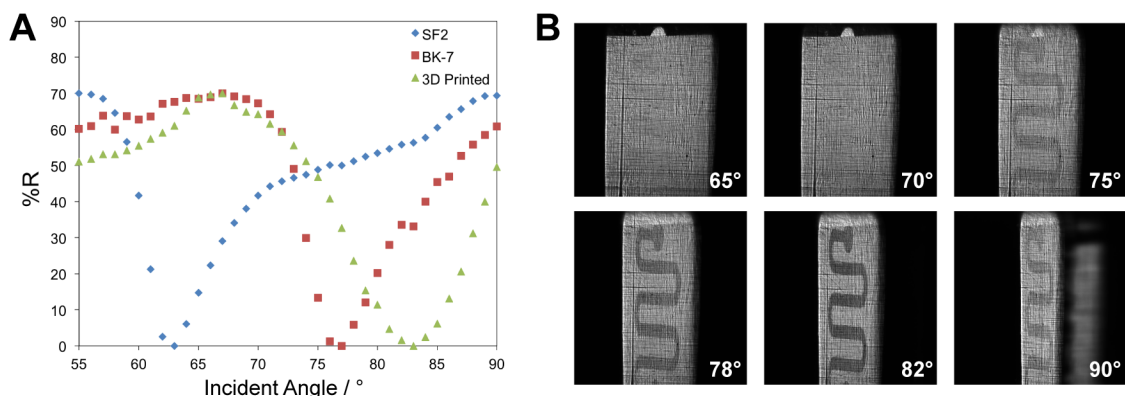


**Figure 7.4.** Surface plasmon resonance activity of 3D printed prisms. (A) Reflectivity curves of 50 nm gold deposited on SF2, BK-7, and 3D printed equilateral prisms. (B) SPR images of PDMS flow channel filled with water under angular interrogation on the gold-coated 3D printed prism surface.

index prisms are typically used to increase the momentum of incident light and fulfill the resonance matching conditions,<sup>30</sup> and must be smooth enough to allow SPP propagation parallel to the surface. 50 nm gold films were evaporated on one face of the 3D printed prisms, and reflectivity spectra are provided in Figure 7.4A, with BK-7 and SF2 materials included for comparison. The dip in reflectivity *ca.* 82° is indicative of SPP generation and optimal matching of the resonance conditions (*e.g.* incident wavelength and angle), which, under this experimental configuration,<sup>31</sup> only occurs through a prism-mediated increase in the wavevector of incident light. Also notable in the spectrum is the critical angle *ca.* 66°, at which light within the prism meets the conditions for total internal reflection. The BK-7 and SF2 prisms, typically used in SPR, show similar patterns though with reflectivity minima occurring at lower incident angles, which are the result of their higher indices of refraction, being 1.517 and 1.648, respectively. There is minimal sacrifice in quality between the 3D printed and commercially obtained prisms for SPR, which can be seen in the SPR images within Figure 7.4B. The reflected images across the SPR active surface are continuous and uniform, with the microchannel flow

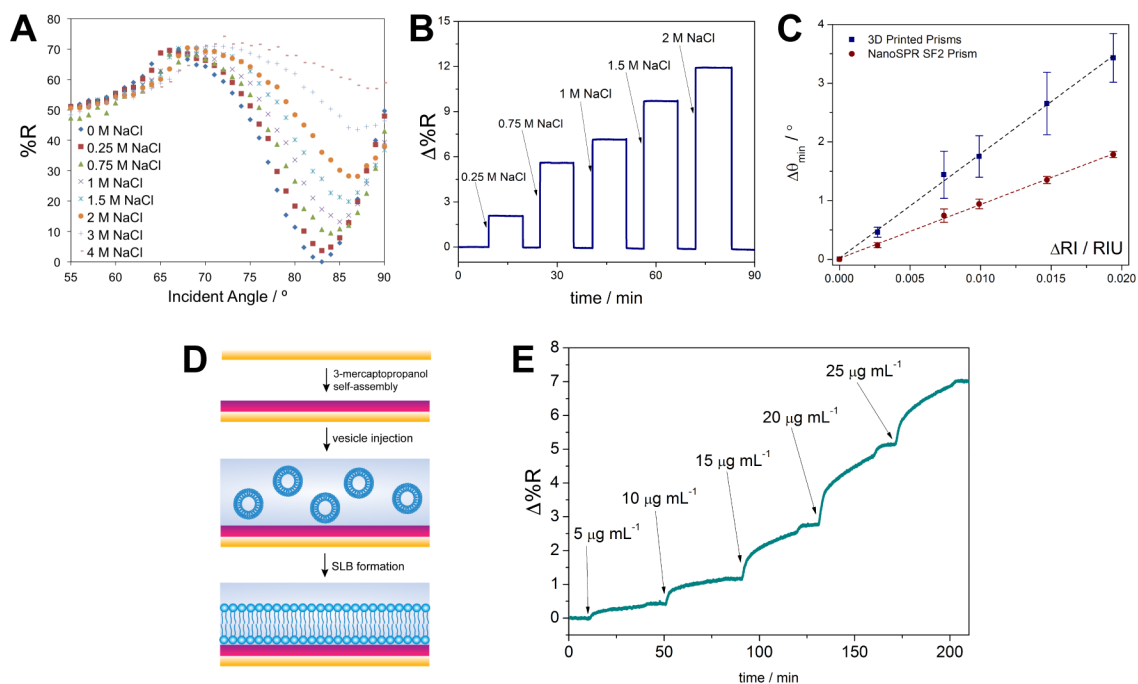


**Figure 7.5.** 3D printed prisms as surface plasmon resonance sensors. (A) Reflectivity spectra of refractive index sensitivity. (B) Real-time monitoring of NaCl injections. (C) Angular refractive index sensitivity compared to a commercial instrument. (D) Approach for supported membrane formation. (E) Biosensing response to cholera toxin on a ganglioside impregnated lipid membrane.

cell used throughout these experiments clearly defined. The difference in contrast between the flow cell and background areas is due to the dielectric sensitive nature of SPR, as the flow cell medium (*i.e.* water) and channel defining material (*i.e.* PDMS) possess significantly different refractive indices of 1.333 and *ca.* 1.4, respectively.

As SPR owes its biosensing capabilities to its dependence on the refractive index of the dielectric near the sensor surface, the refractive index sensitivity was evaluated and compared to a commercial SPR instrument. Static injections of sodium chloride solutions possessing varying indices of refraction ( $n = 1.333 - 1.350$ ) over the gold film were used to establish a rough sensor calibration, and the reflectivity spectra are provided in Figure 7.5A. With each increase in NaCl concentration, the SPR reflectivity dip shifts towards a

higher incident angle and intensity. These injections can be monitored in real-time through either parameter, with a plot of time against  $\Delta\%R$  (*i.e.* normalized intensity) provided in Figure 7.5B. The background noise is remarkably low in this sensorgram, suggesting that the gold-coated 3D printed prisms may perform well for ultrasensitive SPR detection. When the bulk sensitivity was compared to a commercial instrument, the 3D printed prisms performed notably better, which is attributed to the lower refractive index of the cured photopolymer, affecting the SPR resonance conditions and working range of the sensor (Figure 7.5C).<sup>32</sup>

A biosensor for cholera toxin was constructed on the 3D printed, SPR-active surface, using a biomimetic lipid membrane of phosphocholine with the ganglioside receptor, GM<sub>1</sub>, embedded. The prisms were immersed in a mercaptopropanol solution to form a self-assembled monolayer prior to conducting the assay, rendering the gold surface hydrophilic and allowing for supported lipid membrane formation (Figure 7.5D).<sup>33</sup> Utilization of supported membranes is beneficial as they may incorporate specific recognition elements, including native, physiological receptors, while minimizing nonspecific binding from non-target species.<sup>34</sup> The SPR results for cholera toxin binding to this interface are shown in Figure 7.5E. Binding patterns are strong and specific, and more importantly, comparable to established SPR sensors for cholera toxin.<sup>35-36</sup>

***Versatile Sensing Regimes: Dove Prisms.*** An important advantage of 3D printing optical materials is the ability to custom tailor designs to the task at hand. Variations of SPR have included the use of dove prisms, which allow for the arrangement of optical

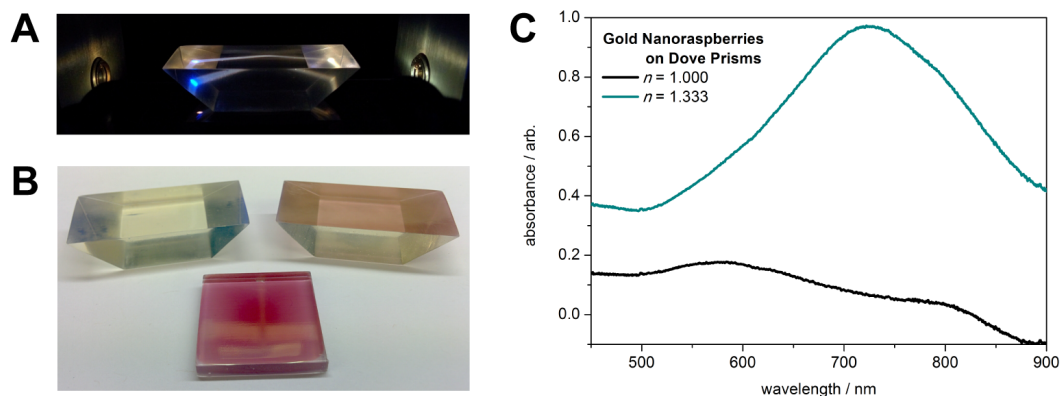


**Figure 7.6.** Localized surface plasmon resonance (LSPR) sensing with 3D printed dove prisms. (A) Optical setup with 3D printed dove prism. (B) Gold nanoraspberry coatings applied to the cured surface. (C) LSPR absorbance spectra of nanoparticles attached to the surface under air and water.

components along a single axis, simplifying the instrumental setup.<sup>37-38</sup> Moreover, gold nanoparticles have been utilized in place of evaporated gold films on these surfaces, circumventing the need for cleanroom facilities and vacuum equipment in sensor fabrication.<sup>39</sup> 3D printing of dove prisms capable of total internal reflection was performed, with the short face measuring  $22 \times 20$  mm, and the long face measuring  $42 \times 20$  mm. The height of the incident light source was manually tuned to allow for total internal reflection within the prism and transmission to the spectrometer along the same axis (Figure 7.6A). Gold nanoraspberries were applied to the surface using a modified layer-by-layer protocol (Figure 7.6B),<sup>25</sup> and the absorbance spectra of the nanoparticle coated prisms under air and water are provided in Figure 7.6C. For each spectrum, background absorbance of an uncoated prism was subtracted. Consistent with standard localized surface plasmon resonance (LSPR) mechanisms, the nanoparticle absorbance peak increases in wavelength and intensity with increasing dielectric refractive index (*e.g.* air to water transfer).<sup>40</sup> This proof-of-concept experiment provides evidence that not only

may prisms be fabricated on-demand through 3D printing, but full sensing materials may be constructed from them entirely using benchtop procedures, thus increasing sensor accessibility to a wide audience of researchers with varying technical backgrounds.

## ■ CONCLUSIONS

While the technology behind 3D printing is still open to improvements, including higher print resolutions and decreased costs, at present the fabrication of 3D printed optics is entirely possible, and potentially, preferred over the purchasing of more expensive materials depending on the application. With 3D printed prisms of varying geometry demonstrated for SPR and LSPR, the construction of optical biosensing materials has been rendered accessible to a large scientific audience. There are indeed instances where more expensive high-refractive index glass materials are more desirable, though researchers will certainly benefit from the rapid prototyping capabilities offered by 3D printing prior to committing greater time and costs to these products. With commercial printer costs ever decreasing, we anticipate wide adoption of these techniques for 3D printed optical components, sensors, and light-guiding regimes.

## ■ REFERENCES

- (1) Standard Terminology for Additive Manufacturing - General Principles - Terminology. ASTM International: **2015**.
- (2) Hull, C. W., Apparatus for Production of Three-Dimensional Objects by Stereolithography. Google Patents: **1986**.
- (3) Kotz, F.; Arnold, K.; Bauer, W.; Schild, D.; Keller, N.; Sachsenheimer, K.; Nargang, T. M.; Richter, C.; Helmer, D.; Rapp, B. E. Three-Dimensional Printing of Transparent Fused Silica Glass. *Nature* **2017**, *544*, 337-+.
- (4) Zhang, Y.; Ge, S. G.; Yu, J. H. Chemical and Biochemical Analysis on Lab-on-a-Chip Devices Fabricated Using Three-Dimensional Printing. *TrAC, Trends Anal. Chem.* **2016**, *85*, 166-180.
- (5) Gross, B.; Lockwood, S. Y.; Spence, D. M. Recent Advances in Analytical Chemistry by 3D Printing. *Anal. Chem.* **2017**, *89*, 57-70.
- (6) Gross, B. C.; Erkal, J. L.; Lockwood, S. Y.; Chen, C. P.; Spence, D. M. Evaluation of 3D Printing and Its Potential Impact on Biotechnology and the Chemical Sciences. *Anal. Chem.* **2014**, *86*, 3240-3253.
- (7) Fichou, D.; Morlock, G. E. Open-Source-Based 3D Printing of Thin Silica Gel Layers in Planar Chromatography. *Anal. Chem.* **2017**, *89*, 2116-2122.
- (8) Glatzel, S.; Hezwani, M.; Kitson, P. J.; Gromski, P. S.; Schurer, S.; Cronin, L. A Portable 3D Printer System for the Diagnosis and Treatment of Multidrug-Resistant Bacteria. *Chem* **2016**, *1*, 494-504.
- (9) Kataoka, E. M.; Murer, R. C.; Santos, J. M.; Carvalho, R. M.; Eberlin, M. N.; Augusto, F.; Poppi, R. J.; Gobbi, A. L.; Hantao, L. W. Simple, Expendable, 3D-Printed Microfluidic Systems for Sample Preparation of Petroleum. *Anal. Chem.* **2017**, *89*, 3460-3467.

- (10) Belka, M.; Ulenberg, S.; Baczek, T. Fused Deposition Modeling Enables the Low-Cost Fabrication of Porous, Customized-Shape Sorbents for Small-Molecule Extraction. *Anal. Chem.* **2017**, *89*, 4373-4376.
- (11) Su, C. K.; Peng, P. J.; Sun, Y. C. Fully 3D-Printed Preconcentrator for Selective Extraction of Trace Elements in Seawater. *Anal. Chem.* **2015**, *87*, 6945-6950.
- (12) Au, A. K.; Bhattacharjee, N.; Horowitz, L. F.; Chang, T. C.; Folch, A. 3D-Printed Microfluidic Automation. *Lab Chip* **2015**, *15*, 1934-1941.
- (13) Chan, H. N.; Shu, Y. W.; Xiong, B.; Chen, Y. F.; Chen, Y.; Tian, Q.; Michael, S. A.; Shen, B.; Wu, H. K. Simple, Cost-Effective 3D Printed Microfluidic Components for Disposable, Point-of-Care Colorimetric Analysis. *ACS Sensors* **2016**, *1*, 227-234.
- (14) Tang, C. K.; Vaze, A.; Rusling, J. F. Automated 3D-Printed Unibody Immunoarray for Chemiluminescence Detection of Cancer Biomarker Proteins. *Lab Chip* **2017**, *17*, 484-489.
- (15) Duarte, L. C.; Chagas, C. L. S.; Ribeiro, L. E. B.; Coltro, W. K. T. 3D Printing of Microfluidic Devices with Embedded Sensing Electrodes for Generating and Measuring the Size of Microdroplets Based on Contactless Conductivity Detection. *Sensors and Actuators B: Chemical*.
- (16) Mandon, C. A.; Blum, L. J.; Marquette, C. A. Adding Biomolecular Recognition Capability to 3D Printed Objects. *Anal. Chem.* **2016**, *88*, 10767-10772.
- (17) Gowers, S. A. N.; Curto, V. F.; Seneci, C. A.; Wang, C.; Anastasova, S.; Vadgama, P.; Yang, G. Z.; Boutelle, M. G. 3D Printed Microfluidic Device with Integrated Biosensors for Online Analysis of Subcutaneous Human Microdialysate. *Anal. Chem.* **2015**, *87*, 7763-7770.
- (18) Loo, A. H.; Chua, C. K.; Pumera, M. DNA Biosensing with 3D Printing Technology. *Analyst* **2017**, *142*, 279-283.

- (19) Roda, A.; Guardigli, M.; Calabria, D.; Calabretta, M. M.; Cevenini, L.; Michelini, E. A 3D-Printed Device for a Smartphone-Based Chemiluminescence Biosensor for Lactate in Oral Fluid and Sweat. *Analyst* **2014**, *139*, 6494-6501.
- (20) Su, C.-K.; Chen, J.-C. Reusable, 3D-Printed, Peroxidase Mimic-Incorporating Multi-Well Plate for High-Throughput Glucose Determination. *Sensors and Actuators B: Chemical* **2017**, *247*, 641-647.
- (21) Pisaruka, J.; Dymond, M. K. A Low Volume 3D-Printed Temperature-Controllable Cuvette for UV Visible Spectroscopy. *Analytical Biochemistry* **2016**, *510*, 52-55.
- (22) Wilkop, T.; Wang, Z. Z.; Cheng, Q. Analysis of Mu-Contact Printed Protein Patterns by SPR Imaging with a LED Light Source. *Langmuir* **2004**, *20*, 11141-11148.
- (23) Nelson, B. P.; Frutos, A. G.; Brockman, J. M.; Corn, R. M. Near-Infrared Surface Plasmon Resonance Measurements of Ultrathin Films. 1. Angle Shift and SPR Imaging Experiments. *Anal. Chem.* **1999**, *71*, 3928-3934.
- (24) Xie, J. P.; Lee, J. Y.; Wang, D. I. C. Seedless, Surfactantless, High-Yield Synthesis of Branched Gold Nanocrystals in HEPES Buffer Solution. *Chem. Mater.* **2007**, *19*, 2823-2830.
- (25) Chen, C.-Y.; Hinman, S. S.; Duan, J.; Cheng, Q. Nanoglassified, Optically-Active Monolayer Films of Gold Nanoparticles for in Situ Orthogonal Detection by Localized Surface Plasmon Resonance and Surface-Assisted Laser Desorption/Ionization-MS. *Anal. Chem.* **2014**, *86*, 11942-11945.
- (26) Clear Photoactive Resin for Form 1, Form 1+ and Form 2 Safety Data Sheet. [https://formlabs.com/media/upload/Clear-SDS\\_u324bsC.pdf](https://formlabs.com/media/upload/Clear-SDS_u324bsC.pdf) (accessed May 22nd, 2017).
- (27) Sultanova, N.; Kasarova, S.; Nikolov, I. Dispersion Properties of Optical Polymers. *Acta Phys. Pol., A* **2009**, *116*, 585-587.

- (28) Beadie, G.; Brindza, M.; Flynn, R. A.; Rosenberg, A.; Shirk, J. S. Refractive Index Measurements of Poly(Methyl Methacrylate) (PMMA) from 0.4-1.6  $\mu\text{m}$ . *Appl Optics* **2015**, *54*, F139-F143.
- (29) Couture, M.; Zhao, S. S.; Masson, J. F. Modern Surface Plasmon Resonance for Bioanalytics and Biophysics. *Phys. Chem. Chem. Phys.* **2013**, *15*, 11190-11216.
- (30) Homola, J.; Yee, S. S.; Gauglitz, G. Surface Plasmon Resonance Sensors: Review. *Sens. Actuators, B* **1999**, *54*, 3-15.
- (31) Kretschmann, E.; Raether, H. Radiative Decay of Non Radiative Surface Plasmons Excited by Light. *Naturforsch., A: Astrophys., Phys. Phys. Chem.* **1968**, *23*, 2135-2136.
- (32) Gupta, G.; Kondoh, J. Tuning and Sensitivity Enhancement of Surface Plasmon Resonance Sensor. *Sens. Actuators, B* **2007**, *122*, 381-388.
- (33) Wang, Z. Z.; Wilkop, T.; Han, J. H.; Dong, Y.; Linman, M. J.; Cheng, Q. Development of Air-Stable, Supported Membrane Arrays with Photolithography for Study of Phosphoinositide - Protein Interactions Using Surface Plasmon Resonance Imaging. *Anal. Chem.* **2008**, *80*, 6397-6404.
- (34) Phillips, K. S.; Han, J. H.; Martinez, M.; Wang, Z. Z.; Carter, D.; Cheng, Q. Nanoscale Glassification of Gold Substrates for Surface Plasmon Resonance Analysis of Protein Toxins with Supported Lipid Membranes. *Anal. Chem.* **2006**, *78*, 596-603.
- (35) Hinman, S. S.; Ruiz, C. J.; Drakakaki, G.; Wilkop, T. E.; Cheng, Q. On-Demand Formation of Supported Lipid Membrane Arrays by Trehalose-Assisted Vesicle Delivery for SPR Imaging. *ACS Appl. Mater. Interfaces* **2015**, *7*, 17122-17130.
- (36) Hinman, S. S.; McKeating, K. S.; Cheng, Q. DNA Linkers and Diluents for Ultrastable Gold Nanoparticle Bioconjugates in Multiplexed Assay Development. *Anal. Chem.* **2017**, *89*, 4272-4279.
- (37) Bolduc, O. R.; Live, L. S.; Masson, J. F. High-Resolution Surface Plasmon Resonance Sensors Based on a Dove Prism. *Talanta* **2009**, *77*, 1680-1687.

- (38) Zhao, S. S.; Bukar, N.; Toulouse, J. L.; Pelechacz, D.; Robitaille, R.; Pelletier, J. N.; Masson, J. F. Miniature Multi-Channel SPR Instrument for Methotrexate Monitoring in Clinical Samples. *Biosens. Bioelectron.* **2015**, *64*, 664-670.
- (39) Yockell-Lelievre, H.; Lussier, F.; Masson, J. F. Influence of the Particle Shape and Density of Self-Assembled Gold Nanoparticle Sensors on LSPR and SERS. *J. Phys. Chem. C* **2015**, *119*, 28577-28585.
- (40) Willets, K. A.; Van Duyne, R. P. Localized Surface Plasmon Resonance Spectroscopy and Sensing. *Annu. Rev. Phys. Chem.* **2007**, *58*, 267-297.

## **CHAPTER 8: Future Biomaterial and Interface Directions**

### **■ INTRODUCTION**

This dissertation has focused on the use of surface plasmon resonance sensors, coupled with nanotechnology and mass spectrometry, for the detection and characterization of environmentally relevant toxins. Core to this work are the utilization of novel interfaces and materials that render these methods applicable to a growing audience. While great effort has been made to establish the methods outlined here, there will always be room for expansion and growth; furthermore, additional questions have been raised that may provide the foundation for future innovations in the field.

### **■ LIPID MEMBRANES AND SURFACE PLASMON RESONANCE**

While certainly not new,<sup>1</sup> the use of surface plasmon resonance for supported lipid membrane studies has been slow to catch on with biophysical researchers, who are more likely to use the quartz crystal microbalance (QCM) technique.<sup>2-5</sup> This may be explained, in part, by the longstanding notion that SPR spectrometers are expensive and highly specialized pieces of laboratory equipment, as the BIAcore<sup>®</sup> product line has remained despite its high performance and sensitivity. Moreover, the concept of an evanescently decaying electromagnetic field, with short (< 200 nm) penetration depths, may appear, at first glance, difficult to design sensors around. However, as noted in Chapter 1, there are many cost-effective and portable SPR spectrometers becoming popular that exhibit high performance in comparison with their historic counterparts. The

Affinité P4SPR instrument,<sup>6</sup> for example, has demonstrated its use within field settings and hospital clinics, with untrained technicians obtaining comparable results to specialized SPR researchers.<sup>7-8</sup> With increasing equipment options and innovations in optical configurations, both instrumental costs and questions regarding widespread utility of the technique are sure to decrease. In regards to designing effective sensors within the SPR sensor penetration depth, the development of nanoscale glass surfaces is still relatively new.<sup>9</sup> QCM sensors provide much greater penetration depths in their measurements, and thus, less specialized equipment and techniques are required to render the surface hydrophilic for supported membrane formation. Ideally, the method developments for LSPR (Chapter 5), SPR (Chapters 2, 3, 4, 7), and SPR imaging (Chapters 3 – 4) will provide sufficient evidence that lipid membrane sensor design is quite versatile and facile for plasmonic techniques, and thereby inspire adoption by other biophysical researchers; however, this remains to be seen.

While the reasons behind its slow adoption may not be entirely clear, plasmonic techniques for supported membrane interrogation are definitely here to stay, gaining traction with each research generation. The Höök research group has been instrumental in these developments beginning with their introduction of plasmonic nanohole sensors capable of supporting lipid bilayers and capturing isolated lipid vesicles.<sup>10-12</sup> Many other groups have adopted these LSPR based methods, including the Dahlin research group in Sweden<sup>13-14</sup> and the Cho research group in Singapore.<sup>4, 15-16</sup> These researchers have explored the hyphenated utilization of QCM and LSPR measurements to establish complementary analytical information.<sup>4, 17</sup> While these methods do provide the same type

of label-free data, utilizing their respective penetration depths for measurements has allowed researchers to pinpoint the z-axis location of binding and diffusion limited events. Tethered liposomes have also remained an active topic within the SPR community, having recently gained attention as both enhancement agents and model surfaces.<sup>18-19</sup> These areas have been the topics of several recent and major reviews, with many more sure to come.<sup>20-21</sup>

Collaborations with membrane adjacent researchers may be critical in expansion of these techniques, and an example of this type of effort was demonstrated in Chapter 2. The Peng group has been exceptionally successful in the development of novel self-assembling lipid compounds for drug delivery,<sup>22-24</sup> and the research undertaken with model lipid systems investigated under SPR was able to confirm many theories of how these constructs interact with the plasma membrane, eventually leading to the creation of a new, hybrid material. Continued experimental collaborations with this group are ongoing, with research directions including the exploration of other synthetic molecule interactions, and the creation of new supramolecular constructs that may have implications for both drug delivery and sensing.

One significant benefit of SPR techniques is their ability to multiplex through imaging analysis, greatly increasing the informational power. The methods developed in Chapter 3 should solidify the foothold of SPR imaging within membrane science, as individually addressable arrays may now be created. Utilization of this on-demand SLB array formation scheme has been extremely convenient throughout further dissertation work, particularly assisting in strengthening the claims within Chapter 4. However, they

were also recently helpful in another collaborative effort involving membrane-embedded synthetic cavitand arrays.<sup>25</sup> Further work in this area is ongoing, with the possibility of antibody immobilization through membrane-embedded cavitand recognition, which would benefit from high-throughput analysis in a manner that is analogous to conventional antibody arrays.

## ■ EXPANSION OF TREHALOSE MEDIATED PRESERVATION

Anhydrobiosis has existed as a part of nature for far longer than humans have been developing analytical assays.<sup>26</sup> As we are just beginning to understand this process from a molecular standpoint, further insights may allow for significant advances in preservation schemes for long-term storage of assay components, with the possibility for resource-limited field and point-of-care deployment. Initial investigation into this area began with the work of Wilkop et al., in which trehalose was applied to preserve unilamellar vesicles for fluorescence measurement.<sup>27</sup> The work conducted in Chapter 3 expanded the utility of these methods for label-free lipid membrane arrays supported by a variety of surfaces, hydrophilic and hydrophobic. A novel frontier in this line is the preservation of tethered lipid bilayer arrays displaying a plethora of complex embedded biomolecules. While tethered lipid bilayers have been explored for many years,<sup>2</sup> the integration of cultured cell derived membranes with near-native protein mobility has only been recently demonstrated.<sup>5,28</sup> Key to these methods are the generation of giant plasma membrane vesicles (GPMVs), which are formed through an apoptotic mechanism as cultured cells are exposed to a high calcium containing buffer.<sup>29</sup> Costello et al. optimized

methods for generating SLBs from GPMVs, and while embedded receptors could be preserved, transmembrane protein mobility was still questionable. These methods were refined in subsequent years through fusion of GPMV-derived liposomes with PEG conjugated liposomes. Application of these to a hydrophilic support tethered the bilayers through a PEG cushion, raising them from the surface and allowing for the retention of embedded transmembrane protein mobility and activity.<sup>28</sup> A natural expansion of this work could include the determination of whether trehalose is also capable of preserving the shape of PEG-conjugated liposomes toward tethered membrane formation, and if so, whether protein activity could also be preserved as part of this process. Such work could result in the fabrication of cell membrane arrays, which would significantly impact the fields of membrane and cancer biology.

While solution based analytical methods were largely unexplored throughout this dissertation (with the exception of some of the nanoparticle work in Chapter 4), trehalose-mediated preservation schemes could also have important implications in this area. For one, trehalose and many other sugars have been noted as cryoprotectants against freezing and lyophilization.<sup>30</sup> Moreover, integration of liposomes into standard assays with trehalose protection may have the potential to extend their storage capabilities. Liposomes have many published techniques for loading with a variety of biomolecular components,<sup>31</sup> and have been suggested to function as molecular vessels on the attoliter scale.<sup>32</sup> Loading vesicles with standard assay constituents (*e.g.* dyes, enzymes, *etc.*) followed by their desiccation with trehalose could ensure their dispersion in the aqueous state within each vesicle, thereby preserving structure and function. Verification of

biological activity retention, as well as the investigation of other environmental effects (*e.g.* temperature, pressure, *etc.*), would be imperative toward assessing the limits of trehalose-mediated preservation with liposome assistance.

## ■ FINAL THOUGHTS: MULTIFUNCTIONAL MATERIAL DEVELOPMENT

Expanding the utility of these proposed methods will likely require new developments in the engineering and materials science areas of assay design. 3D printing is still a relatively young field,<sup>33</sup> though with many early and clear demonstrations throughout analytical science.<sup>34</sup> The research undertaken in Chapter 7 expands the range of this toolkit to optical components, rendering surface plasmon resonance sensors accessible to a very wide audience. Further innovations in this area will include determining the range of parts that can be effectively manufactured by 3D printing (*e.g.* lenses, other prism geometries), development of new photoactive resins possessing higher indices of refraction, and the printing of optical devices with integrated fluidics and predefined sample inputs. The latter area is under active investigation within our research group. On the other hand, utilization of established fabrication techniques toward hyphenation with other instrumentation is also beneficial, for which preliminary demonstrations have been provided in Chapters 5 and 6. Mass spectrometry has been a long-proven and powerful method, and removing the necessity of an externally applied matrix to bridge these measurements with SPR improves the capabilities of both methods. As all of the above areas continue to progress, informational gaps will continue to shrink toward a better understanding of complex biological interactions.

## ■ REFERENCES

- (1) Plant, A. L. Supported Hybrid Bilayer Membranes as Rugged Cell Membrane Mimics. *Langmuir* **1999**, *15*, 5128-5135.
- (2) Castellana, E. T.; Cremer, P. S. Solid Supported Lipid Bilayers: From Biophysical Studies to Sensor Design. *Surf. Sci. Rep.* **2006**, *61*, 429-444.
- (3) Cho, N. J.; Frank, C. W.; Kasemo, B.; Hook, F. Quartz Crystal Microbalance with Dissipation Monitoring of Supported Lipid Bilayers on Various Substrates. *Nat. Protoc.* **2010**, *5*, 1096-1106.
- (4) Ferhan, A. R.; Jackman, J. A.; Cho, N. J. Integration of Quartz Crystal Microbalance-Dissipation and Reflection-Mode Localized Surface Plasmon Resonance Sensors for Biomacromolecular Interaction Analysis. *Anal. Chem.* **2016**, *88*, 12524-12531.
- (5) Richards, M. J.; Hsia, C. Y.; Singh, R. R.; Haider, H.; Kumpf, J.; Kawate, T.; Daniel, S. Membrane Protein Mobility and Orientation Preserved in Supported Bilayers Created Directly from Cell Plasma Membrane Blebs. *Langmuir* **2016**, *32*, 2963-2974.
- (6) Affinité Instruments - SPR Innovations. <http://affiniteinstruments.com/> (accessed May 17th, 2017).
- (7) Zhao, S. S.; Bukar, N.; Toulouse, J. L.; Pelechacz, D.; Robitaille, R.; Pelletier, J. N.; Masson, J. F. Miniature Multi-Channel SPR Instrument for Methotrexate Monitoring in Clinical Samples. *Biosens. Bioelectron.* **2015**, *64*, 664-670.
- (8) Brule, T.; Granger, G.; Bukar, N.; Deschenes-Rancourt, C.; Harvard, T.; Schmitzer, A. R.; Martel, R.; Masson, J. F. Field-Deployed Surface Plasmon Resonance (SPR) Sensors for RDX Quantification in Environmental Waters. *Analyst* **2017**, DOI: 10.1039/c7an00216e.
- (9) Phillips, K. S.; Han, J. H.; Martinez, M.; Wang, Z. Z.; Carter, D.; Cheng, Q. Nanoscale Glassification of Gold Substrates for Surface Plasmon Resonance Analysis of Protein Toxins with Supported Lipid Membranes. *Anal. Chem.* **2006**, *78*, 596-603.

- (10) Dahlin, A.; Zach, M.; Rindzevicius, T.; Kall, M.; Sutherland, D. S.; Hook, F. Localized Surface Plasmon Resonance Sensing of Lipid-Membrane-Mediated Biorecognition Events. *J. Am. Chem. Soc.* **2005**, *127*, 5043-5048.
- (11) Jonsson, M. P.; Jonsson, P.; Dahlin, A. B.; Hook, F. Supported Lipid Bilayer Formation and Lipid-Membrane-Mediated Biorecognition Reactions Studied with a New Nanoplasmonic Sensor Template. *Nano Lett.* **2007**, *7*, 3462-3468.
- (12) Dahlin, A. B.; Jonsson, M. P.; Hook, F. Specific Self-Assembly of Single Lipid Vesicles in Nanoplasmonic Apertures in Gold. *Adv. Mater.* **2008**, *20*, 1436-1442.
- (13) Rupert, D. L. M.; Shelke, G. V.; Emilsson, G.; Claudio, V.; Block, S.; Lasser, C.; Dahlin, A.; Lotvall, J. O.; Bally, M.; Zhdanov, V. P.; Hook, F. Dual-Wavelength Surface Plasmon Resonance for Determining the Size and Concentration of Sub-Populations of Extracellular Vesicles. *Anal. Chem.* **2016**, *88*, 9980-9988.
- (14) Junesch, J.; Emilsson, G.; Xiong, K. L.; Kumar, S.; Sannomiya, T.; Pace, H.; Voros, J.; Oh, S. H.; Bally, M.; Dahlin, A. B. Location-Specific Nanoplasmonic Sensing of Biomolecular Binding to Lipid Membranes with Negative Curvature. *Nanoscale* **2015**, *7*, 15080-15085.
- (15) Zan, G. H.; Jackman, J. A.; Kim, S. O.; Cho, N. J. Controlling Lipid Membrane Architecture for Tunable Nanoplasmonic Biosensing. *Small* **2014**, *10*, 4828-4832.
- (16) Jackman, J. A.; Zhdanov, V. P.; Cho, N. J. Nanoplasmonic Biosensing for Soft Matter Adsorption: Kinetics of Lipid Vesicle Attachment and Shape Deformation. *Langmuir* **2014**, *30*, 9494-9503.
- (17) Dahlin, A. B.; Jonsson, P.; Jonsson, M. P.; Schmid, E.; Zhou, Y.; Hook, F. Synchronized Quartz Crystal Microbalance and Nanoplasmonic Sensing of Biomolecular Recognition Reactions. *ACS Nano* **2008**, *2*, 2174-2182.
- (18) Fenzl, C.; Hirsch, T.; Baeumner, A. J. Liposomes with High Refractive Index Encapsulants as Tunable Signal Amplification Tools in Surface Plasmon Resonance Spectroscopy. *Anal. Chem.* **2015**, *87*, 11157-11163.

- (19) Fenzl, C.; Genslein, C.; Domonkos, C.; Edwards, K. A.; Hirsch, T.; Baeumner, A. J. Investigating Non-Specific Binding to Chemically Engineered Sensor Surfaces Using Liposomes as Models. *Analyst* **2016**, *141*, 5265-5273.
- (20) Fenzl, C.; Hirsch, T.; Baeumner, A. J. Nanomaterials as Versatile Tools for Signal Amplification in (Bio)Analytical Applications. *TrAC, Trends Anal. Chem.* **2016**, *79*, 306-316.
- (21) Jackman, J. A.; Rahim Ferhan, A.; Cho, N. J. Nanoplasmonic Sensors for Biointerfacial Science. *Chem. Soc. Rev.* **2017**, DOI: 10.1039/c6cs00494f.
- (22) Yu, T. Z.; Liu, X. X.; Bolcato-Bellemin, A. L.; Wang, Y.; Liu, C.; Erbacher, P.; Qu, F. Q.; Rocchi, P.; Behr, J. P.; Peng, L. An Amphiphilic Dendrimer for Effective Delivery of Small Interfering RNA and Gene Silencing in Vitro and in Vivo. *Angew. Chem., Int. Ed.* **2012**, *51*, 8478-8484.
- (23) Wei, T.; Chen, C.; Liu, J.; Liu, C.; Posocco, P.; Liu, X.; Cheng, Q.; Huo, S.; Liang, Z.; Fermeglia, M.; Pricl, S.; Liang, X. J.; Rocchi, P.; Peng, L. Anticancer Drug Nanomicelles Formed by Self-Assembling Amphiphilic Dendrimer to Combat Cancer Drug Resistance. *Proc. Natl. Acad. Sci. U. S. A.* **2015**, *112*, 2978-2983.
- (24) Liu, X. X.; Liu, C.; Zhou, J. H.; Chen, C.; Qu, F. Q.; Rossi, J. J.; Rocchi, P.; Peng, L. Promoting siRNA Delivery Via Enhanced Cellular Uptake Using an Arginine-Decorated Amphiphilic Dendrimer. *Nanoscale* **2015**, *7*, 3867-3875.
- (25) Perez, L.; Mettry, M.; Hinman, S. S.; Byers, S. R.; McKeating, K. S.; Caulkins, B. G.; Cheng, Q.; Hooley, R. J. Selective Protein Recognition in Supported Lipid Bilayer Arrays by Tailored, Dual-Mode Deep Cavitand Hosts. *Soft Matter* **2017**, DOI: 10.1039/c7sm00192d.
- (26) Crowe, J. H.; Hoekstra, F. A.; Crowe, L. M. Anhydrobiosis. *Annu. Rev. Physiol.* **1992**, *54*, 579-599.
- (27) Wilkop, T. E.; Sanborn, J.; Oliver, A. E.; Hanson, J. M.; Parikh, A. N. On-Demand Self-Assembly of Supported Membranes Using Sacrificial, Anhydrobiotic Sugar Coats. *J. Am. Chem. Soc.* **2014**, *136*, 60-63.

- (28) Pace, H.; Simonsson Nystrom, L.; Gunnarsson, A.; Eck, E.; Monson, C.; Geschwindner, S.; Snijder, A.; Hook, F. Preserved Transmembrane Protein Mobility in Polymer-Supported Lipid Bilayers Derived from Cell Membranes. *Anal. Chem.* **2015**, 87, 9194-9203.
- (29) Sezgin, E.; Kaiser, H. J.; Baumgart, T.; Schwille, P.; Simons, K.; Levental, I. Elucidating Membrane Structure and Protein Behavior Using Giant Plasma Membrane Vesicles. *Nat. Protoc.* **2012**, 7, 1042-1051.
- (30) Alkilany, A. M.; Abulateefeh, S. R.; Mills, K. K.; Yaseen, A. I. B.; Hamaly, M. A.; Alkhatib, H. S.; Aiedeh, K. M.; Stone, J. W. Colloidal Stability of Citrate and Mercaptoacetic Acid Capped Gold Nanoparticles Upon Lyophilization: Effect of Capping Ligand Attachment and Type of Cryoprotectants. *Langmuir* **2014**, 30, 13799-13808.
- (31) *Liposomes: Methods and Protocols, Volume 2: Biological Membrane Models*. 1 ed.; Humana Press: New York, NY, **2010**; Vol. 606, p XVI, 548.
- (32) Stamou, D.; Duschl, C.; Delamarche, E.; Vogel, H. Self-Assembled Microarrays of Attoliter Molecular Vessels. *Angew. Chem., Int. Ed.* **2003**, 42, 5580-5583.
- (33) Gross, B. C.; Erkal, J. L.; Lockwood, S. Y.; Chen, C. P.; Spence, D. M. Evaluation of 3D Printing and Its Potential Impact on Biotechnology and the Chemical Sciences. *Anal. Chem.* **2014**, 86, 3240-3253.
- (34) Gross, B.; Lockwood, S. Y.; Spence, D. M. Recent Advances in Analytical Chemistry by 3D Printing. *Anal. Chem.* **2017**, 89, 57-70.

## APPENDIX A: Supporting Information for Chapter 2

### ■ MOLECULAR SIMULATION METHODS

#### *Dissipative Particle Dynamics (DPD) and Mesoscopic Bead-Field Hybrid (MBFH)*

**Method.** The simulations in this paper are based on DPD, a mesoscopic coarse-grained simulation method routinely employed for soft materials and biomembrane-containing system calculations.<sup>1-2</sup> The DPD particles (or beads), each representing a group of small molecules or extensive molecular fragments, interact by conservative, dissipative, and random forces, which are pairwise additive.<sup>3</sup> The net force acting on a bead  $i$  can be expressed as  $F_i = \sum_{j \neq i} (F_{ij}^C + F_{ij}^D + F_{ij}^R)$  and is calculated by summation over all other particles within a certain cutoff radius,  $r_c$ , which gives the extent of the interaction range.  $r_c$ ,  $m$ , and  $k_B T$  are the unit distance, the particle mass, and the thermal energy, respectively.

The conservative force represents the excluded volume interactions between particles  $i$  and  $j$  in the dimensionless form  $F_{ij}^C = a_{ij} (1 - r_{ij}) \hat{r}_{ij}$ , where  $r_{ij} = r_i - r_j$ ,  $r_{ij} = |r_{ij}|$ ,  $\hat{r}_{ij} = r_{ij}/r_{ij}$ ,  $a_{ij}$  is the maximum repulsion between particles  $i$  and  $j$ . The dissipative,  $F_{ij}^D = -\gamma \omega(r_{ij})^2 (\hat{r}_{ij} \cdot v_{ij}) \hat{r}_{ij}$ , and random forces,  $F_{ij}^R = \sigma \omega(r_{ij}) \hat{r}_{ij} \zeta / (\delta t)^{1/2}$ , act as heat sink and source, respectively, and the combined effect of the two forces performs as a thermostat, where  $\gamma$  is a friction coefficient related to the thermal noise amplitude  $\sigma$  via the fluctuation–dissipation theorem,  $\sigma^2 = 2\gamma k_B T$ ,  $\omega(r)$  is a weight function,  $\zeta$  is a normally distributed random variable with zero mean and unit variance that is uncorrelated for

different particle pairs,  $\delta t$  is the time step of an integration scheme, and  $v_{ij} = v_i - v_j$  is the relative velocity of the  $i^{\text{th}}$  and the  $j^{\text{th}}$  particles. The equations of particle motion,  $dr_i/dt = v_i$  and  $dv_i/dt = F_i$ , are solved using as integration scheme the velocity-Verlet algorithm.

Finally, when modeling chains two additional forces are acting between bonded beads: a harmonic spring connecting two adjacent particles  $i$  and  $j$   $F_{ij}^b = k_b(r_{ij} - r_0) \hat{r}_{ij}$ , where  $k_b$  is a spring constant and  $r_0$  the equilibrium distance between the particles, and  $F_{ijz}^{\theta} = 1/2 k_{\theta} (1 - \cos(\theta_{ij} - \theta_0))$ , where  $k_{\theta}$  is a spring constant and  $\theta_0$  the equilibrium angle between adjacent beads triples  $ijz$  in a row.

In addition, large scale simulations of hybrid liposomes were performed employing the MBFH method<sup>4</sup> as implemented in *Culgi* (v.9.0, Culgi B.V., Leiden, The Netherlands). From a conceptual viewpoint, the hybrid method allows for different representations of constituents, either coordinate-based (bead) or continuous (bead concentration fields) in a single simulation volume, thus combining the computational efficiency of a field description (for the abundant solvent) with the explicit particle model (for the lipids and dendrons) and overcoming the restrictions of the individual methods. Thus, the MBF-hybrid free energy combines the free energy of a pure field-based system,  $F^f[\{\rho_j\}]$ , the potential energy of a pure particle-based system  $V^B(\{r_i\})$ , and a hybrid coupling interaction free energy  $F^{Cp}[\{\rho_j\}, \{r_i\}]$ . The free energy is:

$$F = F^f[\{\rho_j\}] + V^B(\{r_i\}) + F^{Cp}[\{\rho_j\}, \{r_i\}]$$

The explicit expression for the coupling free energy is:

$$F^{Cp} = \sum_{jk} c_{ji} \int_V \rho_j K(|r - r'_i|) dr$$

which introduces the hybrid coupling parameters  $c_{ji}$  for the binary interaction between a particle  $i$  and a field  $j$ ;  $K$  is a normalized Gaussian kernel.

Accordingly, the total force acting on a bead  $i$  consists in the same forces in DPD plus the new coupling force  $F_i^{Cp}$ , defined as:

$$F_i^{Cp} = - \sum_j c_{ji} \nabla K dr$$

and the contribution to the mean-field chemical potential is:

$$\mu_{MF_i}^{Cp} = \sum_i c_{ji} K(r - r_i)$$

The coarse-grained models of dendron **1-3** reported in Figure S7 were adopted from our recent work.<sup>5</sup> A bead type C was used as the hydrophobic chain building block, a neutral bead type P and a positively charged bead type PC were employed for the non-protonated and terminal charged repeating unit of the dendron, respectively. A further bead type, L, links the hydrophilic and hydrophobic parts together.

In our simulations, each amphiphilic POPC molecule consists of a head group that contains three connected hydrophilic beads (H), and two tails with respective three hydrophobic beads per tail (T) following the model proposed by Ding et al.<sup>6</sup> for lipid membranes.

In explicit solvent calculations (DPD), water molecules were simulated by single bead type W, and an appropriate number of counterions of a charge of  $\pm 1$  were added to preserve charge neutrality and to account for the experimental solution ionic strength. In MBFH simulation, water was model a single Gaussian bead.

On the basis of the models described above, the phosphocholine/dendron **1-3** systems were simulated in a cubic box (maximum cell length  $L = 176$ ) under periodic boundary conditions in three directions using the MBFH method. The hybrid dendrimer/POPC vesicles were pre-assembled imposing a random distribution between the two components (i.e., POPC and dendron). The calculations thereby describe the morphology assumed after thermodynamic equilibration of the components, and representative graphs showing the potential energy and diameter as a function of simulation time for **3**/POPC can be seen in Figure S8. Initially, the solvent field was equilibrated by means of dynamic density functional theory<sup>7</sup> with a diffusion factor of 0.05 and all the beads fixed. In the second step the bead diffusion was turned on (diffusion factor 0.02), and a full hybrid MBF simulation was performed until the system was equilibrated for  $O(10^6)$  simulation steps with a time step of  $\Delta t = 0.02\tau$ .

In an attempt to imitate the SPR experiment at the mesoscale level we modeled the solid silica support as a rigid, non-interacting wall of  $50r_c \times 50r_c$ .<sup>8</sup> A POPC bilayer ( $\approx 3500$  molecules determined based on the head group area for POPC  $a = 0.68 \text{ nm}^2$ )<sup>9</sup> was initially laid down on the top of the flat surface and equilibrated in a solvated environment. Then, one self-assembled dendron **3** micelle<sup>5</sup> was placed in close proximity to the POPC bilayer, the overlapping solvent beads were deleted, and the system was set free to move. These calculations were performed by means of DPD method applying the velocity-Verlet integration algorithm with an integration time step  $\Delta t = 0.02\tau$  for a total  $8 \times 10^6$  simulation steps. A common way to retrieve the DPD time scale  $\tau$  is matching the experimental and simulated diffusion constant for water.<sup>10</sup> This yielded a  $\tau$  value of

approximately 0.06 ns in our simulations for a total simulation time of approximately 10  $\mu$ s.

The repulsive interaction parameters between beads  $a_{ij}$  were derived from atomistic calculations employing a extensively-validated approach developed by our group,<sup>11-15</sup> assuming the interaction parameter for solvent-solvent interaction  $a_{W-W}$  equal to 25, in harmony with a total bead number density of  $\rho = 3/r_c^3$ .<sup>3</sup> According to this procedure and as illustrated in detail in our previous DPD simulations of dendron **3**, we employed  $a_{PC-PC}=25$ ,  $a_{PC-P}=27$ ,  $a_{PC-L}=32$ ,  $a_{PC-C}=80$ ,  $a_{PC-W}=21$ ,  $a_{P-P}=25$ ,  $a_{P-L}=34$ ,  $a_{P-C}=82$ ,  $a_{P-W}=15$ ,  $a_{L-L}=25$ ,  $a_{L-C}=40$ ,  $a_{L-W}=33$ ,  $a_{C-C}=25$ ,  $a_{C-W}=82$ . The repulsive interactions between lipids components are  $a_{H-H}=25$ ,  $a_{T-T}=25$ ,  $a_{H-T}=92$  and with the solvent  $a_{H-W}=21$  and  $a_{T-W}=80$ . The DPD parameters for POPC/dendrimer are  $a_{H-PC}=29$ ,  $a_{H-P}=30.3$ ,  $a_{H-L}=28$ ,  $a_{H-C}=94$ ,  $a_{T-PC}=57$ ,  $a_{T-P}=44$ ,  $a_{T-L}=42$ ,  $a_{T-C}=23$ .

In the MBFH calculations the dimensionless Helfand compressibility parameter for the solvent field was fixed to  $\kappa_H = 4.6$ <sup>16</sup> (for  $\rho = 3/r_c^3$ ) and the hybrid bead-field coupling parameters  $c_{ji}$  were derived in terms of DPD parameters relying on the relation proposed by Fraaije et al.<sup>16</sup>  $c_{ji} = 0.095\Delta a_{ji} + 4.6 = 0.095(a_{ji}-a_{ii}) + 4.6$ , where  $j$  is a field model,  $i$  a bead type, and  $a_{ii}=a_0=25$ .

All simulations were carried out using the software package *Materials Studio* (v. 5.0, Accelrys, San Diego, CA) and *Culgi* (v.9.0, Culgi B.V., Leiden, The Netherlands).

**Calculation of zeta potential.** We calculated the surface electrostatic potential  $\Psi_s$  of the charged dendron micelles according to the formula:<sup>14, 17</sup>

$$\frac{e\sigma_m}{\kappa\epsilon_r\epsilon_0k_BT} = \Psi_s + \frac{\Psi_s}{\kappa r} - \frac{\tau_1^2\kappa r}{\tau_2 - \tau_1\kappa r}$$

where  $\kappa$  is the Debye parameter,  $\sigma_m$  is the micelle surface charge per unit area,  $\epsilon_0$  is the permittivity of vacuum,  $\epsilon_r$  corresponds to the relative permittivity,  $k_BT$  is the product of the Boltzmann constant and absolute temperature,  $e$  is the elementary charge, and:

$$\begin{aligned}\tau_1 &= 2\sinh\frac{\Psi_s}{2} - \Psi_s \\ \tau_2 &= 4\tanh\frac{\Psi_s}{4} - \Psi_s\end{aligned}$$

Accordingly, the electrostatic potential at the diffuse layer (DL) boundary  $\zeta$ , known as the zeta potential, was obtained from the Debye-Hückel approximation as:

$$\zeta = \Psi_s \left( \frac{r}{r + \kappa^{-1}} \right) e^{-1}$$

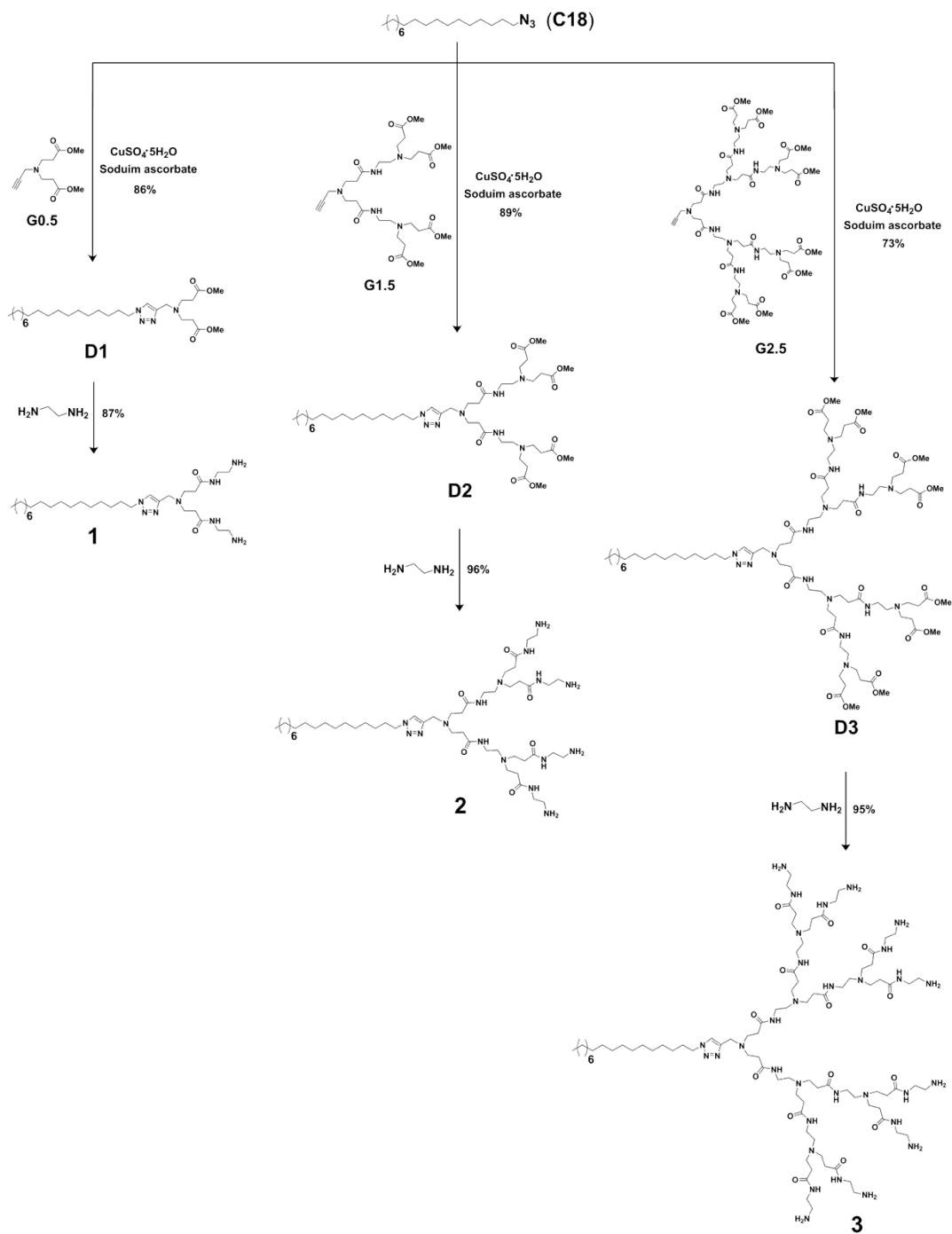
where  $(r + \kappa^{-1})$  is the distance of DL boundary from the center of mass of the micelle.

The Debye parameter  $\kappa$  in the equation of the electrostatic potential  $\Psi_s$  is obtained from the inverse of Debye length given by:

$$\kappa^{-1} = \sqrt{\frac{\epsilon_0\epsilon_r k_B T}{2N_A e^2 I}}$$

where  $N_A$  is Avogadro's number and  $I$  is the ionic strength of the solution.

## ■ SUPPLEMENTARY FIGURES



**Scheme A.1.** Synthesis of amphiphilic dendrimers **1** – **3**.

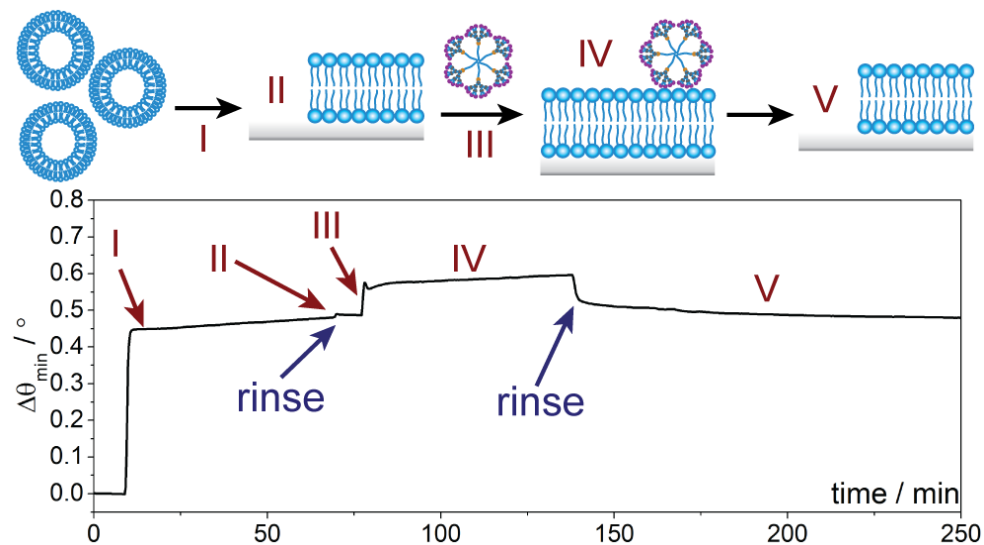


**Figure A.1.** SPR study on fusion of POPC bilayer and transient adsorption of dendrimer **3** micelles with extended rinsing step.

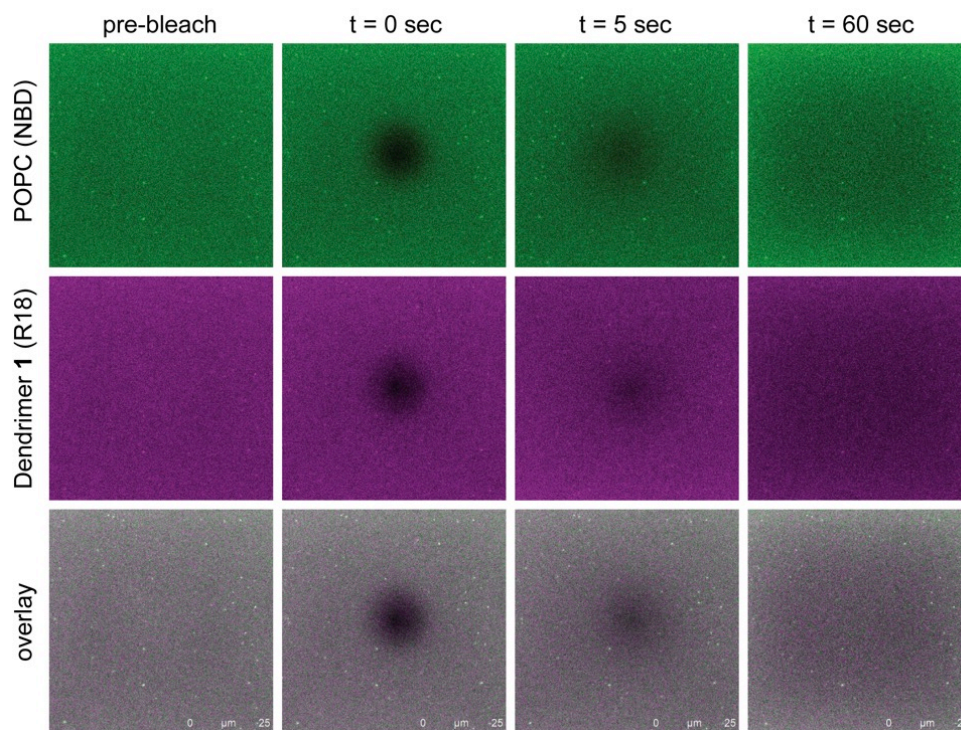


**Figure A.2.** Simultaneous bleaching and recovery of labeled dendrimer micelles and POPC fused within the same membrane. Both areas recover fluorescence within similar amounts of time, indicating integration of both constructs and similar mobilities of each component. Scale bars apply to all images, and represent 25  $\mu\text{m}$ .

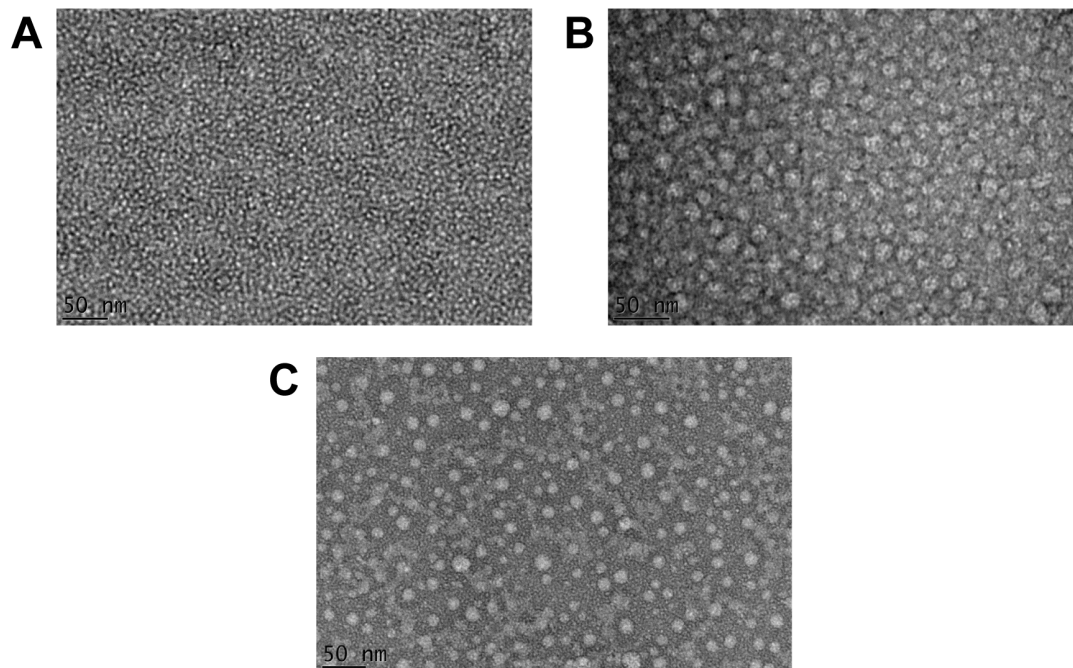


**Figure A.3.** TEM micrographs of dendrimers **1-3** alone assembled into nanomicelles. (A) Dendrimer **1**. (B) Dendrimer **2**. (C) Dendrimer **3**.

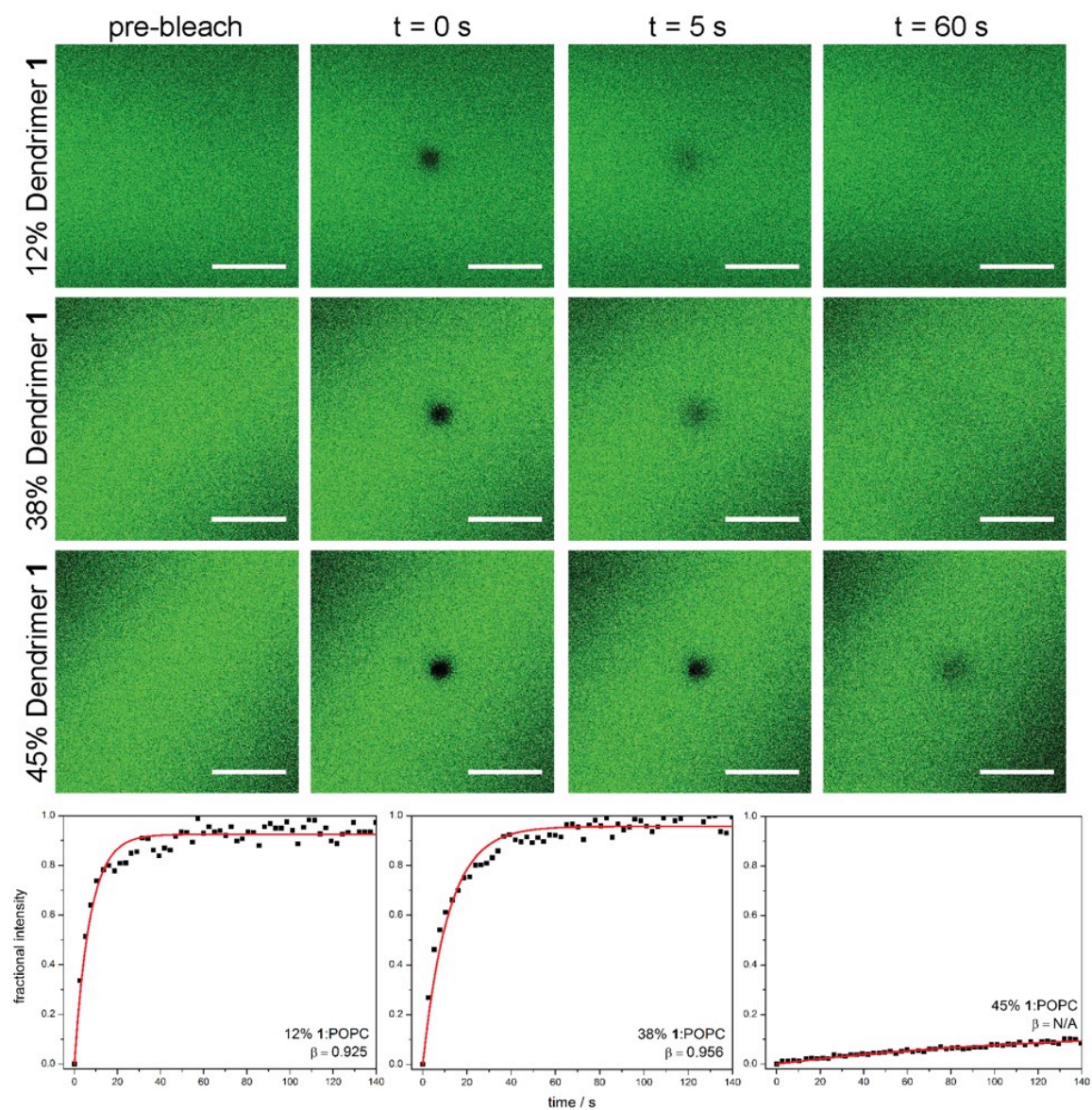


**Figure A.4.** Bleaching and recovery of varying concentrations of dendrimer 1 within POPC membranes. (Top) Fluorescence micrographs, scale bars represent 30  $\mu\text{m}$ . (Bottom) Representative FRAP recovery curves.

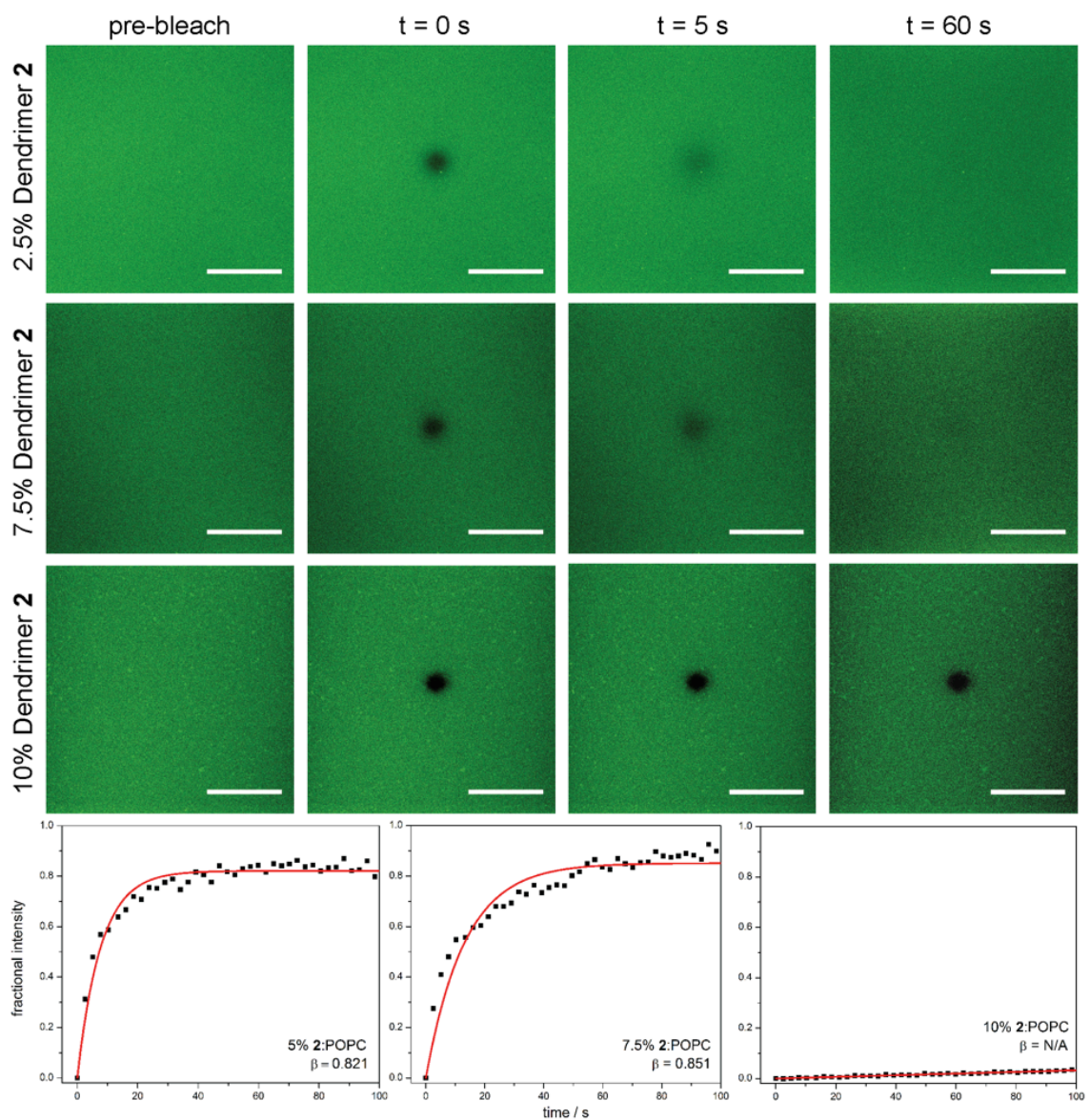


**Figure A.5.** Bleaching and recovery of varying concentrations of dendrimer 2 within POPC membranes. (Top) Fluorescence micrographs, scale bars represent 30  $\mu\text{m}$ . (Bottom) Representative FRAP recovery curves.

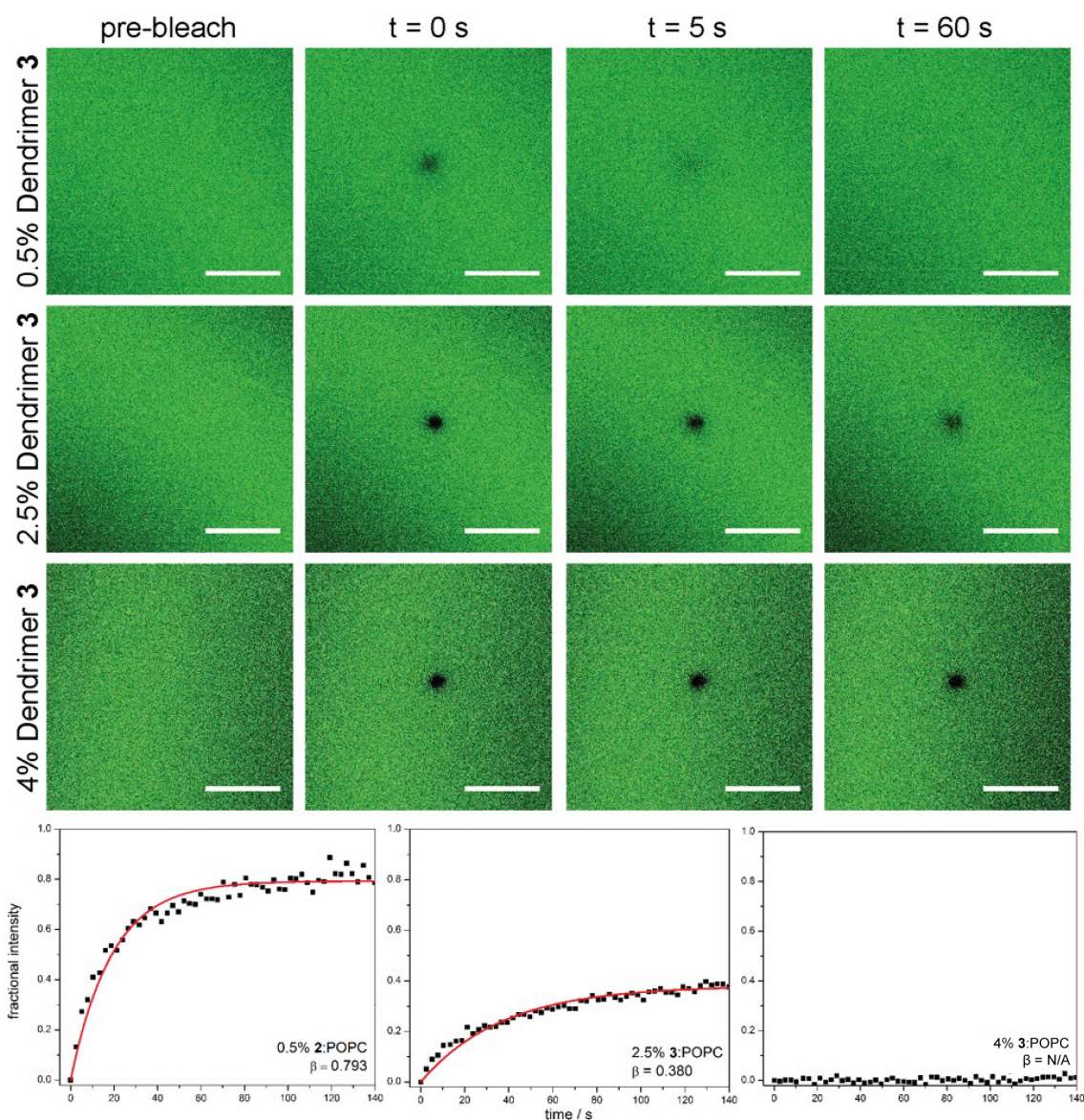


**Figure A.6.** Bleaching and recovery of varying concentrations of dendrimer **3** within POPC membranes. (Top) Fluorescence micrographs, scale bars represent 30  $\mu\text{m}$ . (Bottom) Representative FRAP recovery curves.

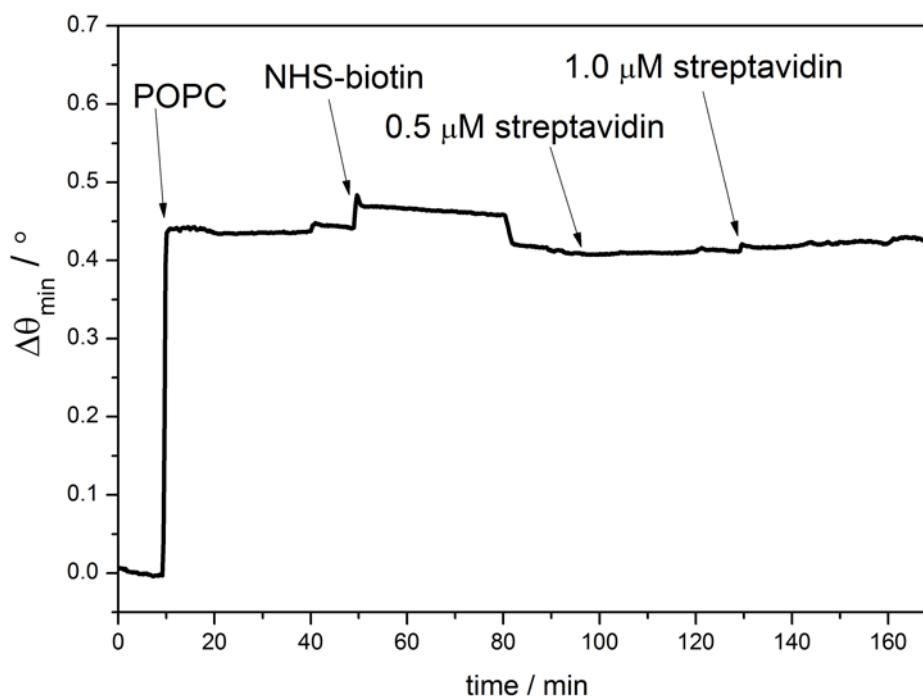


**Figure A.7.** SPR sensorgram depicting attempted derivitization of 100% POPC bilayer with biotin, and streptavidin recognition. There is no increase in resonance angle upon introduction of NHS-biotin or streptavidin, indicating neither interacts with the POPC membrane.

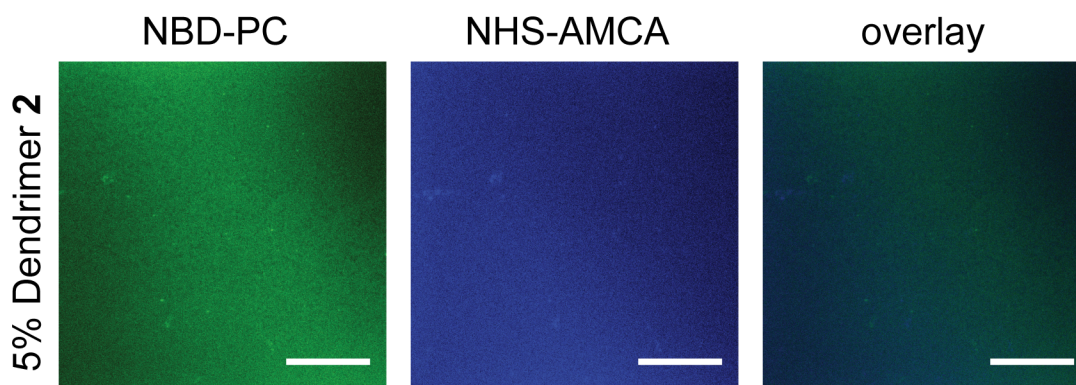


**Figure A.8.** *In situ* derivitization of a 5% 2/POPC hybrid bilayer with NHS-AMCA. Both the NBD (green, labeled PC) and AMCA (blue, labeled dendrimer) images were acquired over the same region for a 2/POPC supported lipid bilayer on glass after NHS-AMCA was applied to the membrane for 15 min and thoroughly rinsed with 1×PBS. Scale bars represent 30  $\mu\text{m}$ .

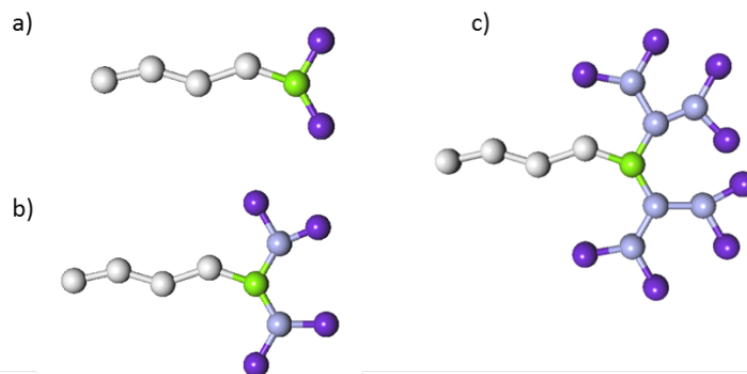


**Figure A.9.** Schematic representation of the coarse-grained DPD models of dendrons **1** (a), **2** (b), and **3** (c). The different bead types are colored as follows: PC, violet blue; P, steel blue; L, chartreuse; C, light gray.

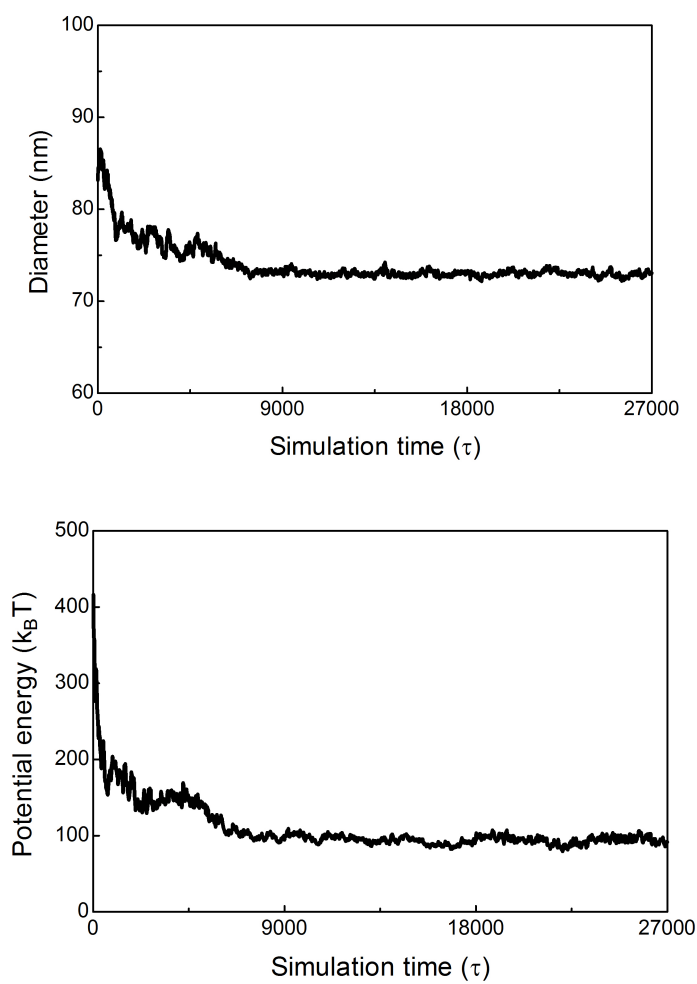


**Figure A.10.** Diameter (top) and potential energy (bottom) as a function of simulation time ( $\tau$ ) for **3**/POPC system equilibration.

## ■ SUPPLEMENTARY TABLES

**Table A.1.** Physical properties of hybrid dendrimer/POPC vesicles.

vesicle composition (n/n) <sup>a</sup>	hydrodyn. dia. (nm, ± SEM)	Đ (PDI)	ζ-potential (mV)	mobility (cm <sup>2</sup> /V•s)
100% POPC	121 ± 6	0.279	0.50	2.80×10 <sup>-6</sup>
5% Dendrimer 1	108 ± 6	0.285	21.7	1.13×10 <sup>-4</sup>
5% Dendrimer 2	90 ± 9	0.294	20.9	1.25×10 <sup>-4</sup>
5% Dendrimer 3	70 ± 4	0.299	24.1	1.09×10 <sup>-4</sup>

<sup>a</sup>Dendrimer percentages (n/n) are relative to POPC content, and total mass concentration for each composition is 1 mg/mL in 1×PBS.

**Table A.2.** Simulated average diameters, surface electrostatic potential (Ψ<sub>s</sub>), and zeta potential (ζ) for the three dendrimer/POPC vesicles.

System	average diameter (nm)	Ψ <sub>s</sub> (mV)	ζ-potential (mV)
1/POPC <sup>a</sup>	105	80.5	22.0
2/POPC <sup>a</sup>	92	79.9	21.6
3/POPC <sup>a</sup>	73	86.5	25.8

<sup>a</sup>The percentage of each dendron in each hybrid vesicle is 5% (n/n), as in real experiments (see Table S1).

## ■ REFERENCES

- (1) Murtola, T.; Bunker, A.; Vattulainen, I.; Deserno, M.; Karttunen, M. Multiscale Modeling of Emergent Materials: Biological and Soft Matter. *Phys. Chem. Chem. Phys.* **2009**, *11*, 1869-1892.
- (2) Shillcock, J. C. Spontaneous Vesicle Self-Assembly: A Mesoscopic View of Membrane Dynamics. *Langmuir* **2012**, *28*, 541-547.
- (3) Groot, R. D.; Warren, P. B. Dissipative Particle Dynamics: Bridging the Gap between Atomistic and Mesoscopic Simulation. *J. Chem. Phys.* **1997**, *107*, 4423-4435.
- (4) Sevink, G. J. A.; Fraaije, J. G. E. M. Efficient Solvent-Free Dissipative Particle Dynamics for Lipid Bilayers. *Soft Matter* **2014**, *10*, 5129-5146.
- (5) Chen, C.; Posocco, P.; Liu, X.; Cheng, Q.; Laurini, E.; Zhou, J. H.; Liu, C.; Wang, Y.; Tang, J.; Dal Col, V.; Yu, T. Z.; Giorgio, S.; Fermeglia, M.; Qu, F. Q.; Liang, Z.; Rossi, J. J.; Liu, M.; Rocchi, P.; Pricl, S.; Peng, L. Mastering Dendrimer Self-Assembly for Efficient siRNA Delivery: From Conceptual Design to in Vivo Efficient Gene Silencing. *Small* **2016**, *12*, 3667-3676.
- (6) Ding, H. M.; Ma, Y. Q. Interactions between Janus Particles and Membranes. *Nanoscale* **2012**, *4*, 1116-1122.
- (7) Fraaije, J. G. E. M. Dynamic Density-Functional Theory for Microphase Separation Kinetics of Block-Copolymer Melts. *J. Chem. Phys.* **1993**, *99*, 9202-9212.
- (8) Toth, R.; Voorn, D. J.; Handgraaf, J. W.; Fraaije, J. G. E. M.; Fermeglia, M.; Pricl, S.; Posocco, P. Multiscale Computer Simulation Studies of Water-Based Montmorillonite/Poly(Ethylene Oxide) Nanocomposites. *Macromolecules* **2009**, *42*, 8260-8270.
- (9) Lindblom, G.; Oradd, G. Lipid Lateral Diffusion and Membrane Heterogeneity. *Biochim. Biophys. Acta* **2009**, *1788*, 234-244.

- (10) Groot, R. D.; Rabone, K. L. Mesoscopic Simulation of Cell Membrane Damage, Morphology Change and Rupture by Nonionic Surfactants. *Biophys. J.* **2001**, *81*, 725-736.
- (11) Wei, T.; Chen, C.; Liu, J.; Liu, C.; Posocco, P.; Liu, X.; Cheng, Q.; Huo, S.; Liang, Z.; Fermeglia, M.; Pricl, S.; Liang, X. J.; Rocchi, P.; Peng, L. Anticancer Drug Nanomicelles Formed by Self-Assembling Amphiphilic Dendrimer to Combat Cancer Drug Resistance. *Proc. Natl. Acad. Sci. U. S. A.* **2015**, *112*, 2978-2983.
- (12) Liu, X. X.; Zhou, J. H.; Yu, T. Z.; Chen, C.; Cheng, Q.; Sengupta, K.; Huang, Y. Y.; Li, H. T.; Liu, C.; Wang, Y.; Posocco, P.; Wang, M. H.; Cui, Q.; Giorgio, S.; Fermeglia, M.; Qu, F. Q.; Pricl, S.; Shi, Y. H.; Liang, Z. C.; Rocchi, P.; Rossi, J. J.; Peng, L. Adaptive Amphiphilic Dendrimer-Based Nanoassemblies as Robust and Versatile siRNA Delivery Systems. *Angew. Chem., Int. Ed.* **2014**, *53*, 11822-11827.
- (13) Bromfield, S. M.; Posocco, P.; Chan, C. W.; Calderon, M.; Guimond, S. E.; Turnbull, J. E.; Pricl, S.; Smith, D. K. Nanoscale Self-Assembled Multivalent (SAMul) Heparin Binders in Highly Competitive, Biologically Relevant, Aqueous Media. *Chem. Sci.* **2014**, *5*, 1484-1492.
- (14) Barnard, A.; Posocco, P.; Fermeglia, M.; Tschiche, A.; Calderon, M.; Pricl, S.; Smith, D. K. Double-Degradable Responsive Self-Assembled Multivalent Arrays - Temporary Nanoscale Recognition between Dendrons and DNA. *Org. Biomol. Chem.* **2014**, *12*, 446-455.
- (15) Jones, S. P.; Gabrielson, N. P.; Wong, C. H.; Chow, H. F.; Pack, D. W.; Posocco, P.; Fermeglia, M.; Pricl, S.; Smith, D. K. Hydrophobically Modified Dendrons: Developing Structure-Activity Relationships for DNA Binding and Gene Transfection. *Mol. Pharmaceutics* **2011**, *8*, 416-429.
- (16) Sevink, G. J. A.; Charlaganov, M.; Fraaije, J. G. E. M. Coarse-Grained Hybrid Simulation of Liposomes. *Soft Matter* **2013**, *9*, 2816-2831.
- (17) Sader, J. E. Accurate Analytic Formulae for the Far Field Effective Potential and Surface Charge Density of a Uniformly Charged Sphere. *J. Colloid Interface Sci.* **1997**, *188*, 508-510.

## APPENDIX B: Supporting Information for Chapter 3

### ■ SUPPLEMENTARY FIGURES

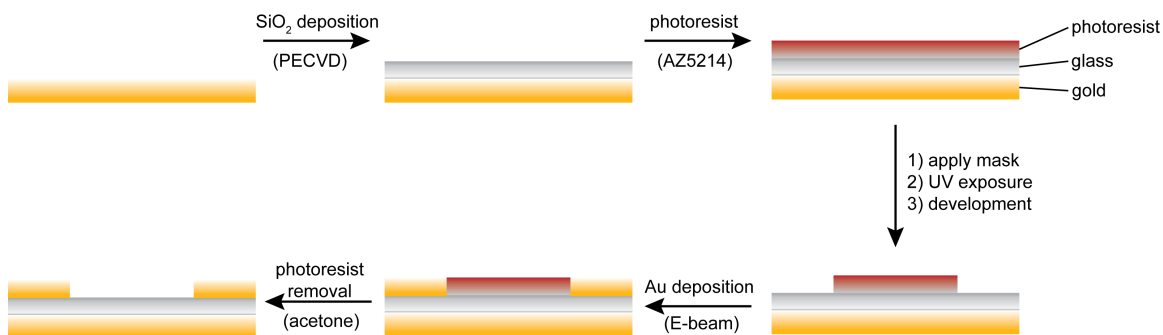


**Figure B.1.** Fabrication process of high-performance gold well SPR imaging substrate.

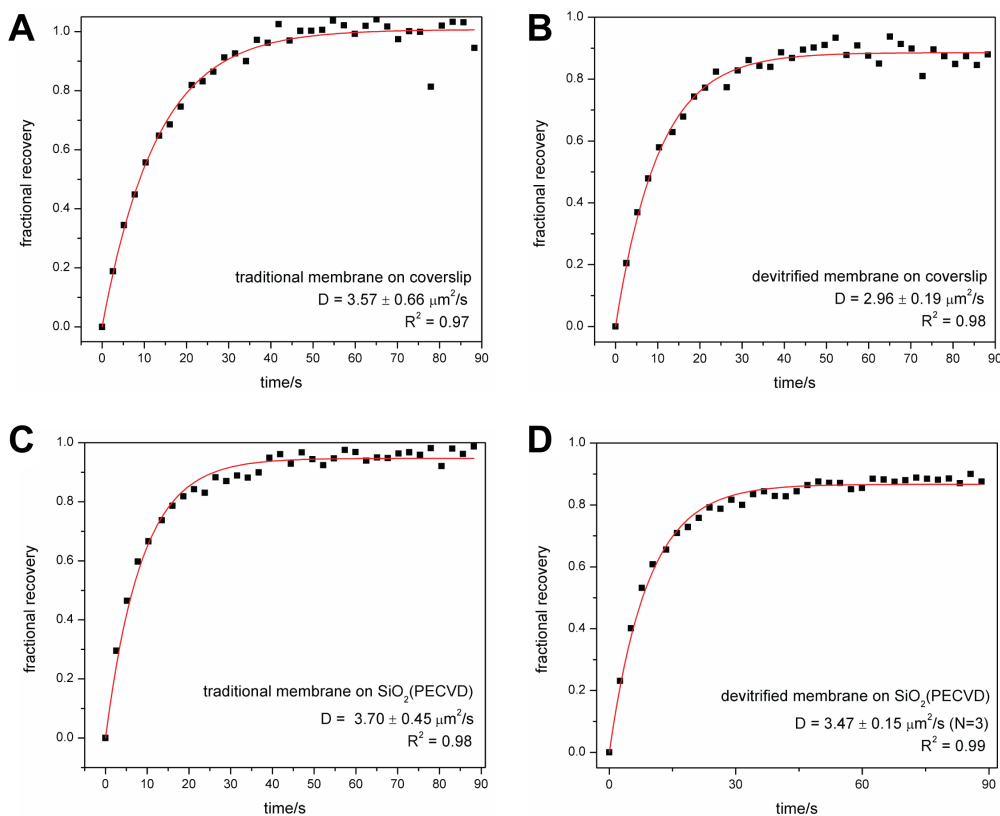


**Figure B.2.** Representative FRAP recovery curves for supported lipid bilayers formed using vesicle injection and devitrification processes on glass coverslips and modified SPR surfaces. All diffusion coefficients are the result of  $n = 3$  experiments. (A) Traditionally formed membrane on glass coverslip. (B) Devitrified membrane on glass coverslip. (C) Traditionally formed membrane on PECVD grown silica. (D) Devitrified membrane on PECVD grown silica.

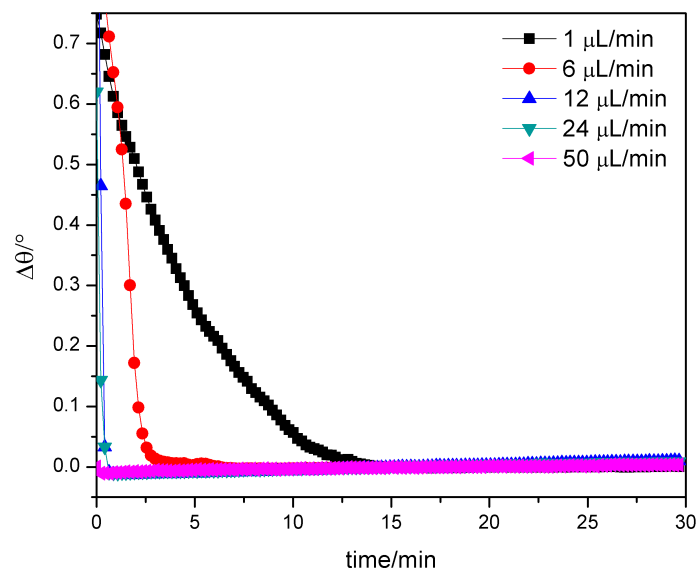


**Figure B.3.** Flow rate effects on devitrification of trehalose alone. Only trehalose in 1×PBS was desiccated in this assay, and no SLBs were added to this mixture.

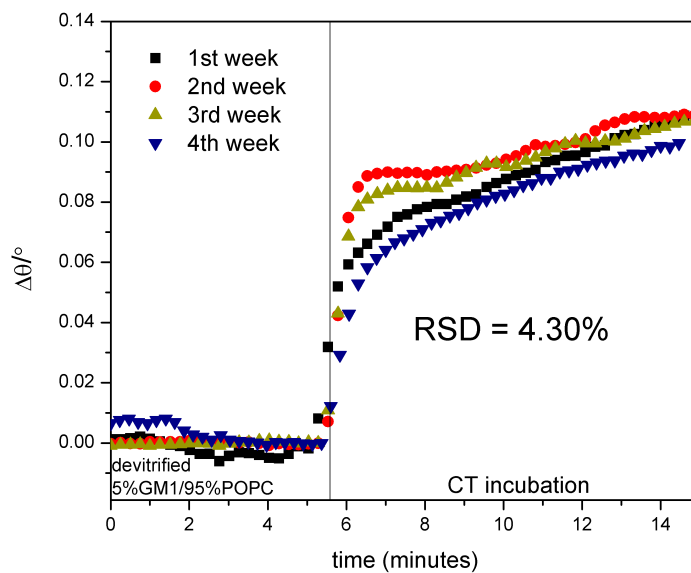


**Figure B.4.** Sensorgrams for cholera toxin binding to membranes obtained from devitrified vesicles that were stored between 1-4 weeks.

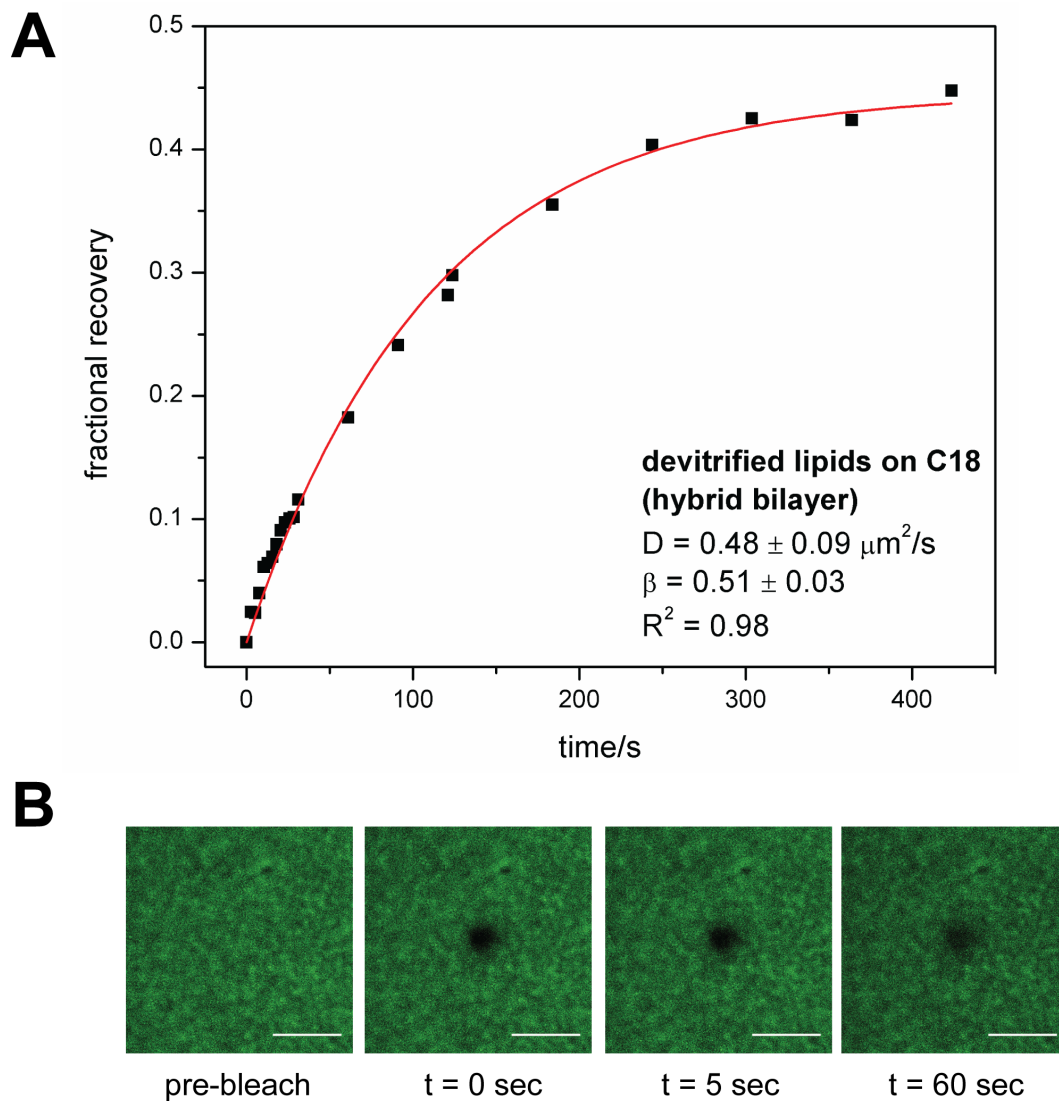


**Figure B.5.** FRAP results from devitrified hybrid bilayer membrane on C18 surface. (A) FRAP recovery curve. (B) Fluorescence microscopy images showing bleaching and fluorophore redistribution of the hybrid bilayer membranes. Scale bar represents 20  $\mu\text{m}$ .

## APPENDIX C: Supporting Information for Chapter 4

### ■ SUPPLEMENTARY METHODS

**Buffer Compositions.** *Phosphate buffered saline (1×PBS)*: 10 mM Na<sub>2</sub>HPO<sub>4</sub>, 1.8 mM KH<sub>2</sub>PO<sub>4</sub>, 137 mM NaCl, 2.7 mM KCl, pH 7.4. *Phosphate buffered Tween 20 solution (PBT)*: 10 mM Na<sub>2</sub>HPO<sub>4</sub>, 0.1% (v/v) Tween 20, pH 7.0. *Phosphate citrate buffer (PCB)*: 200 mM Na<sub>2</sub>HPO<sub>4</sub>, 100 mM trisodium citrate dihydrate, pH 5.0. *2-(N-morpholino)ethanesulfonic acid (MES)*: 10 mM MES, pH 5.5.

**SPR Chip Fabrication.** BK-7 glass microscope slides were first cleaned using a boiling piranha solution (3:1 v/v H<sub>2</sub>SO<sub>4</sub> and 30% H<sub>2</sub>O<sub>2</sub>) for 30 min, followed by rinsing with DI water and drying under compressed air. 2 nm of chromium (0.5 Å s<sup>-1</sup>), followed by 46 nm of gold (1.0 Å s<sup>-1</sup>) were then deposited using electron-beam evaporation (Temescal, Berkeley, CA) at 5×10<sup>-6</sup> Torr in a Class 1000 cleanroom facility (UCR Center for Nanoscale Science & Engineering). To obtain a hydrophilic surface for lipid bilayer formation, *ca.* 4 nm of SiO<sub>2</sub> was deposited on top of the gold layer using plasma enhanced chemical vapor deposition (PECVD) with a Unaxis Plasmatherm 790 system (Santa Clara, CA).<sup>1-2</sup>

**Lipid Vesicle Preparation.** An appropriate amount of lipid stock solution consisting of POPC and 5% (n/n) of biotin-PE or 5% (n/n) GM<sub>1</sub> in chloroform was dried in a glass vial under nitrogen to form a thin lipid film. The vial containing dried lipids was placed in a vacuum desiccator for at least 2 h to remove any residual solvent. The lipids were then resuspended in 1×PBS to a concentration of 1 mg mL<sup>-1</sup>. After vigorous vortexing to

remove all lipid remnants from the vial wall, the suspension was bath sonicated for 30 min. Thereafter, the solution was extruded through a polycarbonate filter (Whatman, 100 nm) to produce small, unilamellar vesicles (SUVs) of uniform size. All vesicle suspensions were used within one week and stored at 4 °C. Arraying of SUVs for multiplexed supported bilayer analysis was performed using trehalose-assisted deposition.<sup>2-3</sup>

**Gold Nanoparticle Synthesis.** Citrate stabilized gold nanoparticles were fabricated by a modified Turkevitch method.<sup>4</sup> For 13 nm spheres, a round bottom flask containing 500 mL of 1 mM gold (III) chloride trihydrate was heated until boiling, after which, 50 mL of 38.8 mM trisodium citrate dihydrate was added. For 30 nm spheres, 510 mL of 0.25 mM gold (III) chloride trihydrate was heated until boiling, and 10 mL of 17 mM trisodium citrate dihydrate was utilized. The mixed solution was boiled and stirred until a deep red color was obtained. After cooling overnight, the nanoparticles were filtered through a cellulose acetate membrane (Whatman, 0.45 µm) and stored in amber bottles at room temperature. Diameter and concentration were determined according to the methods of Haiss et al.,<sup>5</sup> and verified by transmission electron microscopy (Figure C.7).

**MHDA/Biotin Modification.** Biotin functionalization via 16-MHDA monolayer coupling was performed according the procedure outlined by Aslan et al.<sup>6</sup> 1.5 mL of as-prepared 13 nm gold nanoparticles were first centrifuged and resuspended in 1 mL PBT. Following this, 0.5 mL of 0.5 mM 16-MHDA in ethanol was stirred into the nanoparticle solution and incubated overnight. The nanoparticles were cleaned up from excess 16-MHDA by centrifugation and resuspension in PBT at least three times. Thereafter, the

terminal carboxyl groups were activated with 50 mM NHS and 200 mM EDC for 15 min. Excess reagent was cleaned up by centrifugation/resuspension two times, during which, the second resuspension incorporated 22 mM AEE and 2.4 mM BA in PBT. This mixture was incubated for 2 h for the attachment of PEG and biotin to the carboxyl terminals, and the final product was cleaned up through centrifugation/resuspension at least three times.

**Ionic Strength Stability Assays.** NaCl induced aggregation of bare AuNPs, biotin/MHDA/AuNPs, and **bT<sub>20</sub>**/AuNPs was monitored and compared according to a modification of previously established methods.<sup>7-10</sup> All AuNP concentrations were set to 1.5 nM by adding an appropriate amount of AuNPs (suspended in nanopure water), nanopure water, and 5 M NaCl. The NaCl was mixed immediately before measurement in the Cary 50 spectrophotometer, which monitored the absorbance at 620 nm over the course of 5 min using the “Kinetics” program. Thereafter, a post-salting absorbance spectrum was obtained for each nanoparticle solution using the “Scan” program (Figure C.2A, C.2C, C.2E). The  $\Delta A_{620}$  at  $t = 5$  min (Figure C2B, C2D, C2F) were quantified in replicate ( $n = 5$ ) for each nanoparticle solution and salt concentration, and the final values with error bars ( $\pm$  SEM) were plotted together (Figure 4.2B).

**Horseradish Peroxidase Assay.** HRP/**cT<sub>20</sub>**/AuNPs, TMB, and hydrogen peroxide were utilized in a colorimetric plate assay format to demonstrate feasibility of the AuNPs for ELISA. 200  $\mu$ L of 0.1 mg/mL TMB in PCB with 0 – 1 mM H<sub>2</sub>O<sub>2</sub> was added to each microplate well, followed by the addition of 100  $\mu$ L of 1 nM HRP/**cT<sub>20</sub>**/AuNPs ( $d_a \sim 13$  nm) in PCB. After incubating for 20 min (fresh AuNPs) or 1 h (lyophilized AuNPs), the enzymatic reaction was stopped through the addition of 50  $\mu$ L of 2 M H<sub>2</sub>SO<sub>4</sub>. Absorbance

at 450 nm was read within five minutes of stop solution addition on the Biotek microplate reader. For control experiments in which AuNPs were absent (free HRP), a  $1:1 \times 10^6$  working dilution of the enzyme in PCB was added to the TMB/H<sub>2</sub>O<sub>2</sub> wells and analyzed in the same manner as described above.

## ■ SUPPLEMENTARY TABLE

**Table C.1.** Conjugated AuNP Zeta Potentials

Nanoparticle	$\zeta$ -potential (mV)	mobility (cm <sup>2</sup> /V•s)
bare AuNPs	-32.03	$-1.666 \times 10^{-4}$
13 nm <b>T</b> <sub>20</sub> /AuNPs	-53.21	$-2.766 \times 10^{-4}$
30 nm <b>T</b> <sub>20</sub> /AuNPs	-45.37	$-2.359 \times 10^{-4}$
13 nm MHDA/AuNPs	-48.62	$-2.528 \times 10^{-4}$

## ■ SUPPLEMENTARY FIGURES

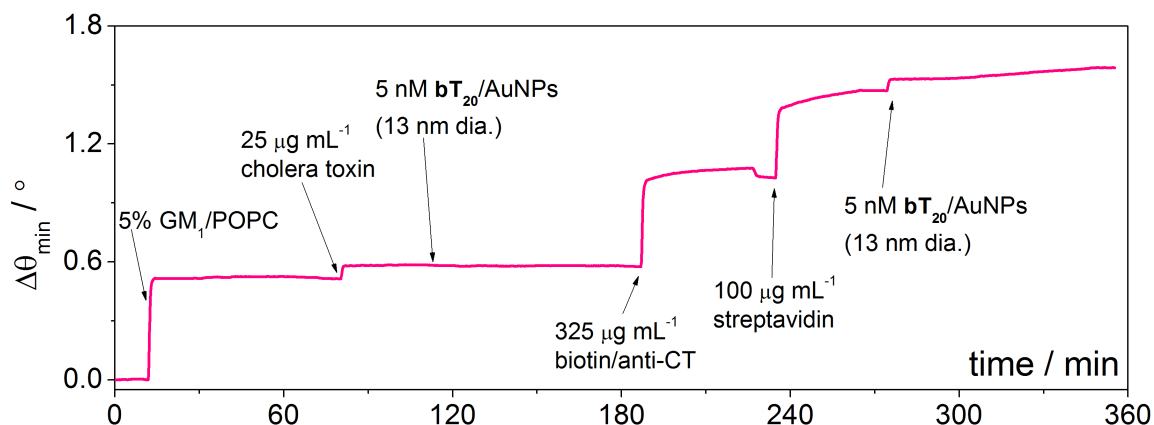


**Figure C.1.** Surface plasmon resonance sensorgram depicting formation of a ganglioside-impregnated supported lipid bilayer, followed by cholera toxin (CT), attempted AuNP recognition, then a biotinylated antibody specific for CT, streptavidin, and another attempt at AuNP recognition. The **bT**<sub>20</sub>/AuNPs only attach to the surface when streptavidin is present.

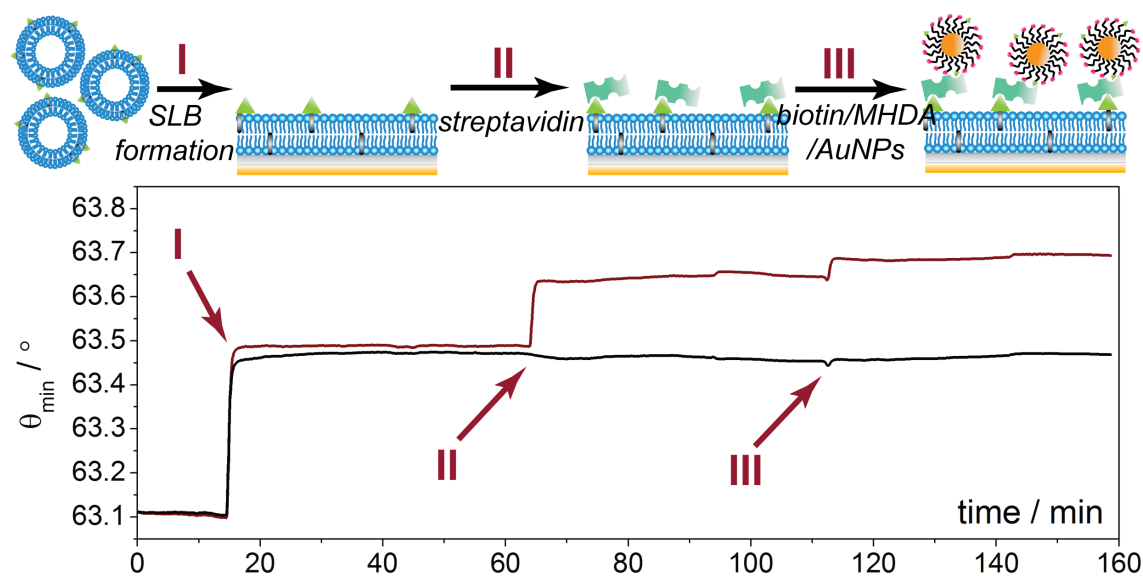


**Figure C.2.** Surface plasmon resonance sensorgram depicting formation of a biotinylated supported lipid bilayer, followed by streptavidin and biotin/MHDA/AuNP recognition. A 100% POPC bilayer is formed in the reference channel and exposed to streptavidin and AuNPs for control purposes.

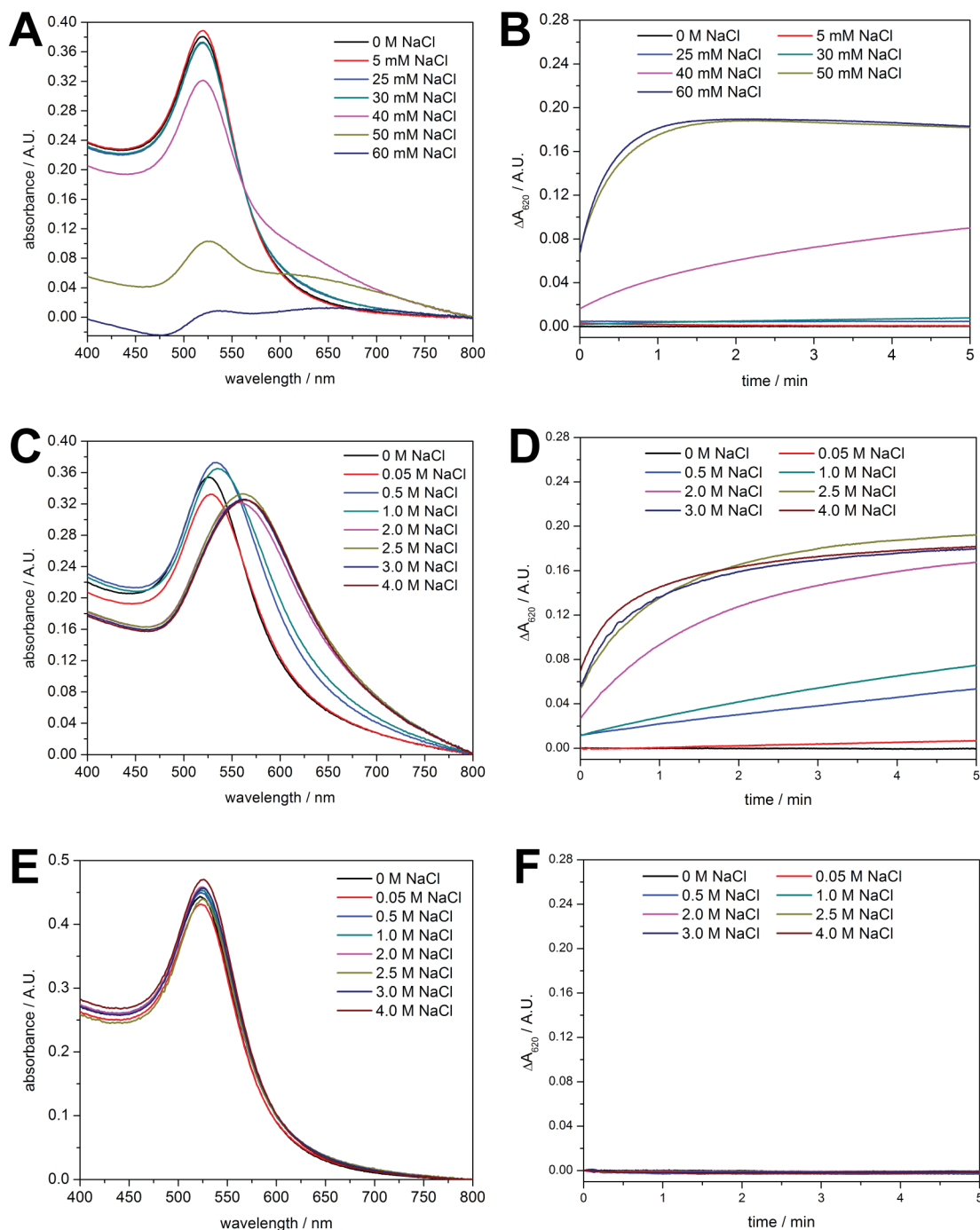


**Figure C.3.** Ionic strength stability assays of bare AuNP (citrate capped), biotin/MHDA/AuNP, and  $bT_{20}$ /AuNP exposures to varying concentrations of NaCl. (A) Bare AuNP absorbance spectra. (B) Bare AuNP  $\Delta A_{620}$  over 5 min. (C) Biotin/MHDA/AuNP absorbance spectra. (D) Biotin/MHDA/AuNP  $\Delta A_{620}$  over 5 min. (E)  $bT_{20}$ /AuNP absorbance spectra. (F)  $bT_{20}$ /AuNP  $\Delta A_{620}$  over 5 min.

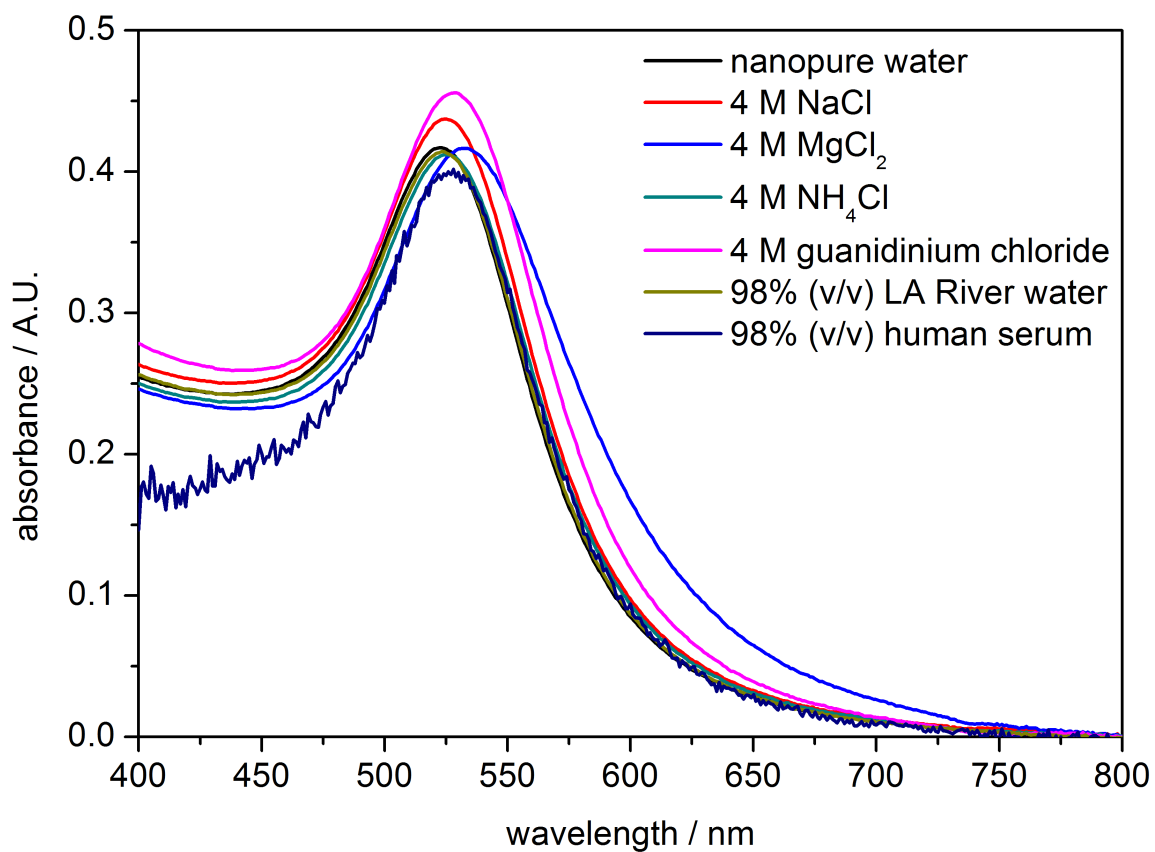


**Figure C.4.** Absorbance spectra of  $\text{bT}_{20}/\text{AuNPs}$  in nanopure water, 4 M NaCl, 4 M  $\text{MgCl}_2$ , 4 M  $\text{NH}_4\text{Cl}$ , 4 M guanidinium chloride, 98% Los Angeles River water, and 98% human serum.

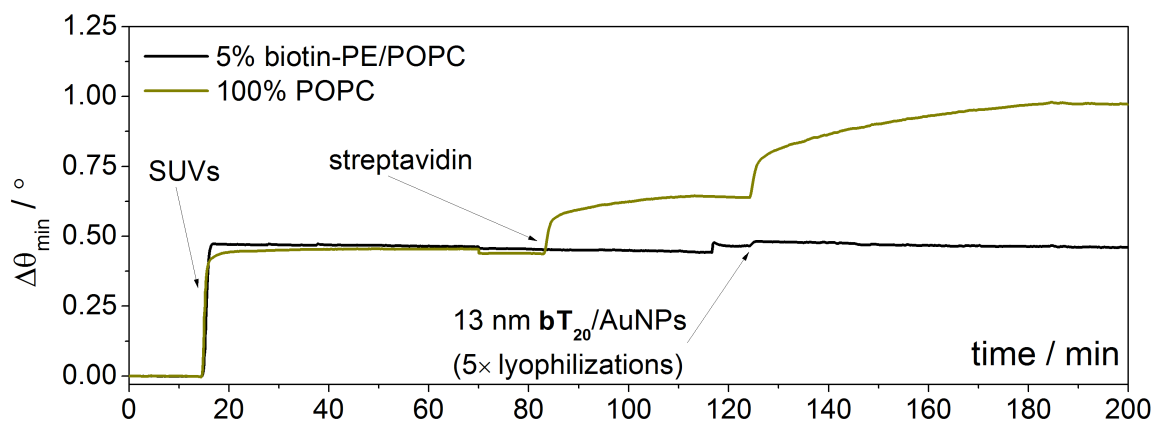


**Figure C.5.** Surface plasmon resonance sensorgram depicting formation of a biotinylated supported lipid bilayer, followed by streptavidin and 13 nm  $\mathbf{bT}_{20}$ /AuNP recognition (lyophilized and resuspended five times). A 100% POPC bilayer is formed in the reference channel and exposed to streptavidin and AuNPs for control purposes.

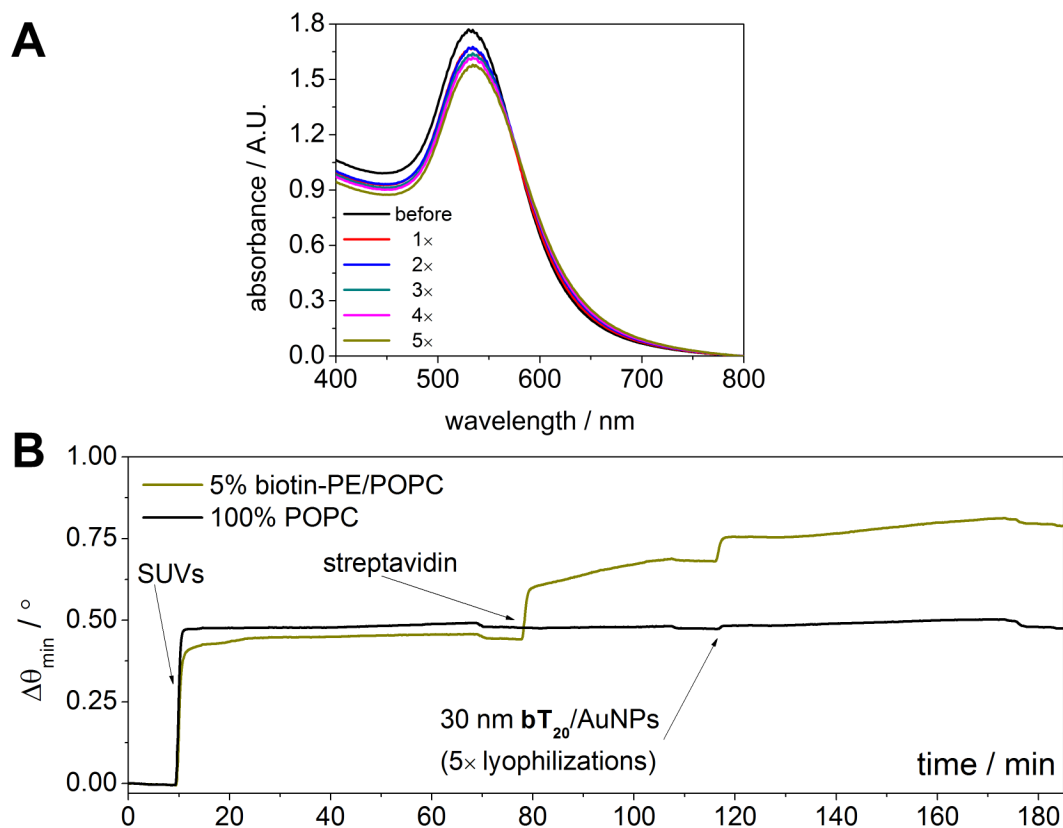


**Figure C.6.** 30 nm  $\mathbf{bT}_{20}$ /AuNP lyophilization studies. (A) Absorbance spectra of 30 nm  $\mathbf{bT}_{20}$ /AuNPs before and after five lyophilization cycles. (B) Surface plasmon resonance sensorgram depicting formation of a biotinylated supported lipid bilayer, followed by streptavidin and 30 nm  $\mathbf{bT}_{20}$ /AuNP recognition (lyophilized and resuspended five times).

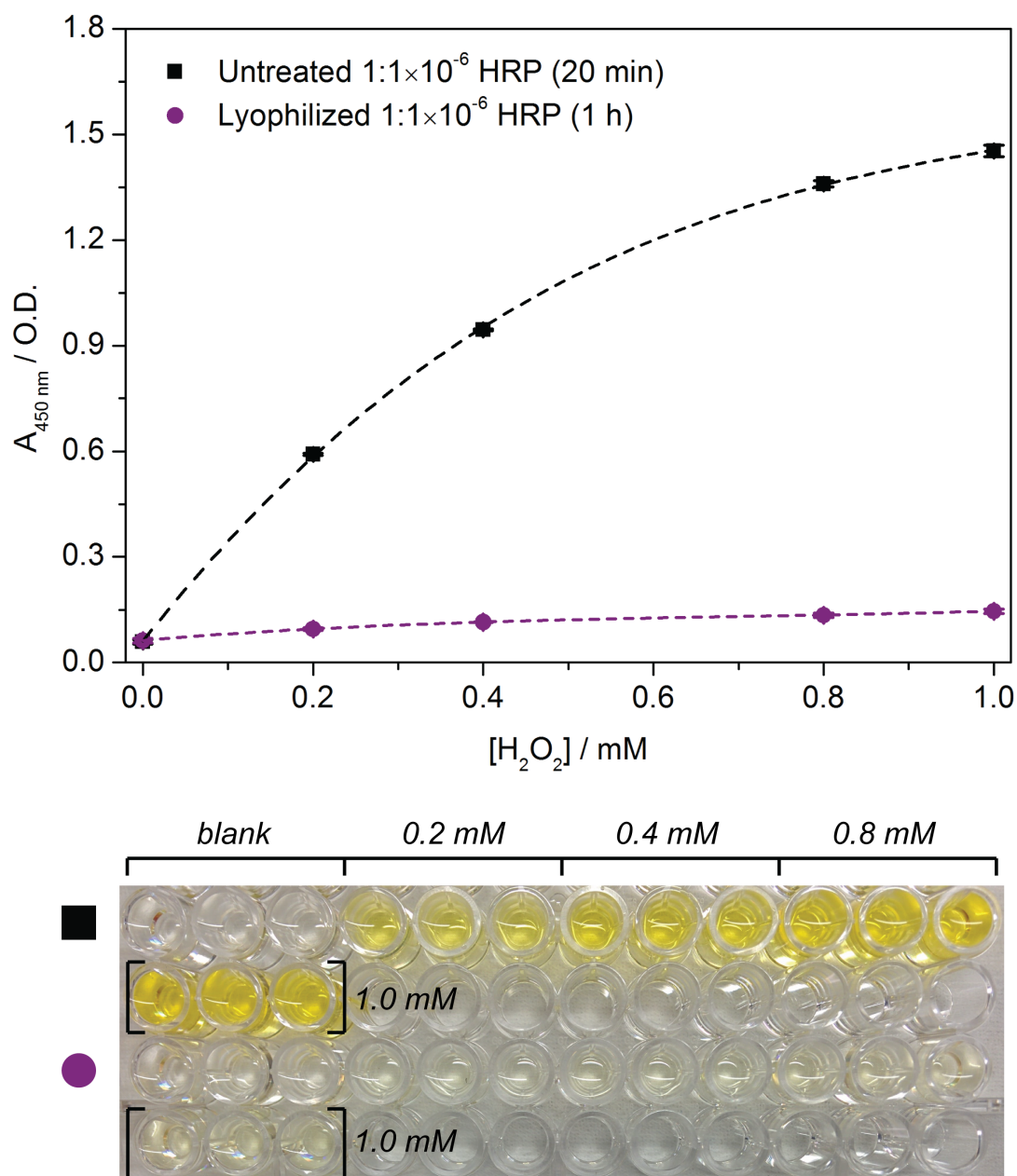


**Figure C.7.** Lyophilization of free horseradish peroxidase (HRP). Results are from hydrogen peroxide assay utilizing TMB and free HRP diluted  $1:1 \times 10^6$  times.

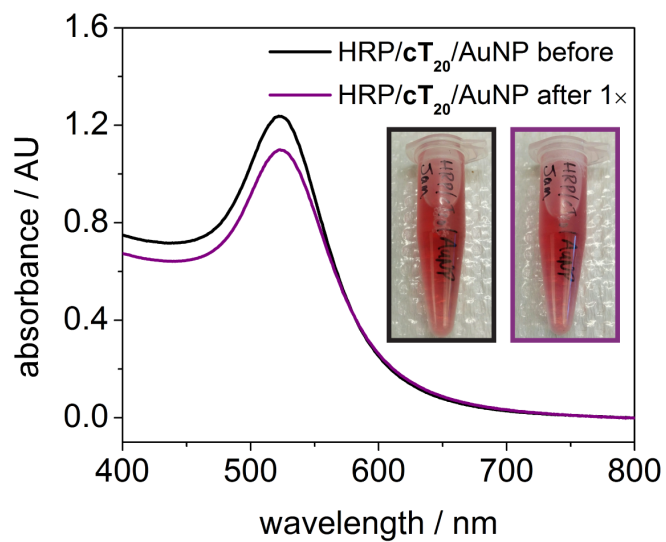


**Figure C.8.** Lyophilization of HRP/cT<sub>20</sub>/AuNPs: absorbance spectra of the HRP/cT<sub>20</sub>/AuNPs before and after lyophilization. Inset photographs correlate with samples used for each absorbance spectrum.

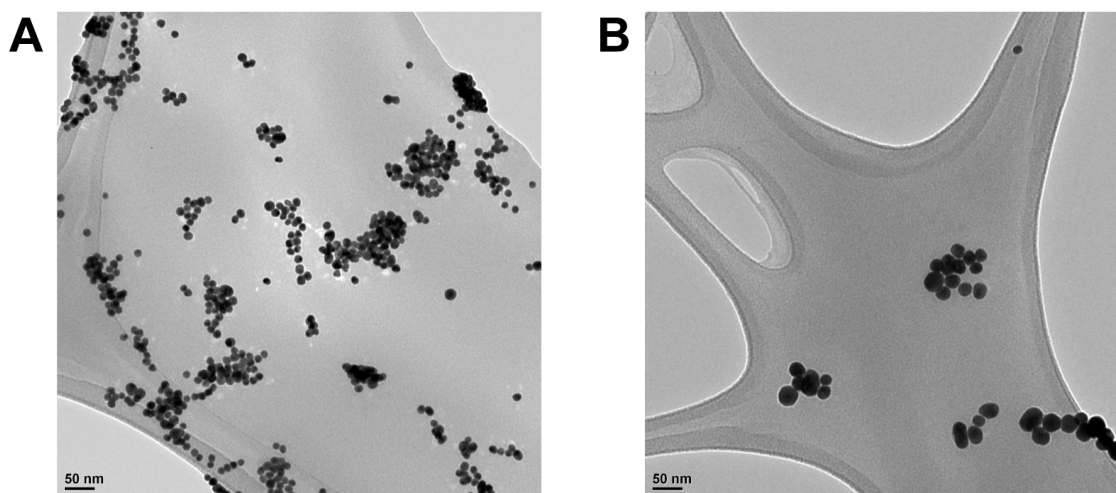


**Figure C.9.** Representative transmission electron micrographs of as-prepared citrate capped (A) 13 nm gold nanoparticles, and (B) 30 nm gold nanoparticles.

## ■ REFERENCES

- (1) Abbas, A.; Linman, M. J.; Cheng, Q. Patterned Resonance Plasmonic Microarrays for High-Performance SPR Imaging. *Anal. Chem.* **2011**, *83*, 3147-3152.
- (2) Hinman, S. S.; Ruiz, C. J.; Drakakaki, G.; Wilkop, T. E.; Cheng, Q. On-Demand Formation of Supported Lipid Membrane Arrays by Trehalose-Assisted Vesicle Delivery for SPR Imaging. *ACS Appl. Mater. Interfaces* **2015**, *7*, 17122-17130.
- (3) Wilkop, T. E.; Sanborn, J.; Oliver, A. E.; Hanson, J. M.; Parikh, A. N. On-Demand Self-Assembly of Supported Membranes Using Sacrificial, Anhydrobiotic Sugar Coats. *J. Am. Chem. Soc.* **2014**, *136*, 60-63.
- (4) Frens, G. Controlled Nucleation for the Regulation of the Particle Size in Monodisperse Gold Suspensions. *Nature* **1973**, *241*, 20-22.
- (5) Haiss, W.; Thanh, N. T. K.; Aveyard, J.; Fernig, D. G. Determination of Size and Concentration of Gold Nanoparticles from Uv-Vis Spectra. *Anal. Chem.* **2007**, *79*, 4215-4221.
- (6) Aslan, K.; Luhrs, C. C.; Perez-Luna, V. H. Controlled and Reversible Aggregation of Biotinylated Gold Nanoparticles with Streptavidin. *J. Phys. Chem. B* **2004**, *108*, 15631-15639.
- (7) Storhoff, J. J.; Elghanian, R.; Mirkin, C. A.; Letsinger, R. L. Sequence-Dependent Stability of DNA-Modified Gold Nanoparticles. *Langmuir* **2002**, *18*, 6666-6670.
- (8) Levy, R.; Thanh, N. T. K.; Doty, R. C.; Hussain, I.; Nichols, R. J.; Schiffrin, D. J.; Brust, M.; Fernig, D. G. Rational and Combinatorial Design of Peptide Capping Ligands for Gold Nanoparticles. *J. Am. Chem. Soc.* **2004**, *126*, 10076-10084.
- (9) Heo, J. H.; Cho, H. H.; Lee, J. H. Surfactant-Free Nanoparticle DNA Complexes with Ultrahigh Stability against Salt for Environmental and Biological Sensing. *Analyst* **2014**, *139*, 5936-5944.

- (10) Gupta, A.; Moyano, D. F.; Parnsubsakul, A.; Papadopoulos, A.; Wang, L. S.; Landis, R. F.; Das, R.; Rotello, V. M. Ultrastable and Biofunctionalizable Gold Nanoparticles. *ACS Appl. Mater. Interfaces* **2016**, 8, 14096-14101.

## Appendix D: Supporting Information for Chapter 5

### ■ SUPPLEMENTARY FIGURES

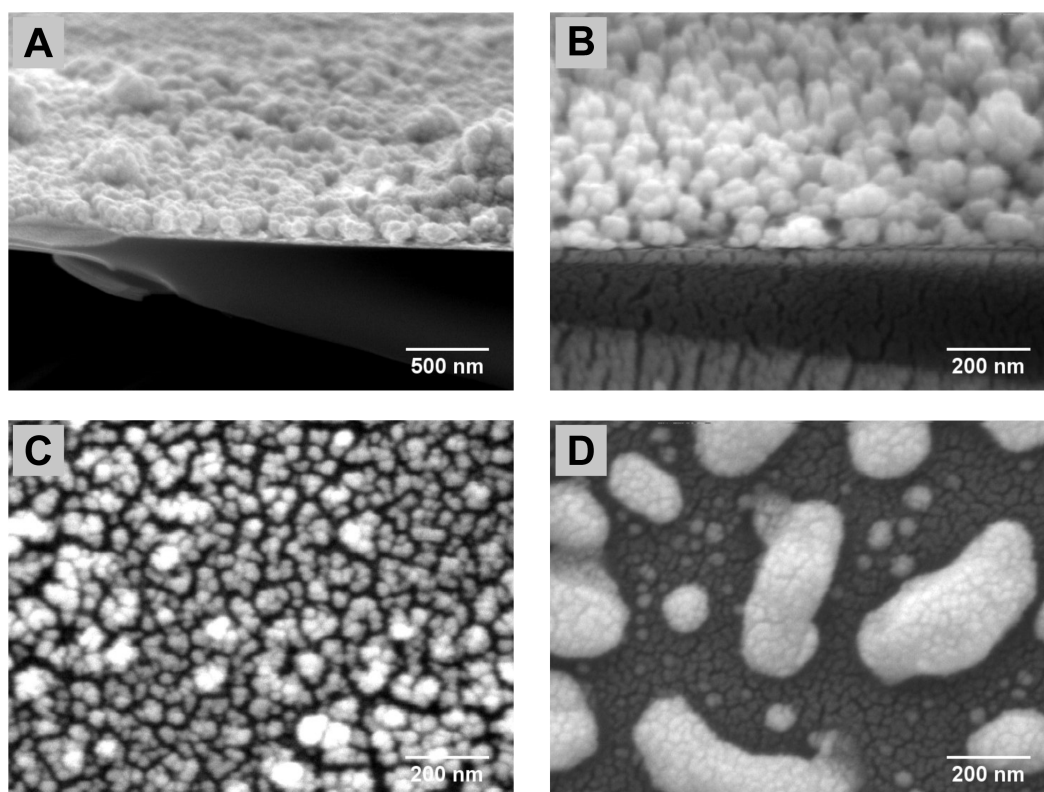


**Figure D.1.** SEM characterization of the nanofilm substrates. (A,B) Images of calcinated AuNP film and the edge on the substrate, collected using a tilt angle. (C) Top-down image of calcinated AuNP film on the glass substrate. (D) Image of a calcinated AuNP film without deposition of the sodium silicate layer leading to amorphous structure and loss of plasmonic activity.

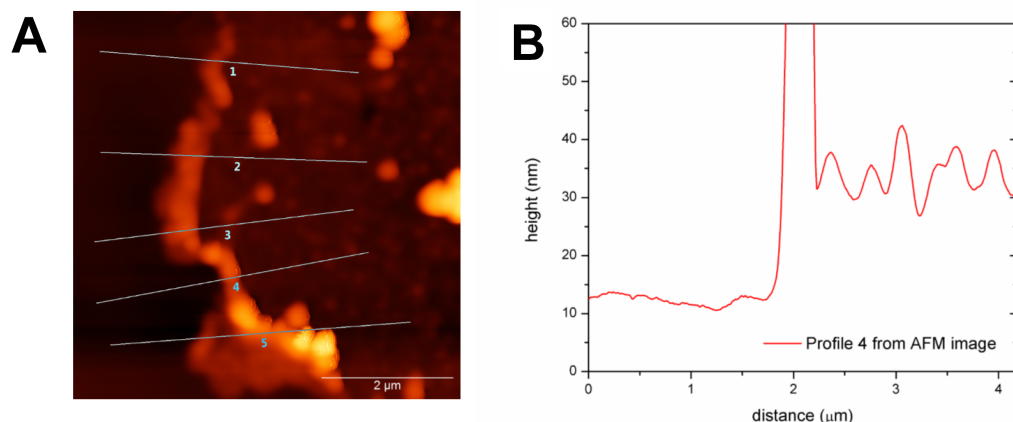


**Figure D.2.** Derivation of film thickness from atomic force microscopy (AFM). (A) AFM image of calcinated gold nanoparticle film, with bare glass exposed to the left. Five height profiles were drawn and the film thickness of  $26.1 \pm 5.7$  nm was derived by subtracting the height of the film from the height of the glass within each of these profiles. (B) Representative line profile from AFM image. Left side represents glass, while right side represents the calcinated AuNP film. The spike in the middle is due to the accumulation of material by the mask used to initially cover the glass surface.

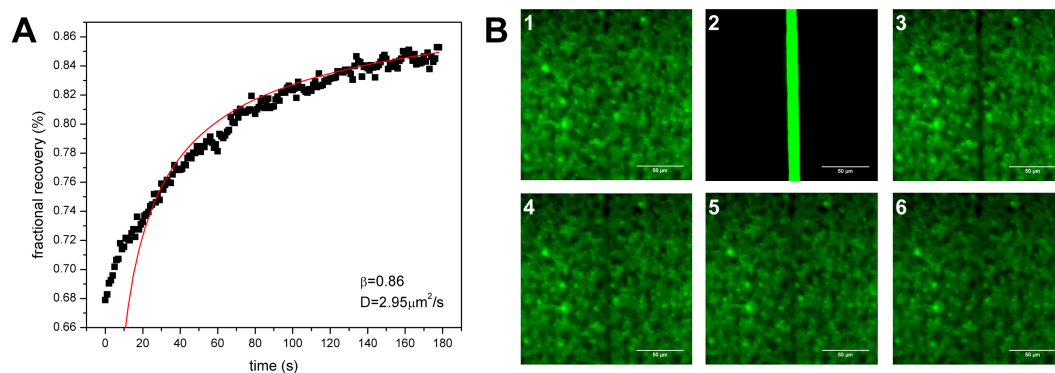


**Figure D.3.** Fluorescence recovery after photobleaching (FRAP) of suspended lipid bilayer. (A) FRAP recovery curve for chicken egg-derived phosphatidylcholine on calcinated gold nanoparticle surface, where  $\beta$  is the mobile fraction and  $D$  is the diffusion coefficient. (B) Fluorescence microscopy images before, during, and after bleaching of lipids. 1 shows the surface before bleaching, 2 shows the bleaching line, and 3-6 show the fluorescence recovery at 0, 60, 120, and 180 s after bleaching, respectively.

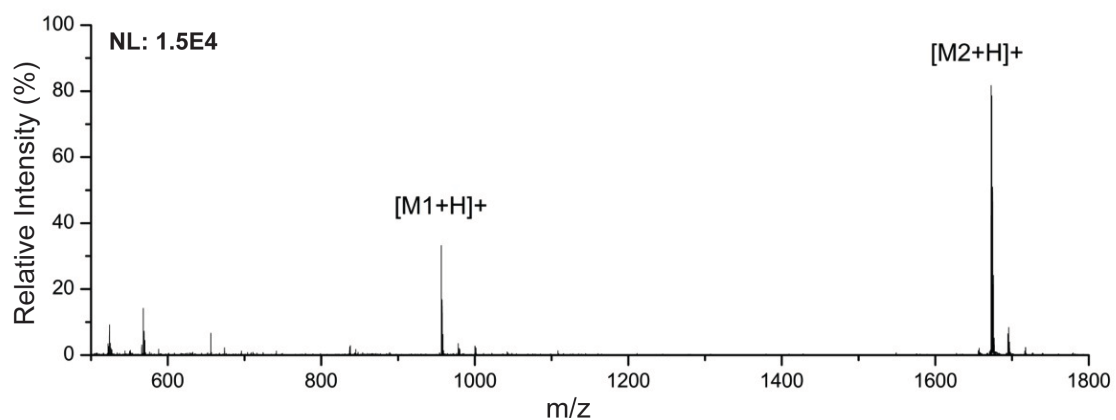


**Figure D.4.** MALDI spectrum of of [Sar1, Thr8]-angiotensin II (M1=956.1) and neurotensin (M2=1672) using CHCA as a matrix.

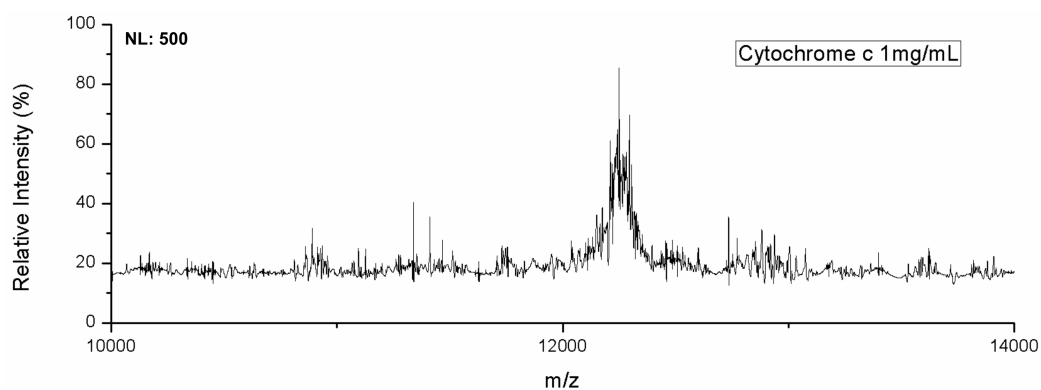


**Figure D.5.** Identification of intact protein by surface-assisted laser desorption/ionization mass spectrometry (SALDI-MS). SALDI mass spectrum of cytochrome c at 1 mg/mL on the calcinated gold nanoparticle film.

## ■ SUPPLEMENTARY TABLE

**Table D.1.** Identified peptide fragments from cytochrome c digest.

Peaks	Theoretical Mass (Da)	Amino Acid Sequence	Position	Experimental Mass (Da) – MALDI <sup>a</sup>	Experimental Mass (Da) – SALDI <sup>b</sup>
<b>C1*</b>	617.7302	KKGER	88-92	617.3	617.3
<b>C2</b>	634.8012	IFVQK	10-14	635.3	---
<b>C3*</b>	648.4079	IFAGIK	82-87	649.3	649.3
<b>C4</b>	779.4484	MIFAGIK	81-87	779.6	779.7
<b>C5</b>	908.2012	MIFAGIKK	81-88	907.7	907.8
<b>C6</b>	965.1412	EDLIAYLK	93-100	964.8	964.8
<b>C7</b>	1169.3366	TGPNLHGLFGR	29-39	1168.9	1168.9
<b>C8*</b>	1435.6735	KGEREDLIAYLK	90-101	1435.2	1435.3
<b>C9</b>	1562.8290	HKTGPNLHGLFGRK	27-40	1563.3	1563.4
<b>C10</b>	1634.9720	IFVQKCAQCHTVEK	10-23	1634.1	1634.1
<b>C11</b>	2139.4470	GITWGEETLMEYLENPKK	57-74	2138.6	2139.7

\*Refers to partially digested cytochrome c peptides by trypsin, not recognized by MASCOT mass fingerprint tool.

<sup>a</sup>MASCOT score: 77, Sequence coverage: 55% (MASCOT, SwissProt), 74% (includes partially digested peptides)

<sup>b</sup>MASCOT score: 73, Sequence coverage: 43% (MASCOT, SwissProt), 74% (includes partially digested peptides)

## APPENDIX E: Supporting Information for Chapter 6

### ■ SUPPLEMENTARY METHODS (from J. Duan, et al.<sup>1</sup>)

**Additional Materials and Reagents.** 3-Mercaptopropionic acid (3-MPA) was from Sigma-Aldrich (St. Louis, MO). Chromium and gold were acquired as pellets of 99.99% purity from Kurt J. Lesker (Jefferson Hills, PA).

**Gold Chip Fabrication.** BK-7 glass substrates were cleaned using a boiling piranha solution (3:1 v/v H<sub>2</sub>SO<sub>4</sub> and 30% H<sub>2</sub>O<sub>2</sub>) for 30 minutes, followed by rinsing with DI water and drying under compressed air. 2 nm of chromium (0.5 Å s<sup>-1</sup>) followed by 46 nm of gold (1.0 Å s<sup>-1</sup>) were then deposited using electron beam evaporation (Temescal, Berkeley, CA) at 5×10<sup>-6</sup> Torr in a Class 1000 cleanroom facility (UCR Center for Nanoscale Science & Engineering).

**Silicate Derivitization.** Gold substrates were immersed in a 10 mM 3-MPA (ethanol) solution overnight, followed by extensive rinsing with ethanol and DI water the next day. PAH (1 mg mL<sup>-1</sup>, pH 8.0) and sodium silicate (22 mg mL<sup>-1</sup>, pH 9.5) were then alternately deposited on the surface using Nalgene pump spray bottles,<sup>2</sup> with DI water rinsing for one minute between each spray. This process was repeated until the designated number of layers was reached, followed by a final DI water rinse and drying under compressed air. Thereafter, the material was heated in a furnace to 450 °C for four hours at a rate of 17 °C min<sup>-1</sup>. Each slide was thoroughly rinsed with ethanol and DI water before use.

## ■ SUPPLEMENTARY FIGURES

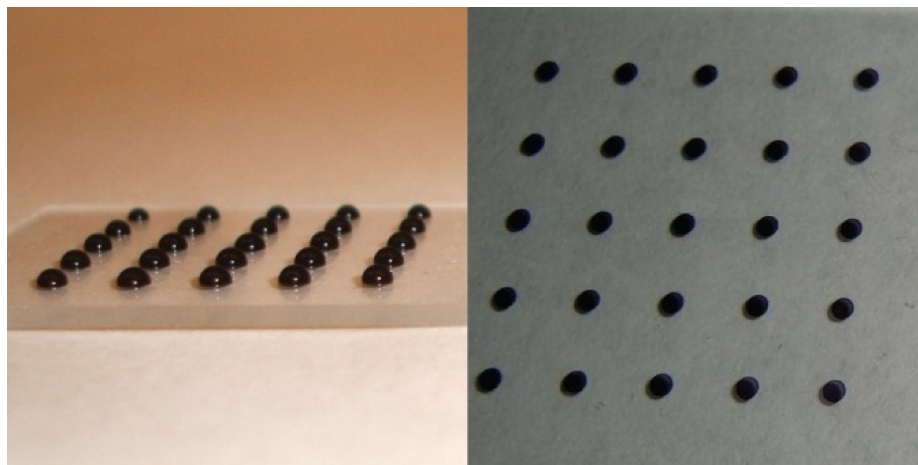


**Figure E.1.** Solution confinement of colloidal gold nanoparticle solutions on photocatalytically patterned glass microscope slides, exhibiting hydrophilic spots with hydrophobic surroundings. (Left) Microarray spots immediately after deposition. (Right) Microarray spots after colloidal suspensions are dried.

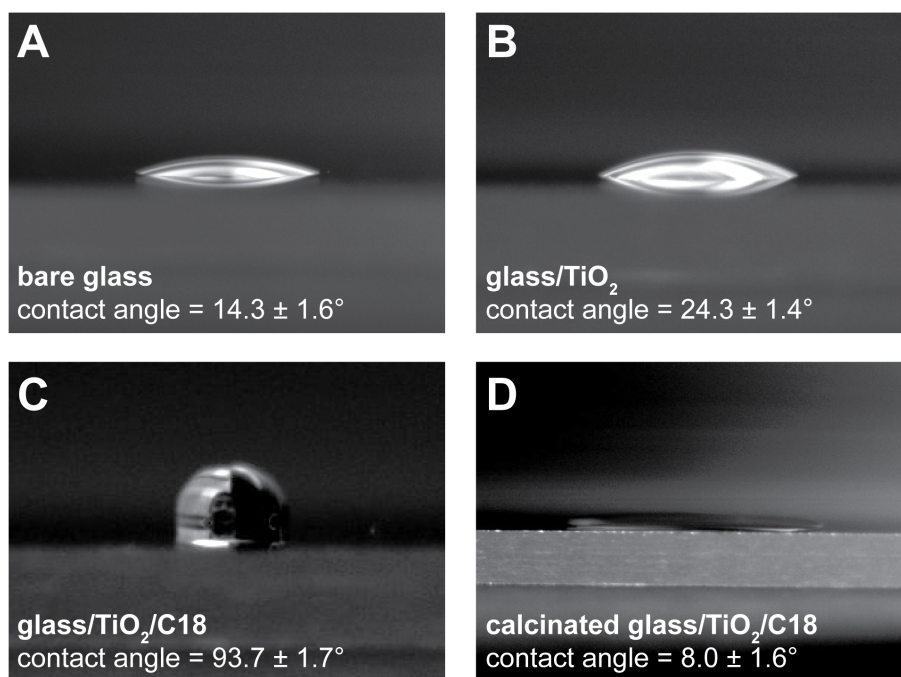


**Figure E.2.** Contact angle measurements at various stages of material fabrication.  $n = 5$  for all reported values. (A) Bare glass slide, cleaned with piranha solution. (B) Glass slide with TiO<sub>2</sub> coating. (C) Glass slide with TiO<sub>2</sub> coating, followed by C18 coating. (D) Calcinated glass slide with TiO<sub>2</sub> and C18 coatings. Decreased contact angle from bare glass is likely due to a thermal annealing effect of the glass surface from the high temperature used during calcination.

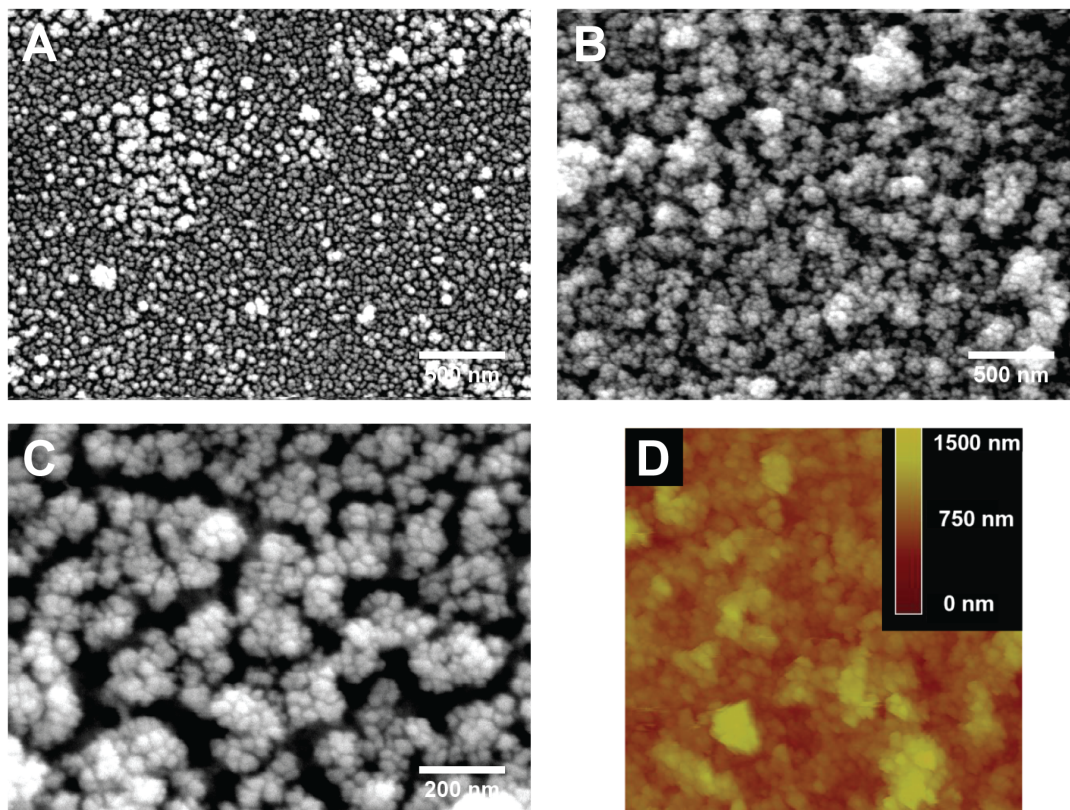


**Figure E.3.** SEM (A-C) and AFM (D) images of calcinated gold nanoparticles. (A) 100,000 $\times$  magnification, scale bar represents 500 nm. (B) 100,000 $\times$  magnification, scale bar represents 500 nm. (C) 250,000 $\times$  magnification, scale bar represents 200 nm. (D) AFM image to visualize z-axis roughness and porosity.

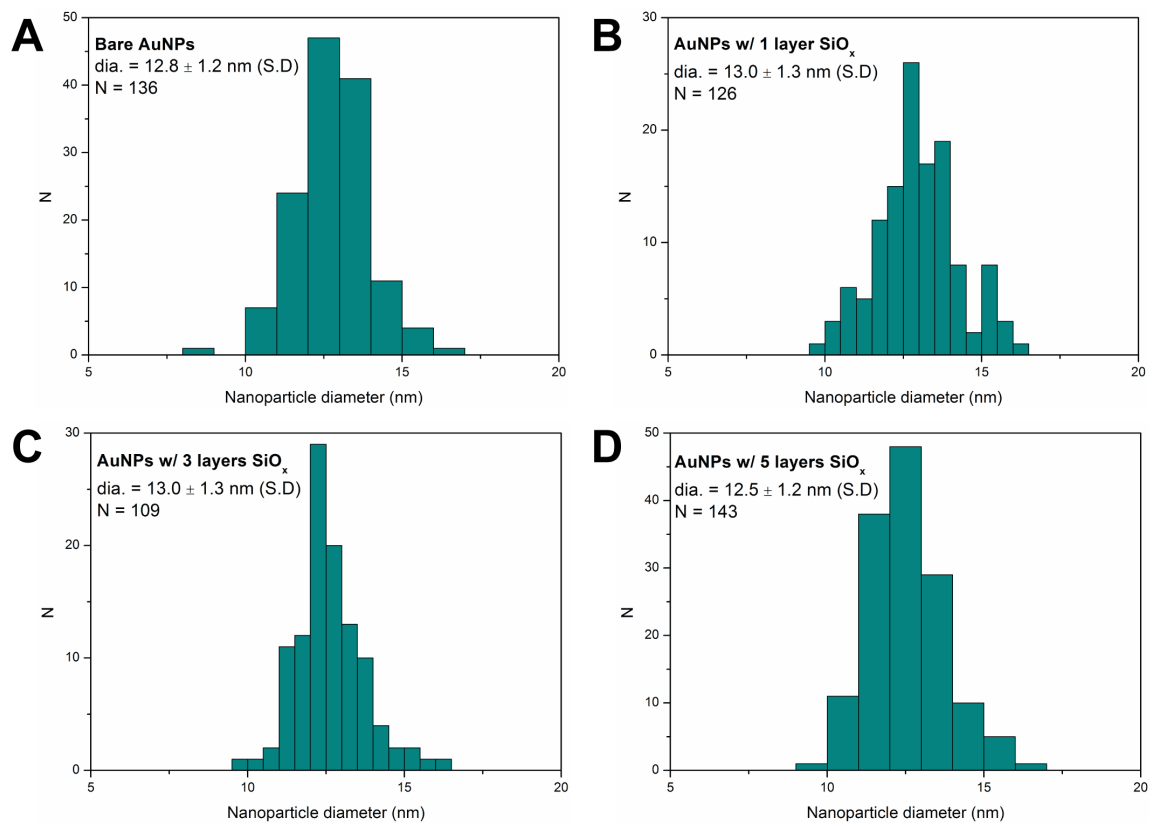


**Figure E.4.** Frequency distributions of diameters for individual nanoparticles in Figure 6.2. Diameters are unaffected by calcination process with silicate coating. (A) Bare AuNs, no treatment. (B) AuNPs with 1 layers of silicate and calcinated. (C) AuNPs with 3 layers of silicate and calcinated. (D) AuNPs with 5 layers of silicate and calcinated.

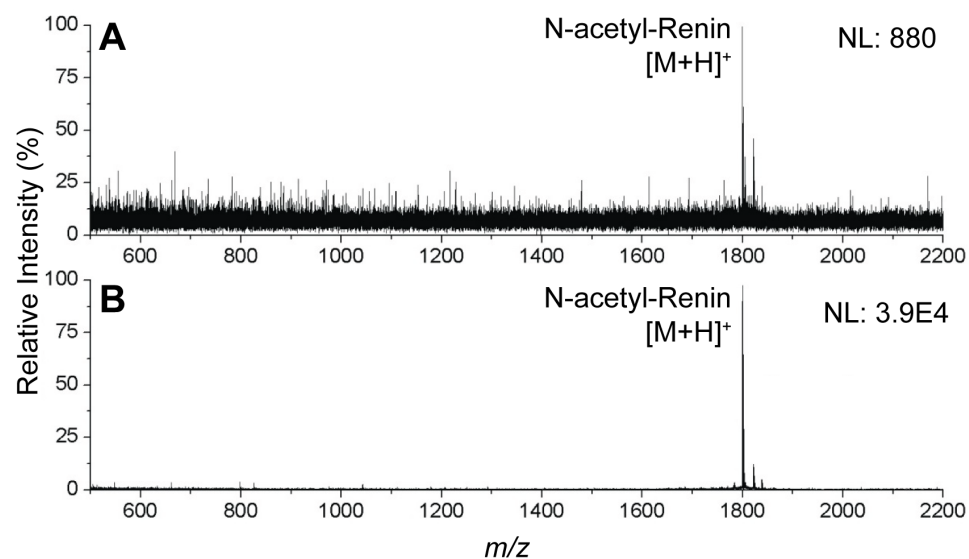


**Figure E.5.** Deposited AuNP-(PAH-silicate)<sub>1</sub> calcination effects on ionization of N-acetyl tetradecapeptide renin substrate. *S/N* ratios are reported for the N-acetyl-Renin peak. (A) Before calcination (*S/N* = 5.5). (B) After calcination (*S/N* = 60).

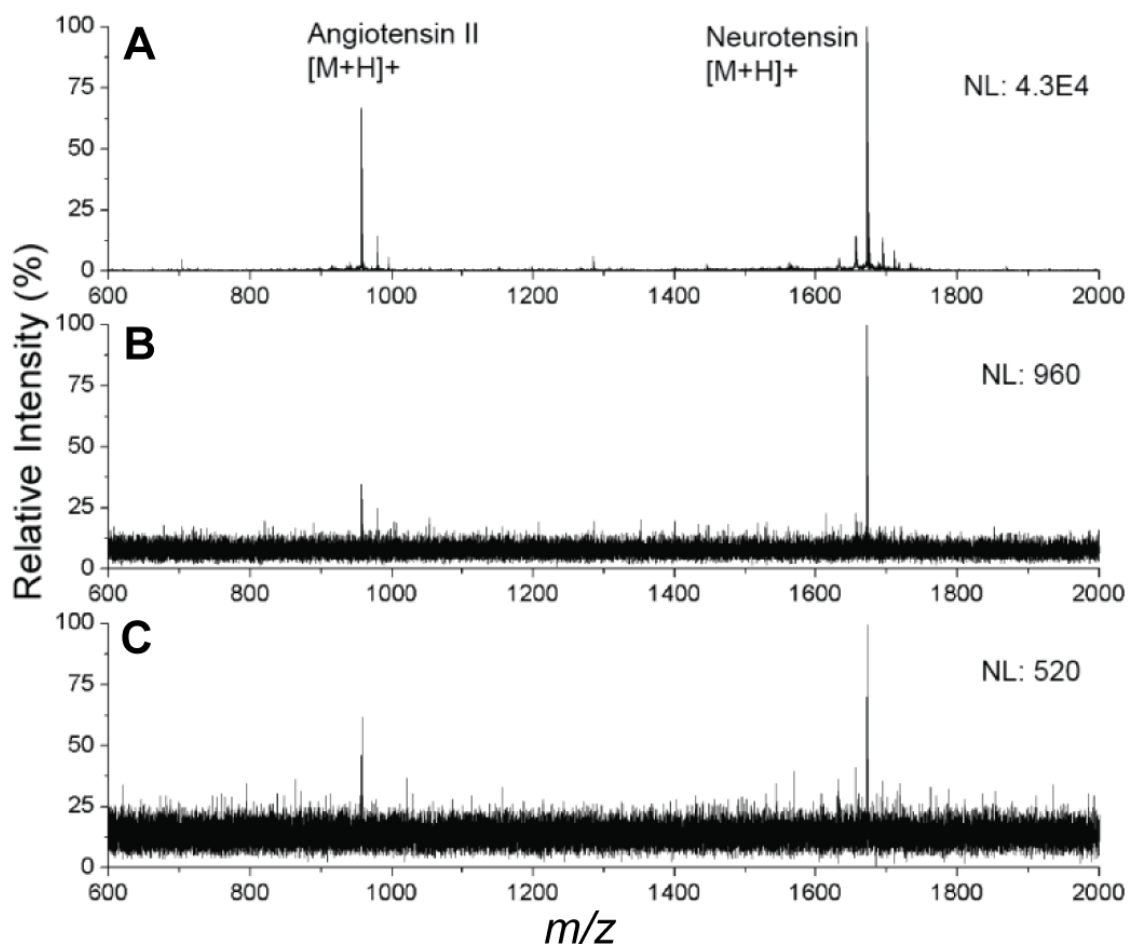


**Figure E.6.** Laser fluence threshold study for ionization of 20 pmol [Sar<sup>1</sup>, Thr<sup>8</sup>]-angiotensin II and neurotensin. (A) Laser fluence = 1900 a.u. (B) Laser fluence = 1600 a.u. (C) Laser fluence = 1450 a.u.

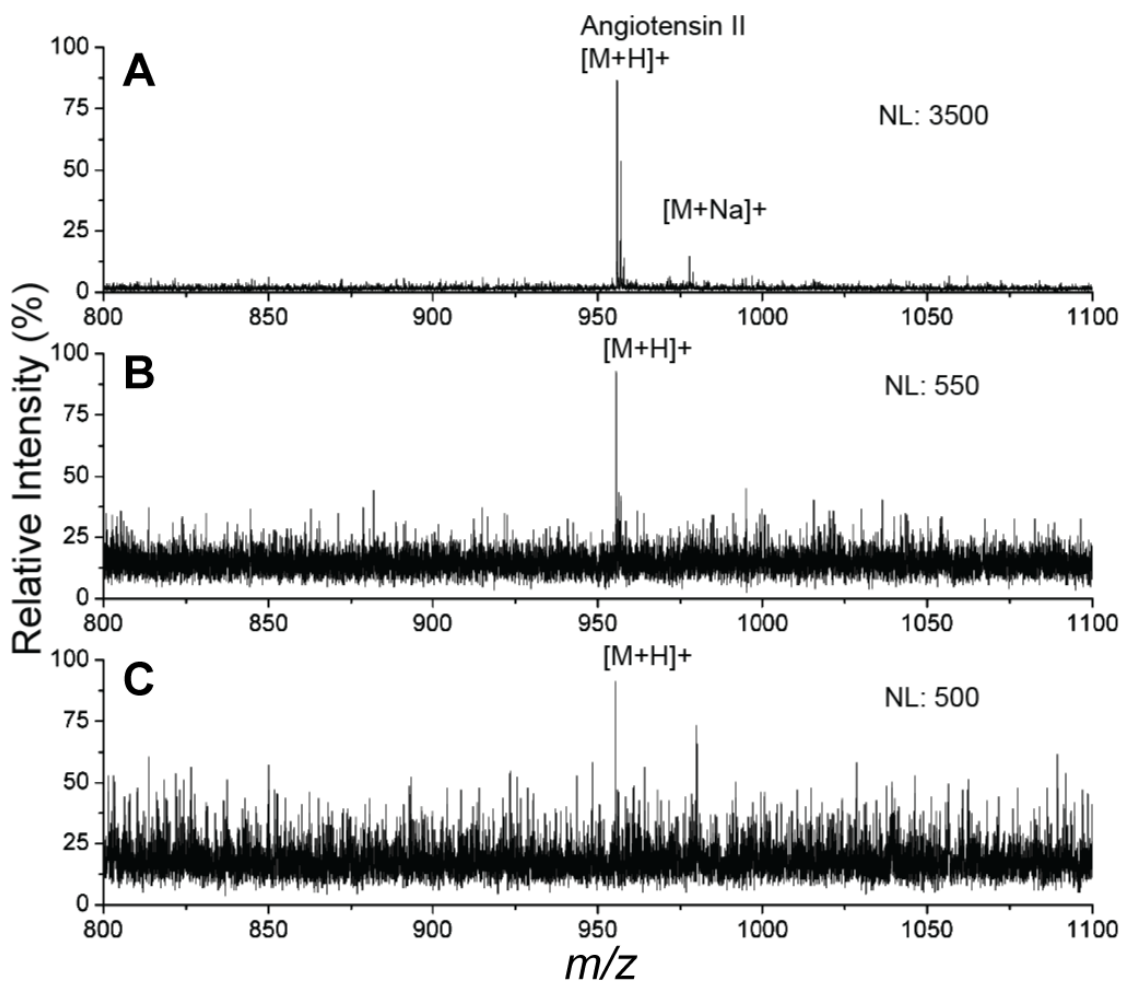


**Figure E.7.** Detection of [Sar<sup>1</sup>, Thr<sup>8</sup>]-angiotensin II in the low femtomole range. (A) 200 fmol. (B) 20 fmol. (C) 2 fmol.

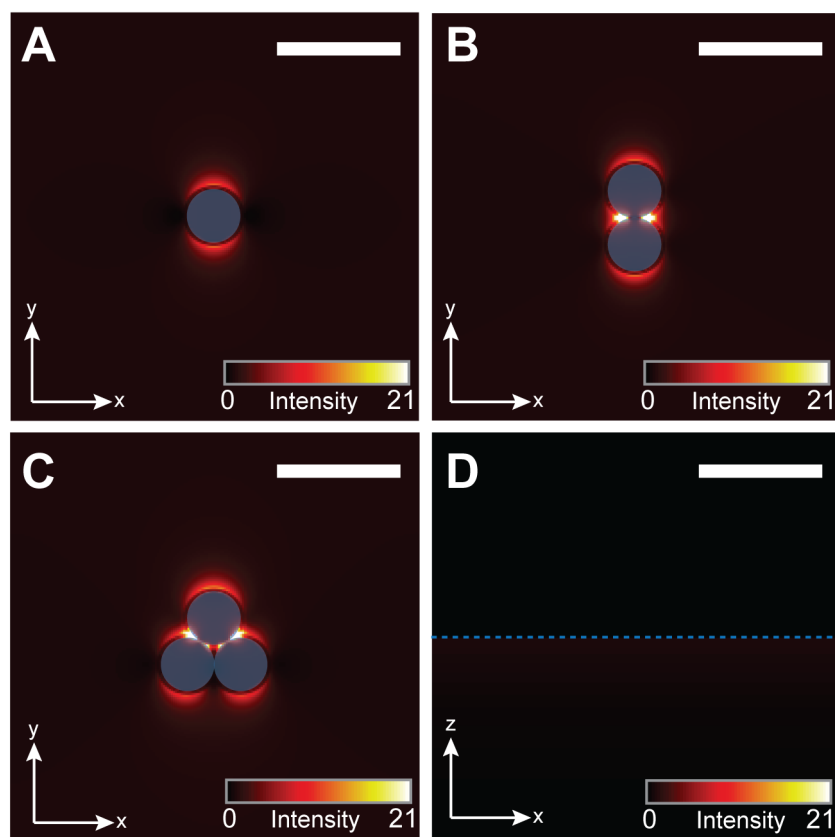


**Figure E.8.** Numerical simulations of plasmonic fields induced by  $\lambda = 520$  nm light source for different nanoscale geometries. Scale bars represent 30 nm and blue represents the gold surface. (A) Single gold nanoparticle. (B) Gold nanoparticle dimer. (C) Gold nanoparticle trimer. (D) Planar gold film.

## ■ REFERENCES

- (1) Duan, J.; Linman, M. J.; Cheng, Q. Ultrathin Calcinated Films on a Gold Surface for Highly Effective Laser Desorption/Ionization of Biomolecules. *Anal. Chem.* **2010**, *82*, 5088-5094.
- (2) Linman, M. J.; Culver, S. P.; Cheng, Q. Fabrication of Fracture-Free Nanoglassified Substrates by Layer-by-Layer Deposition with a Paint Gun Technique for Real-Time Monitoring of Protein-Lipid Interactions. *Langmuir* **2009**, *25*, 3075-3082.